DETERMINATION OF RE(ε'/ε) BY THE SIMULTANEOUS DETECTION OF THE FOUR $K_{L,S} \rightarrow \pi\pi$ DECAY MODES

BY

J. RITCHIE PATTERSON

DECEMBER, 1990

THE UNIVERSITY OF CHICAGO

DETERMINATION OF RE(ε'/ε) BY THE SIMULTANEOUS
DETECTION OF THE FOUR $K_{L,S} \to \pi\pi$ DECAY MODES

A DISSERTATION SUBMITTED TO

THE FACULTY OF THE DIVISION OF PHYSICAL SCIENCES

IN CANDIDACY FOR THE DEGREE OF

DOCTOR OF PHILOSOPHY

DEPARTMENT OF PHYSICS

BY J. RITCHIE PATTERSON

CHICAGO, ILLINOIS
DECEMBER, 1990

ACKNOWLEDGEMENTS

Finally, I thank my parents for their encouragement and moral support all along the way.

ii

TABLE OF CONTENTS

LIST OF ILLUSTRATIONS

LIST OF TABLES

ABSTRACT

The E731 experiment at Fermilab has searched for direct CP violation in $K^0 \to \pi\pi$ decays, which is parametrized by ε'/ε. For the first time all four of the $K_{L,S} \to \pi\pi$ modes were collected simultaneously, greatly facilitating studies of systematic uncertainty. We find $\mathrm{Re}(\varepsilon'/\varepsilon) = -0.0003 \pm 0.0014\,\text{(stat)} \pm 0.0006\,\text{(syst)}$. The result provides no evidence for direct CP violation.

CHAPTER 1

INTRODUCTION

According to the *CPT* theorem [1, 2, 3], particle interactions are invariant under the combined operation of charge conjugation (*C*), parity inversion (*P*) and time reversal (*T*). For a long time it was believed that interactions were also invariant under each of these separately, but in 1956 parity violation was proposed by Lee and Yang [4] to explain the decays of *K* mesons, and the following year it was observed in the nuclear decay of Co^{60} [5]. Some of the symmetry was restored, however, when Landau pointed out that the parity-violating weak interactions were invariant under the combined operation of *C* and *P* [6]. For example, *CP* takes the left-handed neutrino into the right-handed anti-neutrino, both of which are realized in nature, whereas the operation of *C* or *P* alone would produce one of the charge conjugate states, which have not been observed. The notions of *CP* invariance and *T* invariance therefore replaced the earlier belief in invariance under the three separate operations. In 1964, however, Christenson, Cronin, Fitch and Turlay [7] observed *CP* violation in the decays of the neutral kaons and the premise of *CP* conservation had to be abandoned as well. While the violation of parity and charge conjugation is now seen as the result of the left-handedness of *W* boson interactions, even now, twenty-five years after the discovery of *CP* violation, its origins remain a mystery. Although *CP* violation might be a by-product of the Standard Model of electroweak interactions, so far there is no conclusive evidence that this is so,

1

and the possibility remains that it originates from interactions beyond the Standard Model.[1]

1.1 CP Eigenstates in the Neutral Kaon System

Let us look at the phenomenology of the neutral kaon system, including what is known experimentally.[2] The strong interaction produces kaons which are eigenstates of strangeness, the K^0 and $\overline{K}^0$. These are CP conjugates of one another, so that with an appropriate choice of phase we can write

$$CP|K^0\rangle = |\overline{K}^0\rangle$$
$$CP|\overline{K}^0\rangle = |K^0\rangle \ . \tag{1.1}$$

From these we can construct the CP eigenstates

$$|K_1\rangle = \frac{1}{\sqrt{2}}\left(|K^0\rangle + |\overline{K}^0\rangle\right) \qquad CP = +1$$

and

$$|K_2\rangle = \frac{1}{\sqrt{2}}\left(|K^0\rangle - |\overline{K}^0\rangle\right) \qquad CP = -1 \ . \tag{1.2}$$

If CP were conserved by the weak interaction then $|K_1\rangle$ and $|K_2\rangle$ would be the weak eigenstates. In that case they would have well-defined masses and lifetimes with the following CP-conserving decays:

$$
\begin{aligned}
|K_1\rangle &\to \pi^0\pi^0 & CP &= +1 \\
&\to \pi^+\pi^- & CP &= +1 \\
|K_2\rangle &\to \pi^0\pi^0\pi^0 & CP &= -1
\end{aligned}
\tag{1.3}
$$

---

[1] Even if the Standard Model does describe CP violation, its source, like that of parity violation, will await a deeper explanation.

[2] For more extensive discussions, see, for example, the book of Commins and Bucksbaum [8], and the reviews by Jarlskog [9] and Kleinknecht [10].

in addition to other decays to non-eigenstates of *CP*. Because of the large phase space for the $\pi\pi$ final states, the $|K_1\rangle$ would have a much shorter lifetime than the $|K_2\rangle$.

In fact, because *CP* violation is small, this description is almost realized; however, in 1964 it was observed that 0.2% of the time the long-lived, supposedly *CP* odd, kaon decayed to $\pi^+\pi^-$. That this phenomenon demonstrated *CP* violation was confirmed shortly thereafter [11] when interference was observed between the two pion decays of long and short-lived kaons. Before that, another particle with the same mass but different quantum numbers could have been responsible for the decay.

This suggests that the long-lived particle is really a mixture of the *CP* eigenstates:

$$|K_L\rangle \sim |K_2\rangle + \tilde{\varepsilon}|K_1\rangle \ . \tag{1.4}$$

That is, that the long-lived weak eigenstate is primarily *CP* odd, but with a small admixture of the *CP* even $|K_1\rangle$ state.

Let us look at mixing of the eigenstates in more detail. The physical kaons associated with the weak hamiltonian (i.e. those with well-defined mass and lifetime) should each satisfy the time-dependent Schrodinger equation

$$i\frac{\partial \psi}{\partial t} = H\psi \ , \tag{1.5}$$

where *H* is the effective hamiltonian describing the second order ($\Delta S = 2$) weak transitions between the K^0 and $\overline{K}^0$. Since the time dependence of the solutions will be of the form

$$\psi(t) = Ae^{-imt}e^{-\Gamma t/2} \tag{1.6}$$

where *m* and Γ are the kaon mass and decay widths, we can reformulate this as a matrix equation with eigenstates corresponding to the physical kaons. Furthermore, we can separate the hamiltonian into two components of the form

$$\mathbf{H} = \mathbf{M} - i\,\Gamma/2 \tag{1.7}$$

where $\mathbf{M}$ and Γ are the 2 x 2 mass and decay matrices in the K^0 and $\bar{K}^0$ basis, and are separately hermitian. One finds that the eigenstates are

$$|K_L\rangle = \frac{1}{\sqrt{2(1+|\varepsilon|^2)}}\left((1+\varepsilon)|K^0\rangle - (1-\varepsilon)|\bar{K}^0\rangle\right)$$

$$|K_S\rangle = \frac{1}{\sqrt{2(1+|\varepsilon|^2)}}\left((1+\varepsilon)|K^0\rangle + (1-\varepsilon)|\bar{K}^0\rangle\right) \qquad (1.8)$$

where the mixing parameter, ε, is given by

$$\varepsilon = \frac{\langle K^0|\mathbf{H}|\bar{K}^0\rangle - \langle\bar{K}^0|\mathbf{H}|K^0\rangle}{i(\Gamma_S - \Gamma_L)/2 - (m_S - m_L)} \qquad (1.9)$$

with $m_{L,S}$ and $\Gamma_{L,S}$ the eigenvalues of $\mathbf{M}$ and Γ respectively. In terms of $|K_1\rangle$ and $|K_2\rangle$, the eigenstates are

$$|K_L\rangle = \frac{1}{\sqrt{1+|\varepsilon|^2}}\left(|K_2\rangle + \varepsilon|K_1\rangle\right)$$

$$|K_S\rangle = \frac{1}{\sqrt{1+|\varepsilon|^2}}\left(|K_1\rangle + \varepsilon|K_2\rangle\right) \quad , \qquad (1.10)$$

so that we can identify ε with $\bar{\varepsilon}$ in Equation (1.4).

The eigenstates $|K_L\rangle$ and $|K_S\rangle$ reduce to the CP eigenstates $|K_1\rangle$ and $|K_2\rangle$ with CP conserved only if the off-diagonal elements of $\mathbf{H}$ are equal. That is if

$$\langle K^0|\mathbf{H}|\bar{K}^0\rangle = \langle\bar{K}^0|\mathbf{H}|K^0\rangle \quad . \qquad (1.11)$$

In the context of the Standard Model, these are second order weak transitions. In the above calculations, we have assumed that the diagonal elements of $\mathbf{M}$ and Γ were identical, which follows from CPT invariance. Had we not done so, we would have found two distinct values of ε, ε_L and ε_S, for the $|K_L\rangle$ and $|K_S\rangle$ states [12].

In terms of these eigenstates we can now parametrize CP violation in the $\pi\pi$ decays by

$$\eta_{+-} \equiv \frac{\langle \pi^+ \pi^- |T| K_L \rangle}{\langle \pi^+ \pi^- |T| K_S \rangle} \tag{1.12}$$

and

$$\eta_{00} \equiv \frac{\langle \pi^0 \pi^0 |T| K_L \rangle}{\langle \pi^0 \pi^0 |T| K_S \rangle} , \tag{1.13}$$

where T is the effective hamiltonian for the first order ($\Delta S = 1$) transitions. On the basis of the mixing alone, we expect

$$\eta_{+-} = \frac{\langle \pi^+ \pi^- |T| K_2 \rangle + \varepsilon \langle \pi^+ \pi^- |T| K_1 \rangle}{\langle \pi^+ \pi^- |T| K_1 \rangle + \varepsilon \langle \pi^+ \pi^- |T| K_2 \rangle} = \varepsilon \tag{1.14}$$

since by assumption $\langle \pi^+ \pi^- |T| K_2 \rangle = 0$. Similarly,

$$\eta_{00} = \varepsilon . \tag{1.15}$$

From determinations of the K_L and K_S lifetimes and branching fractions and also the ratio $|\eta_{+-}/\eta_{00}|$, the values of $|\eta_{+-}|$ and $|\eta_{00}|$ are $(2.266 \pm 0.018) \times 10^{-3}$ and $(2.245 \pm 0.019) \times 10^{-3}$ respectively [13]. The phase ϕ_{+-} of η_{+-} has been determined by comparison of the time distribution of $\pi^+ \pi^-$ decays with that of $K_L \to \pi^\pm e^\mp \nu$ decays downstream of a regenerator, and by comparison of the time distributions of the $\pi^+ \pi^-$ decays of kaons produced in displaced targets, and is found to be $45.1° \pm 1.0°$[13, 14]. The value of ϕ_{00} is more difficult to measure directly, but from determinations of $\phi_{00}-\phi_{+-}$, it is equal to $45.0° \pm 2.0°$[14, 15]. By *CPT* invariance the values of ϕ_{+-} and ϕ_{00} should be nearly identical.

It is interesting to compare the experimental values of these parameters with that of ε, which can be separately determined by means of the charge asymmetry of the decays $K_L \to \pi^\pm e^\mp \nu$ and $K_L \to \pi^\pm \mu^\mp \nu$. The charge aymmetry, δ, is defined as

$$\delta \equiv \frac{\Gamma\left(K_L \to \pi^- \ell^+ \nu\right) - \Gamma\left(K_L \to \pi^+ \ell^- \nu\right)}{\Gamma\left(K_L \to \pi^- \ell^+ \nu\right) + \Gamma\left(K_L \to \pi^+ \ell^- \nu\right)} . \tag{1.16}$$

Because of the $\Delta S = \Delta Q$ rule, which states that the change in strangeness equals the change in charge in a charged current interaction, the decays to the positively charged leptons (ℓ^+) come from the $|K^0\rangle$ component of the $|K_L\rangle$, and those to the negatively charged leptons (ℓ^-) come from the $|\overline{K}^0\rangle$. Since the decay rates are given by the squares of the decay amplitudes, it follows from Equation (9.4) that for a pure K_L beam

$$\delta = 2\mathrm{Re}\varepsilon , \tag{1.19}$$

assuming that $\Delta S = \Delta Q$ rule is exact. From determinations of δ, $\mathrm{Re}\varepsilon = (1.630 \pm 0.083) \times 10^{-3}$ [13]. To find the phase of ε, we rewrite Equation (1.9) as

$$\varepsilon = \frac{\mathrm{Im}\,\Gamma_{12}/2 + i\,\mathrm{Im}\,M_{12}}{i(\Gamma_S - \Gamma_L)/2 - (m_S - m_L)} , \tag{1.20}$$

where M_{12} are Γ_{12} the off-diagonal elements of the mass and decay matrices. The phase of ε is then given by

$$\arg \varepsilon = -\arctan\left(\frac{\mathrm{Im}\,\Gamma_{12}}{2\mathrm{Im}\,M_{12}}\right) + \arctan\left(\frac{2\Delta m}{\Gamma_S}\right) \tag{1.21}$$

where $\Delta m = m_L - m_S$. The first of these terms is small, $<1°$, while the second is $43.67° \pm 0.13°$ based on determinations of Δm and Γ_S. From these results it follows that

$$|\varepsilon| = (2.25 \pm 0.12) \times 10^{-3} .$$

Within the experimental error, then

$$|\eta_{+-}| = |\eta_{00}| = |\varepsilon| ,$$

which is consistent with asymmetric mixing in the kaon mass matrix followed by CP-conserving decays.

In superweak theories of CP violation [16] the transition $K_L \leftrightarrow K_S$ is the result of a new CP-violating interaction, which is undetectable in other systems, where second order weak effects dominate. Within these theories,

mixing is the only manifestation of *CP* violation. The experimental values of $|\eta_{+-}|$, $|\eta_{00}|$ and $|\varepsilon|$ given above are consistent with this model.

1.2 Direct CP Violation

There is another channel for *CP* violation that we have not yet considered: the direct decay of the $CP = -1$ kaon state to a $CP = +1$ pion state. That is

$$K_2 \to \pi^0 \pi^0 \text{ or } \pi^+ \pi^- .$$

This "direct" *CP* violation, as well as the "mixing" violation just discussed, is predicted to exist by the Standard Model.

To understand direct *CP* violation further, let us consider the isospin composition of the $\pi^+ \pi^-$ and $\pi^0 \pi^0$ states. In terms of the $I = 0$ and $I = 2$ components (the $I = 1$ state is forbidden by the Bose symmetry of the system) they are given by

$$\langle \pi^+ \pi^- | = \sqrt{\frac{2}{3}} \langle 0| + \frac{1}{\sqrt{3}} \langle 2|$$

$$\langle \pi^0 \pi^0 | = -\frac{1}{\sqrt{3}} \langle 0| + \sqrt{\frac{2}{3}} \langle 2| , \qquad (1.22)$$

where $\langle \pi^+ \pi^- |$ is shorthand for the superposition of the $\langle \pi^+ \pi^- |$ and $\langle \pi^- \pi^+ |$ states, and $\langle n|$ labels the state with $I = n$. We now define the following ratios of K_S and K_L transition amplitudes to the two isospin states:

$$\varepsilon_0 = \frac{\langle 0|T|K_L \rangle}{\langle 0|T|K_S \rangle}$$

$$\varepsilon_2 = \frac{1}{\sqrt{2}} \frac{\langle 2|T|K_L \rangle}{\langle 0|T|K_S \rangle}$$

$$\omega_2 = \frac{\langle 2|T|K_S \rangle}{\langle 0|T|K_S \rangle} \qquad (1.23)$$

In terms of these, the parameter η_{+-} is given by

$$\eta_{+-} \equiv \frac{\langle \pi^+ \pi^- |T| K_L \rangle}{\langle \pi^+ \pi^- |T| K_S \rangle}$$

$$= \frac{\sqrt{\frac{2}{3}} \varepsilon_0 + \frac{1}{\sqrt{3}} \sqrt{2} \varepsilon_2}{\sqrt{\frac{2}{3}} + \frac{1}{\sqrt{3}} \omega_2}$$

$$= \frac{\varepsilon_0 + \varepsilon_2}{1 + \frac{1}{\sqrt{2}} \omega_2}$$

$$\approx \varepsilon_0 + \varepsilon_2 - \frac{1}{\sqrt{2}} \varepsilon_0 \omega_2 \ , \tag{1.24}$$

where for the last step we have used the fact that ω_2 is small, about $1/22$.[1] Similarly, we find

$$\eta_{00} \equiv \frac{\langle \pi^0 \pi^0 |T| K_L \rangle}{\langle \pi^0 \pi^0 |T| K_S \rangle}$$

$$\approx \varepsilon_0 - 2 \left(\varepsilon_2 - \frac{1}{\sqrt{2}} \varepsilon_0 \omega_2 \right) . \tag{1.25}$$

Now we would like to relate these expressions to ε and put them into a more transparent form. To do so, we consider the K^0 and $\overline{K}^0$ transition amplitudes to the two isospin final states, given by

$$\langle 0 |T| K^0 \rangle = A_0 e^{i\delta_0} \quad \text{and} \quad \langle 0 |T| \overline{K}^0 \rangle = A_0^* e^{i\delta_0}$$
$$\langle 2 |T| K^0 \rangle = A_2 e^{i\delta_2} \qquad \qquad \langle 2 |T| \overline{K}^0 \rangle = A_2^* e^{i\delta_2} \tag{1.26}$$

where the δ_n are the pion-pion final state phase shifts. Using the phase convention due to Wu and Yang [17] in which $A_0 = A_0^*$, it follows from Equations (1.8) that

$$\varepsilon_0 = \varepsilon$$

---

[1] This is a manifestation of the $\Delta I = 1/2$ rule.

$$\varepsilon_2 = \frac{1}{\sqrt{2}} \frac{i \operatorname{Im} A_2 + \varepsilon \operatorname{Re} A_2}{A_0} e^{i(\delta_2 - \delta_0)}$$

$$\omega_2 = \frac{\operatorname{Re} A_2 + i\varepsilon \operatorname{Im} A_2}{A_0} e^{i(\delta_2 - \delta_0)} \qquad (1.27)$$

Thus, the expressions for η_{+-} and η_{00} become

$$\eta_{+-} \approx \varepsilon + \varepsilon'$$

$$\eta_{00} \approx \varepsilon - 2\varepsilon' \qquad (1.28)$$

where ε' is defined as

$$\varepsilon' = \varepsilon_2 - \frac{1}{\sqrt{2}} \varepsilon_0 \omega_2 \qquad (1.29)$$

and to first order in ε is given by

$$\varepsilon' = \frac{i}{\sqrt{2}} \frac{\operatorname{Im} A_2}{A_0} e^{i(\delta_2 - \delta_0)} \qquad (1.30)$$

From measurement of the pion phase shifts, it is known that the phase of ε' is equal to $37° \pm 5°$[18, 19], i.e., very close to that of ε. Furthermore, since $|\eta_{+-}| \approx |\eta_{00}|$, the magnitude of ε' must be small. The relationships between η_{+-}, η_{00}, ε and ε' are shown graphically in Figure 1.

As we have already seen, one class of models, the superweak, predicts that ε' is equal to zero. The Standard Model, however, allows for a small, but probably non-zero value, with most predictions for $|\varepsilon'/\varepsilon|$ ($\approx \operatorname{Re}(\varepsilon'/\varepsilon)$) lying in the range between zero and 0.005.

Experiments mounted to determine the value of ε' do so by measuring the double ratio of decay rates

$$\mathbf{R} \equiv \frac{\Gamma\left(K_L \to \pi^0 \pi^0\right)/\Gamma\left(K_S \to \pi^0 \pi^0\right)}{\Gamma\left(K_L \to \pi^+ \pi^-\right)/\Gamma\left(K_S \to \pi^+ \pi^-\right)} = \left|\frac{\eta_{00}}{\eta_{+-}}\right|^2$$

$$= \left|\frac{\varepsilon - 2\varepsilon'}{\varepsilon + \varepsilon'}\right|^2$$

$$\approx 1 - 6\,\mathrm{Re}\!\left(\frac{\varepsilon'}{\varepsilon}\right) \ . \qquad (1.31)$$

Any deviation of **R** from unity would signify a non-zero value of $\mathrm{Re}(\varepsilon'/\varepsilon)$. The results of past experiments are tabulated in Table 1. The only evidence for a non-zero value of $\mathrm{Re}(\varepsilon'/\varepsilon)$, and thus direct CP violation, was provided by the NA31 experiment at CERN in 1988. Such an observation, if confirmed, would mark a dramatic advance in our knowledge of CP violation. The result reported in this thesis is the first since the NA31 result and the only other with comparable sensitivity.

This thesis begins with a description of the technique used to determine the value of $\mathrm{Re}(\varepsilon'/\varepsilon)$. It continues in Chapters 3 and 4 with a descrip-
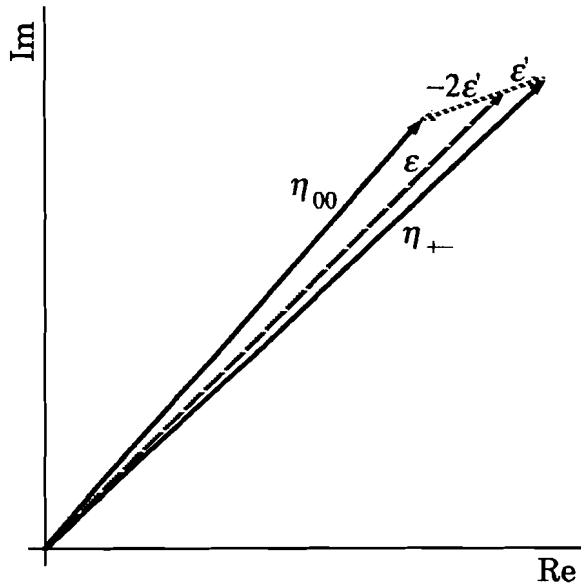
Figure 1. Graphical representation of the parameters of CP violation. The magnitude of ε' and the phase difference between ε and ε' are exaggerated in the figure.

TABLE 1. Recent determinations of $\mathrm{Re}(\varepsilon'/\varepsilon)$. The first errors quoted are statistical, the second systematic.

Collaboration	Year	R	$\mathrm{Re}(\varepsilon'/\varepsilon)$ (10^{-4})
Chicago-Saclay [20]	1985	$1.028 \pm 0.032 \pm 0.014$	$-46 \pm 53 \pm 24$
Yale-BNL [21]	1985	$0.990 \pm 0.043 \pm 0.026$	17 ± 82
Chicago-Elmhurst-FNAL-Princeton-Saclay (Fermilab E731) [22]	1988	$0.979 \pm 0.018 \pm 0.012$	$35 \pm 30 \pm 20$
Dortmund-Edinburgh-Mainz-Orsay-Pisa-Siegen (CERN NA31) [23]	1988	$0.980 \pm 0.004 \pm 0.005$	$33 \pm 7 \pm 8$

tion of the beam line and detector and a summary of the data collection. Reconstruction of the decays to $\pi^+\pi^-$ is the subject of Chapter 5. Chapters 6 and 7 describe analysis of the neutral mode and calibration of the calorimeter used to reconstruct them. Chapter 8 describes the Monte Carlo simulation of the experiment, an important component of the analysis. Finally, Chapter 9 is devoted to extraction of the value of $\mathrm{Re}(\varepsilon'/\varepsilon)$ from the data. The important question of whether the Standard Model correctly accounts for *CP* violation is addressed in the concluding chapter.

CHAPTER 2

THE MEASUREMENT TECHNIQUE

2.1 Overview

The goal of the experiment is to measure the double ratio of kaon decay rates given in Equation (1.31) to better than 1%. To achieve this precision one must observe many $K_{L,S} \to \pi\pi$ decays and carefully control possible sources of bias. Since the experiment was designed with these requirements in mind, many potential biases were suppressed outright. In this chapter, our experimental technique is described, along with our reasons for choosing it. We discuss biases which we hope to eliminate, as well as those which remain and so will require attention in the analysis. The second part of the chapter introduces the principal components of the detector.

2.2 The Double Beam Technique

This experiment employed two nearly parallel beams. In one beam we observed the decays $K_S \to 2\pi$ and in the other we observed the decays $K_L \to 2\pi$. Precise determination of $\mathrm{Re}(\varepsilon'/\varepsilon)$ demands that the relative detection efficiencies of K_S and K_L decays be well-known, and simultaneous observation of the two was crucial to meeting this requirement. In general, the detection efficiency is a function of decay kinematics and detector geometry and response. It can be sensitive to shifts in phototube gains or drift chamber wire efficiencies which can arise from electronic drifts or changes in beam intensity. The experiment could be done by observing K_S and K_L decays to charged and neutral pions in four separate data collection runs, switching between K_L and K_S running by changing the separation between

12

the target and detector. This technique has a drawback: changing the separation between the target and detector affects the flux of all types of particles produced in the target, and therefore the detector response as well, possibly biasing the result. By observing K_S and K_L decays to a common final state simultaneously, the detector response was intrinsically the same for both.

The K_S and K_L beams were produced by generating two parallel K_L beams and then producing K_S in one of them by means of a regenerator. The K_L mesons were produced by protons striking a target, and were then collimated into two beams. These propagated down a long drift volume where short-lived hyperons decayed and charged primary and secondary particles were magnetically swept away. When they entered the experimental hall and one of them struck the regenerator, the beams were composed primarily of K_L mesons.

As a function of proper time t, the kaon decay amplitude to $\pi^+\pi^-$ or $\pi^0\pi^0$ in the regenerated beam is given by

$$\langle \pi\pi | K(t) \rangle_R = \langle \pi\pi | K_S(0) \rangle e^{-\frac{X}{2}} \left(\rho e^{-i\left(m_S - i\frac{\Gamma_S}{2}\right)t} + \eta e^{-i\left(m_L - i\frac{\Gamma_L}{2}\right)t} \right) \quad (2.1)$$

while that in the K_L ("vacuum") beam is given by

$$\langle \pi\pi | K(t) \rangle_V = \langle \pi\pi | K_S(0) \rangle \eta e^{-i\left(m_L - i\frac{\Gamma_L}{2}\right)t} \quad (2.2)$$

where η represents η_{00} or η_{+-} according to the final state, ρ is the amplitude for coherent regeneration, Γ_S and Γ_L are the K_S and K_L decay widths, m_S and m_L are their masses, and the factor e^{-X} accounts for absorption in the extra material in the regenerated beam. The ratio of rates in the two beams is then

$$I(\pi\pi) = e^{-X}\left(\frac{|\rho|^2}{|\eta|^2} e^{-(\Gamma_S - \Gamma_L)t} + 2\frac{|\rho|}{|\eta|} e^{-(\Gamma_S - \Gamma_L)t/2} \cos(\Delta m t + \varphi_\rho - \varphi_\eta) + 1 \right) \quad (2.3)$$

where $\Delta m = m_L - m_S$. The first term describes the exponential decay of the K_S and K_L, the second, their interference downstream of the regenerator, and the third, CP-violating decays in the regenerated beam. For a thick regenerator such as the one used in this experiment, $|\rho| \gg |\eta|$, so that close to the regenerator the first term dominates and $I \propto |\rho/\eta|^2$.

It is known from past experiments [20, 22, 24] that for the momenta of interest here, the regeneration amplitude is proportional to the kaon momentum P_K raised to a power. Theoretically, this follows from single Regge exchange, in this case the ω trajectory [25]. We extract the value of $\mathrm{Re}(\varepsilon'/\varepsilon)$ by fitting Equation (2.3) to the charged and neutral data for three quantities: the value of this power, the value of $|\rho/\eta|$ at an arbitrary fixed energy, and the difference between η_{00} and η_{+-}, which is proportional to $\mathrm{Re}(\varepsilon'/\varepsilon)$.

Use of the regenerator reduced susceptibility to several possible sources of systematic error. Because coherently regenerated kaons are produced in the forward direction, their transverse divergence is the same as that of K_L from the target. Selection criteria depending on the transverse momentum of the decay products, important for background rejection, were therefore unbiased. Furthermore, it was not necessary to understand the dependence of detector acceptance on the kaon momentum direction.

A second advantage of using a regenerator to produce K_S is that it leads to similar momentum spectra for decays in the vacuum and regenerated beams. This is an accident of the regeneration phenomenon, but is important because momentum smearing due to imperfect detector resolution then affects the K_S and K_L in nearly the same way. The accident occurs because $|\rho| \propto P_K^{-0.6}$, so the momentum spectrum of the regenerated kaons, essentially all of which decay in our apparatus, is proportional to $f(P_K)P_K^{-1.2}$, where $f(P_K)$ is the momentum spectrum of the K_L beam, while, because of Lorentz contraction of the limited decay volume, the spectrum of decaying K_L mesons is proportional to $f(P_K)P_K^{-1}$. Thus, the spectra of decaying kaons from the two beams differ only by the factor $P_K^{0.2}$.

Because regeneration is well-understood, it could be used to check our analysis. In particular, from past experiments, the power describing

the dependence of ρ on P_K is known for our regenerator to within a few percent. This power can be compared with the value we obtain in our fit.

Use of the regenerator has powerful advantages as we have described, but it also has potential drawbacks. One of these is that neutrons in the beam interact in the regenerator and can generate background. For several reasons this effect was unimportant. First, by careful design of the collimators, neutrons accounted for only 50% of the particles in the regenerated beam. Second, most neutron interactions in the regenerator were identified by embedded layers of scintillator and contributed less than 0.1% background to the final data samples.

The second drawback of regenerators is more important. The regeneration amplitude ρ describes coherent regeneration; however, diffractive and inelastic regeneration, in which the kaon acquires transverse momentum, also occur, and decays from K_S produced in these processes must be subtracted from the coherent signal. This subtraction was very small ($\approx 0.1\%$) for charged decays, where the transverse momentum acquired by the kaon in the regenerator could be reconstructed. For neutral decays, however, the transverse momentum of the kaon was not measured, so the subtraction, while straightforward, was much larger.

When using spatially separated K_S and K_L beams, biases can arise from features of the detector which distinguish between the beams. For example, in this experiment, the beams were vertically separated, so a difference in the responses of the upper and lower halves of the detector could have affected the relative reconstruction efficiencies of their decays. Differences in the intensities or momentum spectra of the two beams could have further distinguished their decays. To avoid bias from the differences between the upper and lower beams, the regenerator alternated between them about once per minute, following each beam spill.

Although the technique described above minimizes the effect of many potential sources of bias, others remain which must be treated properly. Of these the most important is the difference in decay vertex distributions along the beam axis for K_S and K_L due to the difference in their lifetimes. To correct for variations in detector acceptance as a function of the decay vertex position we relied on a Monte Carlo simulation of the experiment,

described in detail in Chapter 8. The detector configuration was chosen to make the acceptance as uniform as possible and to make it easy to understand.

In principle, we could have avoided these acceptance corrections. The NA31 experiment at CERN attempted to reduce such corrections by moving the K_S target or regenerator along the beam line, so that the K_S decay distribution more closely approximated that of the K_L. This technique, however, precludes use of parallel K_L and K_S beams because the K_S target train can obstruct upstream K_L decays, in a way that could be difficult to quantify. The NA31 experiment therefore collected K_L and K_S decays separately, sacrificing the many advantages of the double beam technique.

The last important source of systematic error for experiments measuring $\text{Re}(\varepsilon'/\varepsilon)$ is uncertainty in the absolute knowledge of the kaon momentum and decay vertex position. Together these determine the proper time of each decay, which appears in the expression for the ratio of decay distributions (2.3). Knowledge of the kaon momentum is also necessary for the power law fit of the regeneration amplitude. In practice, it is easy to determine the absolute energy and vertex position for the charged decays. Determining these for the neutral decays depends on the absolute calibration of the electromagnetic calorimeter used to detect photons and this is a major challenge posed to the experiment.

In the data discussed here, all four kaon decay modes were collected simultaneously. This feature distinguishes them from the rest of the data taken during the same run, and from all previous data used to measure $\text{Re}(\varepsilon'/\varepsilon)$. Although this is not crucial to the analysis, it allows us to quantify diffractive and inelastic regeneration using $K_S \to \pi^+\pi^-$ decays, for which the full track information is available, and to apply the results to $K_S \to \pi^0\pi^0$ decays, whose reconstruction is less complete. Simultaneous collection of charged and neutral decays also provided a powerful constraint of the Monte Carlo simulation of the experiment used to calculate the relative K_L and K_S acceptances: the beam divergence and kaon momentum spectra had to describe both modes.

2.3 Detector Requirements

The detector is composed of two principle systems. The first is a drift chamber spectrometer used to reconstruct the charged decays, and the second is the electromagnetic calorimeter used to detect the four photons produced in neutral decays. In addition, there are a number of auxiliary detectors used to trigger and to reject background.

2.3.1 Detection of $K_{L,S} \rightarrow \pi^+ \pi^-$

The spectrometer consists of four drift chambers with an analyzing magnet between the second and third. Each chamber provides the position of the charged particles in the plane transverse to the beam, allowing reconstruction of the particle trajectories. The horizontal and vertical track views are matched with one another by appealing to the calorimeter or other counter banks. The point of closest approach of the trajectories is taken as the decay position of the kaon.

The momentum of a particle is inversely proportional to the bend angle of its track in the analyzing magnet. For two body decays, knowledge of the track momentum, along with the assumption that the particles are both pions, allows reconstruction of the kaon invariant mass. Because the momentum resolution is good, the two particle invariant mass calculated for other charged decay modes tends to be well separated from that measured for true two pion decays. The two particle invariant masses of $K_L \rightarrow \pi^+ \pi^- \pi^0$ and CP-conserving $K_L \rightarrow \pi^+ \pi^- \gamma$ decays are separated from the peak by at least 15 times its width, and few $K_L \rightarrow \pi^{\pm} e^{\mp} \nu$ decays are consistent with $K_L \rightarrow \pi^+ \pi^-$ decay.

The particle momentum also allows electron identification by comparison with the energy which the particle deposits in the electromagnetic calorimeter. Electrons deposit all of their energy into the calorimeter, so the ratio of energy to momentum (E/p) is close to unity, while charged hadrons and muons generally deposit only a small fraction of their energy there, so that $E/p < 1$. Electron identification allows efficient rejection of the

copious $K_L \to \pi^{\pm} e^{\mp} \nu$ decay, and availability of momentum-analyzed electrons is valuable for calibration of the calorimeter.

2.3.2 Detection of $K_{L,S} \to \pi^0 \pi^0$

Neutral pions decay almost exclusively to two photons, so the final state of the $\pi^0 \pi^0$ decays generally consisted of four photons. In order to detect the photons, we used a lead glass electromagnetic calorimeter. Electrons and photons hitting the calorimeter shower electromagnetically and the resulting Cerenkov light, detected with photomultiplier tubes, is nearly proportional to the particle energy. The impact position of the incident particle can be determined from energy sharing between blocks.

Using the energy and position information for the four photons from kaon decay, one can pair the photons so that they are consistent with two π^0 decays occurring at a single position along the beam axis. This position is then the kaon decay vertex and using it, the kaon invariant mass can be reconstructed. In contrast to the charged decays, the transverse position of the decay vertex is unknown, but the center of energy of the photons at the lead glass gives one point on the kaon trajectory.

Good calorimeter resolution allows precise measurement of the longitudinal position of the kaon decay vertex and improves background rejection. The largest background to $K_L \to \pi^0 \pi^0$ decays is $K_L \to \pi^0 \pi^0 \pi^0$ decays in which two of the six photons are lost, either because they miss the lead glass, or because their showers fuse with others in the calorimeter. Good energy and position resolutions make it possible to recognize events with four showers but invariant mass far from that of a kaon. Fine transverse segmentation of the calorimeter also helps resolve overlapping photon showers.

Lead glass was chosen for the calorimeter because its energy and position resolutions were good, and because its fast Cerenkov light signals can reduce background from out-of-time particles.

2.3.3 Other detector components

In addition to the charged spectrometer and electromagnetic calorimeter, a number of counter banks were employed. These contributed to the trigger, identified escaping photons from $K_L \to \pi^0\pi^0\pi^0$ decays, and helped provide well-defined boundaries to the fiducial volume of the detector. They are described in detail in the next chapter.

2.4 The Accelerator

The experiment was performed at the Fermi National Accelerator Laboratory using protons from the Tevatron. The Tevatron is a storage ring which delivers 800 GeV protons to the fixed target experiments. The resulting kaons decaying in our apparatus had energies between 20 and 250 GeV.

The high energy of the kaons had experimental advantages. First, the resolution of the calorimeter improved at high energies. Second, the increased decay length of the boosted kaons improved the reconstructed decay vertex resolution in the kaon rest frame. And finally, the advantageous power law dependence of the regeneration amplitude on the kaon momentum is valid only at high energies.

2.5 Conclusion

We have now outlined the overall technique of the experiment and emphasized the features crucial to its success. The aspects that are particularly important are the acceptance calculation and response of the lead glass calorimeter. Because of the design of the experiment, many other aspects are less critical. In the following chapters we will look in more detail at the detector, the data, and the important systematic issues.

CHAPTER 3

THE DETECTOR

This chapter describes production and collimation of the two kaon beams and the apparatus which detected their decays.

3.1 Beam production

A schematic of the target, collimation and sweeping regions of the beam line is shown in Figure 2. Kaons were produced by an 800 GeV proton beam incident on a beryllium target. Protons were delivered once per minute in a 22 s spill containing between 5 x 10^{11} and 10^{12} protons. The spill itself was divided into $\sim 10^9$ 2 ns "buckets", the proton occupancy of which varied by a factor of two or more within each spill.

The target was a 36 cm beryllium rod aligned with the proton beam, with a diameter of 2.2 mm, about twice that of the beam. Starting 9 m from the target was a 5.8 m copper two hole collimator oriented 5.3 milliradians from the proton beam direction in the horizontal plane. The holes were 6.65 mm square at the upstream end, intercepting 3.1 nanosteradians each, and were separated vertically by 5.8 mm. Additional collimation was provided by slabs located 25.5 m and 49.2 m from the target and adjustable collimators at 51.5 m and 83.5 m.

Several sweeping magnets removed charged particles from the beams. Blocks of beryllium (51 cm long) and lead (7.6 cm long) located just downstream of the copper collimators absorbed neutrons and photons. To further reduce neutron contamination, an additional 46 cm beryllium absorber lay in the beam which was to be regenerated. By the time the beams entered the decay volume about 100 m from the target, most Ξ, Λ,
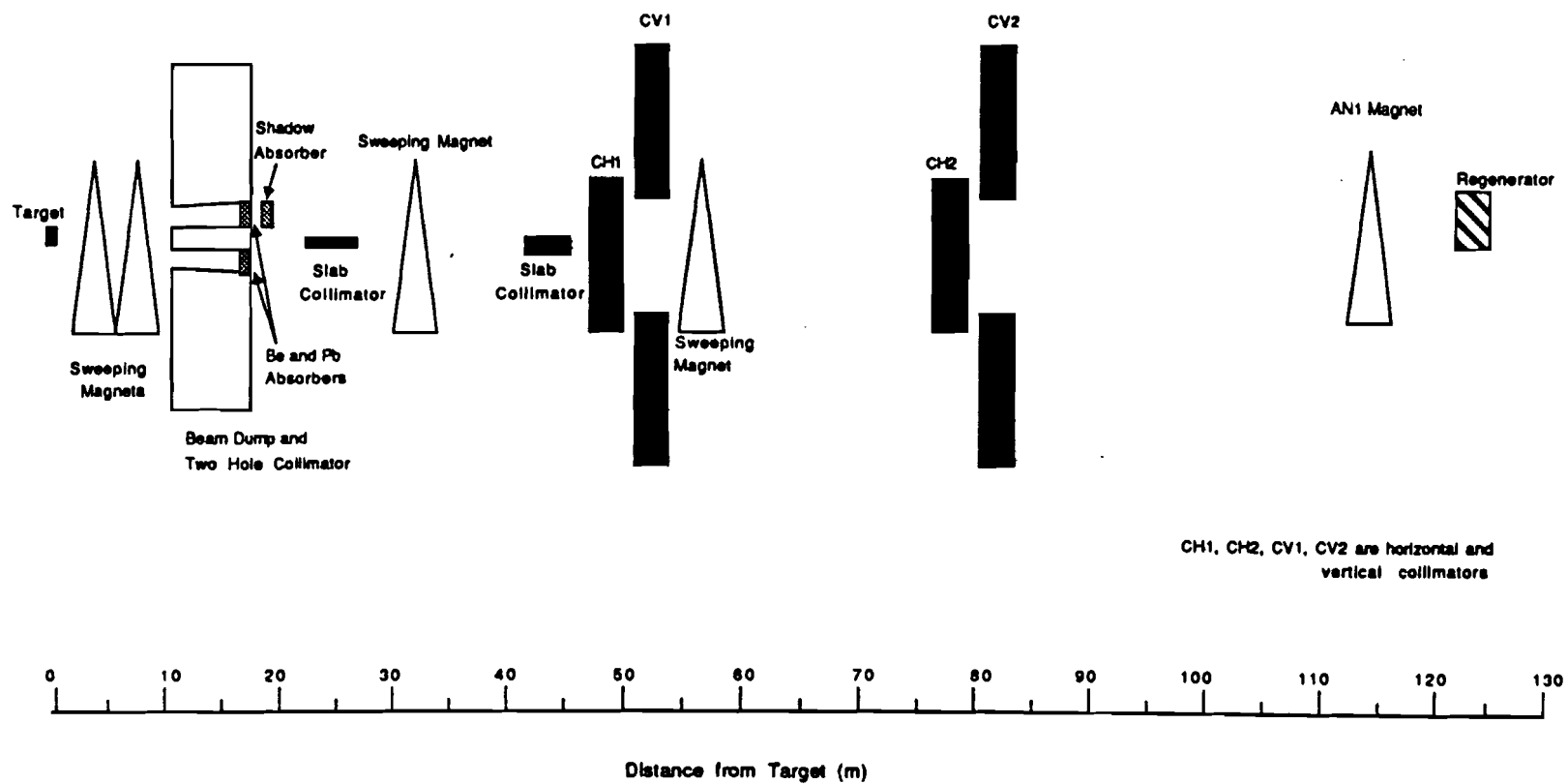
Figure 2. The target and collimators.
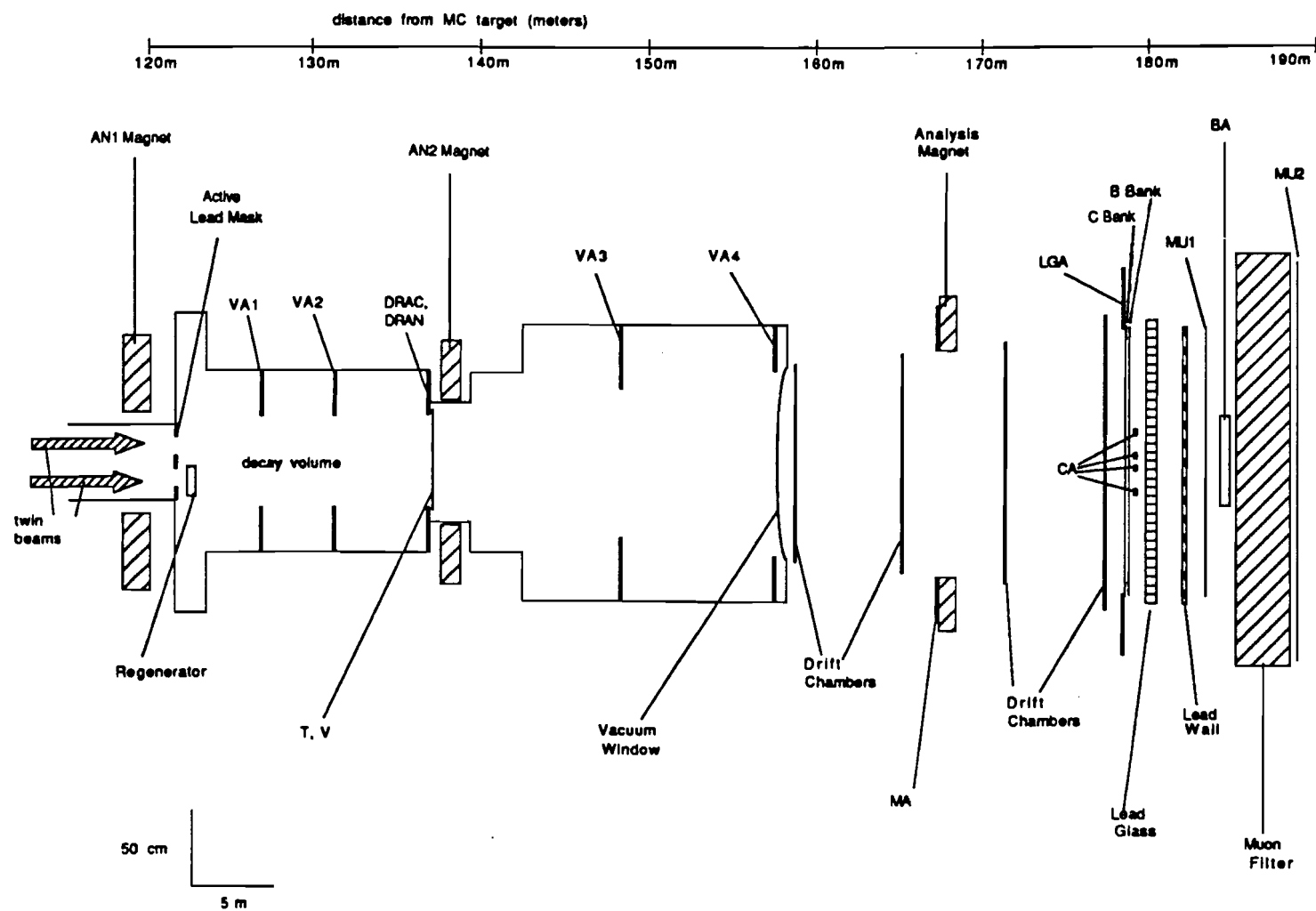
Figure 3. The decay volume and detector.

and K_S particles had decayed, leaving in the regenerated beam roughly equal numbers of K_L and neutrons, with Λ and K_S content of 0.05% and 10^{-8} respectively.

3.2 The Experimental apparatus

A schematic of the decay region and detector is shown in Figure 3, and the positions and dimensions of the individual components are listed in Table 2. Their radiation lengths, which determine the interaction rate of the decay particles as they pass through, appear in Table 3.

3.2.1 The Regenerator

The regenerator, shown in Figure 4, was composed of four 19.05 cm blocks of B_4C. Following each block was a layer of 0.635 cm scintillation counters used to detect and veto inelastic scattering (known as the "regenerator anti" or "RA"). The last of these counters was preceded by 1.27 cm of lead in which photons converted to electron-positron pairs, which were then detectable in the scintillator. Thus, the RA provided a sharp edge in the decay position of both charged and neutral decays from the regenerated beam.
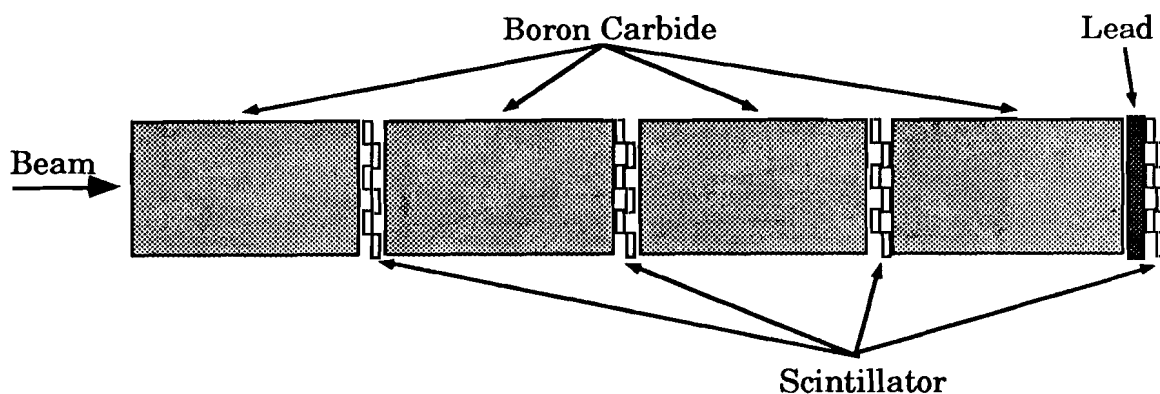
Figure 4. The regenerator.

TABLE 2. Positions and dimensions of the detector elements.

Detector element	Distance from target	Transverse dimensions
Pinching Anti (PA)	116.118 m	
Sweeper Anti (SA)	117.81 m-121.36 m	16.2 cm x 28.58 cm
Lead Mask (AM)	121.893 m	
Regenerator	123.550 m	
Vacuum Anti 1 (VA1)	127.855 m	inner radius: 30.3 cm outer radius: 59.5 cm
Vacuum Anti 2 (VA2)	132.819 m	inner radius: 30.3 cm outer radius: 59.5 cm
Veto counter (V)	137.792 m	49.7 cm x 61.9 cm
Trigger counter (T)	137.815 m	49.7 cm x 61.9 cm
DRAC	137.826 m	
DRAN	137.866 m	outer radius: 60.8 cm
Separator Magnet (AN2)	139.008 m	
Vacuum Anti 3 (VA3)	149.309 m	inner radius: 50.2 cm outer radius: 88.5 cm
Vacuum Anti 4 (VA4)	158.291 m	inner radius: 60.6 cm outer radius: 88.9 cm
Vacuum Window	158.965 m	radius: 61 cm
Chamber 1	159.292 m	1.27 m x 1.27 m
Chamber 2	165.867 m	1.42 m x 1.57 m
Magnet Anti (MA)	166.836 m	inner: 1.82 m x 1.49 m outer: 2.09 m x 2.13 m
Analyzing magnet (AN4)	168.865 m	vertical aperture: 1.47 m
Chamber 3	171.857 m	1.57 m x 1.73 m
Chamber 4	178.004	1.78 m x 1.78 m
Lead Glass Anti (LGA)	178.710 m	ID: 1.8 m; OD: 2.64 m clipped height: 2.11 m.
C Bank	179.502 m	1.9 m x 1.8 m
B Bank	179.520 m	2.0 m x 2.1 m
Collar Anti (CA)	180.700 m	inner edge: 11.64 cm outer edge: 17.46 cm
Lead Glass (PbG)	181.089 m	radius: ~0.91 m
MU1	183.996 m	2.0 m x 2.2 m
Back Anti (BA)	185.047 m	20.32 cm x 40.64 cm
MU2	189.914 m	2.54 m x 2.44 m

TABLE 3. The number of radiation and interaction lengths in the detector elements.

Detector Element	Number of Radiation lengths	Number of Interaction lengths
HDRA V	0.0033	
HDRA T	0.0033	
Vacuum window	0.0025	
Drift Chamber 1	0.0034	
Drift Chamber 2	0.0040	
Drift Chamber 3	0.0038	
Drift Chamber 4	0.0021	
Field wire	0.0057	
Sense wire	0.0064	
B bank	0.04	
C bank	0.04	
Collar Anti	8.1	
Lead Glass	18.74	2.2
Lead Wall	21.4	0.7
Back Anti	28.1	1.3

3.2.2 Decay volume

The kaon beams traveled in an evacuated pipe starting just downstream of the two hole collimator. In order to reduce interactions of the kaons and their decay products, this evacuated pipe continued without interruption to the first drift chamber, growing in diameter along the length of the apparatus to accommodate the decay particles as they drifted apart. At the downstream end of the pipe was a vacuum window 122 cm in diameter, composed of 0.127 mm of mylar and 0.584 mm of Kevlar 29. The pressure in the pipe was less than 0.015 torr throughout the run.

3.2.3 The Charged Spectrometer

The trajectories and momenta of charged pions and other particles were measured with a drift chamber spectrometer, consisting of four chambers with an analyzing magnet located between the second and third as shown in Figure 3. Each chamber consisted of two horizontal and two vertical drift planes. The field and sense wires were arranged in a hexagonal pattern as shown in Figure 5, with 0.635 cm spacing between adjacent sense wires. The gas used was a 50% argon-50% ethane mixture with 0.5% ethanol for additional quenching. The drift velocity was about 50 μm/ns, with a maximum drift time of 150 ns.

Each wire output was connected to a Le Croy 4291B time to digital converter (TDC), operated in common stop mode. The time distribution of hits on a chamber plane under typical running conditions is shown in
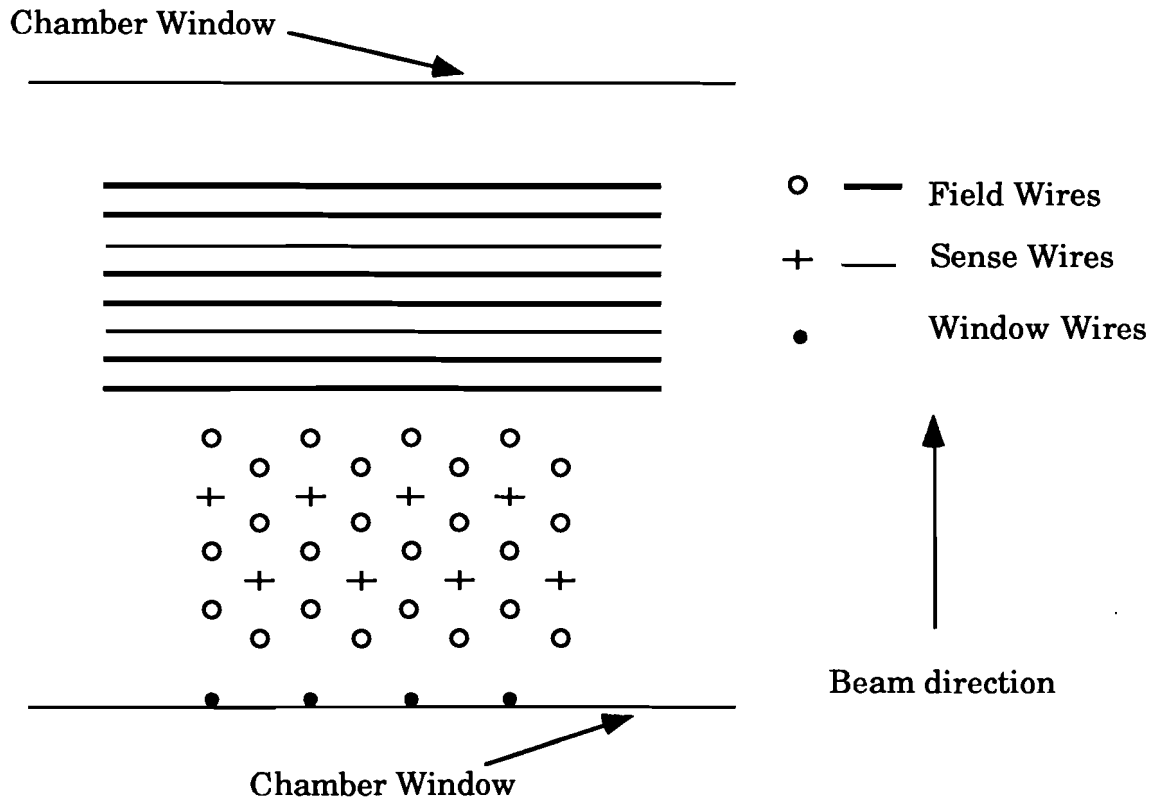
Figure 5. Cross-section of a drift chamber.
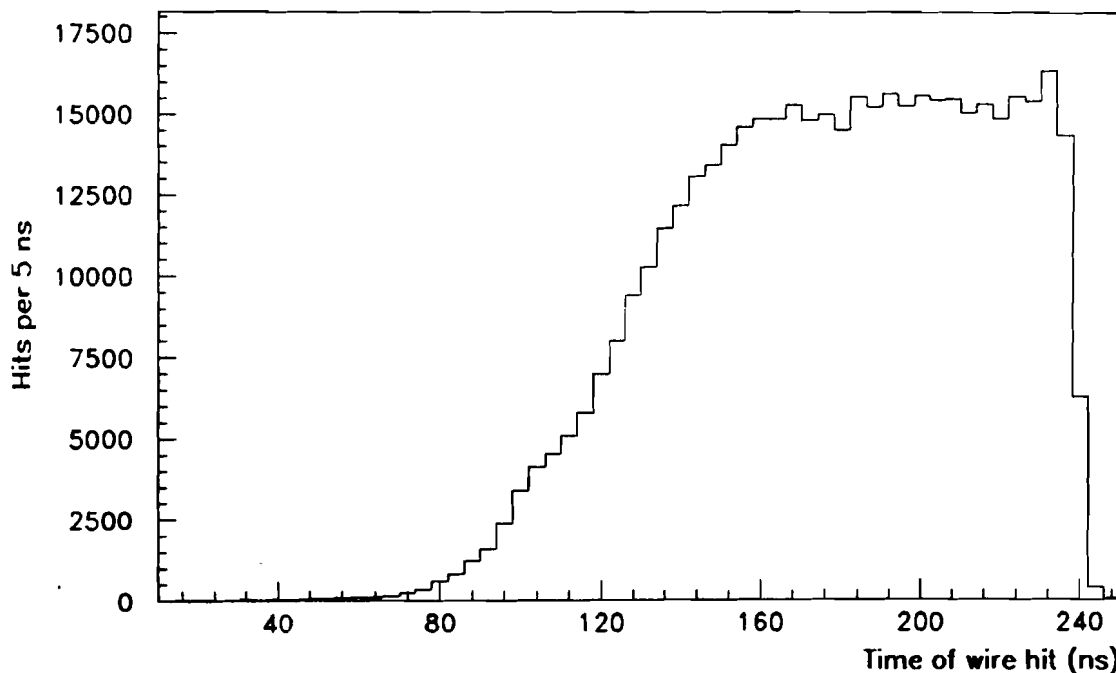
Figure 6. The time distribution of hits associated with pion tracks in one of the drift chamber planes.

Figure 6. Hits near 240 ns originated from particles passing near the sense wire, while those below 100 ns originated from particles passing through the outer reaches of the cell. On average, the wire efficiency was 96.8% for the inner two planes of each chamber and 99.3% for the outer two.

The magnet provided a transverse momentum kick of about 0.200 GeV/c. The length of the pole face was about 1 m along the beam direction, and the vertical opening between the pole faces was 1.46 m. Additional magnets, *AN1* and *AN2*, which could deliver vertical and horizontal momentum kicks respectively, were employed only during some special calibration runs.

To reduce multiple scattering, large plastic bags of helium with thin windows at each end filled the gaps between the chambers.

3.2.4 The Electromagnetic Calorimeter

A lead glass calorimeter measured the positions and energies of photons and electrons. It consisted of 804 blocks of Schott F-2 lead glass

(radiation length X_0=3.21 cm), each 5.8 x 5.8 x 60.2 cm³ aligned parallel to the beam. The blocks were arranged in a circular array with two beam holes through the middle as shown in Figure 7. The radius of the array was about 0.92 m.

In order protect the phototubes that detected light produced in the lead glass, the entire array was housed in a small light tight room. The room also allowed good temperature control. Using a standard household thermostat and heating/cooling system, the temperature of the phototubes and bases was constant within a fraction of a degree, so that possible gain drifts due to temperature variation were negligible.

The dimensions of each block were separately measured (the transverse dimensions varied by a few tenths of a millimeter), and their positions within the array were chosen to approximate an ideal grid as closely as possible.

As alluded to above, the Cerenkov light produced in an electromagnetic shower in a block was observed with photomultiplier tube mounted on the back. The block assembly is shown in Figure 8. Each block was wrapped in 0.0005 inch aluminized mylar. The phototube was encased in a magnetic shield and pressure mounted on the back of the block. Optical contact between the block and phototube was provided by a silicon gel with an index of refraction of 1.45, which lay between that of the glass (1.6) and the photomultiplier tube face (1.4). Embedded in the gel was a Wratten 2A filter, which reduced sensitivity to variations in shower depth (see Chapter 6). The phototube used was Amperex 2202, a ten stage tube with a bialkali photocathode. Voltage on the base was modest, typically –1200V, providing gains of 1.2×10^5.

High voltage for the array was provided by four Le Croy 1880 high voltage supplies, which allowed independent adjustment of the voltage of each photomultiplier via CAMAC. A one volt change caused roughly a 1% change in gain. During the run the voltages were adjusted once every two weeks to compensate for changes in signal size. Between changes they were monitored to ensure that each was within a volt of its assigned voltage. From the gain stability of the phototubes we know that in fact the voltages were constant to a fraction of a volt.
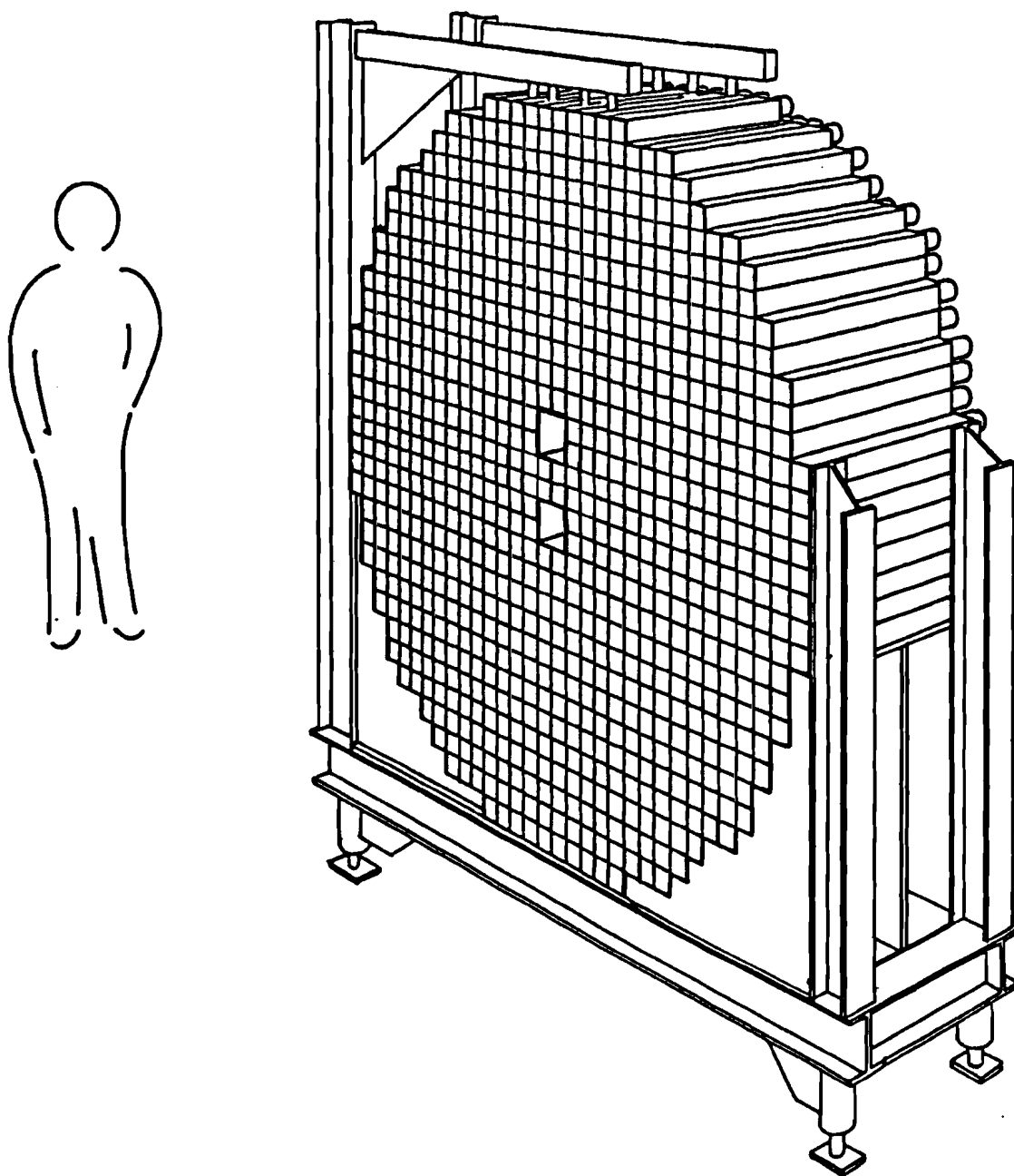
Figure 7. The lead glass calorimeter.

The signals from the phototubes traveled through 275 feet of cable (necessary to allow for formation of the trigger), and then were integrated over a 150 ns gate and digitized in nine fastbus Le Croy 2280 analog to digital converters (ADC's). These are 12 bit bilinear ADC's: for low pulse height signals ("low range") they operate in a high gain mode, while for large pulse height signals ("high range") the gain is reduced by a factor of eight, so that the dynamic range is extended to that of a 15 bit ADC. In the low range the ADC gain is 20 counts / picocoulomb, corresponding to about 5 MeV of incident particle energy per count. The high range / low range knee was at about 3700 low range counts, between 15 and 20 GeV of incident particle energy.

Before entering the ADC's, small portions of the signals from the lead glass blocks were tapped off at two places. First, at the patch panel where the signals left the lead glass house, one eighth of each signal was removed and then summed in groups of nine blocks each. These 92 "Adder" signals were then summed in order to calculate the total energy deposit in the array ("E_T"). The Adder signals were recorded using Le Croy 2280 ADC's, but with a short 30 ns gate, to allow offline identification of out of time clusters. A small part of each lead glass signal was also tapped off just before it entered the ADC for use by a hardware cluster finder which was part of the neutral decay trigger.

Changes in gain of the lead glass blocks and phototubes were tracked with a xenon flash lamp. Once every other second during data taking the lamp flashed and the signal in each lead glass block was recorded. A
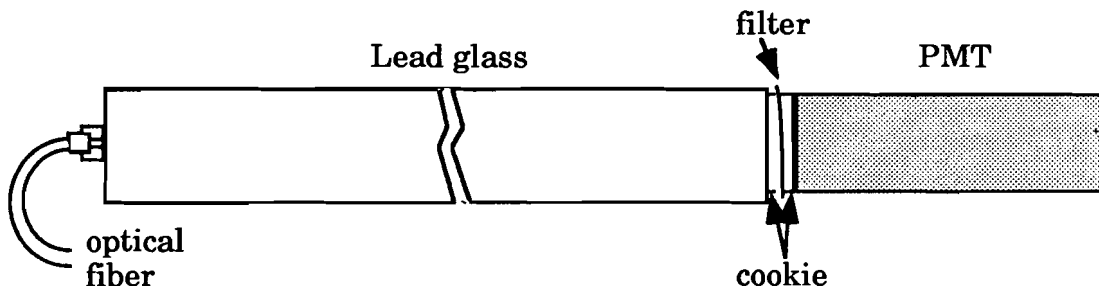
Figure 8. A lead glass block and PMT.

xenon lamp with a quartz window was chosen because its spectrum is similar to that of Cerenkov light. This particular lamp showed good flash to flash brightness stability, with fluctuations of about 3%. Glass fibers distributed the light from the flash to all the blocks. A large bundle of thin fibers looked directly at the flash, and was then split into 35 smaller bundles. A second, smaller fiber bundle further divided each of these 24 ways. Each of these daughter fibers was then mounted to the front face of a lead glass block using a small lucite fixture. The mean flasher signal size was 7600 counts per block, equivalent to an energy deposit of 38 GeV.

In earlier experiments using this lead glass array, phototube gain increases of as much as 10% were observed over the first few seconds of each spill as the particle flux ramped. It was found that low level ambient light on the tubes could reduce the size of these changes by an order of magnitude or more. In this experiment, low level light shone on each block at all times. The light was provided by 35 LED's, each located at one of the junctions between the first and second fibers used to distribute flasher light. A small power supply provided 2.6 mA of current to each LED.

During the run the lead glass blocks, particularly those near the beam pipes, yellowed due to radiation damage. The light loss, about 5% per week in the worst blocks, could have compromised the energy resolution, and complicated calibration. In order to cure this damage, at least partially, these blocks were periodically exposed to intense UV light. For this purpose two 400 W mercury vapor lamps were available. Curing occurred whenever the accelerator went down for four days or more for scheduled shutdowns or due to failure of a magnet or some other part of the Tevatron, main ring or injector. These down periods were sporadic, but on average occurred once a month. One such shutdown immediately preceded the data taking period described in this thesis, and the glass was cured at that time.

3.2.5 Counter banks

A number of scintillation and lead-lucite counters identified charged particles and photons in the apparatus. These counters provided fast

information for the triggers, detected particles escaping from the fiducial volume of the detector, and provided well defined edges to the fiducial volume of the detector, thereby simplifying acceptance calculations. Counters used for each of these purposes will be described in this section, and their dimensions and characteristics are summarized in Table 2.

Scintillation counter banks

Two scintillation banks were used in the $K_{L,S} \to \pi^+\pi^-$ trigger to identify charged particles passing through the spectrometer. The first of these was composed of two 1 mm thick layers of scintillator, one segmented horizontally ("V") and the other vertically ("T" or "trigger plane"). As described shortly, veto counter planes surrounded the scintillator, and together they were known as the "HDRA", shown in Figure 9. For the bulk of the $\pi^0\pi^0$ data collected during the run, a 0.5 mm lead sheet was inserted between the T and V counters for photon conversion, but for the data discussed in this
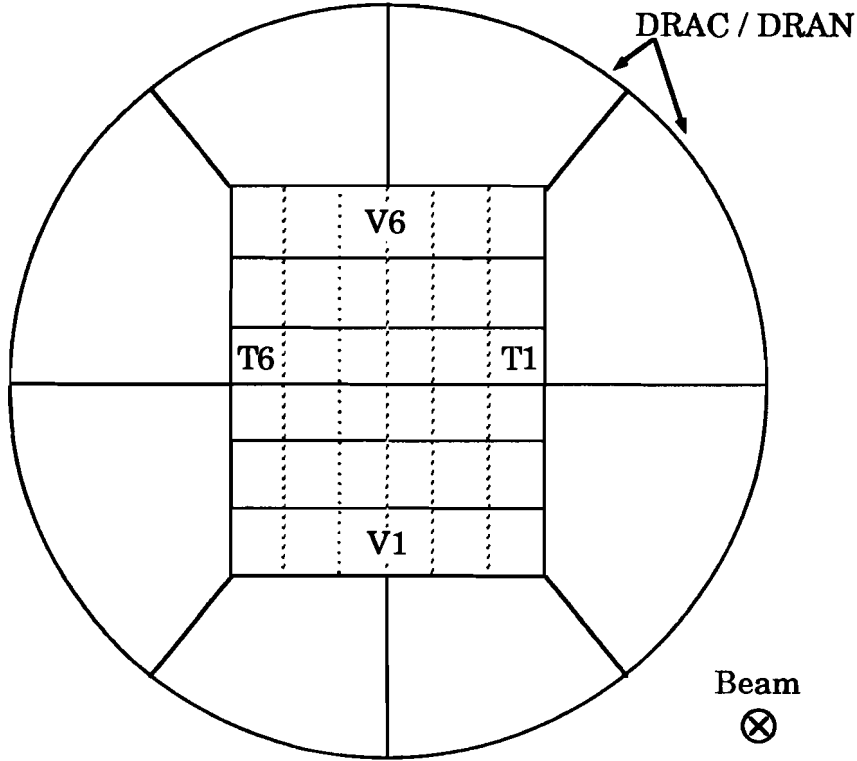
Figure 9. The HDRA.

thesis, that lead had been removed. The second pair of scintillation planes ("B" and "C") were composed of 1 cm thick scintillator, segmented as shown in Figure 10 and Figure 11 respectively.
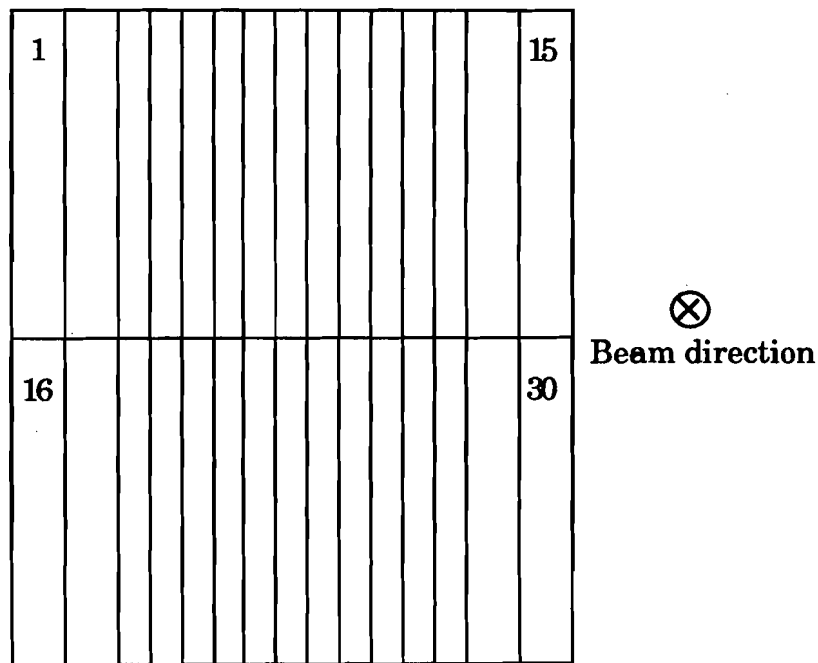
Figure 10. The B bank.
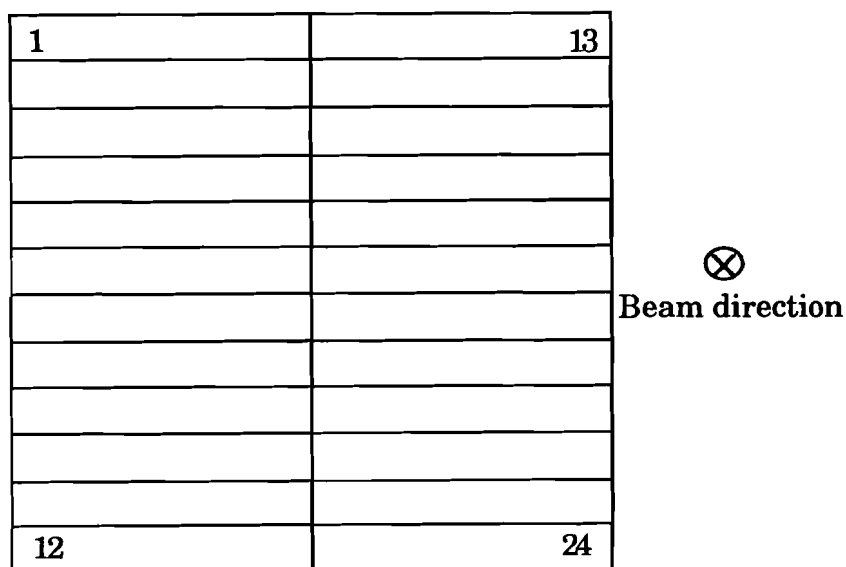
Figure 11. The C bank.
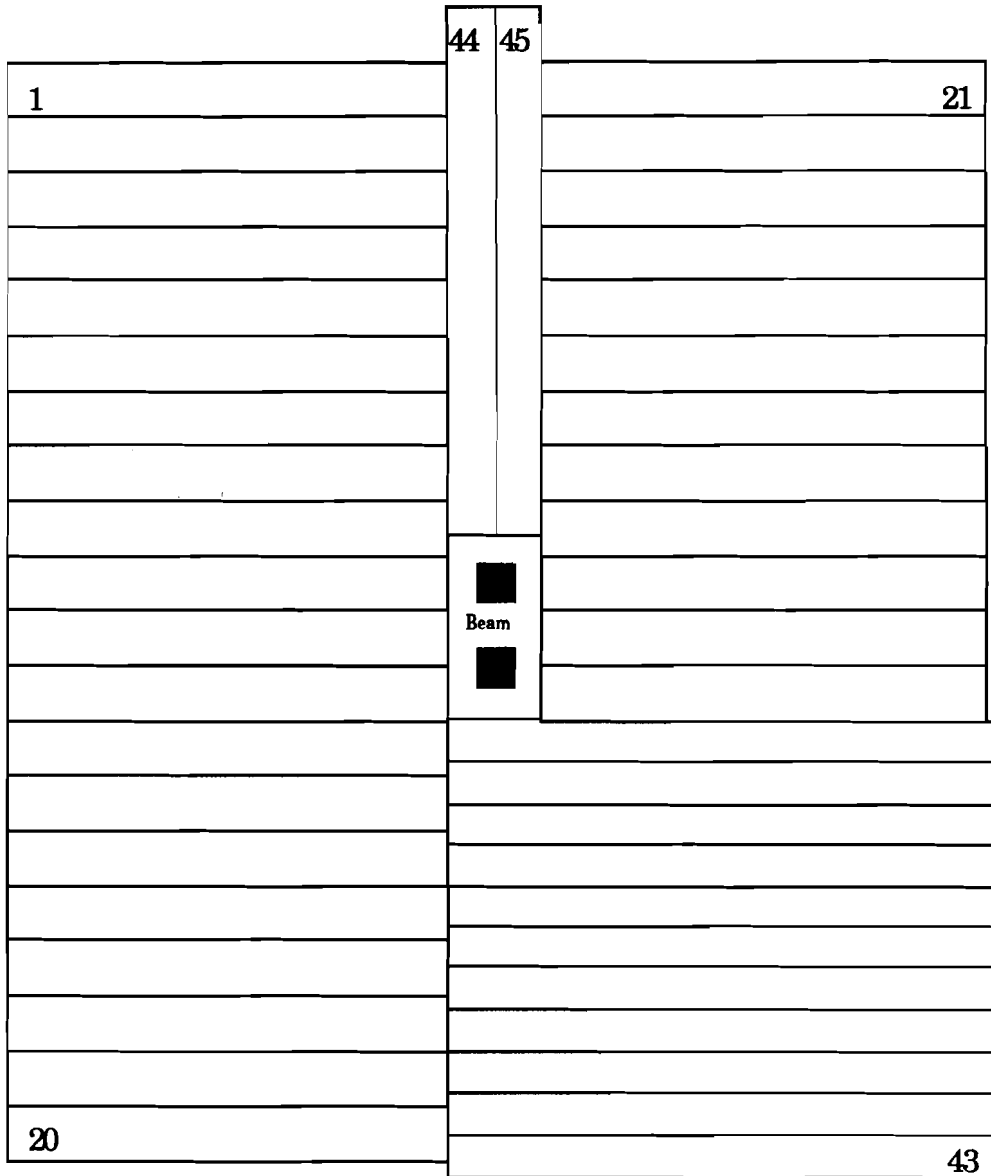
Figure 12. The MU1 bank.

In order to identify hadronic decays, and in particular to allow us to reject them at the trigger level, a 12.0 cm thick lead wall followed by a scintillator plane ("MU1") was constructed just downstream of the lead glass calorimeter (see Figure 12). Most hadrons showered in the wall, spraying charged particles into the scintillator, while electrons and photons were completely absorbed in the calorimeter and lead wall. To protect against

leakage into MU1 from showers occurring near the beam pipes, a thick lead collar cut off all direct lines of sight from the calorimeter.

Muons above 5 GeV were identified with greater than 99.9% efficiency in a scintillation bank ("MU2") which followed a 3 m thick steel wall at the far downstream end of the apparatus.

Several components of the detector were added in order to simplify acceptance determination. One of these was a lead mask, located just upstream of the regenerator, which provided a single well-defined limiting aperture for all upstream decays. The "Active Mask" ("AM") consisted of two 2.54 cm thick lead sheets, with a holes cut out of the middle to allow the passage of the beams, followed by a layers of scintillator, as shown in Figure 13.
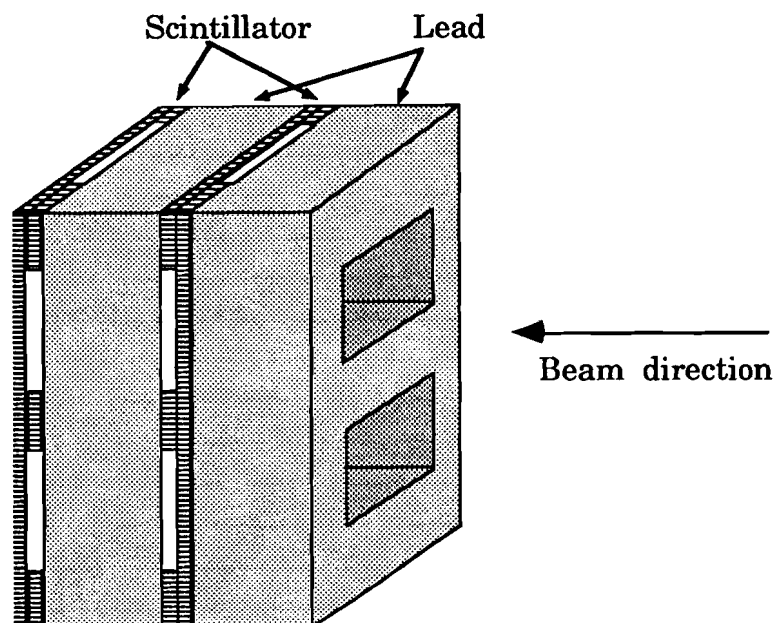
Figure 13. The lead mask and anti counter.

Photon Veto Counters

The largest background to $K_L \to \pi^0 \pi^0$ decays was $\pi^0 \pi^0 \pi^0$ decays in which two of the six photons missed the lead glass or were hidden in one of the other photon showers. In order to reduce this background, and, to a lesser extent, backgrounds with charged particles, a series of counter

banks, known collectively as the "photon vetoes", detected particles leaving the fiducial volume of the detector. The furthest upstream of these, the "Pinching Anti" ("PA"), consisted of a layer of lead followed by scintillator collaring the beam pipe. The others, the four "Vacuum Antis" ("VA"s), the "Magnet Anti" ("MA") and the "Lead Glass Anti" ("LGA"), consisted of a layer of scintillator for detecting charged particles, followed by several layers of lead and lucite in which photons converted to elecron-positron pairs and were detected as shown in Figure 14. Their configurations in the plane transverse to the beam appear in Figures 15 to 17. Finally, veto counters surrounded the T and V planes of the HDRA which consisted of a layer of scintillator ("DRAC") followed by a layer of lead and a second scintillator plane ("DRAN") (see Figure 9).
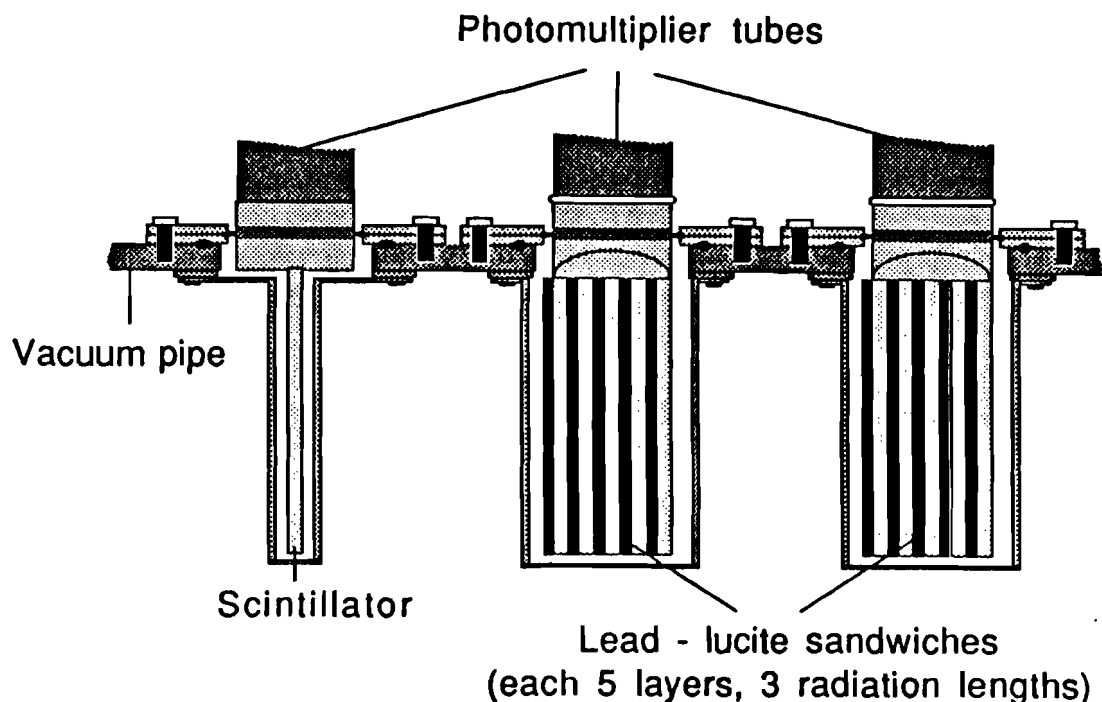
Figure 14. Cross-section of the VA, MA and LGA counters.
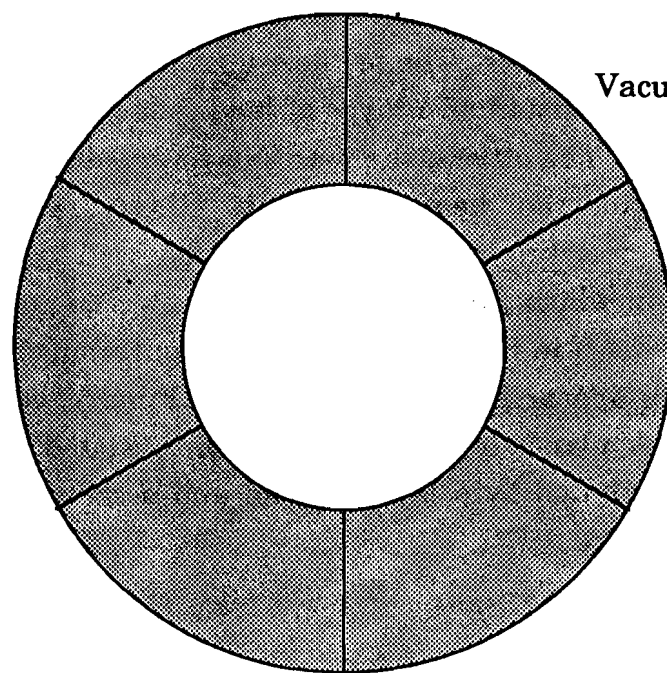
Vacuum Antis 1 & 2
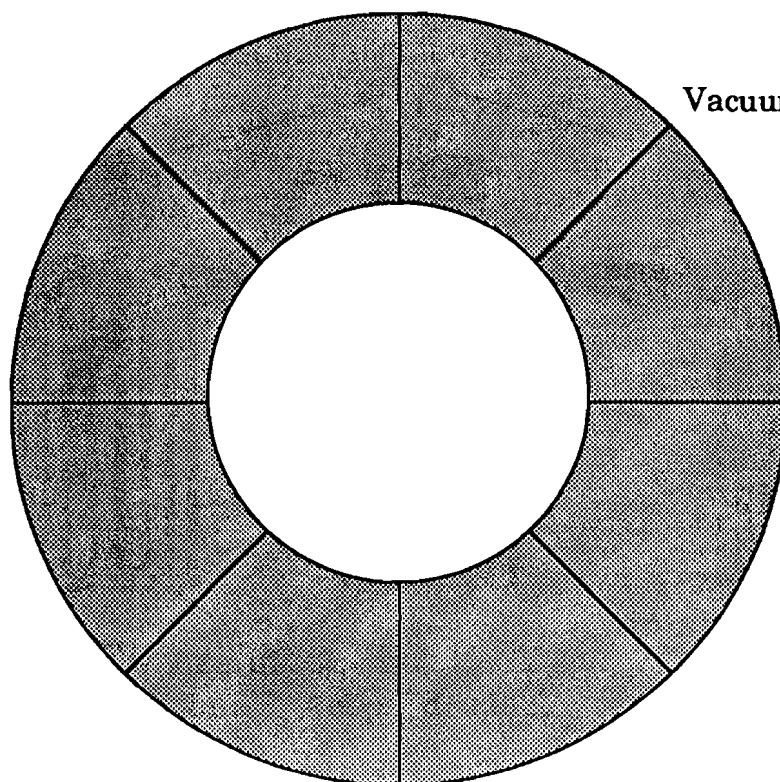
Vacuum Antis 3 & 4

Figure 15. The Vacuum Antis.

MA

Beam direction
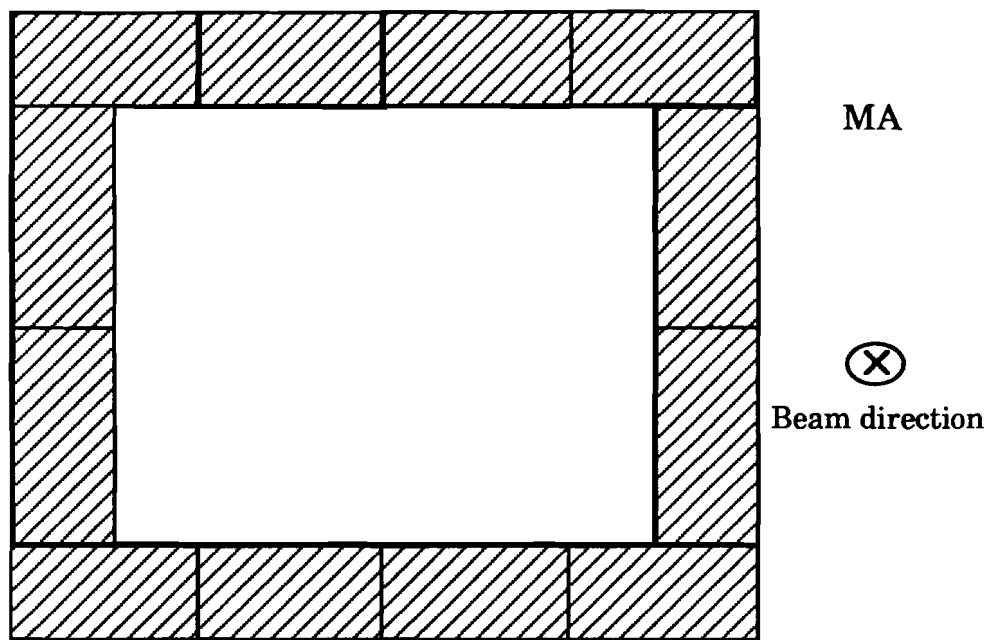
Figure 16. The Magnet Anti.

LGA

Beam direction
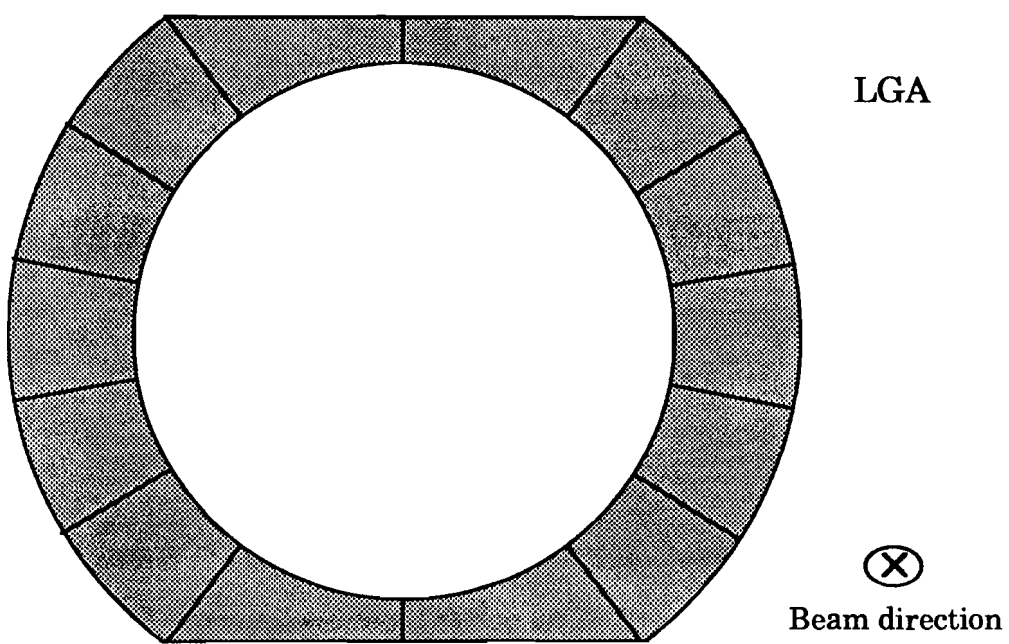
Figure 17. The Lead Glass Anti.

An additional veto counter, the "Back Anti" ("BA") (see Figure 18), was placed in the beams downstream of the lead glass calorimeter in order to detect photons escaping down the beam pipes. This counter was 48 layers of lucite sandwiched with layers of 0.33 cm thick lead. The lucite layers were segmented, alternately horizontally and vertically, so that they could withstand the high counting rates in the beam, with light produced in each group of eight horizontal or vertical layers observed by a single phototube. The total thickness was 28.1 radiation lengths.

The second counter used to simplify the acceptance calculation was a small collar around the beam holes through the center of the lead glass calorimeter. Photons showering very near the pipes risked misreconstruction if the shower was not completely contained in the glass. Since the amount of energy lost is sensitive to the details of electromagnetic shower development, the misreconstruction rate could be very difficult to calculate.
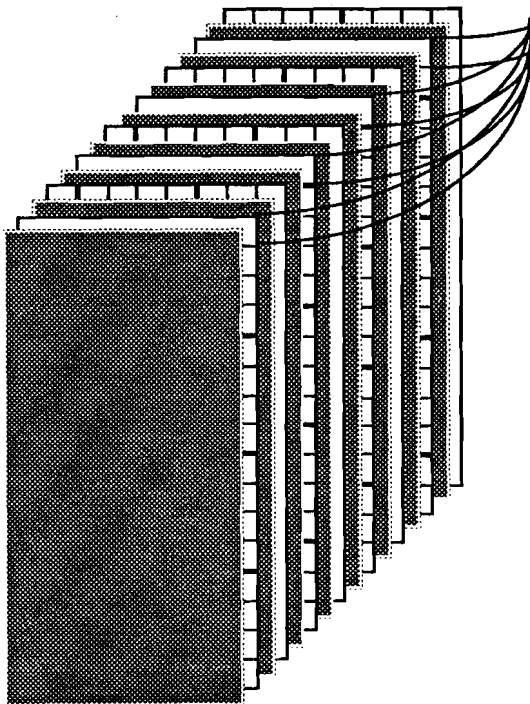
Figure 18. One of the three sections of
the Back Anti. The curves indicate a representative group of light guides.

By placing a collar composed of a photon converter followed by scintillator around the inner half of the blocks surrounding the beam hole, photons in danger of misreconstruction could be vetoed, with a well known hardware edge defining the acceptance. This counter, the "Collar Anti" ("CA"), consisted of 4.45 cm of copper and 2.8 cm of lead (8 X_0 total) in which 99.8% of photons converted into electron-positron pairs, followed by a layer of scintillator 0.635 cm thick, as shown in Figure 19.

3.2.6 The Coordinate system

A coordinate system, centered on the nominal target position, labelled positions in the experimental apparatus. The z axis was taken to be the line connecting the target and the center of the lead glass array (i.e., along the beam direction), and the x and y axes were perpendicular to this, oriented horizontally and vertically respectively, with $+y$ in the upward direction.

Copper   Lead   PMT

Scintillator

Beam hole

Side view   Beam view
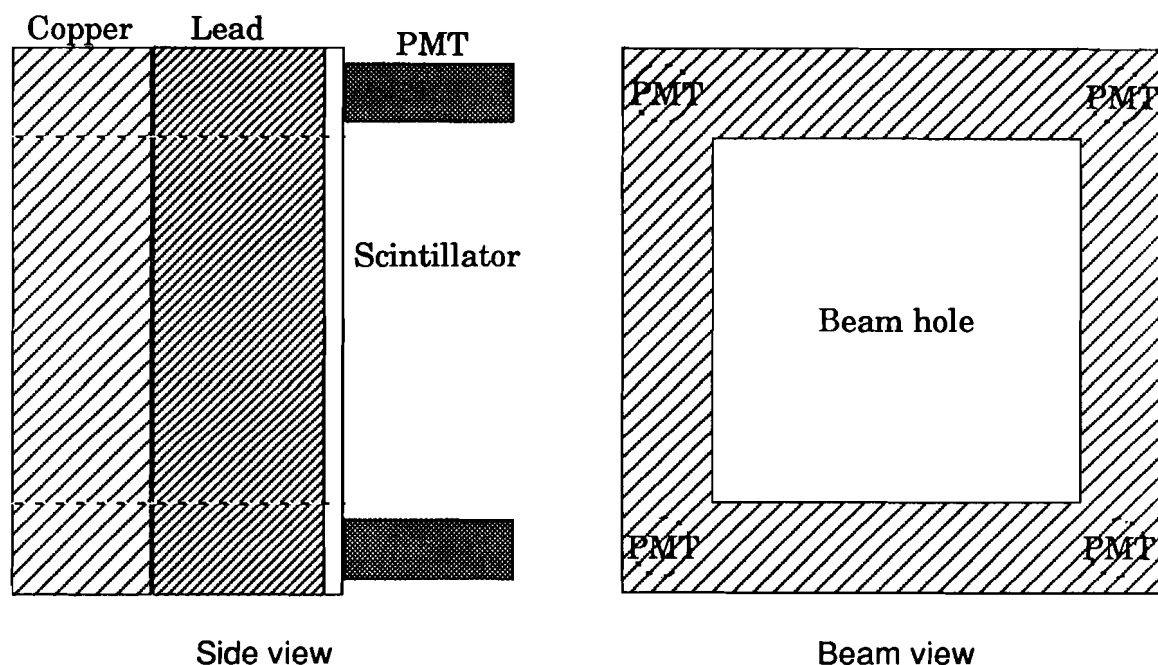
Figure 19. The Collar Anti.

3.3 Triggers

In order to reduce deadtime and limit the number of events recorded on magnetic tape, we relied on triggers designed to identify candidate two pion kaon decays. In this data set, distinct triggers were simultaneously employed for the charged and neutral decays. The trigger was divided into two levels. The first level trigger, formed about 450 ns after the event occurred, was based primarily on information from the counter planes and on the total energy deposit in the lead glass, and initiated signal conversion in the ADC's and TDC's. The second level trigger, which arrived about 20 μs later, and was based on more sophisticated analysis of event topology, could abort the event.

3.3.1 The charged mode trigger

The $K_{L,S} \rightarrow \pi^+\pi^-$ trigger looked for a two track final state with topology consistent with two body decay. The first level trigger was formed using signals from the T and V counters at the downstream end of the decay region and from the B and C banks which followed the spectrometer. It required that the total analog pulse height in either T or V (or both) be greater than 1.5 times that expected for a minimum ionizing particle. These scintillation planes defined the downstream end of the "decay region", or the region along the beam axis in which $K_{L,S} \rightarrow \pi^+\pi^-$ could occur and satisfy the trigger.

At the B and C banks, it was required that two tracks be observed and that they pass through diagonally opposite quadrants of the scintillator. This was done by requiring that there be at least one minimum ionizing both the east and west halves of the vertically segmented ("B") bank, where hits in the middle staves, 8 and 23, satisfied the requirement of either half, and that minimum ionizing particles pass through at least two separate staves. Similarly, it was required that particles pass through the upper and lower halves of the horizontally segmented ("C") bank, where the four middle staves, 5-8 and 17-20, satisfied the trigger condition of both halves. As a further requirement on the track separation, triggers were aborted

unless there were hits on both the east and west sides of the x planes of the second drift chamber. This last requirement, which comprised the second level trigger, decreased the trigger rate by 30%, largely by reducing contamination from $K_L \to \pi^{\pm} e^{\mp} \nu$ and $K_L \to \pi^+ \pi^- \pi^0$ decays.

In order to reject events in which a kaon or neutron interacted inelastically in the regenerator, events with a signal in the RA counter following the last B_4C block were vetoed. Events with activity in PA, AM, VA2, VA3, VA4 or the lead-lucite of LGA were also vetoed.

Finally, in order to reject $K_L \to \pi^{\pm} \mu^{\mp} \nu$ decays, we vetoed any event with a signal in the MU2 counter.

Fermilab provided a 53 Mhz RF signal synchronized with the buckets of the beam spill. In order ensure that the time of the trigger was independent of the particle trajectories, this RF signal defined the trigger timing. Its stability with respect to the passage of particles through the detector was monitored and occasional drifts of about 0.5 ns were corrected.

3.3.2 The Neutral Mode Trigger

The goal of the neutral mode trigger was to select events with four photons from $K_{L,S} \to \pi^0 \pi^0$ decays, as well as $K_L \to \pi^0 \pi^0 \pi^0$ decays with six photons in the calorimeter for systematic studies. As mentioned above, the largest background to the four photon decay was $K_L \to \pi^0 \pi^0 \pi^0$ decay in which one of the photons missed the lead glass and/or two nearby photons fused into a single cluster. In order to keep the trigger rate manageable, it was necessary to reject as many of these background events as possible at the trigger level.

The trigger required E_T of at least 28 GeV in the lead glass, and no signal in any of the photon vetoes except VA1, which suffered a large counting rate from particles produced in interactions in the regenerator.

Events with a photon escaping down the beam pipes were vetoed with the BA. Because the BA was placed directly in the beam, many hadrons interacted in it. These could be distinguished from photons because they characteristically deposited their energy deep in the counter. Events were

vetoed in the trigger only if a total of more than 5 GeV was deposited in the first two thirds of the BA, and less than 10 GeV was visible in the third.

In order to reject $K_L \to \pi^+\pi^-\pi^0$ decays, we vetoed events with energy deposition in MU1 equivalent to 5 or more minimum ionizing particles.

Events were rejected by the trigger with greater than 25 minimum ionizing particles passing through the CA scintillator. The high threshold guaranteed that events were not vetoed because of albedo from good photon showers.

The second level neutral trigger consisted of a hardware cluster counter (HCF) which allowed us to trigger on the number of clusters in the calorimeter. The cluster finder identified isolated islands of blocks with greater than 1 GeV of energy deposit each, integrated over a 20 ns gate. The cluster finding algorithm are described in detail in References [26] and [27]. The entire process took about 20 μs after initiation by a first level trigger with all the components described above. By allowing us to accept only events with four or six clusters, the HCF reduced the trigger rate by a factor of ten. To monitor its performance, we accepted 0.05% of the triggers independent of the HCF result.

As for the charged trigger, the RF signal provided by Fermilab determined the trigger timing.

3.3.3 Other Triggers

Several ancillary triggers were provided events for calibration and systematic studies. They were:

– The "Muon" trigger, which required coincident hits in the B bamk and MU2, and provided events useful for determining detector efficiency and alignment.

– The $K_L \to \pi^\pm\mu^\mp\nu$ trigger, which was identical to the $\pi^+\pi^-$ trigger except that a hit in MU2 was required, and was useful for background studies.

– The "Accidental" trigger, which allowed studies of the sources and effects of random particles passing through the apparatus. The trigger

was a scintillator telescope pointed at the target, but out of the line-of-sight of the collimators. Its rate was therefore proportional to the instantaneous beam intensity, but were not contingent on activity in the detector.

– The "Pedestal" trigger, which sampled the ADC signals at random using an inhibited readout threshold.

– The "Flasher" trigger, which flashed the xenon lamp in order to monitor the gains of the lead glass blocks.

Together, these auxilliary event types comprised 7% of the triggers recorded each spill.

3.4 The Data acquisition system

The data acquisition system, which ran on a PDP 11/43, collected the digitized signals from all detector elements, assembled them into a single event buffer, and logged them to magnetic tape. In the test run of this experiment, the amount of data recorded was limited by the amount of information that could be written to standard 6250 bpi reels over the 22 second beam spill. In this run, storage of the data in memory buffers allowed the data acquisition system to write tape between spills as well as during them, thereby tripling throughput.

3.5 Conclusion

This completes the description of the hardware used in the experiment. The next chapter will describe the data collection run and the particle fluxes and trigger rates in the beamline.

CHAPTER 4

DATA COLLECTION

4.1 Overview

The data were collected during the Fermilab fixed target run lasting from June, 1987 to February, 1988. The first two months of the run were used to tune the detector and triggers: collection of useable data began on August 1, 1987. This thesis describes the analysis of a subset of the data collected during the three week period from January 2 to January 25, 1988.

This chapter will describe the main features of the run, including the factors influencing the trigger rates and the number of $\pi\pi$ decays collected during the run, the information recorded with each trigger, and online and offline monitoring of the data. The chapter will conclude with the features that distinguish the data included in this analysis from the rest of the data collected during the run.

4.2 The Beam Intensity and the $\pi\pi$ Yield

The main objective during the data collection run was to maximize the yield of reconstructed $\pi\pi$ decays. Once the detector was performing well and the triggers optimized, this was primarily a function of the number of protons hitting the target during each Fermilab beam spill. At low beam intensities the yield increased roughly linearly with the proton flux; however, as shown in Figure 20, the yield fell for intensities greater than about 0.8×10^{12} protons per spill. One reason for this was the deadtime of the data acquisition system, which limited the rate at which we could record data. In addition, the extra random particles which passed through the detector

45

at high intensities sometimes vetoed good events or thwarted their reconstruction in the offline analysis. These effects markedly reduced the number of decays collected and had potential systematic consequences.

4.2.1 Livetime

Of the two effects limiting the yield, the deadtime cost us more events. When a trigger was accepted, the data acquisition electronics digitized the ADC and TDC and other signals, compiled the results and wrote it to a memory buffer. Additional triggers generated during this process were lost. The fractional livetime ℓ of the data acquisition system is given by

$$\ell = \frac{1}{1 + s\tau} \tag{4.1}$$

where s is the raw trigger rate and τ is the time required to process a single accepted trigger. For our data acquisition system, the deadtime was about
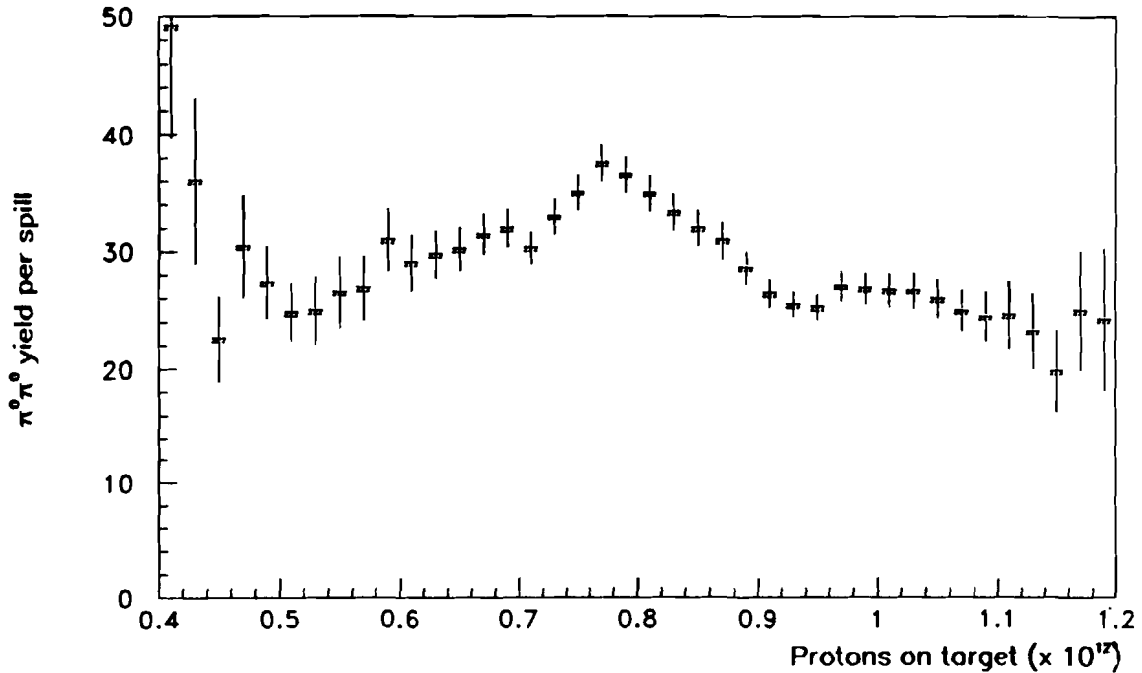
Figure 20. The number of reconstructed $\pi^0 \pi^0$ decays per spill as a function of the proton beam intensity. Both coherent and noncoherent K_S have been included.

1.5 ms per event. Under typical running conditions, the trigger rate was 0.6 khz, so that the data acquisition system was about 50% live. Thus, the deadtime halved the number of events recorded during the run.

The exact livetime depended on the position of the regenerator. The intensity of the upper beam was about 8% higher than that of the lower beam. This together with the fact that the majority of the kaon flux and triggers originated from the vacuum beam, lead to a 2% higher livetime when the regenerator was up.

4.2.2 Ambient Particle Flux

Vetoes and event misreconstruction due to the passage of extra particles through the detector had less impact on the $\pi\pi$ event yield than did deadtime; however, unlike deadtime, it could have distorted the observed double ratio of $K \to \pi\pi$ decay rates. The possible biases will be discussed in detail in Chapter 9. Here we will simply identify the origins of the particles that lead to the loss.

Table 4 shows the counting rate in selected counter banks averaged over a typical 22 second spill. The large rate in the muon counter bank MU2 reveals the identity of many of the particles passing through the detector: they are muons largely produced in our beam dump. The counting

TABLE 4. The counting rates in selected counters for a typical spill. During this spill 0.86 x 10^{12} protons hit the target.

Counter bank	Singles Rate
Regenerator Anti 4	0.58 Mhz
Vacuum Anti 1 (scint.)	1.73 Mhz
Vacuum Anti 2 (scint.)	1.11 Mhz
Vacuum Anti 3 (scint.)	1.01 Mhz
Vacuum Anti 4 (scint.)	0.93 Mhz
B bank	1.52 Mhz
Lead glass ($E_t >$ 28 GeV)	0.06 Mhz
MU2	1.15 Mhz

rate in the B bank, whose area is half that of MU2, indicates that muons account for about half of the particle flux through downstream end of the spectrometer. Interactions of the beam with the B and C bank scintillator (which had no beam holes) probably account for most of the remainder of the B bank rate.

An additional source of particles was inelastic interactions in the regenerator. The K_L flux at the regenerator was about 60% that in the vacuum beam because of the Shadow Absorber, and was matched with an equal flux of neutrons, for a total of roughly 0.4 Mhz. About 90% of the kaons and neutrons interacted in the regenerator, so we expect a rate of about 0.4 Mhz in the Regenerator Anti, roughly consistent with observations. Particles produced in these interactions illuminated the other nearby counters, particularly Vacuum Antis 1 and 2: in spite of their increasing areas, the rates in the successive VA counters decline as they get further from the regenerator.

Kaon decays were a final source of particles outside the beams. From the reconstructed kaon decay rate, corrected for acceptance (see Chapter 9) and deadtime, the K_L flux in the vacuum beam is known to be about 0.3 Mhz at this proton beam intensity. Only 3% of the kaons decay in the region from 110 to 179.5 m, and so their contribution to the particle flux is quite small, about 0.01 Mhz. Because the regeneration amplitude is small, the contribution to the rate due to K_S decays is also negligible.

The rates we have been discussing have been averaged over an entire 22 sec spill, but variations in occupancy of the ~10^9 buckets which compose each spill could lead to instantaneous rates significantly different from the average value. Evidence for this comes from the time distribution of hits in the counter banks. For example, Figure 21 shows the time distribution of hits in the RA with respect to the time of "Accidental" triggers (see Section 3.3.3). Each of the peaks corresponds to one bucket; hits are randomly distributed among them, except for the bucket which contained the trigger, where the number of hits is larger by almost a factor of two. This ratio of peak areas, p_{11}/p_{12}, is determined by the bucket to bucket fluctuations in occupancy: The probability of an accidental trigger is proportional to the proton beam occupancy of the bucket I, as is the probability that a particle
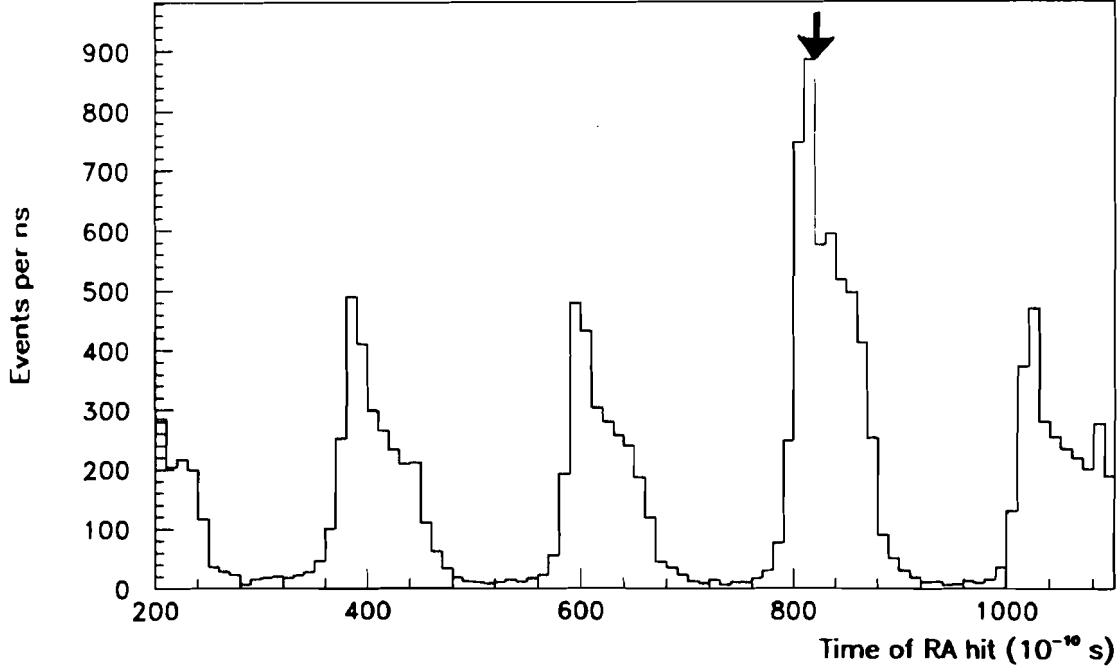
Figure 21. The time distribution of hits in the Regenerator Anti for"Accidental" triggers. The arrow indicates the time of the trigger.

will hit in the regenerator. Since these two events are uncorrelated, the probability that they both occur in the same bucket is proportional to I^2. It is easy to show that the rms intensity fluctuation of the buckets is given by

$$\frac{\sigma_I}{\langle I \rangle} = \sqrt{\frac{p_{11}}{p_{12}} - 1} = 91\%.$$

(4.2)

These large fluctuations in occupancy of the buckets are consistent with those seen in the 2π samples, indicating that the Accidental trigger sampled the detector with the same intensity distribution as the kaon decays. This fact will be important to systematic studies discussed in Chapter 9.

There are also variations in intensity during the spill on a macroscopic scale, as shown in Figure 22. The intensity ramps up over a few seconds at the start of the spill, and there are two large dips to zero intensity at three and thirteen seconds when beam was extracted to other experiments.

4.2.3 Trigger Rates

For the bulk of the data described in this thesis we chose to operate with 7×10^{11} protons/spill hitting the target, where the yield was maximized. Because of variations in machine tuning, there were 20% fluctuations from spill to spill and day to day. During approximately the first week of the run, the beam intensity was about 10^{12} protons/spill. Figure 23 shows the intensity distribution of spills in this data set.

The number of triggers written to tape in each event category during a typical spill is shown in Table 5. The charged triggers, dominated by $K_L \to \pi^\pm e^\mp \nu$ decays, were prescaled to allow collection of an adequate number of $\pi^0 \pi^0$ decays.

4.3 Information Recorded

The run consisted of about 14,000 spills, the data from which filled roughly 1000 6250 bpi 9-track magnetic tapes.
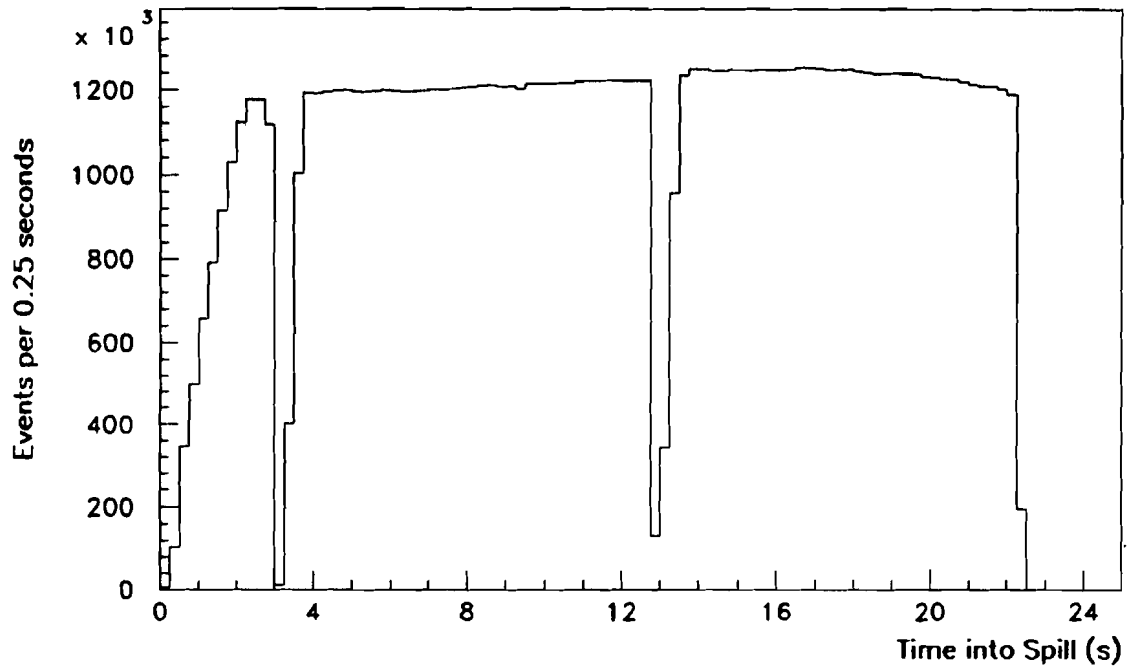
Figure 22. The proton beam intensity as a function of time into the spill.

For each event, detailed information about the activity in all elements of the detector was recorded, as well as some general information identifying its trigger type, the run, spill and event number, and the position of the regenerator and upstream absorber. The information recorded for each detector element is given in Table 6. In addition to these, all signals used to form the triggers were latched and saved, as were their arrival times. To enable studies of out-of-time particles, we recorded the total energy in the lead glass during the buckets immediately preceding and following the trigger. Finally, two miscellaneous items were saved: the time of the trigger with respect to the start of the spill, and as a measure of the instantaneous beam intensity, the total number of counts in the RA in a 100 μs period following the trigger.

The data blocks containing drift chamber TDC and lead glass ADC were the largest. To minimize the number of ADC channels recorded, a 5 count (25 MeV) readout threshold was applied to the signal in each, yield
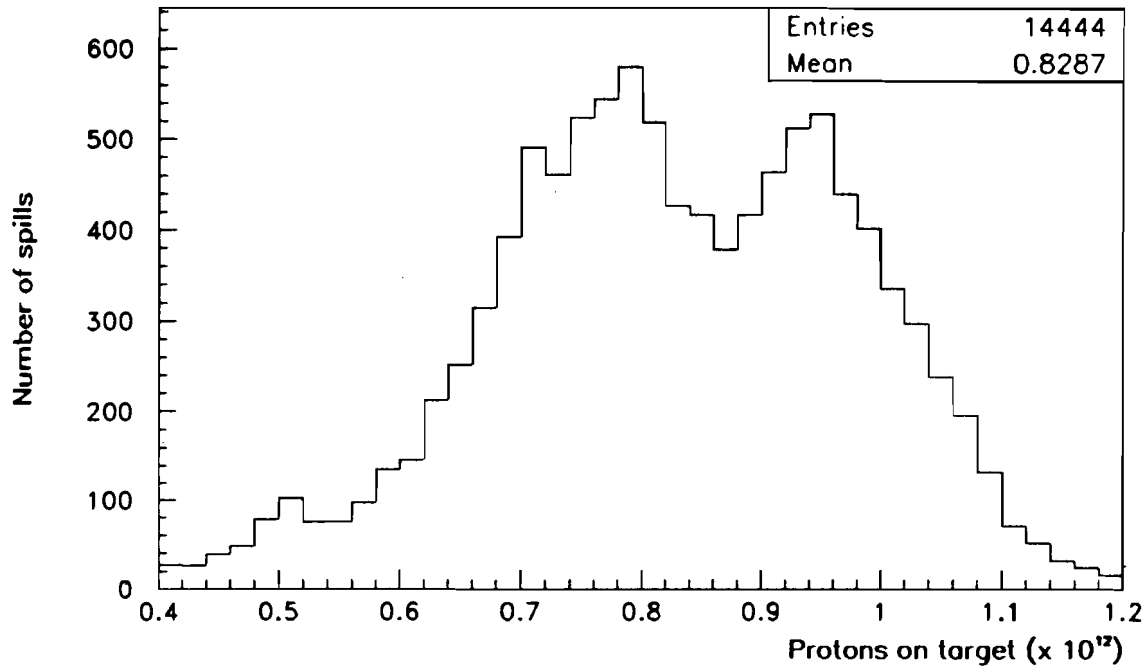
Figure 23. The intensity distribution of the proton beam for the data described in this thesis.

TABLE 5. The number of events recorded during a typical spill. During this spill 0.86 x 10^{12} protons hit the target. Also shown is the prescale rate of each trigger.

Trigger	Events/spill	Prescale factor
Charged	3,399	8
Neutral	3,207	
Kmu3	190	100
Muon	109	2^{16}
Accidental	96	20
ADC Pedestal	50	
Lead glass flasher	21	

ing about 40 blocks for an average neutral trigger. The total event size averaged 500 16-bit words.

Special information was saved at the beginning and end of each spill. At the beginning, the value of the pedestal subtracted by the ADC's from each signal was recorded. At the end, the characteristics of the spill were summarized: the total number of protons hitting the target, the counting rate in most of the counter banks, the number of events satisfying each level of the neutral and charged triggers, profiles of the proton beam, the currents in the magnets in the decay region and detector, and last, readings from temperature monitors on the lead glass calorimeter and ADC's.

4.4 Data Monitoring

In order to ensure that the detector was working properly, the data were carefully monitored. First, while we were running, every thousandth event written to magnetic tape was routed to a μVAX, which histogrammed the energy deposit in the lead glass blocks, the times of drift chamber hits, the latch bits and other primitive quantities. These histograms were monitored by physicists on shift, and the μVAX was programmed to flag anomalies. In addition, once every eight hours (fifteen tapes) one of the data tapes

TABLE 6. The information recorded for each detector element.

Detector element	ADC	Latch	TDC
Accidental trigger counters		•	
Pinching Anti (PA)		•	
Sweeper Anti (SA)		•	
Active Mask (AM)		•	
Regenerator (RA)		•	
Vacuum Antis (scint.)		•	
Vacuum Antis (γ)	•		
Veto counter (V)	•	•	
Trigger counter (T)	•	•	
DRAC	•	•	
DRAN	•		
Drift Chambers			•
Magnet Anti (scint.)		•	
Magnet Anti (γ)	•		
Lead Glass Anti (scint.)		•	
Lead Glass Anti (γ)	•		
C Bank		•	
B Bank	•	•	
Collar Anti (CA)	•		
Lead Glass (PbG)	•		
Adders	•		
MU1	•		
BA	•		
MU2		•	

was analyzed offline. The resulting plots of both primitive and higher level quantities, such as drift chamber wire efficiencies, hardware cluster finder energy thresholds, and finally, the kaon invariant mass, were studied and compared with the nominal distributions.

4.5 Special Runs

Special runs were taken to study systematic effects and to calibrate the detector. Those intended for systematic studies will be described as they become relevant to the discussion, but the calibration runs were done regularly and are briefly described here.

4.5.1 Muon Runs

Once a day, data were collected for muons passing straight through the detector, with no current in any of the magnets in the detector region. These runs, which took only several minutes to do, were used to determine the relative transverse positions of the drift chambers as described in Chapter 5. The absolute position of the chamber system with respect to the rest of the detector were later determined using other charged track data.

Other muon data were collected with slightly different triggers to calculate efficiencies and gains of some of the detector elements. For example, a small scintillation counter placed in front of the BA was used to trigger on muons for its calibration.

4.5.2 Electron Calibration Runs

In order to calibrate the lead glass calorimeter, once every two weeks data were collected from momentum-analyzed electrons sprayed over the calorimeter. In order to produce an electron beam, the lead absorbers near the target were removed to enhance the photon content of the beam, and some of these photons were converted to electron-positron pairs in a sheet of 0.13 mm copper and 0.08 mm titanium inserted in the beam 73.4 m downstream of the target. The electron beam then passed through the vertical and horizontal separating magnets, *AN1* and *AN2* (see Figure 3) which

spread them into a band across the face of the calorimeter. By appropriate choice of magnet currents, the band could be rotated about the beam axis across the calorimeter, so that after eight magnet settings, all blocks had been illuminated. With additional settings, the momenta of the electrons and positrons could be varied as well.

One calibration run, consisting of 16 tapes of data and about one million electrons, was used for the analysis of the data described in this thesis.

4.6 Features Special to this Data Set

There are several distinctions between the data described in this thesis and the rest of the data collected by E731. For the bulk of the data, neutral and charged data were collected separately, with slight differences in the detector for the two running modes. In particular, during neutral running, an 0.5 mm lead sheet was inserted between the T and V counters at the downstream end of the decay region to convert one of the four photons. The photon conversion was a convenient signature for triggering, and the resulting electron-positron pair could be tracked in the spectrometer, allowing reconstruction of the transverse position of the decay vertex and calculation of the transverse momentum of the kaon acquired in the regenerator. Neutral decays without a photon conversion were also recorded.

For charged mode running, the lead sheet was removed, and, in order to improve the momentum resolution for the pions, the magnetic field strength was increased by a factor of two, to the limits of the magnet. The magnet used to separate the electron-positron pair in neutral mode running was turned off. A readout threshold of 100 MeV was applied to the lead glass ADC's in order to avoid writing out unnecessary information and keep the number of magnetic tapes manageable.

During charged running, the $\pi^0\pi^0$ trigger requiring photon conversion could not be used because the lead sheet was absent and the magnet settings were inappropriate, but the $\pi^0\pi^0$ trigger not requiring photon conversion was active, and events satisfying it were recorded. A large number of neutral decays were accepted during charged running; however, because

of the high ADC readout threshold, it will be more difficult to achieve the desired calibration precision for these events.

During a three week period near the end of the run, the lead sheet was removed and the magnets were set for charged mode running, and at the same time, the lower ADC readout threshold was used. Conditions were therefore optimal for both $K_{L,S} \to \pi^+\pi^-$ and $K_{L,S} \to \pi^0\pi^0$ decays without a photon conversion, and data for both were collected simultaneously. Data taken during this period comprise about 20% of the full E731 data set. Their analysis is presented in this thesis.

We continue, then, with analysis of the data, beginning with the $K_{L,S} \to \pi^+\pi^-$ decays.

CHAPTER 5

ANALYSIS OF THE CHARGED DECAYS

5.1 Overview

The data analysis occurred in two stages. In the first, which took place six months after the end of the data collection run, loosely selected candidate $\pi^0\pi^0$ and $\pi^+\pi^-$ events on the 1000 magnetic tapes were channeled into separate data streams. The candidate $\pi^0\pi^0$ and $\pi^+\pi^-$ samples each filled fourteen 6250 bpi magnetic tapes, a manageable number for in depth data analysis. In the second stage, which spanned the following fifteen months, the selection criteria and detector calibration were refined, and the data studied in detail. At all stages, selection criteria were blind to the K_S or K_L origin of each decay.

In this chapter, analysis of the charged decays, $K_{L,S} \to \pi^+\pi^-$, is described, beginning with the charged spectrometer used to reconstruct them.

5.2 Track Reconstruction

5.2.1 Track Finding

A typical charged decay is shown in Figure 24. The analyzing magnet imparted x momentum to the particle, so tracks were bent in the x view, but were essentially straight in y.
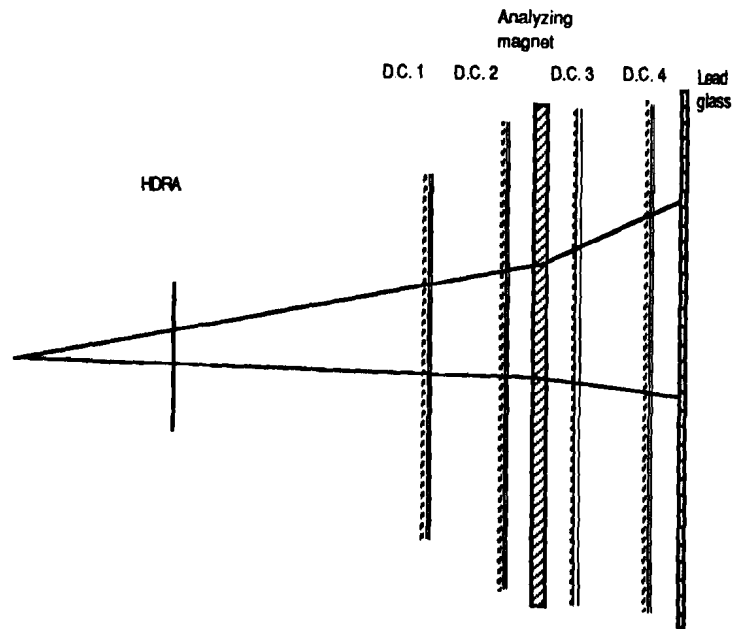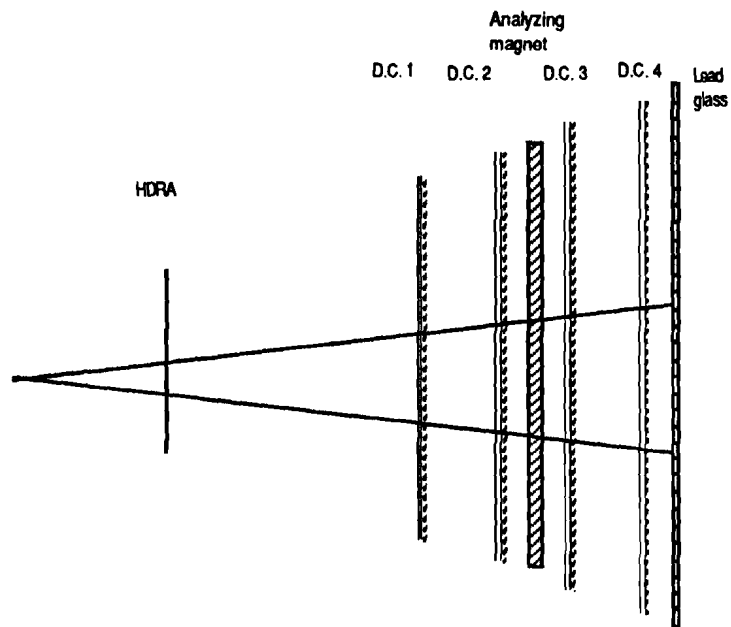
Figure 24. Schematic of a $K_{L,S} \to \pi^+ \pi^-$ decay.

The track finding algorithm will be described in detail in the thesis of L. K. Gibbons [28], and will only be outlined here. In the x view, track segments were found separately in the chambers upstream and downstream of the analyzing magnet, and those consistent with a single track bending in the midplane of the analyzing magnet were paired. In the y view, straight tracks through all four chambers were identified. Each combination of two wire hits, with one hit in the first chamber and one in the last, defined a candidate track segment, where hits with times outside the range $10 < t < 250$ ns were excluded (the time distribution of hits is shown in Figure 6). Upstream segments were included only if they pointed within 5 cm of the trigger plane, while downstream segments were included only if they pointed within 8 cm of the lead glass and met an upstream track at the midplane of the magnet within ± 3 cm. A "road" was formed 1 1/2 chamber cell widths about the imaginary line connecting the hit wires in the first and last chambers, and all the hits on wires lying in the road formed a track. Finally, a χ^2 was calculated for each track segment using the timing information of hits on wires lying in the road. The χ^2 distribution is shown in Figure 25 for identified pion track segments. In the analysis, a loose cut at $\chi^2 = 30$ was applied.

Tracks in the y view were found using the same algorithm, except that the roads spanned all four chambers. Once the hits were identified, the tracks were fit in upstream and downstream segments. Separating the segments accomodated the slight bend in the magnet due to the small z component of the magnetic field.

Because muons passed through the detector at random times, there were frequently stray hits in the drift chambers, about 8 on average. Many of these tracks passed through the detector significantly earlier or later than the kaon decay, so that the times measured for their hits were shifted with respect to the actual drift time through the cell. Because the time window for the hits was 240 ns long, few of these could be identified by the time of the hit alone, but the hit position information which was derived from the measured times (by a procedure described shortly), could identify combinations of hits inconsistent with an in-time track. Each chamber had two layers of wires in each direction (x and y), offset from one another as

shown in Figure 5. Generally a track left hits on wires in each layer, with the sum of distances of the hits from the two wires equal to the total width of the cell. In the track reconstruction, a loose cut was made on this sum in order to eliminate out-of-time particles: tracks with more than one out-of-time pair were discarded.

The x and y views of the tracks were paired with one another by matching them with clusters in the lead glass calorimeter. For each possible combination of x and y tracks, we counted the tracks which pointed within 7 cm of a cluster. Thus, for each x-y pairing in a two track event, the number of matches could be 0, 1, or 2. We chose that x-y pairing which yielded the most matches. If two pairings matched the same number of clusters, so that the choice was ambiguous, then the one which minimized the total track to cluster distance was chosen.
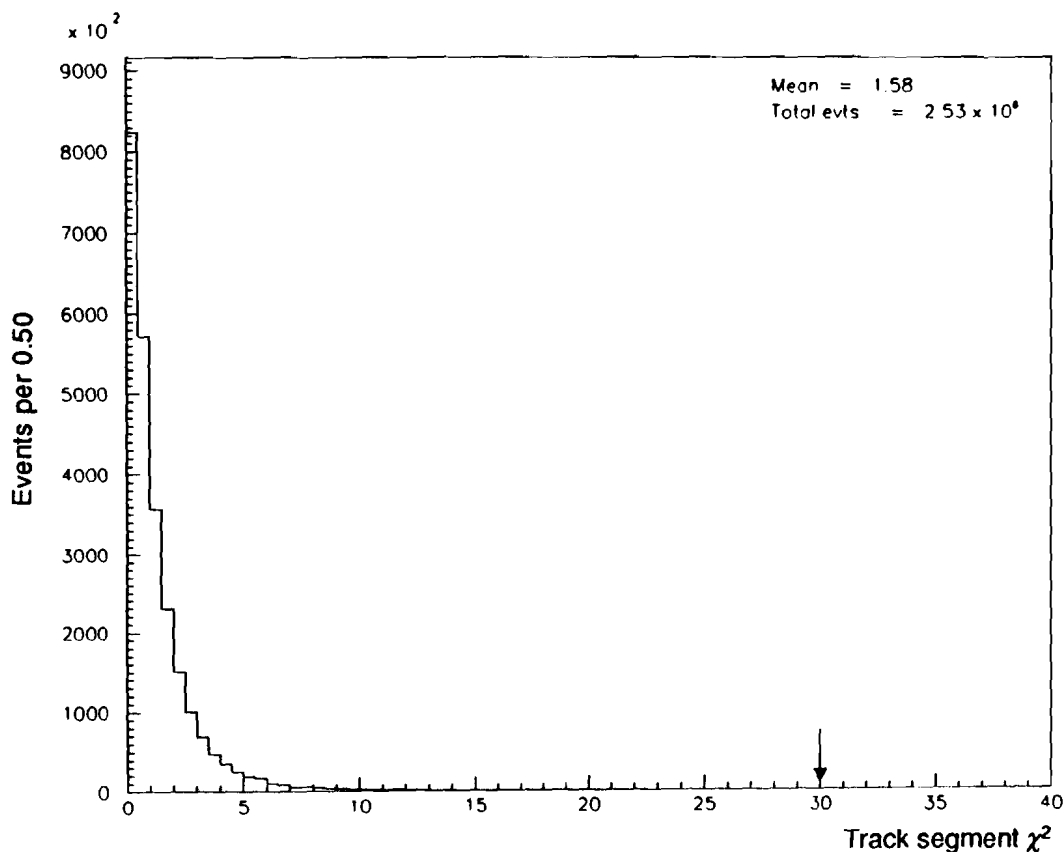
Figure 25. The χ^2 distribution of identified π track segments. There are two degrees of freedom in the fit. The arrow indicates the position of the cut.

5.2.2 Chamber Calibration

Track reconstruction depended on accurate knowledge of the positions of the drift chamber wire planes. Their relative offsets were determined by studying the tracks of muons taken during the special daily runs with all analyzing magnets turned off. The offsets varied slowly with time, with occasional jumps when minor repair work had been done. The offsets and rotations of the second and third chambers with respect to the first and fourth were found by demanding that the muon tracks be straight. Typically, these offsets were less than 1 mm. An overall screw rotation of the chamber system about the z axis was found by applying the requirement that the two tracks from $K_L \rightarrow \pi^{\pm} e^{\mp} \nu$ decays lie in a plane. The net rotation of each chamber was typically less than 300 μr. Rotations about the x and y axes were one mrad or less and had negligible effect on the reconstructed tracks.

Finally, the chamber system as a whole was aligned within the rest of the detector, whose coordinate system was defined by the kaon production target and the lead glass calorimeter. These two objects were assumed to be fixed in space throughout the run. To align the chamber system, we first calculated the average offset between tracks extrapolated into the lead glass calorimeter and the center positions of clusters determined from the calorimeter. Next, we found the target position in the chamber coordinate system by extrapolating the fully reconstructed kaon momentum in two-body decays to the production target. The chamber positions were then adjusted to bring the cluster offsets to zero and the target to its nominal position.

To be useful for track reconstruction, the time of each hit had to be converted to a position within the chamber cell. In order to determine this function, we chose a sample of charged data, and applied the assumption that the track illumination was uniform across the cell. The distance of the track from the wire as a function of hit time t, $d(t)$, was then given by

$$d(t) = L \frac{\int_0^t N(t')dt'}{\int_0^{t_{max}} N(t')dt'}$$

where $N(t)$ is the time distribution of hits, L is the cell size, and t_{max} is the maximum drift time. This function was determined using two track data, and was periodically updated to account for small variations in chamber gas composition and pressure. After correcting for the travel time of the signal along the wire, the position resolution was 100 μm per wire plane.

The momentum p of a track was related to its bend angle $\Delta\theta$ in the magnet via

$$p = \frac{P_{x_{AN4}}}{\Delta\theta}$$

where we have assumed that $\Delta\theta$ is small. The "momentum kick", $P_{x_{AN4}}$, delivered by the magnet is given by

$$P_{x_{AN4}} = ke\int_{path}(\mathbf{B} \times d\mathbf{l})_x \ .$$

where $d\mathbf{l}$ is taken along the path of the particle, $\mathbf{B}$ is the field strength of the magnet, and k is a constant which depends on the system of units. The mean value of $P_{x_{AN4}}$ was about 0.2 GeV/c. It varied by about 2% over the aperture and was mapped following the run. The map was made on a 5.1 cm grid in the transverse plane with point to point accuracy of about 0.1%. The mapped field strength was used in the analysis, and the effect of the residual uncertainty on the momentum resolution was small.

In order to reduce systematic error in an accompanying measurement of the charge asymmetry of $K_L \rightarrow \pi^{\pm}e^{\mp}\nu$ decays, the magnet polarity was reversed about once each day, and each time, the overall field strength of the magnet changed slightly, 0.4% or less. The sizes of the changes were determined from shifts in the reconstructed kaon mass. The residual uncertainty in the momentum scale was < 0.04%.

The momentum resolution of the spectrometer was limited by the measurement of the track bend angle. The root mean square uncertainty in momentum due to the chambers themselves, based on the 100 μm hit resolution and chamber geometry was $0.011\%p$ (*GeV/c*).

Additional momentum smearing arose from multiple scattering of the tracks, which changed the apparent bend angles in the analyzing magnet. Only material between chambers 1 and 4 contributed. This included the wires and gas of chambers 2 and 3, as well as the windows of the chambers and helium bags, the number of radiation lengths of each of which is listed in Table 3. The total was $0.007\ X_0$. Using the approximate expression for the root mean square scattering angle in a plane of a relativistic particle passing through X radiation lengths [13]

$$\theta_{MS} = \frac{14.1 MeV/c}{\sqrt{2}p}\sqrt{X}\left(1 + \tfrac{1}{9}\log_{10}X\right) \quad \text{(radians)}$$

one finds that the contribution of multiple scattering to the resolution is 0.46%. The total momentum resolution is then

$$\left(\frac{\Delta p}{p}\right)^2 = (0.46\%)^2 + \left(0.011\%p[GeV/c]\right)^2$$

For pions from $K_{L,S} \to \pi^+\pi^-$ decay, whose mean momentum was about 35 GeV/c, the momentum resolution was thus about 0.6%.

5.3 Selection Criteria for $\pi\pi$ Decays

5.3.1 Event Reconstruction

Events were accepted with two tracks in the x and y views, and at least one cluster in the calorimeter to allow track matching. Both tracks were required to be fully contained in the fiducial volume of the detector: tracks that did not pass through the trigger scintillation plane (HDRA), the vacuum window, or the magnet aperture were assumed to have scattered heavily or to be a muon unassociated with kaon decay and were rejected.

The decay vertex of two track events was assigned to the point of closest approach of the extrapolated upstream track segments. For accepted events, the two tracks were required to come within 4σ of intersecting, where σ was the uncertainty in the distance of closest approach due to chamber resolution and scattering.

The position of the kaon in the x-y plane at the z of the regenerator told us whether it had originated in the vacuum or regenerated beam. To calculate this position, we extrapolated back to the regenerator along the trajectory defined by the total vector momentum of the two tracks (upstream of the magnet) and the decay vertex position. The results are shown in Figure 26. Events extrapolating into the same half plane (upper or lower) as the regenerator were assumed to have originated in the regenerated beam, and the others were assumed to have originated in the vacuum beam.

For candidate $K_{L,S} \to \pi^+\pi^-$ decays, the tracks were assumed to be pions, and the invariant mass was calculated according to

$$m_{\pi\pi} = \sqrt{\left(\sqrt{|\mathbf{p}_1|^2 + m_\pi^2} + \sqrt{|\mathbf{p}_2|^2 + m_\pi^2}\right)^2 - |\mathbf{p}_1 + \mathbf{p}_2|^2}$$

where $\mathbf{p}_1$ and $\mathbf{p}_2$ are the momenta of the two tracks. The distribution of $m_{\pi\pi}$ is shown in Figure 27 for two track events. The kaon peak is visible for vacuum decays, but with about 88% background, predominantly due to $K_L \to \pi^\pm e^\mp \nu$ decays. Decays in the regenerated beam have much less background. Like the vacuum beam decays, most of the background is due to $K_L \to \pi^\pm e^\mp \nu$ decays, in this case from the 6% of K_L mesons which are transmitted through the upstream absorber and regenerator. The peak at the kaon mass (0.4977 GeV/c²) has a width (sigma) of 3.5 MeV/c². Ultimately, those within the range $484 < m_{\pi\pi} < 512$ MeV/c² were accepted.

5.3.2 Non-$\pi\pi$ Background Rejection and Subtractions

The background $K_L \to \pi^\pm e^\mp \nu$ decays were most easily identified and rejected by the energy deposit E of the electron in the lead glass calorimeter. The distributions of the ratio of energy deposit E to track momentum p of identi-
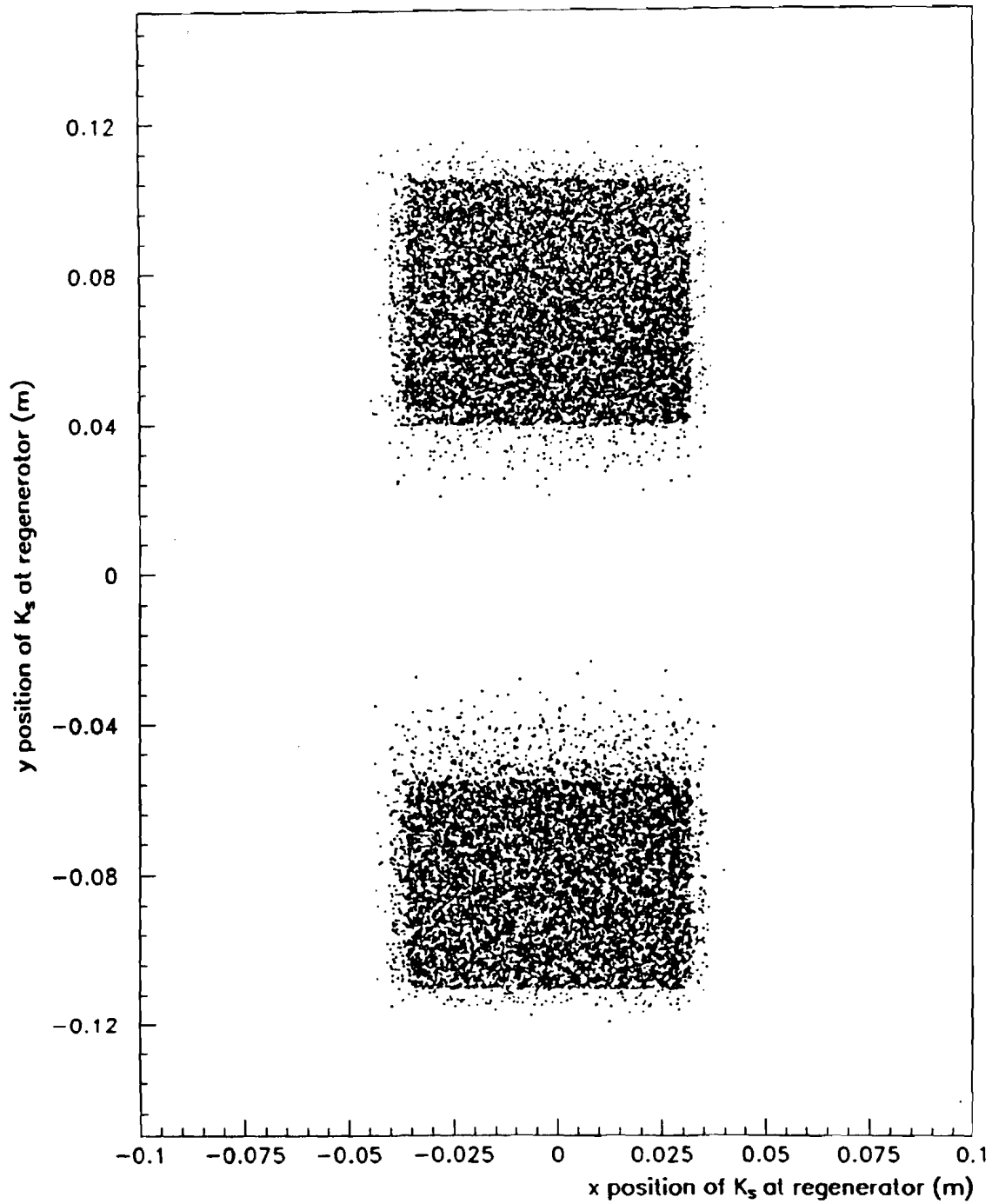
Figure 26. The transverse position of the reconstructed kaon at the plane of the regenerator.
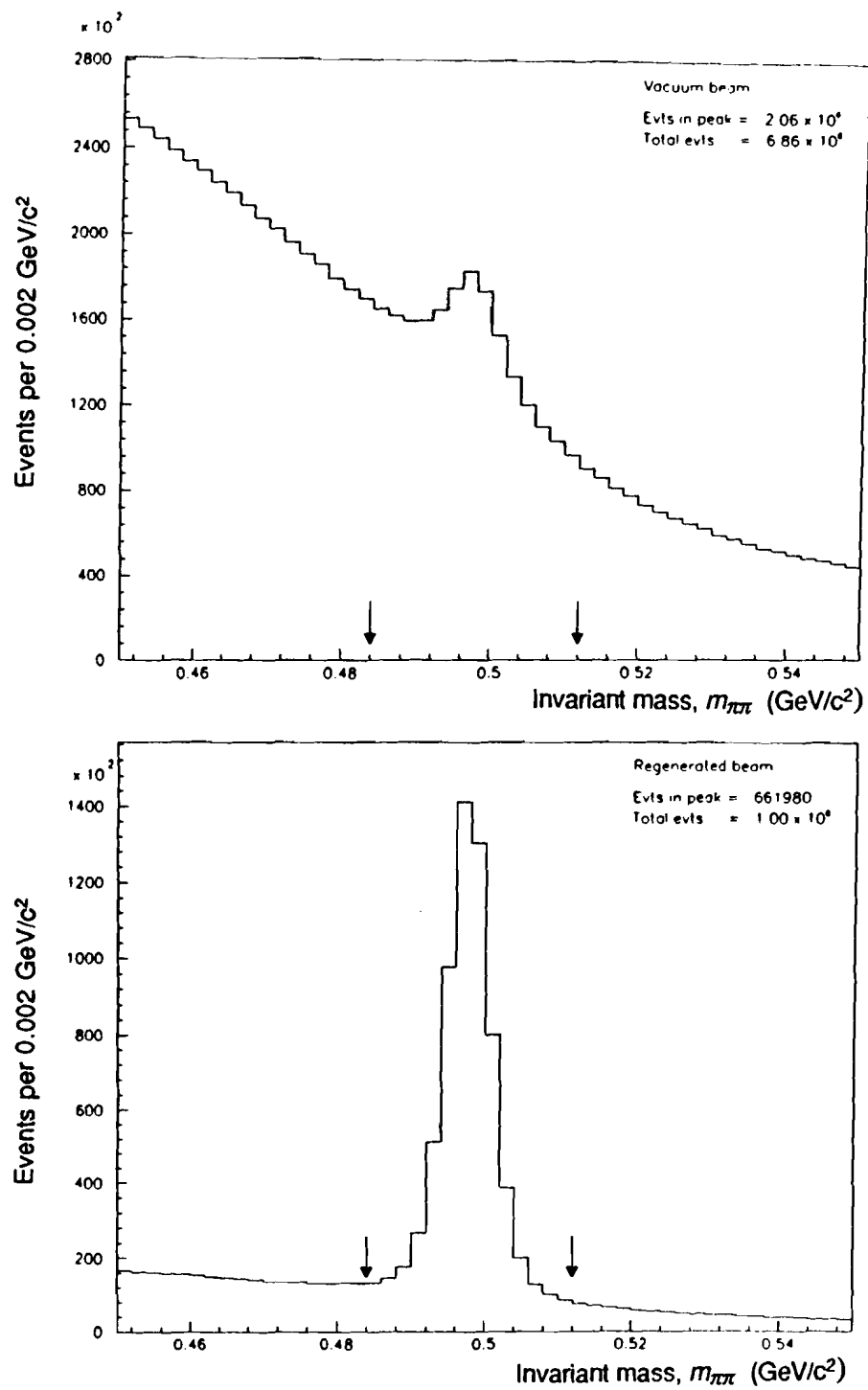
Figure 27. The two pion invariant mass distribution of all two track events in the vacuum and regenerated beams. The arrows indicate the positions of the cut.

fied pions and electrons are shown in Figure 28. An electron deposited essentially all of its energy in the lead glass calorimeter, so that neglecting resolution, the ratio of energy to momentum was unity. On the other hand, about half of the charged pions hitting the glass generated only the Cerenkov light of a single charged particle, comparable in light output to a 0.7 GeV electromagnetic shower. The other pions initiated a hadronic shower, which deposited only some of its energy in the calorimeter, so that E/p was less than unity. For candidate $\pi^+\pi^-$ events, it was required that E/p of both tracks be less than 0.80, a cut which retained 94% of good $\pi^+\pi^-$ decays, and eliminated more than 99% of the $K_L \to \pi^\pm e^\mp v$ decays. Events were rejected if either track missed the calorimeter or hit within 1/2 lead glass block width of either beam hole, where significant energy loss was likely. For events in which one of the tracks hit the calorimeter in the vertical stripe containing the beam holes and the x separation of the two tracks at the calorimeter was less than 2 cm, the probability of mismatching the x view of tracks with the clusters and miscalculating E/p, was high. Such events were discarded.

The $K_L \to \pi^\pm e^\mp v$ decays were further distinguished from $\pi^+\pi^-$ decays by a two-track momentum component transverse to the beam arising from the missing neutrino momentum. We define

$$P_t^2 = \left| \mathbf{p}_1 + \mathbf{p}_2 \right|^2 \sin^2 \theta$$

where θ is the angle between the two-track momentum vector and a line joining the target to the position of the two track trajectory at the z of the regenerator, as shown in Figure 29. A P_t^2 calculation based on the decay vertex rather than the regenerator would maximize $K_L \to \pi^\pm e^\mp v$ rejection; however, as is described later on, using the regenerator facilitated analysis of K_S scattering in the regenerator, and was adequate for $K_L \to \pi^\pm e^\mp v$ background rejection. The P_t^2 distribution of decays from the vacuum beam are shown in Figure 30. A cut was applied at 250 (MeV/c)². Most of the $K_L \to \pi^\pm e^\mp v$ decays lie at $P_t^2 < 10,000$ (MeV/c)². Events further out in the tail are due to kaons which scattered in the HDRA trigger plane. The size of the residual background to the $\pi^+\pi^-$ sample after all cuts was determined
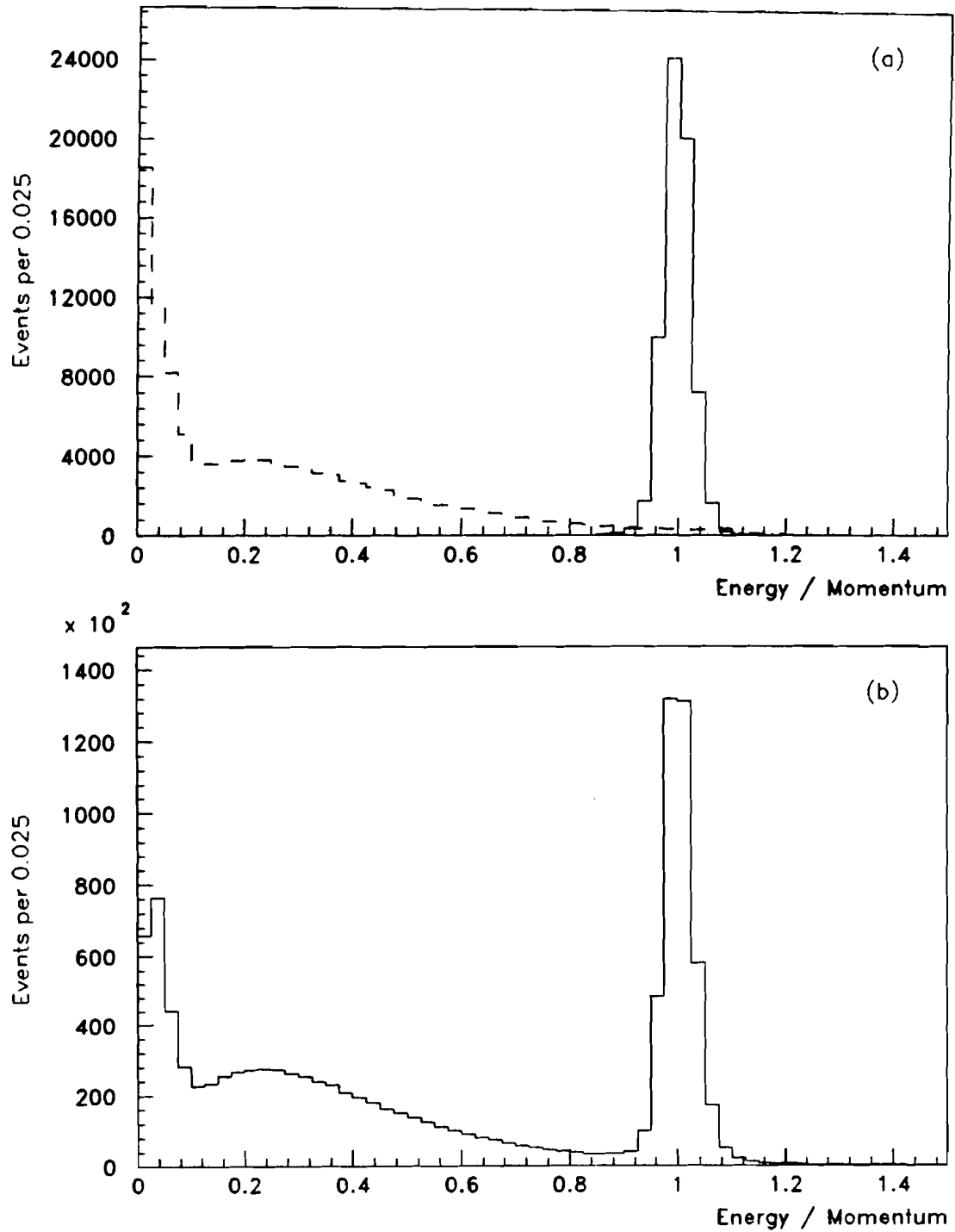
Figure 28. The ratio of energy deposit in the lead glass to track momentum (E/p). (a) Pions (dashed line) and electrons (solid line). (b) The maximum E/p of the two tracks hitting the glass in two track events.

by extrapolating under the peak at $P_t^2 = 0$; however, before describing this procedure, selection criteria to remove other sources of background will be described.

A few Λ's and $\overline{\Lambda}$'s were produced in the target or in the decays of short-lived hyperons from the target, and their respective decays to $p\pi^-$ and $\overline{p}\pi^+$ were responsible for small backgrounds. To reject them, events were cut if they satisfied three criteria. First, the ratio of the magnitudes of the larger to smaller track momenta had to be greater than three. Second, the invariant mass had to be consistent with a Λ ($1.1 < m_\Lambda < 1.3$ GeV/c^2) when the higher momentum particle was assumed to be the proton, and finally, the Λ energy had to be greater than 100 GeV. The last requirement was applicable because only energetic Λ's produced at or near the target in short-lived hyperon decays survived as far as the decay volume. After these cuts, contamination by Λ's was negligible.

The $K_L \to \pi^\pm \mu^\mp \nu$ background was rejected by means of the muon filter, consisting of a scintillator plane downstream of 3 m of steel. Events with a signal in the scintillator were eliminated by the trigger. In addition, events for which the efficiency of the muon filter was compromised were rejected off-line. These included events with tracks extrapolating outside the scintillator bank or with momentum below 7 GeV/c, since these could range out in the steel and avoid the veto. About 5% of the pions produced in
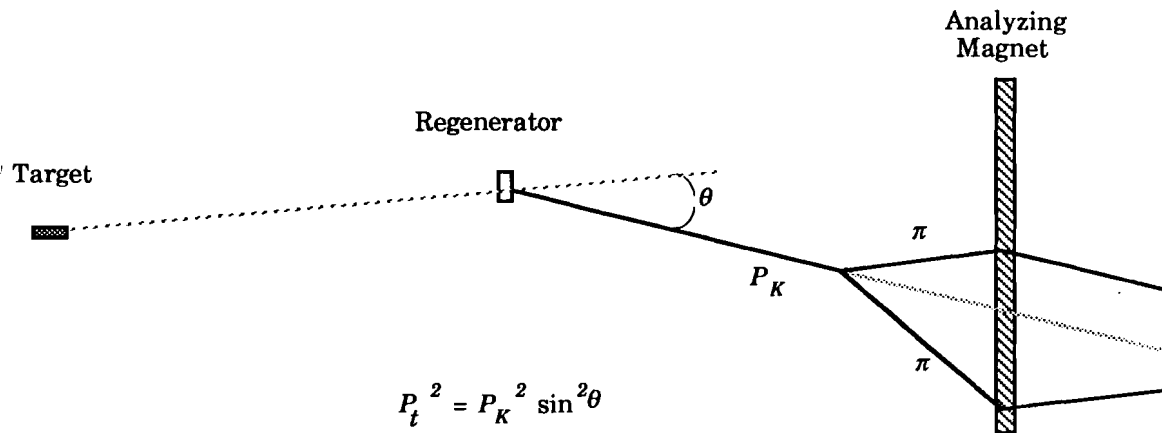
Figure 29. The geometric construction used to calculate the P_t^2 of the kaon.
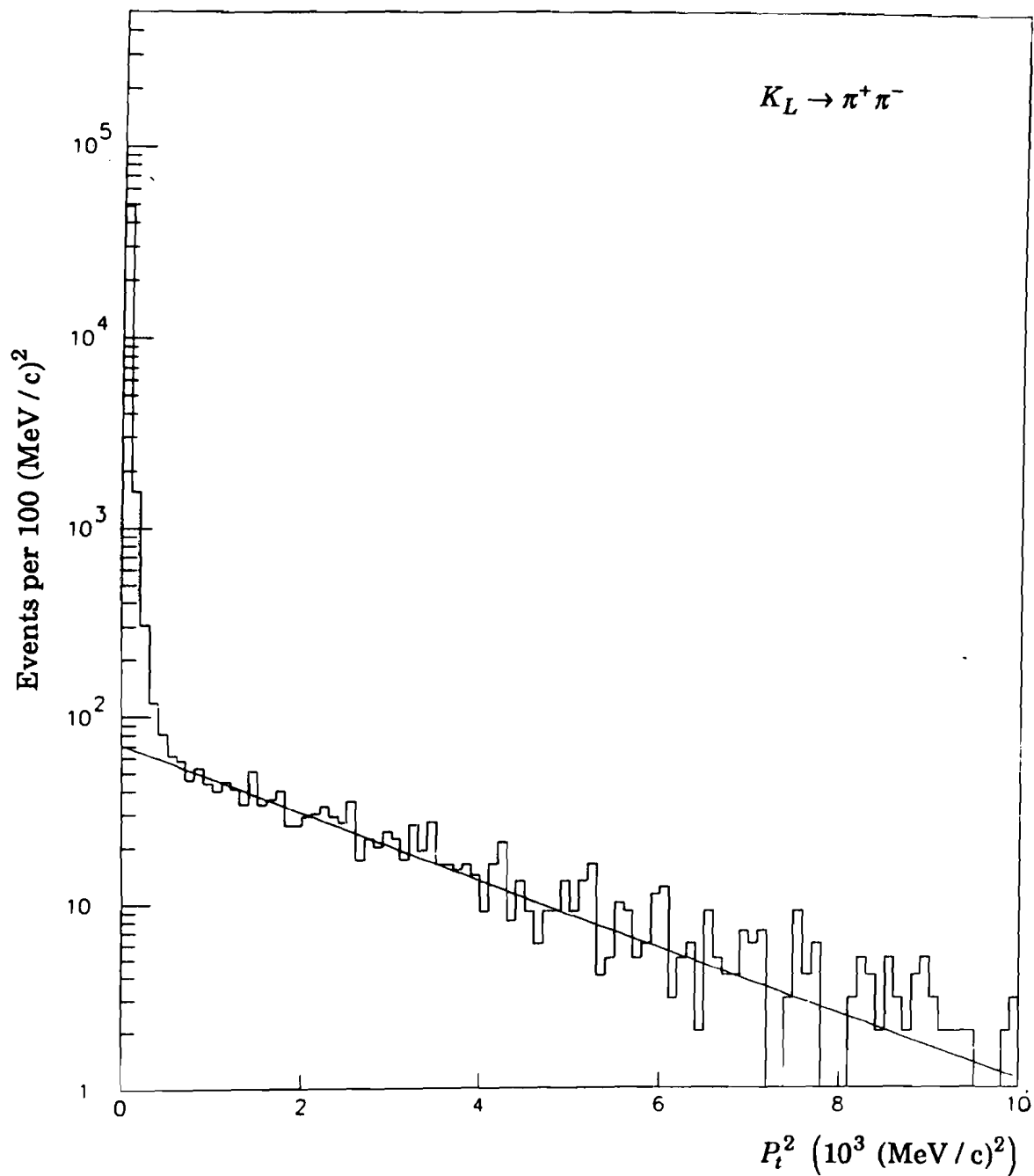
Figure 30. The P_t^2 distribution of two track decays in the vacuum beam after all cuts. The solid line is a fit to the data described in the text.

$K_{L,S} \to \pi^+\pi^-$ decays decayed in flight and were then misreconstructed or vetoed by the muon filter. While the momentum spectra of decaying K_S and K_L were very similar, their decay vertex distributions were not, resulting in an asymmetry in the fraction of pions decaying of about 0.2%. This effect was accounted for in the Monte Carlo as described in Chapter 8.

The $K_L \to \pi^+\pi^-\pi^0$ decays were also copious and therefore a potential source of background. Because the π^0 energy was missing, however, the reconstructed invariant mass was well below the kaon peak, and with the relatively narrow accepted mass window, these decays contributed negligible background.

The final source of background was $K_L \to \pi^+\pi^-\gamma$ decays. The $\pi^+\pi^-\gamma$ final state arises from two sources. The first, $\pi^+\pi^-$ decays with an inner bremsstrahlung photon, is common to K_L and K_S. In these decays, the photons are often soft, and contribute a low side tail to the $\pi\pi$ mass peak. Because the probability of radiation is the same for K_L and K_S, however, no bias results. The second source is the "direct emission" CP-conserving decay $K_L \to \pi^+\pi^-\gamma$, whose branching ratio is about 2% that of $K_L \to \pi^+\pi^-$ [29]. In this case, the photon has center of mass energy k which peaks at about 100 MeV. Since $m_{\pi\pi} \approx m_K - k$, the reconstructed two track mass is well separated from the kaon peak. Only events where k is less than 14 MeV lie within the cut around the kaon mass peak. From past experiments and our own studies, which will be published elsewhere, the probability of this is very small: the total expected contribution to the K_L data sample is only about one event.

The distributions in the kaon energy E_K and decay vertex z after all cuts are shown in Figures 31 and 32. Kaons were accepted with $40 < E_K < 150$ GeV and with $120 < z < 137$ m. For reasons described in the chapter on the extraction of $\mathrm{Re}(\varepsilon'/\varepsilon)$, the energy and z cuts were the same for the neutral and charged decays, with the choice of cuts motivated by neutral mode considerations. One feature beneficial to analysis of the charged decays, however, is immediately visible: the z distribution of decays in the vacuum beam in this region is quite uniform, indicating that the detector acceptance was roughly independent of vertex position for charged decays. Far upstream decays in the vacuum beam were choked off by the lead mask at z
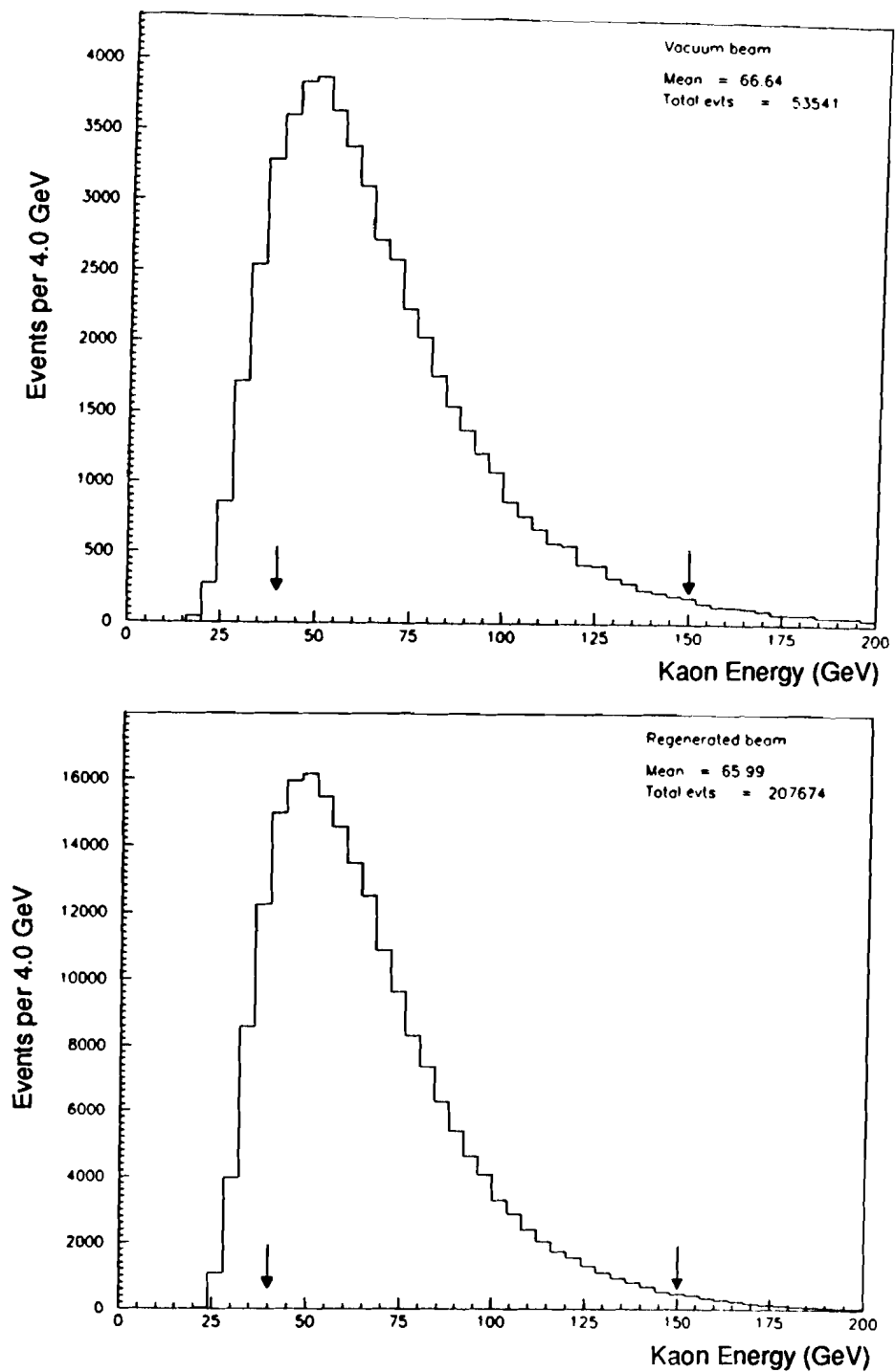
Figure 31. The kaon energy distribution for decays in the vacuum and regenerated beams. The arrows indicate the position of the cut.
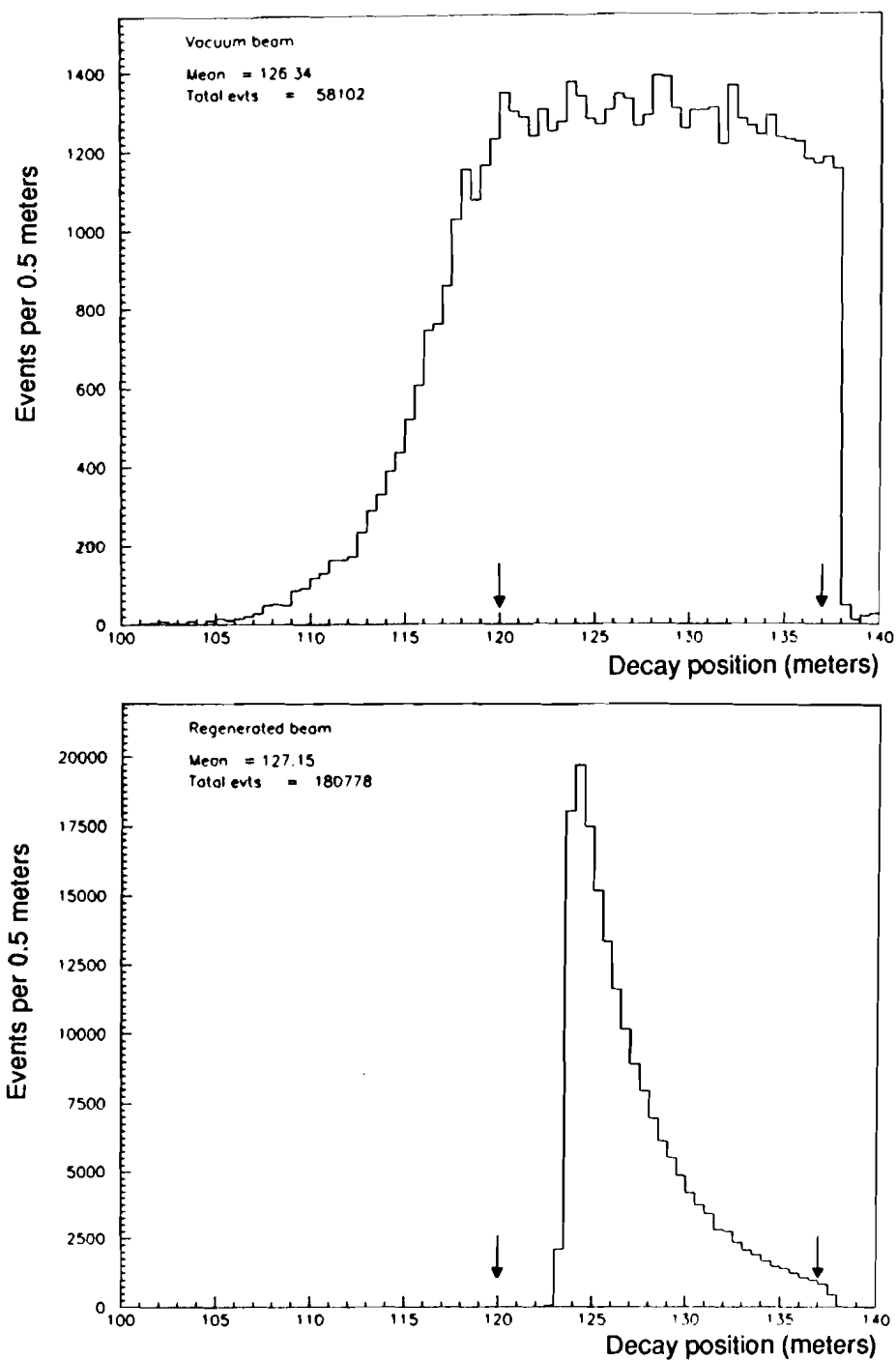
Figure 32. The decay vertex (z) distribution of decays in the vacuum
and regenerated beam. The arrows indicate the position of the cut.

TABLE 7. The effect of cuts (applied in series) on the $K_{L,S} \to \pi^+\pi^-$ data. The backgrounds given are the percent of the events within $0.484 < m_{\pi\pi} < 0.512$ GeV/c^2

Cut	Coherent $\pi^+\pi^-$ Event Loss	Non $\pi^+\pi^-$ Bkgd. (regenerated)	Non $\pi^+\pi^-$ Bkgd. (vacuum)
None (accepted by trigger)		19 %	88 %
Track quality	14 %	17	88
Fiducial volume	30	17	88
$E/p < 0.80$	6	2	25
Λ	1	2	23
$p_\pi > 7$ GeV/c	2	2	16
$P_t^2 < 250$ (MeV/c)^2	<0.01	<1	<1

= 121.9 m, while the sharp edge at the downstream end of the distribution was due to the trigger plane at $z = 137.8$ m. In the regenerated beam, the edge at $z = 123.5$ m was due to the scintillator veto plane at the downstream end of the regenerator. The z resolution was about 20 cm at the upstream end of the decay region, and 10 cm at the downstream end, where the track angles were more favorable. Because of the resolution, the two edges defined by scintillation counters are not perfectly sharp.

Table 7 lists all the cuts applied and the number of events with $0.484 < m_{\pi\pi} < 0.512$ GeV/c^2 surviving at each stage, along with an estimate of the background level for the vacuum and regenerated decays. The "Fiducial volume" cut, where the most good events are lost, includes all cuts based on the positions of the pion trajectories, such as the requirements that they hit the lead glass and muon filter scintillators, but not the vertical stripe down the center of the lead glass. These cuts were imposed because they were easy to simulate with the Monte Carlo, and reduced the sizes of backgrounds that might have been more complicated. Thus, applying them simplified determination of the detection efficiency which we must know as a function of z to extract the final result. The later cuts, particularly E/p and P_t^2, which are a little subtler, cut few $\pi^+\pi^-$ decays.

The $\pi^+\pi^-$ invariant mass distributions are shown in Figure 33 after all cuts. The shapes of the distributions in the two beams are essentially identical. This was important, because it guaranteed that when we applied the cut on the invariant mass, the fraction of events lost was the same for the K_S and K_L samples. Furthermore, it is indicative of the very similar momenta spectra and detector resolutions in effect for kaons from the two beams. To a large extent, the latter is expected to be the same for the two because they were collected simultaneously, but because of differences in the beams themselves, small differences were possible.

The background remaining under the peak is < 0.03% for the K_S decays, and is about 0.3% for the K_L decays, dominated by $K_L \to \pi^\pm e^\mp \nu$. The exact size of the background in the K_L sample was determined by fitting theshape of the P_t^2 distribution, and extrapolating below the cut at $P_t^2 = 250$ (MeV/c)² (see Figure 30). The fit curve was the sum of two exponentials: a fairly flat component describing $\pi^+\pi^-$ produced in interactions in the HDRA trigger plane, given by $\exp(-64P_t^2)$, and a steeper component due to $K_L \to \pi^\pm e^\mp \nu$ background, fit in the region from $2000 < P_t^2 < 10{,}000$ (MeV/c)², and given by $\exp(-424P_t^2)$. Extrapolating the curve under the peak, we found a total background of $(0.32 \pm 0.06)\%$ (168 events), where the uncertainty was determined by varying the form of the background curve and the domains on which the fit was done. The residual $K_L \to \pi^\pm \mu^\mp \nu$ background, estimated to contribute about 0.05%, was included in the subtraction.

For the final analysis and systematic studies, it was necessary to know the backgrounds as a function of kaon momentum and vertex position. Because they are similar kinematically, the z distribution of $K_L \to \pi^\pm e^\mp \nu$ decays faking $\pi^+\pi^-$ is expected to be very similar to that of good $\pi^+\pi^-$ decays, and indeed, when the data were divided into 4 regions of z, and the background fraction was determined in each, no variations were seen. We therefore used a constant background fraction as a function of z. Its dependence on the kaon momentum was determined by binning the data in 10 GeV momentum bins, fitting the P_t^2 distribution in each bin, and extrapolating under the region with $P_t^2 < 250$ MeV² as described above. In the very high momentum bins, there were very few events and only weak momentum dependence, and several bins were summed and fit together. Because
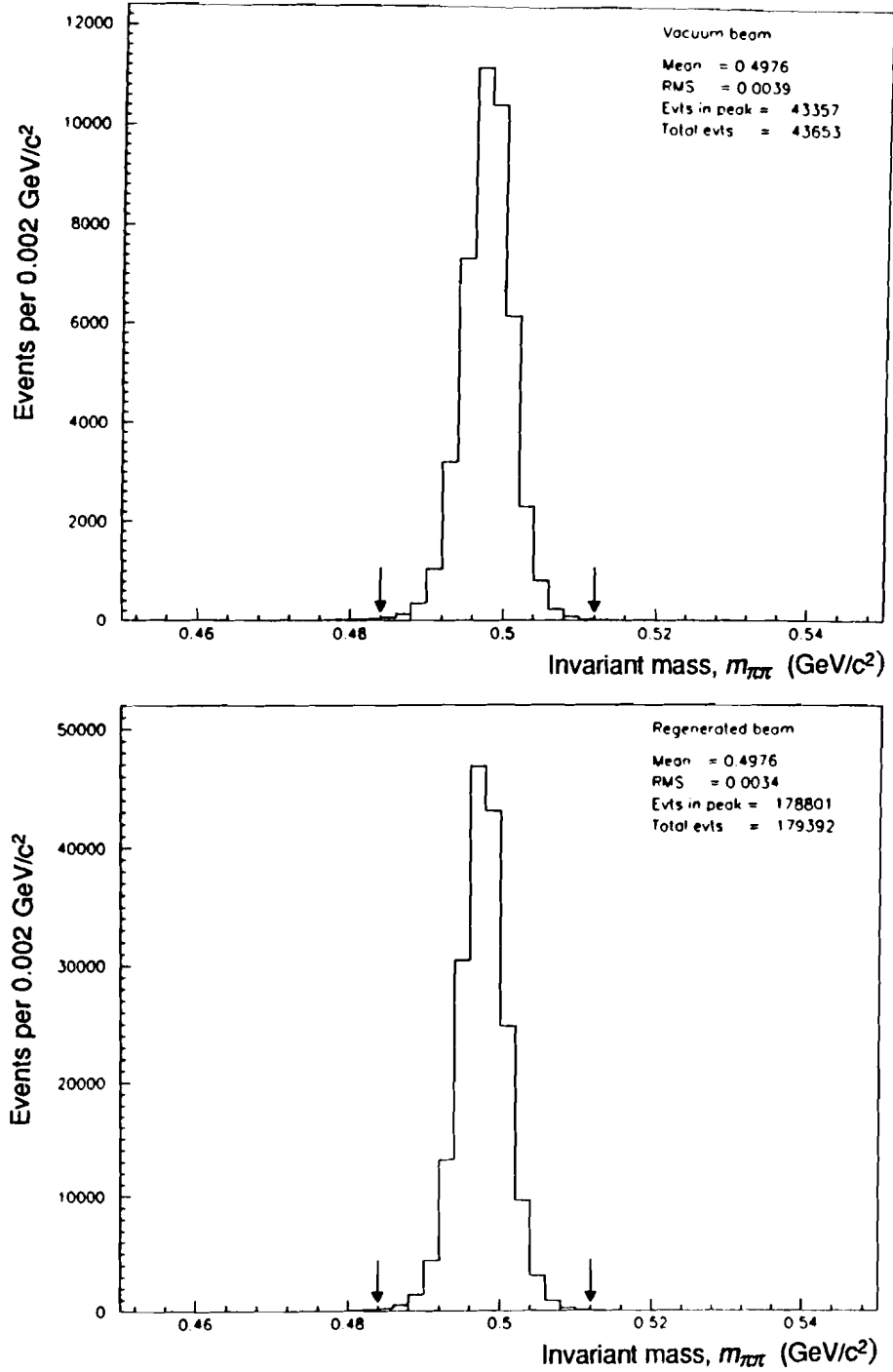
Figure 33. The two pion invariant mass distribution of two track decays after all cuts for the vacuum and regenerated beams. The arrows indicate the position of the cut.

the two track energy of $K_L \to \pi^\pm e^\mp \nu$ decays was less than the full kaon energy, the background is slightly higher in the low momentum bins.

5.3.3 Non-Coherent Background

In this experiment the value of $\text{Re}(\varepsilon'/\varepsilon)$ was extracted from the ratio of K_L to coherently regenerated K_S decays. When the K_L beam hits the regenerator, K_S are produced not only through coherent regeneration, but also through other processes. In our analysis, these non-coherent K_S, which comprised a third of the K_S produced, were cut from our data sample. Why did we discard all this data? There are several reasons. First, it allowed us to check the analysis by comparing the momentum dependence of the regeneration amplitude ρ measured in the neutral and charged modes. Second, inclusion of non-coherent K_S would have required understanding the detection efficiency as a function of scattering angle, something that we needed only roughly understand with the current technique. Finally, the subtraction of non-coherent events was well understood, and the statistical power of the data was limited not by the number of K_S, but the number of K_L decays, so that the increased statistical uncertainty on $\text{Re}(\varepsilon'/\varepsilon)$ due to the subtraction was small.

Subtraction of the non-coherent fractions was done using the P_t^2 distribution of the K_S. The desired coherent K_S lay at $P_t^2 = 0$, while non-coherent components generally had large P_t^2, and could be subtracted by extrapolation under the forward peak. In order to understand this difference in P_t^2 distributions, and to anticipate the size and shape of the non-coherent components, we will briefly describe the various regeneration processes here. For more detailed discussions, see the early papers by Case [30] and Good [31] and the review by Kleinknecht [32].

Regeneration generally occurs through interactions of incident kaons with the nucleons of the regenerator. In elastic scattering, all kaons scattered through the same angle undergo the same phase shift. Because the K_L and K_S have almost identical Compton wavelengths, the phase difference between the incident K_L beam and the forward scattered K_S is almost constant (at least over distances less than about 8 m). Thus, the K_S

produced in the forward direction from scattering off the separate nuclei of the regenerator are coherent. Coherence is rapidly lost, however, for kaons produced at non-zero ($\theta \geq 10^{-8}$ radians) scattering angles. In this case, because of the large separation of the scatterers compared with the kaon wavelength, $\hbar/P_K \approx 0.03$ fm, small variations in the separation between scatterers and in the beam momentum and divergence lead to relative phase shifts and loss of coherence.

A second form of regeneration is "diffractive". This arises from elastic scattering which is coherent off the nucleons in a single nucleus of the regenerator. Because the typical size of the nucleus is fairly small, a few fermi, coherence is maintained out to measurable scattering angles, and, for thin regenerators, a diffraction pattern develops, with minima at momentum transfers of a few hundred MeV. For thick regenerators, the diffraction pattern is mostly smeared out by multiple scattering of the kaons. The amplitude of diffractive regeneration in the forward direction is proportional to $A^{0.76}$ [24], where A is the atomic weight of the nucleus, and minimization of diffractive regeneration is a principle reason for choosing a regenerator made of a low Z material.

The third regeneration process arises from inelastic scattering of the kaon. Because the energy of the kaon is affected, there is no possibility of coherence from this process. Here the kaon can scatter through very large angles, and the regenerated kaons are roughly uniformly distributed in P_t^2. Like diffractive regeneration, the probability of inelastic regeneration falls with the Z of the regenerator. Often, multiple particles are produced in inelastic interactions. This feature made them identifiable in the experiment using the scintillators following each of the four blocks of the regenerator.

The P_t^2 distribution of $K_S \rightarrow \pi^+ \pi^-$ decays is shown in Figure 34. The large peak in the forward direction is clearly visible, with its width, which is less than 50 (MeV/c)^2, resulting from our finite resolution. At $P_t^2 = 0$, the background is shared about equally between inelastic and diffractive regeneration, but from past experiments and studies of regeneration we know that the diffractive component for our regenerator, which contains both B_4C and lead, falls roughly like $\exp(-P_t^2 (\text{MeV/c})^2 / 40{,}000)$, so events at large P_t^2
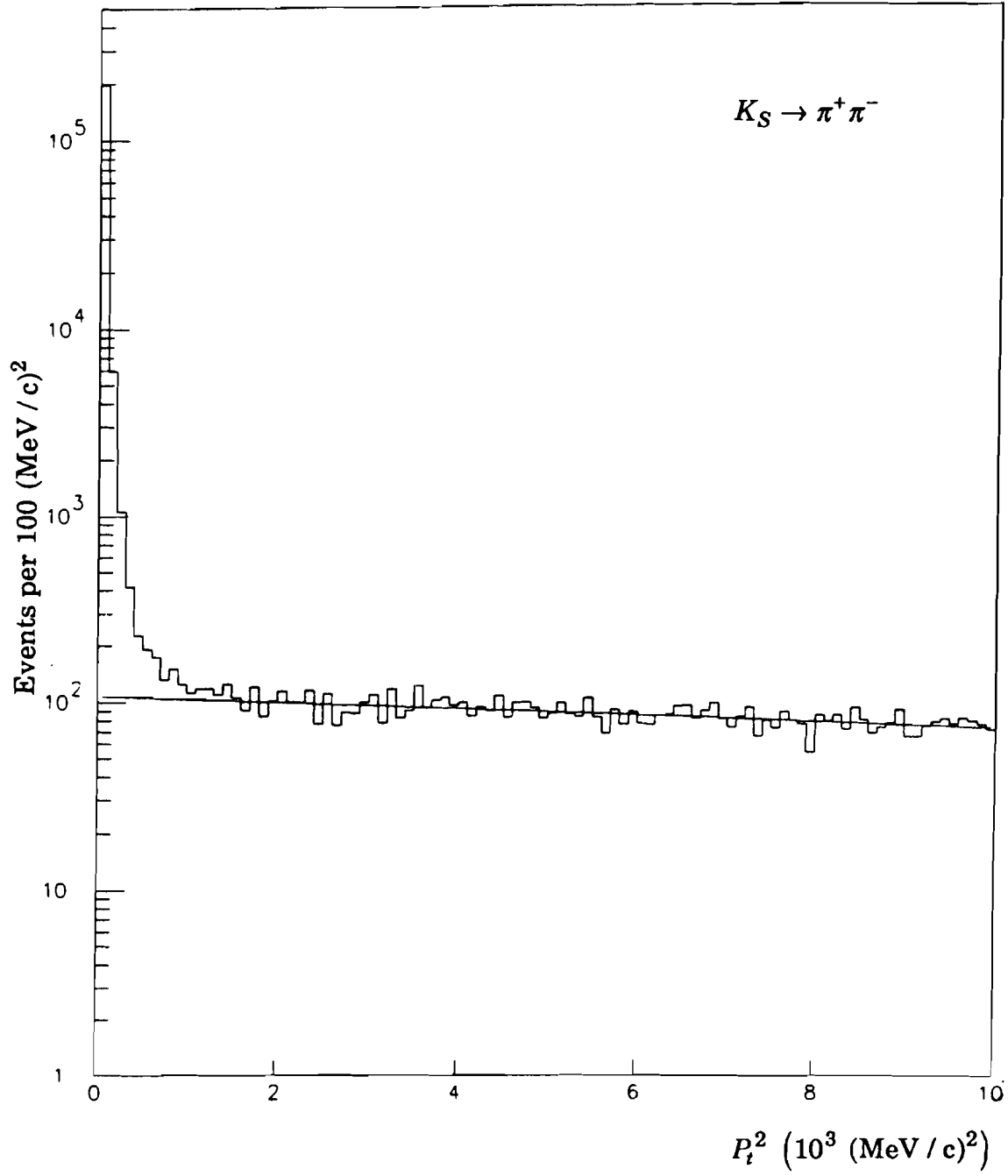
Figure 34. The P_t^2 distribution of two track decays in the regenerated beam after all cuts. The solid line is a fit to the data described in the text.

are due to inelastic regeneration. Qualitatively, one observes little change in slope of the P_t^2 distribution as one moves inward from the purely inelastic tail to the region where diffraction contributes, implying that, as expected, the diffractive contribution is small. For both the K_S and K_L distributions (see Figure 30), a small enhancement for $100 < P_t^2 < 500$ (MeV/c)^2, due to the $K_{L,S} \to \pi^+\pi^-\gamma$ radiative decays discussed in Section 5.3.2.

In order to subtract the non-coherent background, an exponential was fit to the data. Based on the fit, the fraction of non-coherent events with P_t^2 below the cut at 250 (MeV/c)^2 is (0.13±0.01)%.

5.4 The Final Samples

The total number of events in each momentum bin and the background fraction appear in Table 8. In all bins the background is small. The final background corrected sample consisted of 43,218 events in the vacuum beam and 178,571 in the regenerated beam.

TABLE 8. The number of events in each momentum bin and the background fraction.

P_K (GeV/c)	Vacuum beam		Regenerated beam	
	Events	$K_L \to \pi^{\pm}e^{\mp}\nu$ Background	Events	Non-coherent K_S
40 - 50	9330	0.22 %	38993	0.14 %
50 - 60	8899	0.36	37904	0.13
60 - 70	7133	0.42	31544	0.13
70 - 80	5462	0.33	23138	0.13
80 - 90	3992	0.31	16367	0.13
90 - 100	2945	0.30	11295	0.12
100 - 110	1989	0.29	7400	0.12
110 - 120	1424	0.28	4944	0.12
120 - 130	992	0.28	3447	0.11
130 - 140	684	0.27	2299	0.10
140 - 150	507	0.27	1472	0.10
Total	43357	0.32	178803	0.13

CHAPTER 6

CALIBRATION OF THE LEAD GLASS CALORIMETER

6.1 Overview

This chapter will discuss calibration of the lead glass calorimeter used to reconstruct the $K_{L,S} \to \pi^0\pi^0$ decays. Accurate calibration was important to efficient event reconstruction and identification of backgrounds. It also was central to reducing systematic errors which could result from errors in the reconstructed kaon energies and decay positions. We begin with a review of these systematic sensitivities and the requirements they impose on the calibration.

The value of $\text{Re}(\varepsilon'/\varepsilon)$ is extracted from the total number of kaon decays observed in the vacuum and regenerated beams, selected, among other things, on the basis of their decay position. A shift in the measured decay position changes the events included in the final data sample and can therefore systematically affect the value of $\text{Re}(\varepsilon'/\varepsilon)$ that we measure. The accuracy required for the decay position depends on the choice of fiducial region, but a simple estimate is that to determine the double ratio of kaon decays within 0.2%, the systematic shift of the decay vertex position should be less than 10 cm.

For $\pi^0\pi^0$ decays, the distance of the decay vertex from the calorimeter was determined from the following expression:

$$z_c^2 = \sum_{\substack{i=1,4 \\ j=i+1,4}} \frac{E_i E_j r_{ij}^2}{m_K^2} \, , \tag{6.1}$$

where the E_i is the energy of the ith photon, r_{ij} is the separation between the ith and j^{th} photons at the lead glass, and m_K is the kaon invariant mass. The 10 cm requirement on z_c, which lies between 40 m and 70 m, implies that the absolute energies and photon separations should be known within about 0.2%. The systematic uncertainty in photon separation is about 0.1%, resulting from the uncertainty in the average transverse dimension of the lead glass blocks. Determining the absolute energy response of the calorimeter over the range from 1 to 70 GeV sufficiently accurately is the bigger challenge, and our efforts to do so are the central topic of this chapter.

In addition to controlling the energy shift to 0.2%, it is also crucial to understand the resolution of the measured vertex position. Because of energy smearing, kaons decaying near the boundaries of the fiducial region may be excluded from the final data sample. As we shall see in the next chapter, the decay vertex of a $K_{L,S} \rightarrow \pi^0\pi^0$ decay can be calculated from the weighted average of the decay vertices of the two neutral pions, and its uncertainty is therefore proportional to the uncertainties in the pion vertices. From Equation (6.1), the pion vertex resolution is given by

$$\frac{\sigma_{z_c}}{z_c} = \frac{1}{2}\left[\left(\frac{\sigma_{E_i}}{E_i}\right)^2 + \left(\frac{\sigma_{E_j}}{E_j}\right)^2 + 8\left(\frac{\sigma_x}{r_{ij}}\right)^2\right]^{\frac{1}{2}} \tag{6.2}$$

where σ_{E_i} and σ_{E_j} are the uncertainties in the energies of the two photons produced in the decay, and σ_x is the uncertainty in their transverse coordinates (x or y) in the lead glass, assumed here to be the same for all photons. On average, σ_x is about 3 mm, and is easily determined by comparison with the precisely known positions of extrapolated tracks. Understanding the energy smearing σ_{E_i} is more difficult. It has a complicated dependence on

the photon energy E_i and has non-gaussian tails. (Equation (6.2) is therefore only an approximate expression.)

In practice, the effect of smearing on the number of decays we observe in the fiducial region was determined using a Monte Carlo simulation of the experiment, which, among many other things, models the smearing observed in the data. Thus, the ultimate uncertainty in $\mathrm{Re}(\varepsilon'/\varepsilon)$ due to resolution comes from the imperfect simulation of smearing in the Monte Carlo. The kaon decay vertex resolution was about 1.1 m, and to determine the ratio of K_L to K_S decays with the desired accuracy, that of the Monte Carlo had to be the same within ± 0.04 m. From Equation (6.2), this requirement implies that the photon energy resolution in the Monte Carlo should be the same as that in the data within ± 1% added in quadrature.

Our lead glass calorimeter consists of 804 blocks of Schott F-2 lead glass (see Figure 8), each one 5.82 x 5.82 x 60.17 cm^3 in size, oriented parallel to the beams as shown in Figure 7. One radiation length is 3.21 cm. When a photon or electron hits one of the blocks an electromagnetic shower develops. The energy of the incident particle is determined by observing the Cerenkov light radiated by the charged particles in the shower, in our case by means of a photomultiplier tube mounted on the back of each lead glass block. For each recorded event, one obtains the number of ADC counts n_i associated with the ith block in the array above a small (5 count) threshold, where n_i is expected to be proportional to the charge from the ith PMT integrated over a 150 ns gate. The PMT signal in turn is proportional to the amount of light reaching the photocathode over roughly the same interval.

Conversion from the number of ADC counts n_i to the incident photon energy can be separated into two steps. First, given the number of counts in each of the N blocks of the array, n_i, $i=1,N$, we determine the total amount of light from the shower incident on the photocathodes. This involves identifying the shower in the calorimeter and summing the counts in the N_s blocks associated with the shower, weighted by their gains g_i

$$\sum_{i=1,N_s} n_i/g_i \quad .$$

A few small corrections must be applied to the raw sum to account for electronic effects and energy not included in the sum for one reason or another, and to treat overlapping showers properly. The total corrected sum is then proportional to the amount of light reaching the photocathode.

Given the total amount of light reaching the photocathodes, the second step is to determine the energy of the photon that produced it. The relationship between the photon energy and the light reaching the photocathode depends on shower development and Cerenkov light production and collection. To study it we used the EGS electromagnetic shower Monte Carlo [33][1] together with a simple simulation of Cerenkov light production and collection. Unlike the ADC count sum and corrections, which are largely specific to our experiment, the results of the studies of shower development are quite general, and are relevant to all Cerenkov calorimeters with similar geometry: those with the long dimension of the block roughly parallel to the direction of travel of the incident particle, with a phototube or other light collection device mounted on the back face.

This chapter begins with a description of a simple model of Cerenkov light production and collection. It will turn out that the response of the calorimeter to electrons and photons, both the absolute signal size and the resolution, is primarily a function of the block length and the effective light attenuation length for Cerenkov light in the block. Given the values of these parameters, the amount of light reaching the photocathodes as a function of the incident electron or photon energy can be accurately predicted within an overall multiplicative constant. This prediction can be used directly to generate signals in the Monte Carlo simulation of the detector. Applied in reverse, it allows us to convert from the total corrected signal size to incident particle energy, as required for the data analysis.

The first important parameter, the block length measured in radiation lengths, is well known. The goal of the calibration is to extract from the data the values of the other two parameters, the Cerenkov light absorption coefficient and the overall gain of each block. The technique used to do

---

[1] Many studies of electromagnetic shower development in lead glass have been done. Those of Atwood [34] and Longo and Sestili [35] are particularly useful.

this is described in the section on calibration, as is the procedure for converting from the number of ADC counts to the total light deposit. The time dependence of the calibration constants is also discussed.

The final task is to use the results of the shower studies along with the constants determined in the calibration to analyze the data, and to simulate showers accurately in the Monte Carlo of the beamline and detector. We can test the results of the calibration in a variety of ways. For example, $K_L \rightarrow \pi^{\pm} e^{\mp} \nu$ decays provided a copious supply of electrons with well-determined momenta. Second, we can compare the position of the upstream edge of the K_S decay distribution with the known position of the regenerator.

For the purposes of this experiment, however, equally important tests of the calibration are based on comparison of data with Monte Carlo. This is largely because of ambiguities associated with studying inherently non-gaussian distributions such as the measured π^0 invariant mass peak: should the nominal π^0 mass be aligned with the peak of the distribution, with its mean, or with something else? The question can only be answered by comparison with a known standard, in this case, a Monte Carlo simulation of the calorimeter including the full non-gaussian response. Agreement between data and Monte Carlo distributions give us confidence that both are treated correctly. While this would not be the case if the Monte Carlo included many free parameters, here the full response of the calorimeter is predicted using only the length of the lead glass blocks, and the absorption and gain of each one.

6.2 Shower Development and Light Collection

We begin with a description of our simple model of shower development. It is not a rigorous analysis, but it lends itself to practical application, and as we shall see, it describes the response of the calorimeter remarkably well.

Although our ultimate interest is the calorimeter response to photons, we start with electron showers. These are simpler, and the results will be relevant to photons. Furthermore, electrons are a clean and conve-

nient tool for gain-matching the calorimeter, and if we can understand the difference in calorimeter response to electrons and photons, it will help us apply electron calibration results to photon data properly. Furthermore, successful prediction of the calorimeter response to both electrons and photons will increase confidence in the model as a whole.

6.2.1 Electron Showers

When an electron strikes the lead glass, an avalanche of particles develops, and the Cerenkov light from the charged particles in the shower is detected. For an electron of energy E, let us define the shower distribution function $f(E,t)dt$ as the fraction of the total Cerenkov light emitted in an infinitesimal slice of the glass between depths t and $t+dt$, extending to infinity in the transverse plane. The shape of the distribution fluctuates significantly from shower to shower, but for the moment, we consider only the distribution averaged over many showers. The function $f(E,t)$ is normalized so that

$$\int_0^\infty f(E,t)dt = 1 \quad . \tag{6.3}$$

The function $f(E,t)dt$ is shown in Figure 35 for several electron energies, as calculated by the EGS electromagnetic shower Monte Carlo for Schott F-2 lead glass. The shower grows rapidly, peaks and then fades away. The depth of the shower peak increases logarithmically with incident particle energy E. The decay of the shower is roughly exponential, with a decay length of about $2\,X_0$.

We now consider propagation of the Cerenkov light from its point of production to the back face of the lead glass. Cerenkov radiation is produced at a well defined angle θ_c with respect to the shower particle direction of travel, given by

$$\cos\theta_c = 1/n\beta \quad , \tag{6.4}$$

where $n = 1.6$ is the index of refraction of the lead glass, and β is the particle velocity. Thus, if we ignore the angular divergence of the shower particles and the small deviations of β from unity, all the light produced at a certain

depth t into the block travels the same distance $(L-t)/\cos\theta_c$ to the back face of the glass, where L is the length of the block and $\theta_c = 51°$ for our lead glass.

In propagating from the production point to the back of the glass, Cerenkov light produced near shower maximum undergoes between 5 and 10 reflections at the block boundaries, and most of the light reflects at least once. The blocks in our array are optically isolated from one another, so light which is not reflected is lost. For $\beta = 1$, the Cerenkov light production angle is exactly equal to the maximum angle at which light will be totally internally reflected at the block boundaries. Thus, light produced by shower particles travelling parallel to the block axis is totally internally reflected as it propagates toward the tube, while some of that produced by shower particles travelling off-axis escapes.

Thus, the total number of photoelectrons produced at the photocath-
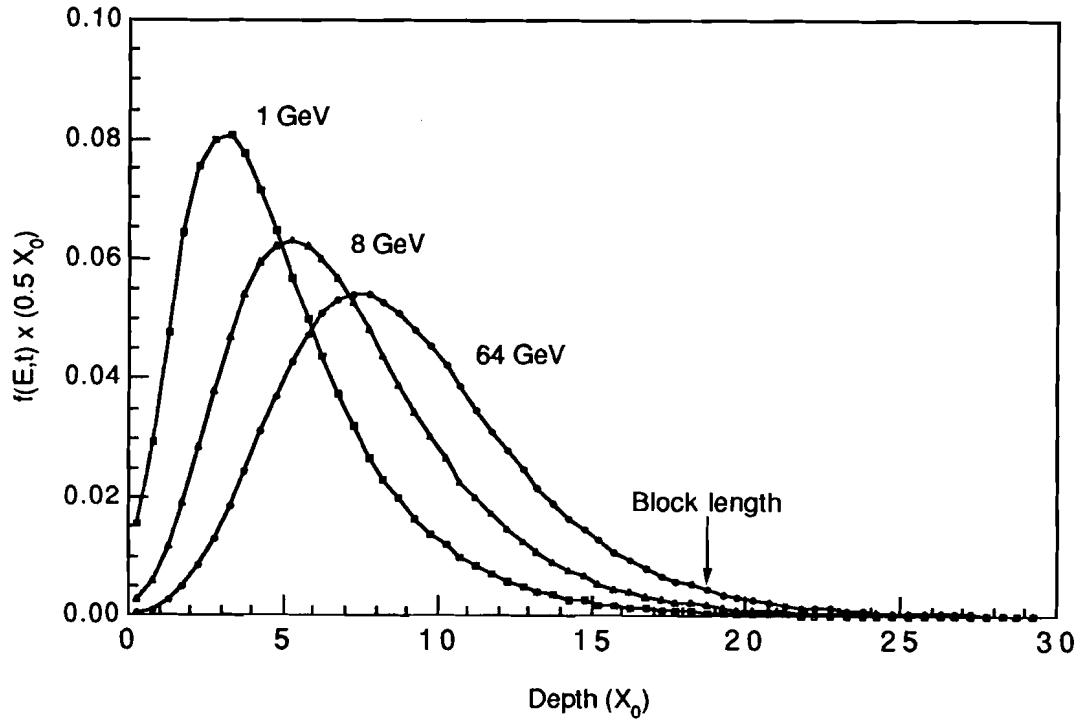
Figure 35. Cerenkov light production as a function of depth into the shower for 1, 8 and 64 GeV electrons, based on an EGS simulation of 3200, 800 and 300 showers respectively.

odes of the PMTs, for a normally incident electron of energy E is given by

$$I = g_0 E \int_0^L f(E,t) e^{-\alpha_c (L-t)/\cos \theta_c} dt \quad , \tag{6.5}$$

where α_c is the attenuation length of the Cerenkov light. The proportionality constant g_0 is the amount of light produced per GeV of incident shower energy, reduced by the quantum efficiency of the photocathode and the fraction of the back face of each block covered by the photocathode. Because of the multiple bounces and the spatial extent of the shower, the Cerenkov light is uniformly distributed across the block by the time it reaches the back face. The factor g_0 also includes an overall correction factor for light loss in reflection and variation in the path length of the light due to the angular divergence of the shower particles.

Equation (6.5) assumes that the absorption coefficient is constant over the spatial extent of the shower. We observed variations in the value of α_c of 8 to 10% from block to block (neglecting the very few blocks in which radiation damage was significant), which could safely be ignored as long as the effective value within any single shower was known accurately. Equation (6.5) also neglects the wavelength dependence of α_c. The Cerenkov light production spectrum falls like λ^{-2} and thus is peaked in the ultraviolet end of the sensitive range of the bialkali photocathode. As shown in Figure 36, the absorption of F-2 lead glass varies rapidly in this region. Recall that in this experiment, light with $\lambda < 430$ nm was absorbed by a Wratten 2-A filter placed between each block and PMT. Its absorption curve is also shown in Figure 36. With the filter in place, the absorption coefficient is constant within a few percent for all accepted light, with a total loss in light of about 50%. Besides allowing us to neglect the wavelength dependence of the absorption, the advantage of the filters is that the phototube sees only that part of the Cerenkov spectrum in which the value of α_c is small. Since, as we shall see, the nonlinearity and resolution of the calorimeter both increase with α_c, it will turn out that the sacrifice in photostatistical resolution is compensated for by reduction in other sources of smearing.

For simplicity let us introduce the effective absorption coefficient α, defined as

$$\alpha = \alpha_c / \cos\theta_c \quad , \tag{6.6}$$

so that Equation (6.4) becomes

$$I = g_0 E \int_0^L f(E,t) e^{-\alpha(L-t)} dt \quad . \tag{6.7}$$

The results shown in the rest of this chapter will all refer to this effective absorption coefficient. For our glass, the mean value of α as determined from calibration data was about $0.030\ X_0^{-1}$.

We now investigate Equation (6.7) in order to develop a qualitative understanding of the calorimeter response. When combined with light attenuation, there are two features of the function $f(E,t)dt$ which lead to non-linearities in response. The first effect is the logarithmic increase in depth of shower maximum as a function the electron energy: fits to $f(E,t)dt$ show that the depth of the shower peak t_{max} increases with the incident electron energy according to
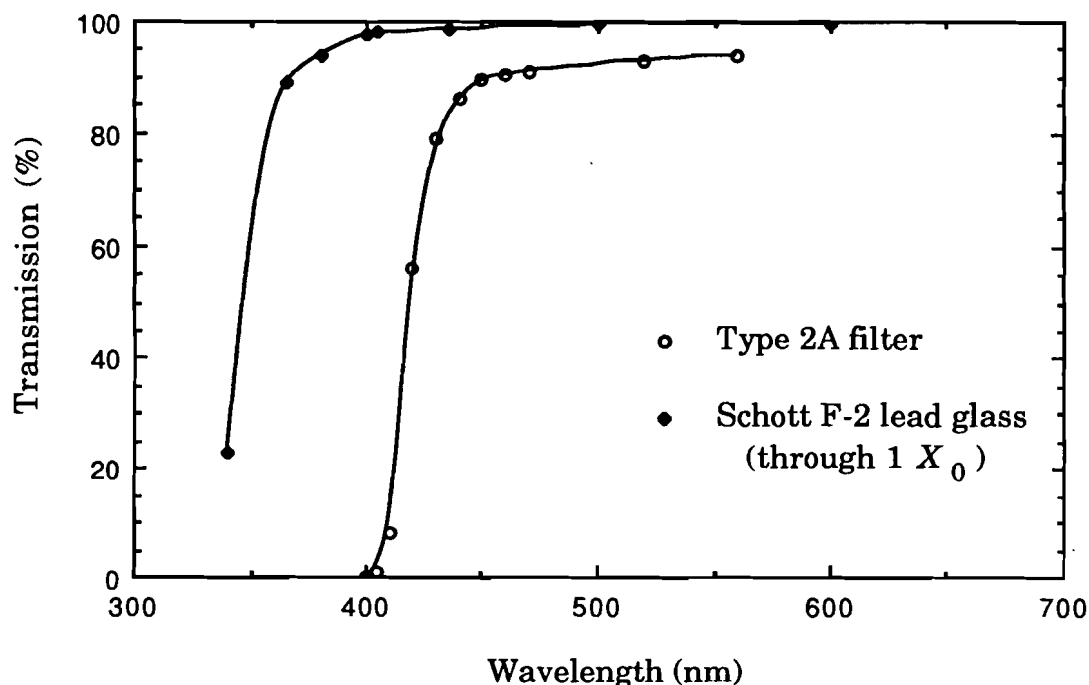
Figure 36. Light transmission through F-2 lead glass and the Wratten filter placed in front of the photocathodes.

$$t_{\text{max}} = 1.022 \ln E + 3.15 X_0 \ , \qquad\qquad (6.8)$$

where E is measured in GeV. If all Cerenkov light were produced at shower maximum, this logarithmic dependence combined with exponential light attenuation would result in a signal size that increased as a power of the shower energy, according to

$$I \propto E^r \ , \qquad\qquad (6.9)$$

with r a linear function of the absorption coefficient. The fraction of light transmitted in blocks of our length is shown as a function of energy E for several values of the absorption coefficient α in Figure 37. The nearly power law dependence is seen, as well as the increase in the nonlinearity for higher absorption coefficients. At all energies, the loss of signal due to
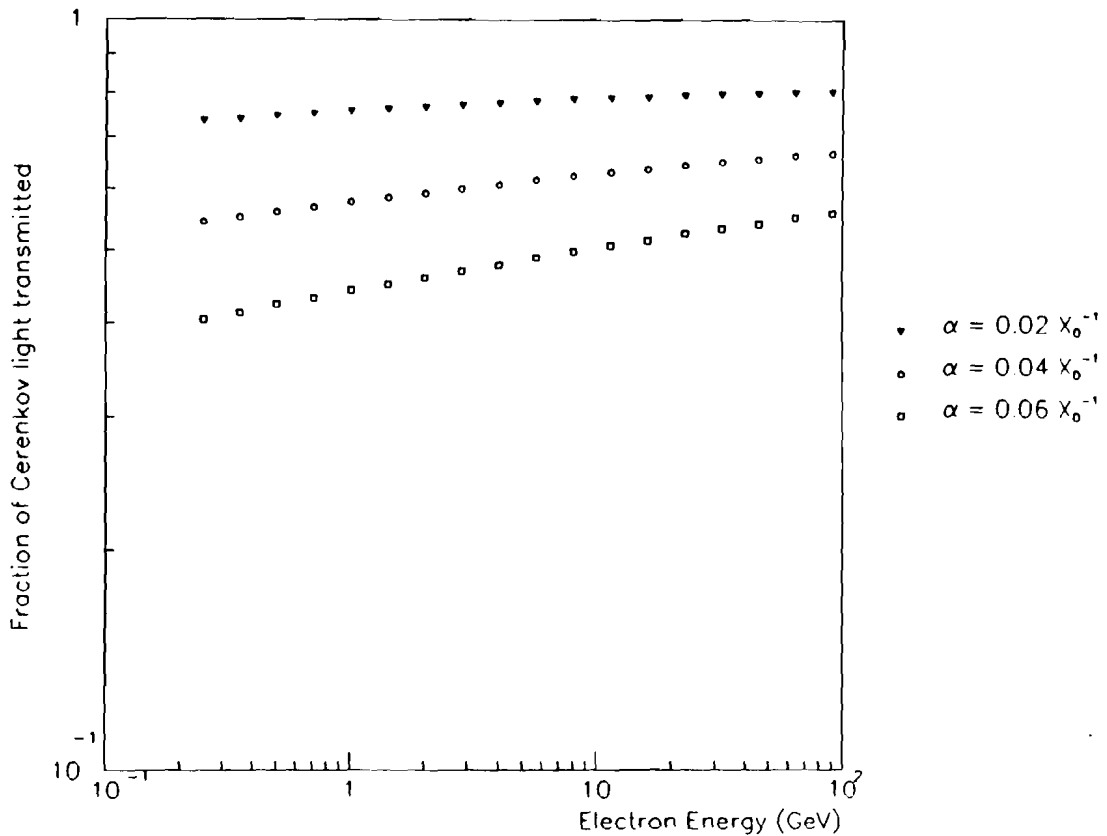
Figure 37. The fraction of light transmitted through the blocks as a function of electron energy for $\alpha = 0.02 \ X_0^{-1}$, $0.04 \ X_0^{-1}$, and $0.06 \ X_0^{-1}$.

absorption is significant. For a 10 GeV electron and $\alpha = 0.03\ X_0^{-1}$, almost 40% of the Cerenkov light is absorbed.

The second effect is the incomplete longitudinal containment of the shower within the blocks. For our blocks, which are $18.74 \pm 0.10\ X_0$ long, 0.3% of the charged shower particles leak out the back for a 1 GeV shower and 3% leak out for a 64 GeV shower. This loss in signal for energetic electrons turns out to be an advantage: it partially compensates for the increase in light transmission for their showers.

6.2.2 Photon Showers

Now consider a photon of energy E striking the lead glass. At some depth t_0 it converts to an electron and positron with energy fractions r_1 and r_2 respectively. These shower in the glass as described above, except that the block length is effectively reduced from L to $\ell = L - t_0$. The number of photoelectrons produced is therefore given by

$$I = E\int_0^{L-t_0}\left(r_1 f(r_1 E, t) + r_2 f(r_2 E, t)\right)e^{-\alpha(L-t_0-t)}dt \quad . \tag{6.10}$$

In general, the signal is larger for photons than electrons because the Cerenkov light is produced closer to the tube. A larger fraction of the shower particles do leak out the back of the block; however, this effect is smaller than the increase in light transmission, given typical lead glass transparencies.

In what follows we will refer to the "effective block length" ℓ. For electrons, the effective block length is identical to the physical block length, so $\ell = L$, while for photon showers, $\ell = L - t_0$.

6.3 Monte Carlo Shower Simulation

6.3.1 Electron Shower Simulation

The integral in Equation (6.7) can be calculated analytically using a parametrization of the function $f(E,t)dt$ such as that given for photon showers by Longo and Sestili [35], which is accurate to a few tenths of a percent

along the full length of the shower. When these small discrepancies occur in the downstream end of the distribution, however, they are amplified with respect to the rest of the shower because of the lack of light attenuation and errors as large as 1% or 2% in the predicted size of the signal can result.

We therefore chose instead to calculate the integral in Equation (6.7) numerically, using results of the EGS electromagnetic shower Monte Carlo directly. The EGS program simulates the showers in full, including pair production, bremsstrahlung, and Möller, Bhabha, and Compton scattering. We then studied the expected glass response as a function of incident particle energy taking into account production and collection of Cerenkov radiation. We find that the attenuation of the Cerenkov light in the lead glass leads to nonlinear calorimeter response as a function of particle energy, and limits energy resolution.

As shown in Table 9, showers were generated at each of eighteen energies from 0.25 to 90.5 GeV using the composition of the lead glass provided to us by the manufacturer. The computer time required to generate each shower was proportional to the shower energy, and was about 51 seconds for 90.5 GeV showers on the Fermilab Amdahl 5890. The CPU time limited the number of high energy showers we could practically generate. For each shower, the number of charged particles contained in cells measuring $0.5\,X_0$ in depth and $0.36 \times 0.36\,X_0^2$ (0.2×0.2 blocks[2]) in the transverse plane was recorded (see Figure 38), weighted by

$$1-\frac{1}{n^2\beta^2} \quad ,$$

which is proportional to the probability that the particles would emit Cerenkov radiation. Here n is the index of refraction of the glass. Thus, the full three-dimensional shower shape was saved. The impact point of the incident electron was distributed randomly across the center cell.

In Figure 39, we plot the ratio of the integrated cell contents to the incident particle energy E as a function of the electron energy, averaged over all showers. Within the statistical error, no nonlinearity is observed. Thus the normalization of $f(E,t)dt$ given in Equation (6.3) leads to the correct

TABLE 9. The number of EGS electron showers
generated at each energy.

Energy (GeV)	Number of showers
0.250	3200
0.354	3200
0.500	3200
0.707	3200
1.000	3200
1.414	3200
2.000	3200
2.828	2262
4.000	1600
5.657	1131
8.000	800
11.314	565
16.000	400
22.627	564
32.000	400
42.255	423
64.000	300
90.510	210

expression in Equation (6.7), which assumes that the amount of Cerenkov light produced is proportional to the shower energy. If lead glass blocks were "perfect", that is free of attenuation and infinitely large, then the amount of light observed would be proportional to the particle energy.

For any absorption α, the amount of light reaching the PMT is proportional to the "fractional signal", $F(E,\alpha,\ell)$, given by

$$F(E,\alpha,\ell) = \int_0^\ell f(E,t)e^{-\alpha(\ell-t)}dt \quad . \tag{6.11}$$

The distribution of fractional signals is shown in Figure 40 for 1, 8, and 64 GeV EGS showers with $\alpha = 0.03\ X_0^{-1}$ and ℓ is equal to our block length. It is nearly symmetric, with a non-zero width due to fluctuations in the shower depths, which leads to variations in the fraction of light collected. For low energy showers, which are completely contained in the glass, there is a small high side tail due to unusually deep showers, while for high energy
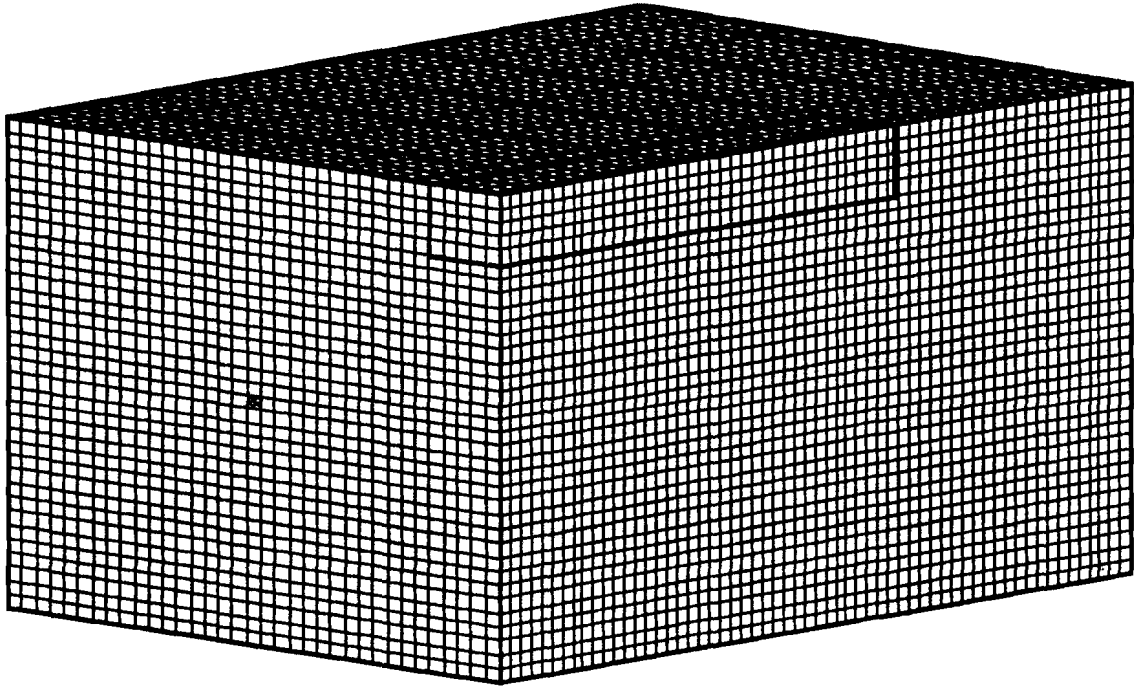
Figure 38. The cells used in the shower simulation. The incident electrons are randomly distributed over the (shaded) center cell. For comparison, the heavy lines indicate the dimensions of a lead glass block.

showers the tail is smaller because shower leakage out the back of the block partially compensates for fluctuations in light collection.

On average, we expected the mean fractional signal at energy E to be proportional to the signal observed in the data, and we expected the width of the distribution to describe one of the contributions to the observed resolution. Figure 41 shows the fractional signal versus energy for several block lengths for $\alpha = 0.03\ X_0^{-1}$. For low energy showers, a short block provides the largest signal; however, at some energy, signal loss out the back becomes larger than the effect of absorption, and for energies above this point, the signal size falls rapidly with energy. Not surprisingly, the energy at which this rollover occurs increases with block length. Thus, given the range of shower energies, one can choose a block length which maximizes
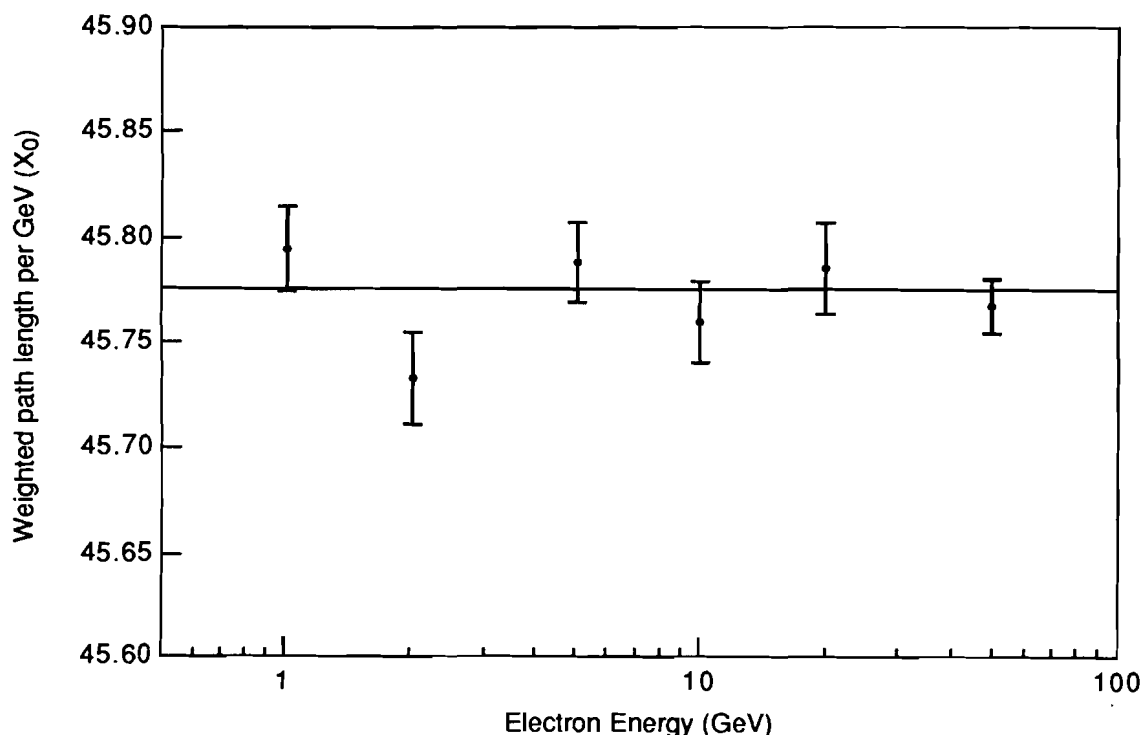
Figure 39. The total track length per GeV of incident electron energy as a function of electron energy. Each track has been weighted by the probability that it will Cerenkov radiate, with unit probability corresponding to a track with $\beta = 1$. The line is at the average value of all points, $45.776X_0$ per GeV.

Energy = 1 GeV

Mean = 0.660
RMS = 0.019
Entries = 3200

Energy = 8 GeV

Mean = 0.698
RMS = 0.016
Entries = 800

Energy = 64 GeV

Mean = 0.728
RMS = 0.012
Entries = 300
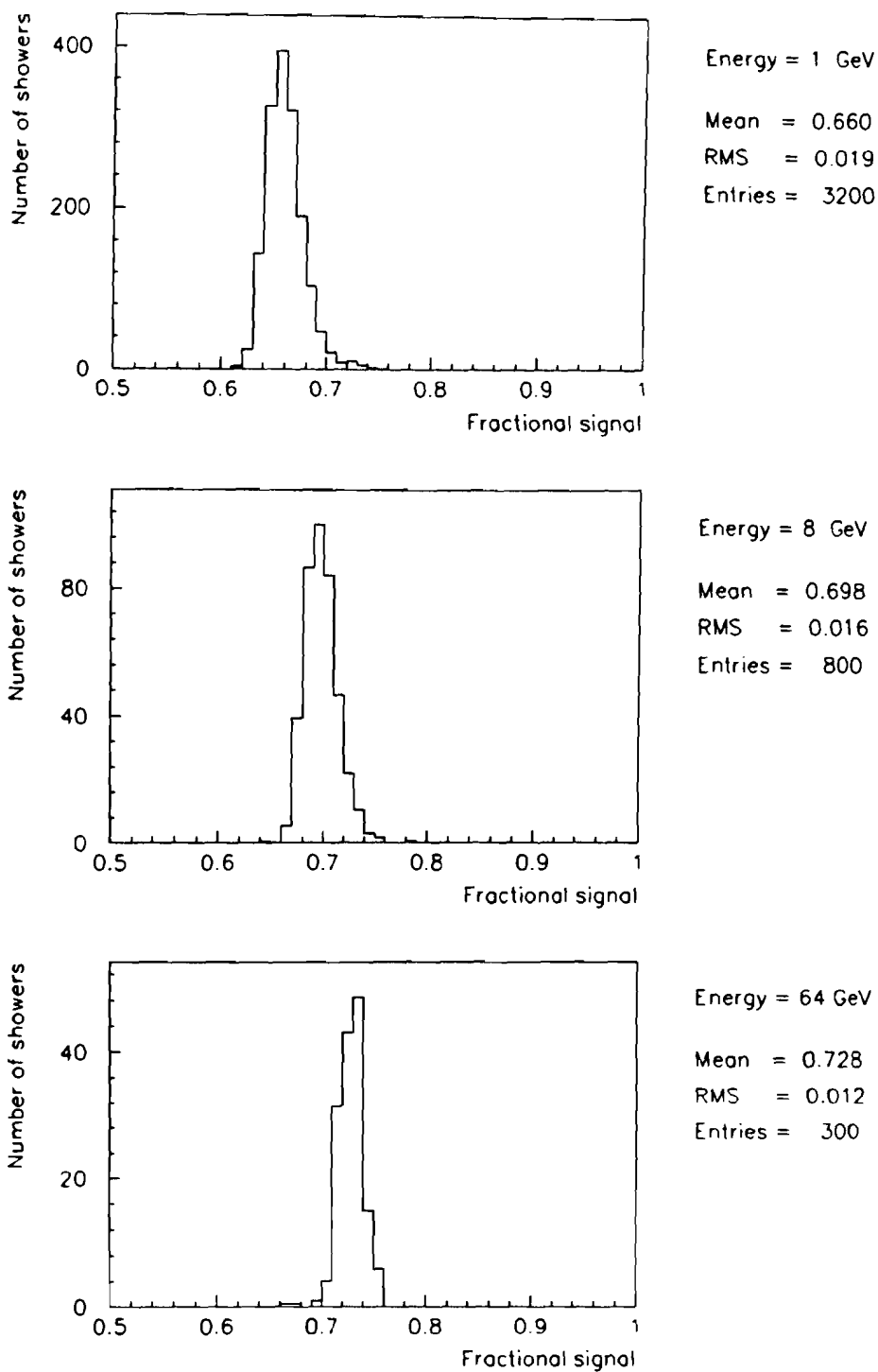
Figure 40. The distribution of fractional signals for 1, 8, and 64 GeV EGS showers with $\alpha = 0.03 \ X_0^{-1}$.

the photoelectron yield. If our main concern were signal size (rather than resolution), blocks of our length would be ideally suited to showers in the range of one to three hundred GeV.

For use in the data analysis, we created two tables which stored quantities proportional to the means and widths of the fractional signal distributions as a function of the shower energy, E, absorption coefficient, α, and the block length, L. The first of these tables, $C(E,\alpha,\ell)$, contained the mean value of $F(E,\alpha,\ell)$ divided by the factor

$$c_\alpha \equiv e^{-\alpha(L-s)} \quad , \tag{6.12}$$

with $s = 5.157$, which is approximately the fractional signal of a 1 GeV electron shower. With this normalization, the table contents were close to unity (see Figure 42), a feature which was very convenient to the analysis, as we
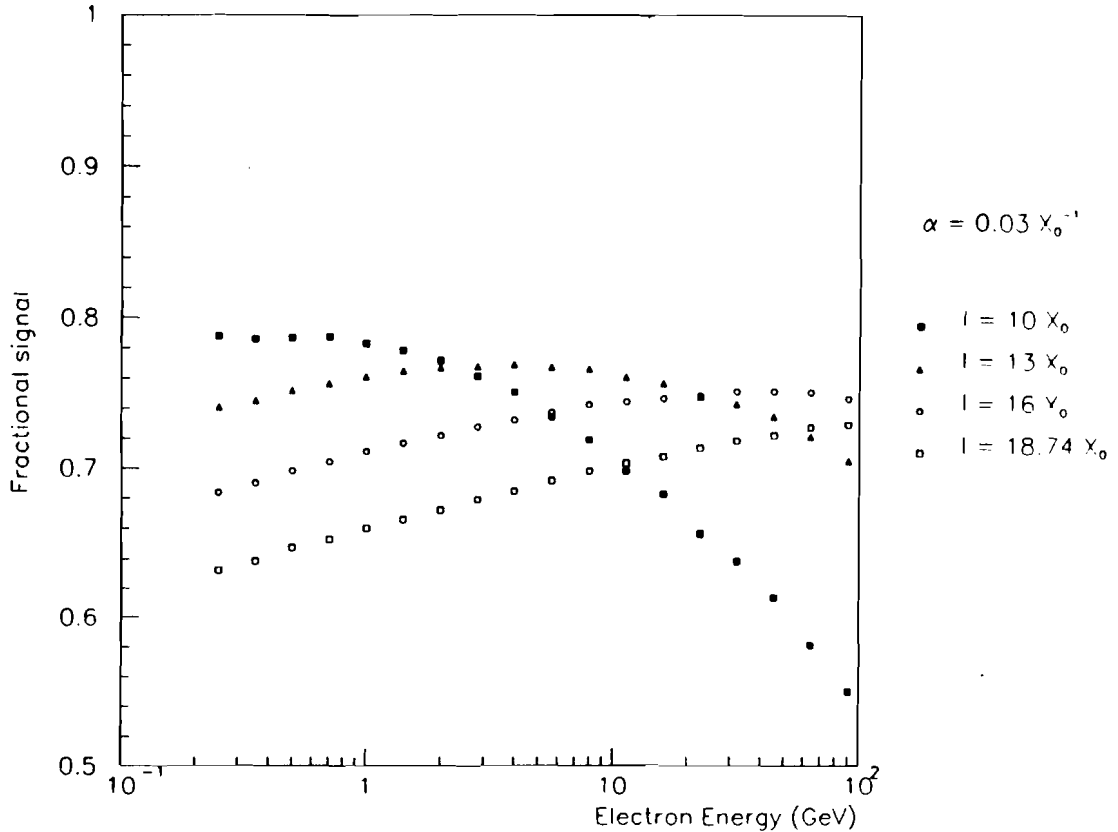
Figure 41. The fractional signal versus energy for several block lengths with $\alpha = 0.03\ X_0^{-1}$.

shall see later on. Thus, its contents were

$$C(E,\alpha,\ell) = \frac{1}{c_\alpha}\left\langle \int_0^\ell f(E,t)e^{-\alpha(\ell-t)}dt \right\rangle \quad , \tag{6.13}$$

where the angled brackets indicate that the average was taken over all showers of energy E. In terms of the table, I_e, the average number of photo-electrons produced for an electron shower with length L is then given by

$$I_e = g_0 c_\alpha E C(E,\alpha,L) \quad . \tag{6.14}$$

The table was binned in the logarithm of the energy as in Table 9, and in even steps of 0.002 X_0^{-1} in the absorption coefficient α, and of 0.5 X_0 in the effective block length ℓ. Queries to the table returned a linear interpolation between the nearest points. As we will see later, the table was used in the
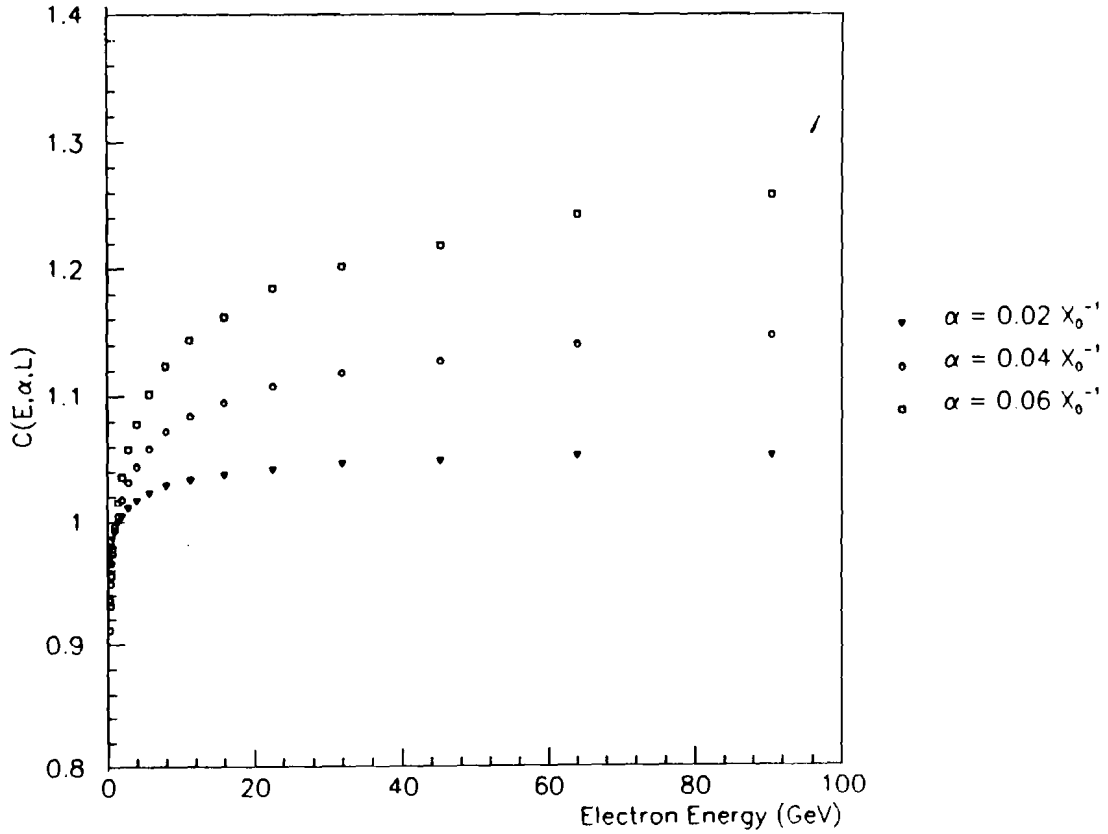
Figure 42. The contents of the table, $C(E,\alpha,\ell)$ as a function of electron energy for $\ell = L = 18.74\,X_0$.

data analysis to predict the particle energy E given the total number of photoelectrons observed, I_e.

The second table, $S(E,\alpha,\ell)$, contained the root mean square widths of the fractional signal distributions, divided by c_α, and was proportional to the fluctuation in the number of photoelectrons as a result of fluctuations in the shower shape. It will be used to predict the resolution of the lead glass.

6.3.2 Photon Shower Simulation

As mentioned earlier, a photon shower is made up of an electron and a positron shower occurring in an effectively shortened lead glass block, with the total number of photoelectrons produced given by Equation (6.10). To calculate the expected signal, photons of energy E were allowed to convert at depth t_0 into the glass according to the probability distribution $e^{-7t_0/9X_0}$, and the electron and positron were respectively assigned energy fractions r_1 and r_2 (with $r_1+r_2=1$), distributed according to the Bethe-Heitler spectrum [36]. The average signals of the electron and positron were then obtained from the table $C(E,\alpha,\ell)$, and were added to give the total photon signal:

$$I_\gamma = Eg_0 c_\alpha [r_1 C(r_1 E,\alpha,L-t_0) + r_2 C(r_2 E,\alpha,L-t_0)] \qquad (6.15)$$

Figure 43 shows the distribution of fractional signals I_γ/E for photons with energies 1, 8 and 64 GeV. The tails on the high sides of the distributions (see Figure 40 for comparison) are due to photons which convert deeper in the block, for which attenuation of the Cerenkov light is small. This can be seen from Figure 44, which shows the total light reaching the tube as a function of t_0 for several photon energies. For small t_0, signals increase with t_0, while at very large conversion depths leakage dominates and the light yield falls. Figure 45 shows the mean amount of light reaching the PMT as a function of energy for several block lengths, based on all events within a $\pm$ 25% window centered on the peak. This is similar to the behavior of electron showers (Figure 41), but because of the conversion depth, rollover occurs at slightly lower energies.
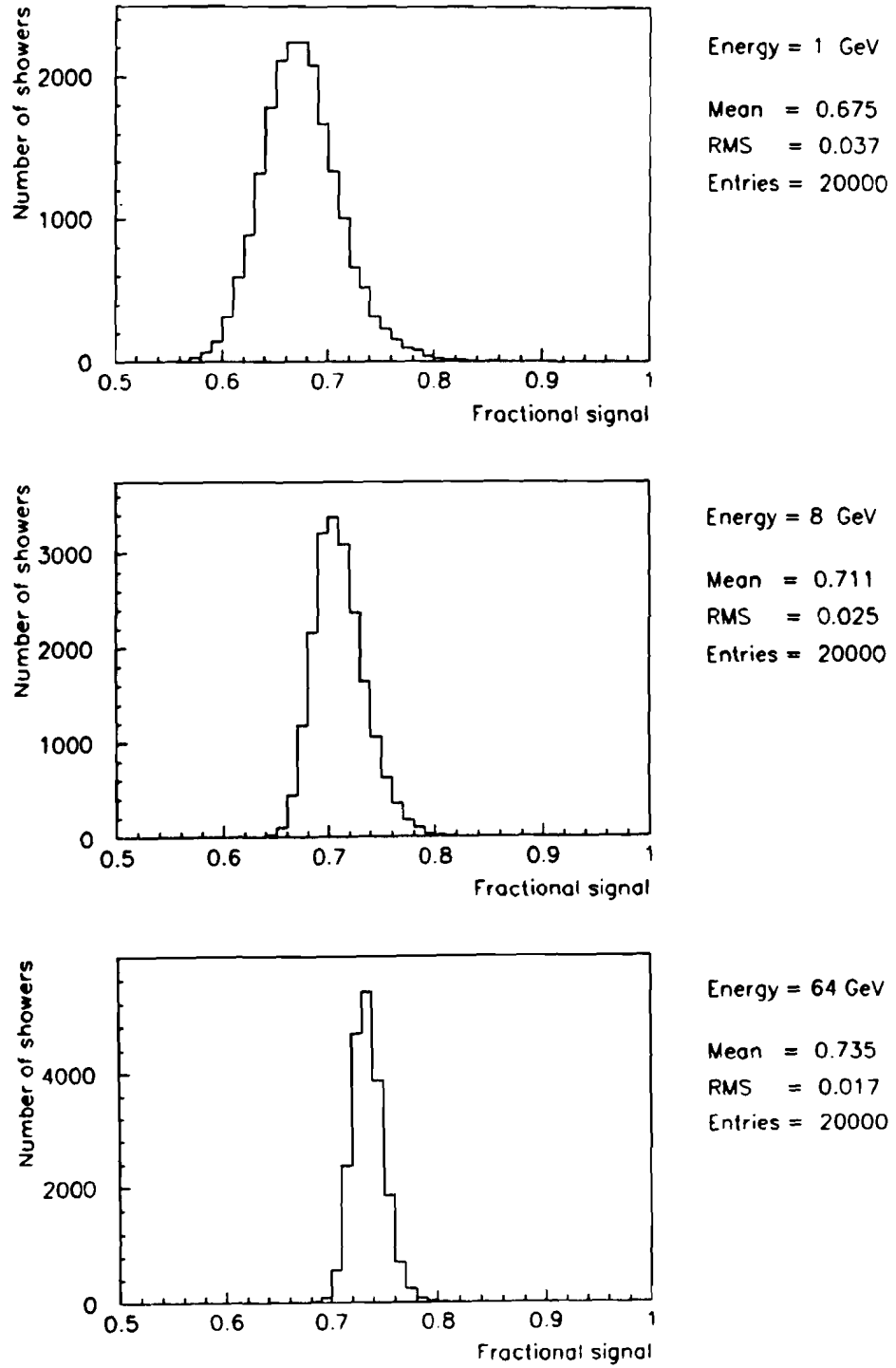
Figure 43. The distribution of fractional signals I_γ/E for photons with energies 1, 8 and 64 GeV.

The simple photon shower Monte Carlo told us the amount of light to expect for some given value of the conversion depth, t_0, and electron and positron energy fractions, r_1 and r_2. For photons in the data, the values of t_0, r_1 and r_2 were unknown; however, the mean signal could be predicted by averaging the right hand side of Equation (6.15) over many showers appropriately distributed in these variables. The ratio of average photon to electron signal sizes $\langle I_\gamma/I_e \rangle$ is thus

$$\left\langle \frac{I_\gamma}{I_e} \right\rangle \equiv R(E,\alpha) = \left\langle \frac{r_1 C(r_1 E, \alpha, L - t_0) + r_2 C(r_2 E, \alpha, L - t_0)}{C(E,\alpha,L)} \right\rangle_{t_0, r_1, r_2} . \qquad (6.16)$$

where the subscript on the right of the brackets indicates an average over these quantities. The function $R(E,\alpha)$ was tabulated, with the same energy
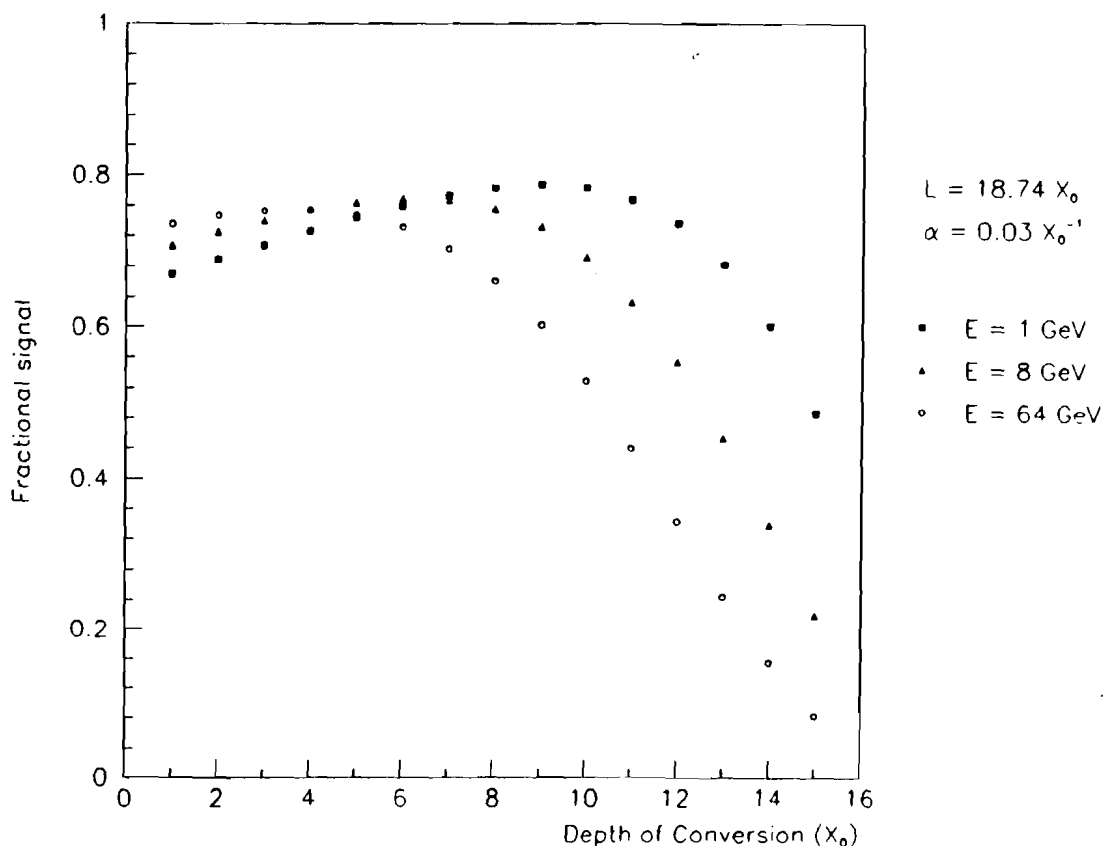
Figure 44. The fraction of light reaching the PMT as a function of t_0 for several photon energies.

and absorption bins as $C(E, \alpha, \ell)$. Its contents, the ratio of photon to electron signal size, are plotted versus the incident particle energy E for several values of the absorption α in Figure 46. In general the photon signal is larger, by 2.5% at 1 GeV for $\alpha = 0.03 \ X_0^{-1}$, because the Cerenkov light from its shower is produced nearer the photocathode. The ratio decreases somewhat at high energies, to 1% at 64 GeV, because of the extra leakage of shower energy out the back of the block for photon showers.

6.4 Calorimeter Energy Resolution

6.4.1 Shower Fluctuations

The resolution for electron showers is intrinsically limited by two effects. The first is the finite number of photoelectrons produced at the pho-
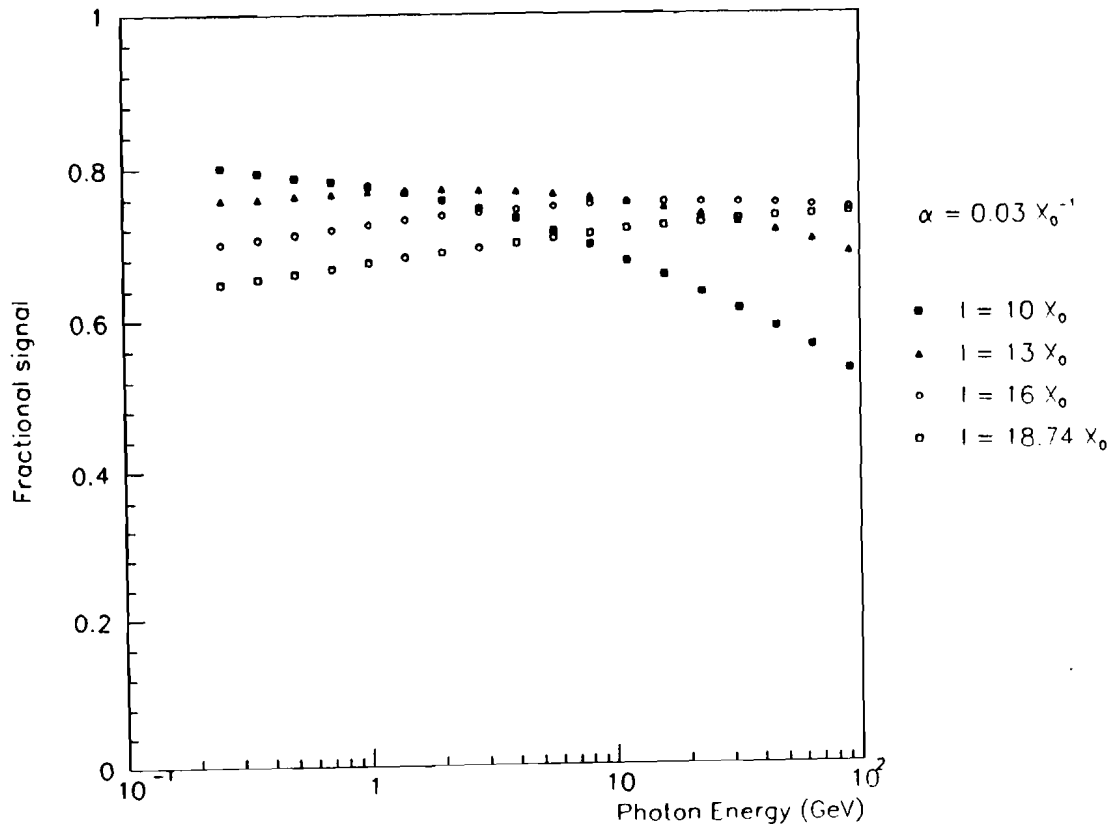
Figure 45. The fraction of light reaching the PMT as a function of photon energy for several block lengths.

tocathode, which leads to statistical smearing of the signal. The fractional size of the smearing decreases with shower energy, with approximately a $1/\sqrt{E}$ dependence. This will be discussed in more detail shortly.

The second limitation arises from fluctuations in the showers themselves. As an illustration of shower fluctuations, the distribution of shower particles along the length of the block is shown for several individual 1, 8 and 64 GeV electron showers in Figure 47. The fluctuations are largest at low energies where statistical fluctuations in the number of shower particles at any given depth are large. Because of light absorption, these fluctuations affect the amount of light observed. The rms width of the electron signals due to shower fluctuations (from Figure 40) is plotted as a function of electron energy in Figure 48 for several values of α and block lengths. Surprisingly, the resolution is best when the block length is such that be-
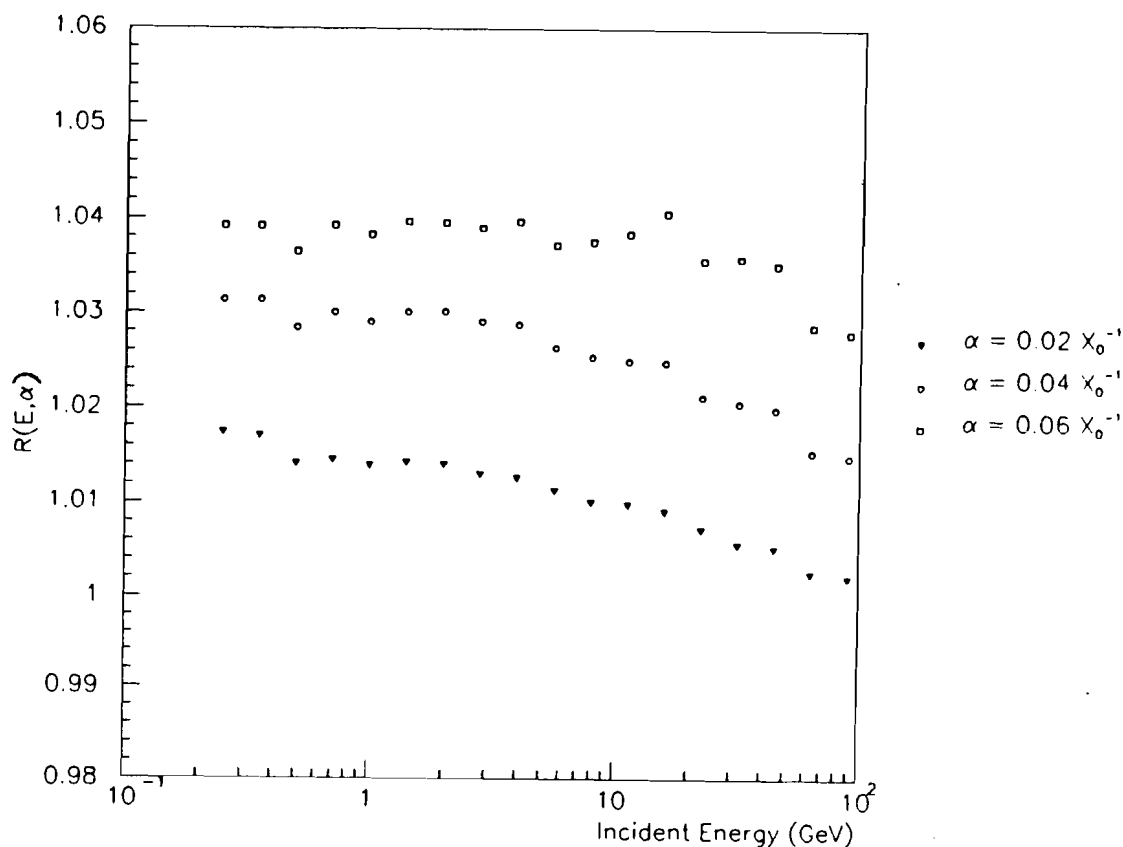
Figure 46. The ratio of photon to electron signals, $R(E,\alpha)$ versus the incident particle energy E for several values of α.
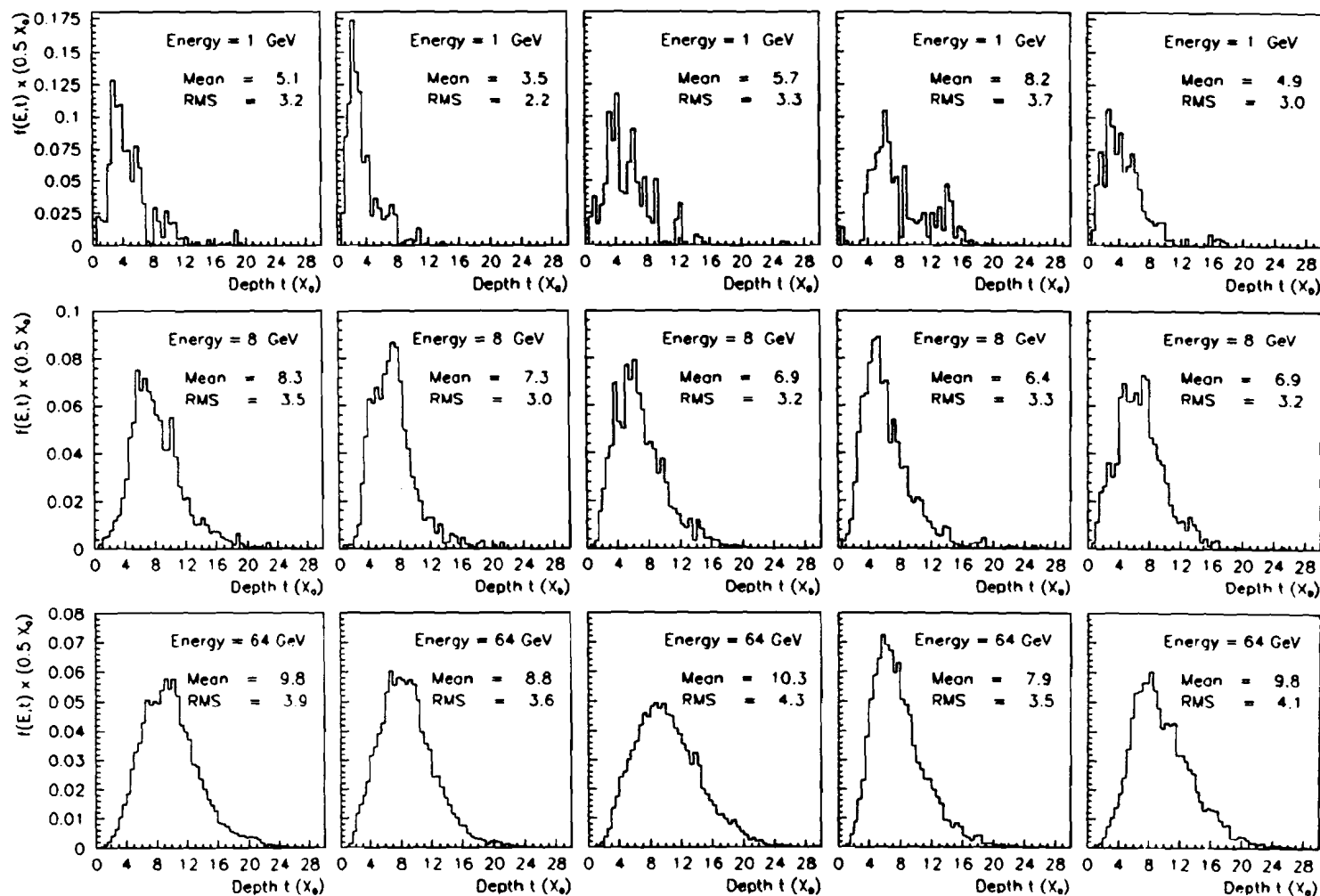
Figure 47. The longitudinal distribution of Cerenkov light produced in individual 1, 8 and 64 GeV electron showers.
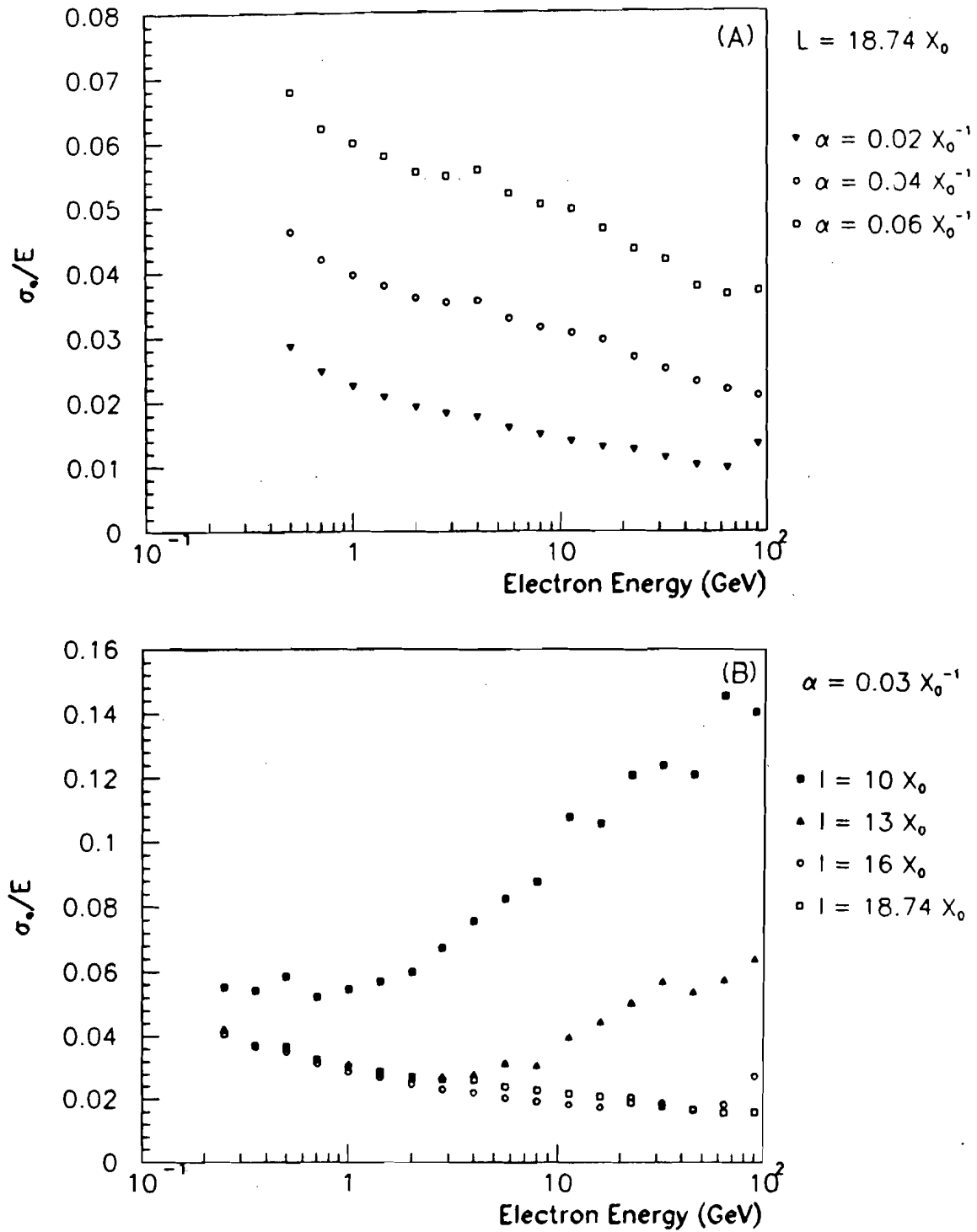
Figure 48. The energy dependence of the rms width of electron signals due to shower fluctuations for several values of (A) the absorption coefficient, and (B) block length.

tween 2% and 5% of the energy of an average shower is lost out the back of the block, because then a change in the shower leakage compensates for any change in light collection due to a shower fluctuation. The typical resolution of a 1 GeV electron of about 3% is consistent with expectations based on the variations in the mean shower depth (see Figure 47) together with $\alpha = 0.03\ X_0^{-1}$. The fluctuations of the 64 GeV showers are less, and the resolution is about twice as good.

The resolution of a photon shower σ_γ is simply that of the two component electron showers added in quadrature:

$$\sigma_\gamma = \sqrt{\sigma_{e1}^2 + \sigma_{e2}^2}\ .\tag{6.17}$$

taking into account the increase in σ_{e1} and σ_{e2} due to fluctuations in the effective block length. Variation in the photon conversion depth degrades the resolution considerably, again because of light absorption. The fractional signal distribution is not normally distributed; however, as a rough measure of the resolution, its rms width, calculated with cuts at $\pm\ 25\%$ around the peak, is plotted versus photon energy in Figure 49 for several values of α and block length. Comparison with Figure 48 shows that the photon energy resolution is worse than the electron energy resolution by 1% or more.

6.4.2 Photostatistical Energy Smearing

We turn now to the contribution to energy smearing due to σ_{pe}, the statistical fluctuations in the production of electrons at the photocathode and first multiplication stages. It was determined for our array by studying the width of a signal free of shower fluctuations: that of the flash lamp installed to track long term gain drifts of the individual blocks. After eliminating the effect of variations in flash brightness by normalizing to the pulse area averaged over the array $\langle \mu \rangle$, the fractional widths of the signals showed the expected $1/\sqrt{\mu}$ dependence on the flasher brightness as it was varied with neutral filters. The average width at a fixed flasher brightness corresponded to $N_e = 2.60$ photoelectrons per ADC count.
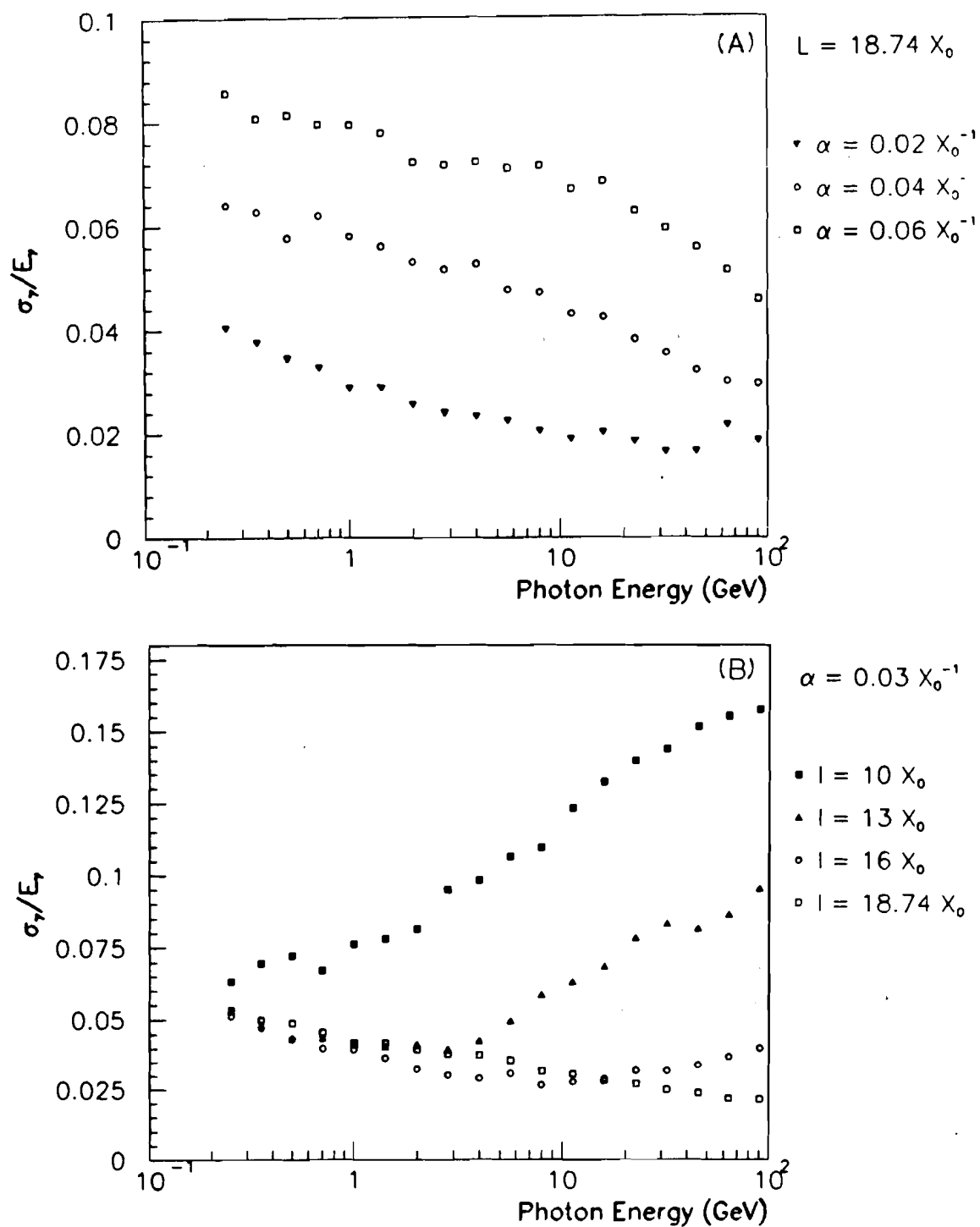
Figure 49. The energy dependence of the rms width of photon signals due to shower fluctuations for several values of (A) the absorption coefficient, and (B) block length.

For an electron shower starting at depth t_0 into the block, the total number of photoelectrons produced is given by

$$I = g_0 c_\alpha EC(E, \alpha, L - t_0) \quad . \tag{6.18}$$

The quantity $g_0 c_\alpha$ gives the number of photoelectrons per GeV when $C(E, \alpha, L - t_0) = 1$, which occurs at about 1 GeV for electron showers (i.e., $t_0 = 0$). From calibration (see Section 6.7), we know that the mean gain of the array at this energy is 206 ADC counts per GeV, so

$$g_0 c_\alpha = 206 N_e$$
$$= 536 \text{ photoelectrons} / GeV \quad .$$

The error due to photostatistics determined by the total number of photoelectrons:

$$\frac{\sigma_{pe}}{E} = \frac{1}{\sqrt{I}}$$

$$= \frac{1}{\sqrt{g_0 c_\alpha EC(E, \alpha, L - t_0)}}$$

$$= \frac{4.32\%}{\sqrt{EC(E, \alpha, L - t_0)}} \quad , \tag{6.19}$$

where E is measured in GeV. Since $C(E, \alpha, L)$ is generally between 1.0 and 1.15 (see Figure 42), the photostatistical error lies between $4.0\%/\sqrt{E}$ and $4.3\%/\sqrt{E}$ for incident electrons, and is slightly smaller for the two electrons produced by an incident photon.

Adding the effects of photostatistics and shower fluctuations in quadrature, we find the total expected resolution for electron and photon showers, plotted for several values of α in Figure 50. Recall that the photon resolution is not gaussian, so these plots serve only as guides to the photon resolution, not as a full description. The plots show that the resolution is significantly better when the absorption coefficient is small. This is the advantage of using the filter: by transmitting only light for which the absorption coefficient is small, the filter improves the resolution of the lead glass. The larger photostatistical uncertainty caused by the filter is unimportant

above about 4 GeV for electrons and 2.5 GeV for photons where the resolution is dominated by shower fluctuations.

The contributions to the resolution are plotted versus $1/\sqrt{E}$ in Figure 51 for $\alpha = 0.03\ X_0^{-1}$ and $L = 18.74\ X_0$. The total resolution is reasonably well described by the simple $a + b/\sqrt{E}$ parametrization often quoted in the literature. This result was not inevitable, since the resolution due to fluctuations is energy dependent, and so does not lead to simple separation into a constant added to a term describing photostatistical fluctuations. A reasonable fit is 1.1% + 5.0%/$\sqrt{E}$. This is the intrinsic resolution of this type of lead glass arranged with longitudinal geometry.

As shown in Figure 52, the photon resolution is about 1% worse than the electron resolution at all energies.

6.5 Application to a Multiple Block Array

So far we have treated the showers as if they are confined to a single block of the array. In reality, about nine blocks of our array participated in a typical shower. Each of these blocks has n_i ADC counts associated with it, which for the time being, we shall assume is proportional to I_i, the number of photoelectrons produced in its PMT:

$$n_i = h_i I_i \quad , \tag{6.20}$$

where h_i is the combined gain of the ith PMT and ADC. We will now define the block gain g_i such that

$$\sum_{i=1,N_s} n_i / g_i = EC(E, \alpha, L) \quad , \tag{6.21}$$

where N_s is the number of blocks participating in the shower. Since $C(E, \alpha, L)$ is of order unity, the ratio n_i/g_i is approximately equal to the energy deposit in the ith block. By comparison with Equation (6.13), we see that

$$g_i = g_0 c_\alpha h_i \quad . \tag{6.22}$$
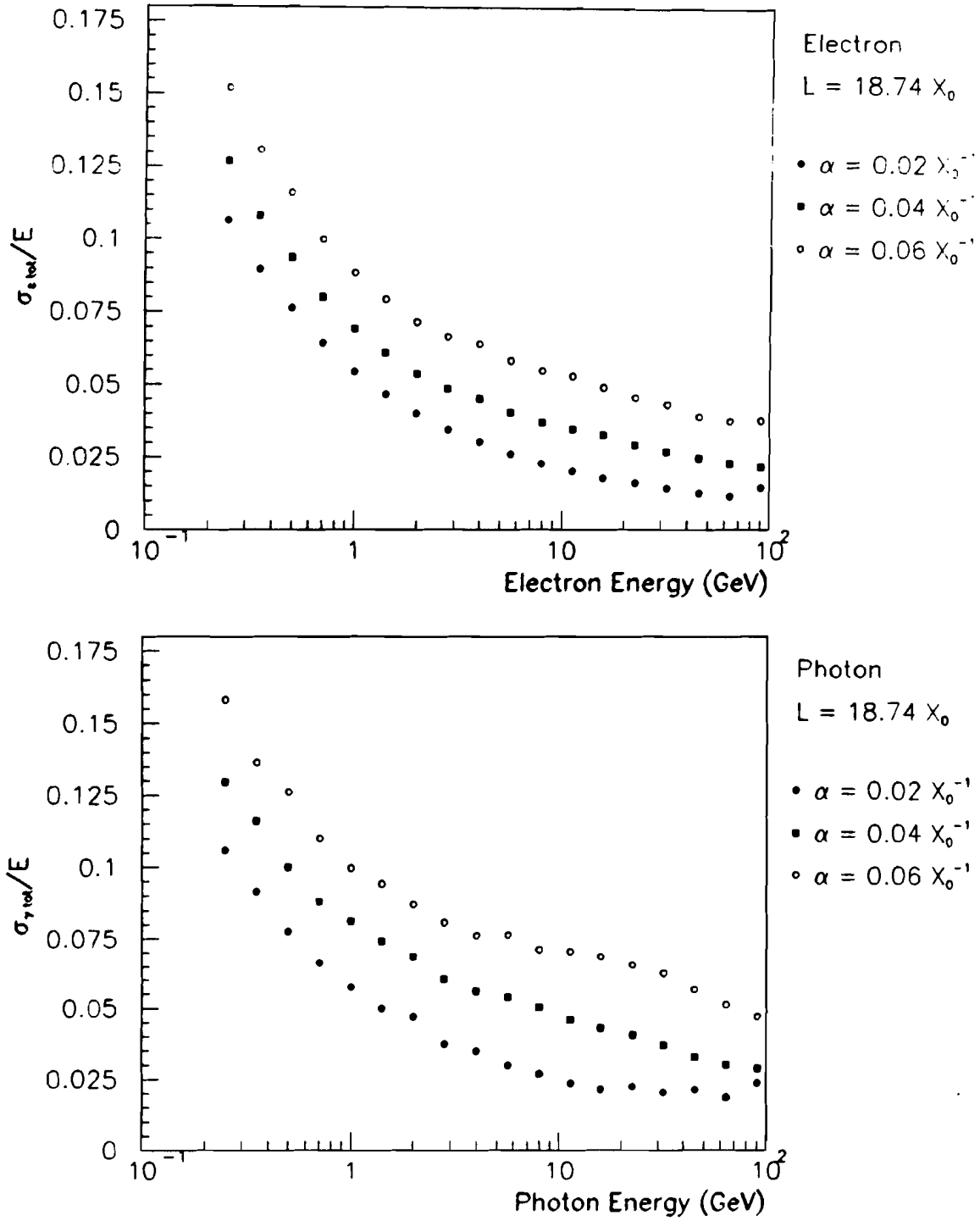
Figure 50. The total resolution of electron and photon showers for several values of the absorption coefficient.

It is the value of g_i that we will extract in the calibration procedure, along with the value of the average absorption in each block α_i.

Finally, we define the measured shower energy E_m, such that

$$E_m = \sum_{i=1,N_s} n_i / g_i \quad .$$

(6.23)

Neglecting nonlinearity, this quantity gives the total energy deposit in the array.

6.6 Cluster Energy Extraction

Now we turn to the problem of extracting particle energies from the raw ADC information written to magnetic tape. This is a two step process. In the first, we identify showers and determine the total amount of light
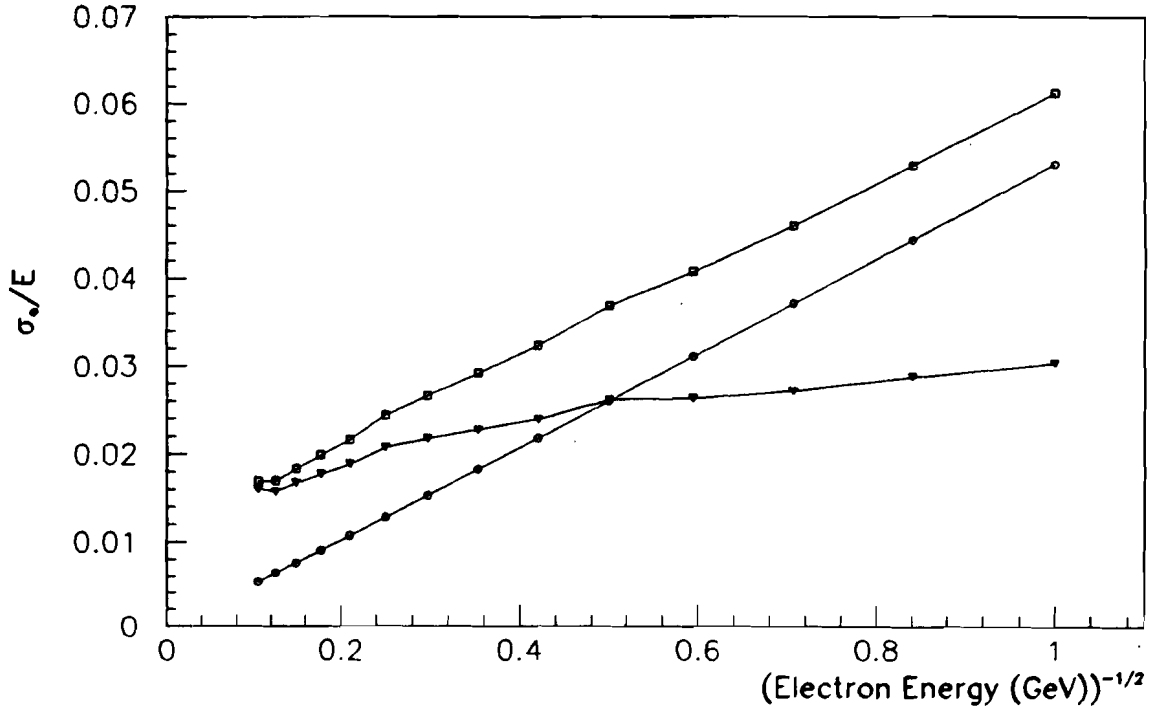
Figure 51. The resolution of electron signals as a function of $1/\sqrt{E}$. The open circles indicate the photostatistical contribution, the triangles the contribution due to shower fluctuations, and the open squares the sum of the two added in quadrature.
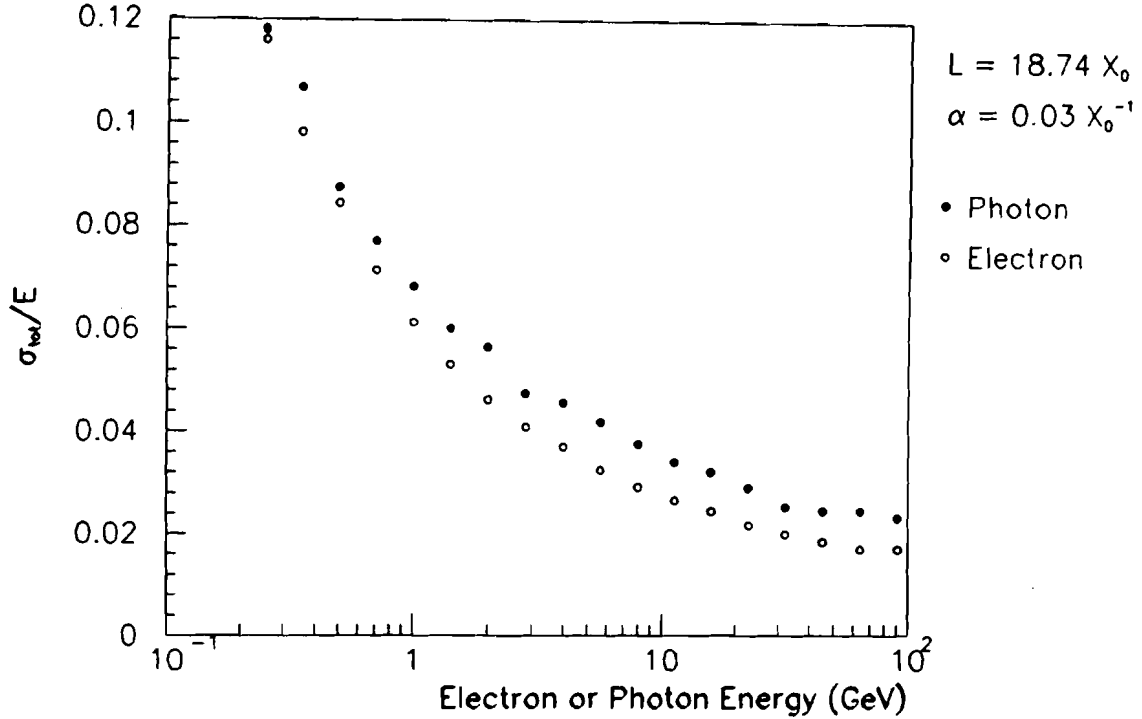
Figure 52. The energy dependence of the total resolution of electron and photon signals.

reaching the PMT's. In the second, we apply the results of the shower studies to extract the incident particle energy.

In previous sections, when we have discussed the number of ADC counts associated with individual blocks, we have assumed that the ADCs were ideal: that the number of counts observed, n_i, was proportional to the number of photoelectrons produced in the photocathode. In the real data, this assumption is invalid because of the ADC readout threshold, which discarded on-line the signals of blocks with fewer than 5 ADC counts (25 MeV). Nonlinearity in the response of the PMT bases or ADCs would also have affected this proportionality, as would shifts in the ADC pedestals. In order to distinguish the number of ADC counts observed experimentally from the ideal number, we introduce the variable n_{r_i}, which is the number of raw ADC counts actually observed in the data. Later we will apply corrections for the deviation of n_{r_i} from n_i.

We are now ready to describe the process of shower identification.

6.6.1 Cluster finding

The purpose of the cluster finder was to identify showers in the glass and to sum the energies of participating blocks. In general, there were nine participating blocks, with about 98% of the shower energy deposited in a 3 by 3 block region. The cluster finding algorithm identified a local energy maximum above the HCF threshold as the central block of a cluster. About 85% of the shower energy was contained in this block when an electron or photon struck its center. To calculate the raw cluster energy E_{raw}, gain corrected ADC counts were added from the nine blocks in a 3 by 3 block region about the cluster center:

$$E_{raw} = \sum_{3by3} \frac{n_{ri}}{g_i} \quad .$$ (6.24)

Sometimes, two showers fused such that the peaks of two clusters could be identified, but the participating blocks overlapped. To divide the energy appropriately between the two showers, we used a table of average shower shapes which, given the location of the cluster center and the cluster energy, predicted the energy deposit in the surrounding blocks. While neither the cluster energy nor its center was well known at the outset because of the overlap, after several iterations of partitioning the energy in the individual blocks and recalculating the location of the cluster centers and their energies, both could be determined accurately.

Given the value of E_{raw}, several corrections were required to calculate the true signal E_m associated with the shower. These are discussed in the following sections.

Threshold Corrections

Because of the 25 MeV (5 count) readout threshold on each ADC channel, often a few of the nine blocks had $n_i = 0$ even though a small amount of energy had been deposited in them. The number of such blocks depended on the shower energy: on average 4.1 blocks were below threshold for a 2 GeV shower, while only 1.2 blocks were below for an 8 GeV shower. The corrections were determined with special electron data runs in which

the readout threshold was inhibited, so that the full number of counts (including pedestal) was recorded for every block in the array. A plot of this loss as a function of energy is shown in Figure 53. For our threshold the variation in loss with the position of the cluster in the block was less than 0.1%, and was ignored.

Radial Leakage

In summing the energy deposition of a shower, only contributions from the nine blocks about the cluster center were included; however, a small fraction of the shower energy was deposited outside this region. The loss was determined using the full readout calibration electron data, and is plotted as a function of the observed energy in Figure 54. It decreases by about 1% between 1.5 and 5 GeV, and then is essentially energy independent. The errors shown are statistical, but at low energies uncertainty in the pedestals may be equally important: a shift of only 0.2 counts per block
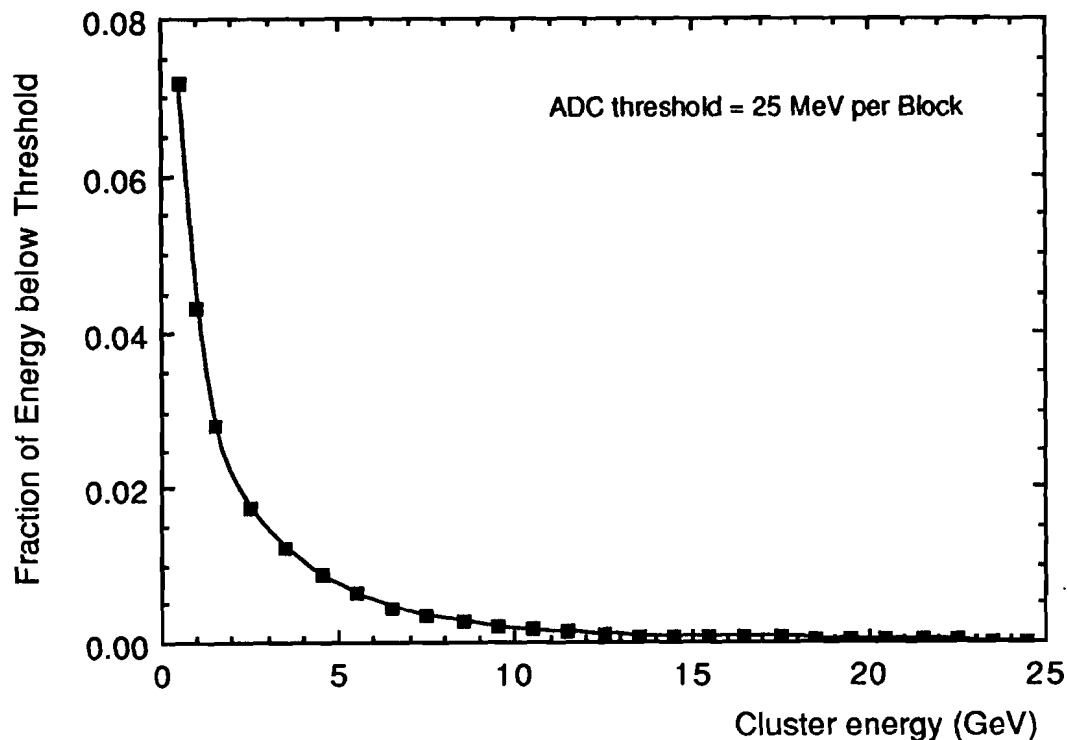
Figure 53. The fraction of cluster energy in blocks below the readout threshold.

would cause the low energy behavior. The radial loss of the EGS showers, also shown in Figure 54, is nearly energy independent. The solid line indicates the correction applied to clusters in the data.

The size of the loss varied by about 0.2% with the position of the impact point of the incident particle across the face of the central block. Since the variation was small and the cluster position imprecisely known, results freer of systematic error were achieved by applying the same correction to all clusters independent of the impact point. It was in the same spirit that the decision was made always to include ADC information from the same 3×3 set of blocks about the cluster center: correction for the unobserved counts was simplified and more likely to be accurate on average.

Leakage off the Edge of the Array

When one or more of the nine central blocks of a cluster was absent, special care had to be taken in calculating the energy sum. This occurred
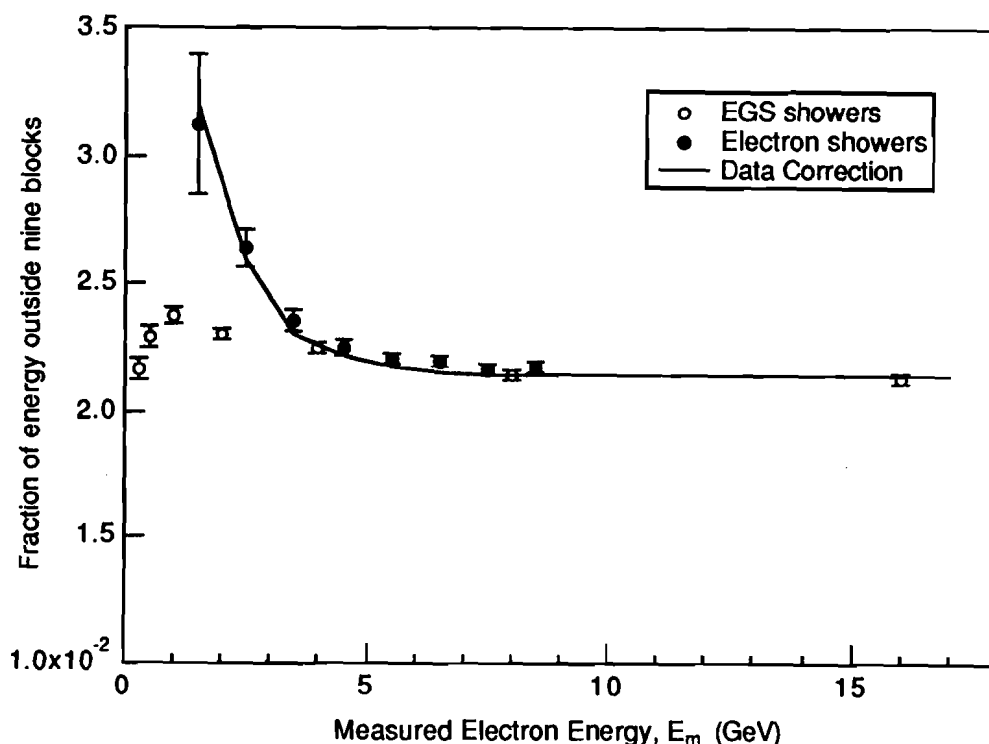
Figure 54. The fraction of shower energy deposited outside the 3×3 block cluster region.

both for clusters located near one of the two beam holes and for those near the outer edge of the array. Such clusters were divided into two categories. In the first, the center of the cluster was located within 1/2 block of the edge. In this case, the energy loss could be severe, possibly as high as 50%, so we discarded events containing such clusters. Around the beam hole this cut was made in hardware: electrons and photons in this region fired the Collar Anti.

Clusters in the second category were located further than 1/2 block from an edge. For these clusters corrections were applied which depended on which of the nine blocks were missing: for each missing corner block the correction was 0.6%, and for each missing side block the correction was 1.1%.

Other Corrections

In addition to the effects just described, anomalous ADC pedestal or ADC or PMT gain shifts could have affected the signals. In fact, we observed shifts in the ADC pedestals of about one count, which increased with the ADC signal conversion rate. During calibration running, the trigger rate was larger, and so were the pedestal shifts -- as much as five counts in some blocks. These shifts were measured as a function of rate using special data with inhibited readout threshold, and also in the standard data. In the analysis, the necessary corrections were made in conjunction with the ADC readout threshold correction described above.

In the early part of the test run for this experiment, the gains of the PMT's were also rate dependent, increasing over the first few seconds of each spill as the intensity ramped. These shifts, which had been larger than 5% in some blocks, were reduced to less than 0.1% in this run by illuminating the photocathodes at all times with light emitting diodes as described in Chapter 3.

6.6.2 Determination of the Incident Particle Energy

In the previous sections the corrections to the raw cluster energy required to calculate E_m were discussed. Taken together, the total correc-

tion ranges between about 2% for clusters above 10 GeV, to 5% for 2 GeV clusters, where the variation is dominated by the ADC readout threshold correction. If we represent the total multiplicative correction factor by the quantity κ, which is within a few percent of unity, then

$$E_m = \kappa E_{raw} = \kappa \sum_{3\times 3} \frac{n_{ri}}{g_i} \quad . \tag{6.25}$$

From Equations (6.21) and (6.23), the incident electron energy E_e is given by

$$E_e = \frac{E_m}{C(E_e,\alpha,L)} \quad . \tag{6.26}$$

For photons, the signal is larger by the factor $R(E,\alpha)$ (see Equation (6.16)):

$$E_\gamma = R(E_\gamma,\alpha)\frac{E_m}{C(E_\gamma,\alpha,L)} \quad . \tag{6.27}$$

Equations (6.26) and (6.27) have the complication that their right hand sides depend on the incident particle energy, which is unknown. Here we take advantage of the nearly power law functional form for the energy,

$$E_e = E_m{}^\beta \quad . \tag{6.28}$$

The residual of fits of a power law to $E_e C(E,\alpha,L)$ for typical values of α are less than 1% at all relevant energies, as shown in Figure 55. The best fit value of the power β is plotted as a function of α in Figure 56. The relationship between β and α is approximately linear, as anticipated earlier, and in the range $0.03 < \alpha < 0.04 \ X_0^{-1}$ described by

$$\beta = 1.0058 - 0.9106\alpha \quad . \tag{6.29}$$

Thus, in order to determine the incident energy E_e of an electron, we use Equation (6.28) to estimate its value, where the value of β is determined from the absorption of the central block of the cluster, and then use the estimated value of E_e to evaluate the right hand side of Equation (6.26). For

photons, we estimate the energy in the same way, but also multiply by the constant factor 1.02 to approximate $R(E,\alpha)$, and then evaluate Equation (6.27). Because for $\alpha = 0.03\ X_0^{-1}$, the value of $C(E,\alpha,L)$ changes by only 10% over the full energy range, and $R(E,\alpha)$ changes by only 1%, the <1% difference between the true and approximated values of E lead to an error of less than 0.03% on the finally determined value of the incident particle energy.

6.7 Calibration

We now know how to extract electron and photon cluster energies from the data. We also have everything we need to understand the nonlinearity and resolution and the difference in the calorimeter response to electrons and photons as a function of the block gains g_i and effective absorptions α_i. It remains to determine the values of α_i of the lead glass blocks, and the gains g_i of their phototubes and ADCs.
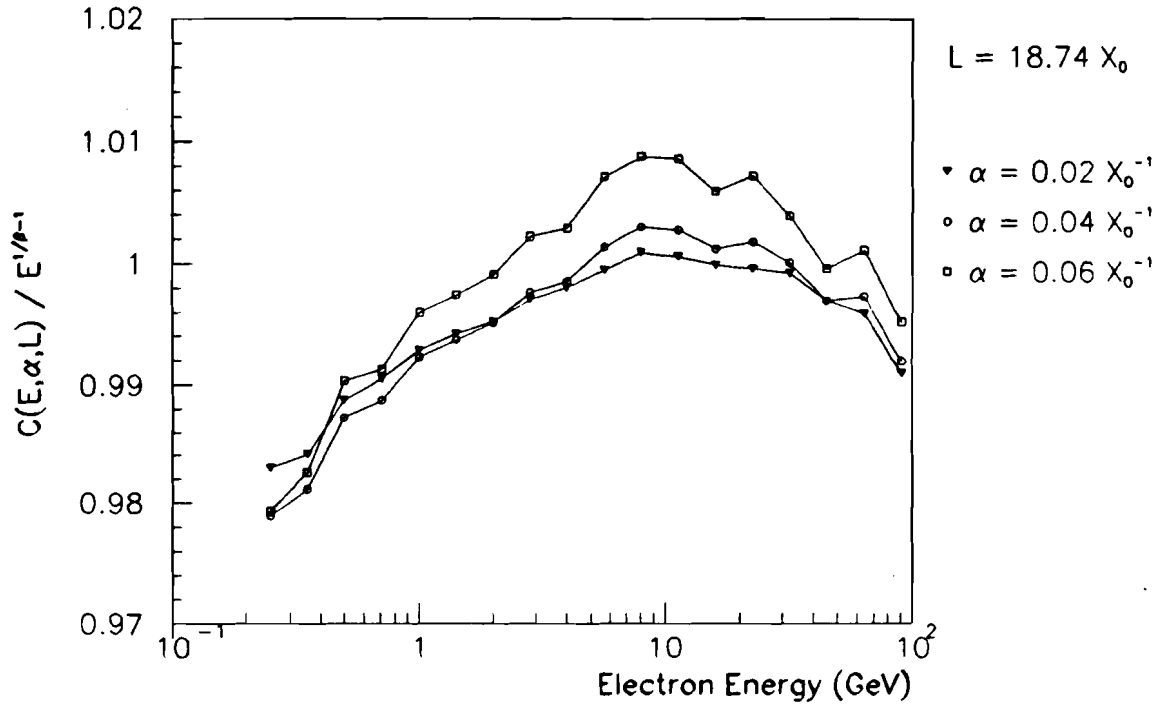
Figure 55. The fractional difference between the full non-linearity function $C(E,\alpha,L)$ and a power law fit to the nonlinearity.

6.7.1 Data Samples Useful for Calibration

Several categories of data were useful for calibration. First, special electron calibration runs were done in alternate weeks during the run. These were very important during the run for immediate calibration of the glass, so that the gains could be matched, as required by the hardware cluster finder. These data were valuable after the run as well because they were very clean, their statistical power was considerable, consisting of about 1 million momentum analyzed electrons distributed across the 804 blocks of the array per calibration run, and they provided a "snapshot" of the glass response, in that within each calibration run, time dependent changes in response were negligible.

Momentum analyzed electrons were also plentiful within the regular data sample from the copious $K_L \rightarrow \pi e \nu$ decays accepted by the trigger. It was important to check gains determined using the calibration data because the running conditions during the special calibration runs differed significantly from those during standard running. The proton beam inten-
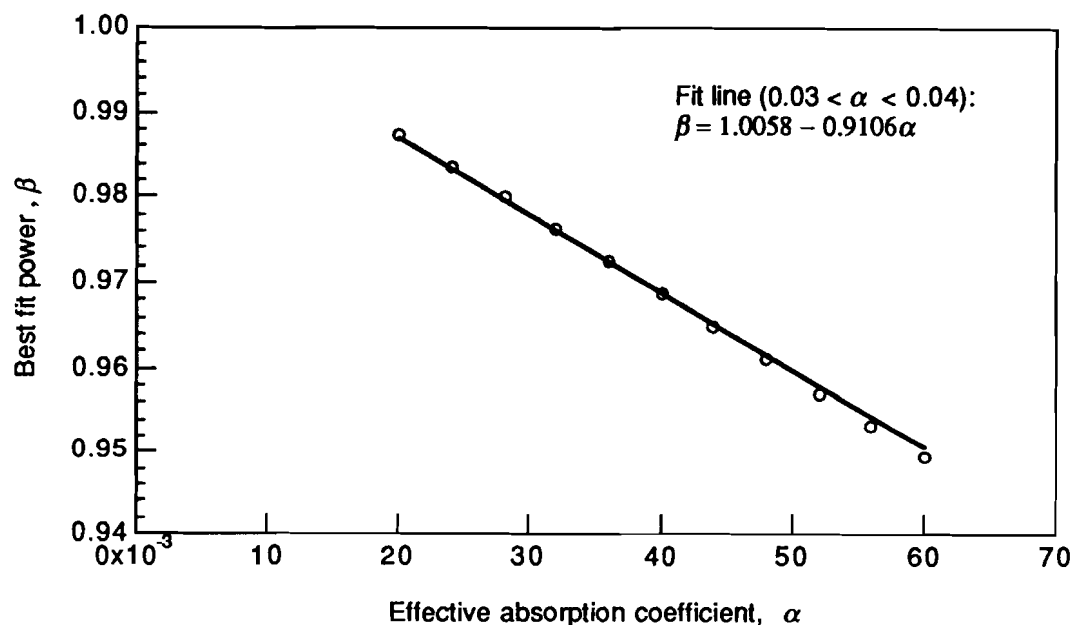
Figure 56. Best fit power to the nonlinearity as a function of the effective absorption coefficient. The line is a fit over the range $0.03 < \alpha < 0.04$.

sity was lower by almost an order of magnitude, so the ambient particle flux through the detector was significantly lower, and additional beryllium placed in the beams further reduced the neutron interaction rate in the regenerator. In addition, because the electron flux was considerable during calibration runs and the trigger was efficient, the trigger rate was significantly higher than during usual data collection, introducing sensitivity to possible rate dependent electronic effects.

The ultimate goal, of course, was to determine the response of the lead glass to photons. This was best studied using $K_L \to \pi^+\pi^-\pi^0$ decays. For these decays, the position of the decay vertex could be accurately determined by extrapolating the drift chamber tracks back to the point of closest approach. Once the distance of the decay vertex from the glass z_c was known, the π^0 invariant mass m_π depended only on the two photon energies E_1 and E_2 and their separation in the lead glass, r_{12}:

$$m_\pi{}^2 = \frac{E_1 E_2 r_{12}{}^2}{z_c{}^2} \quad . \tag{6.30}$$

Since r_{12} was relatively well determined, comparison of the measured m_π with its nominal value tested the measurement of the photons' energies.

The data also contained many $K_L \to \pi^0\pi^0\pi^0$ decays which could in principle be used to calibrate the calorimeter; however, because there are six photons originating from an unknown decay vertex, it is a formidable task to extract useful calibration information from these, and for this experiment it was not necessary to do so.

The $\pi^0\pi^0$ decays were not used for block to block calibration, but were used to fine tune the absolute energy scale of the array as a whole, by adjusting the position of the downstream end of the regenerator in the data with respect to the Monte Carlo. This procedure is described in the chapter on systematic uncertainties. A special class of $\pi^0\pi^0$ events produced in the HDRA trigger plane was also valuable as a check of the absolute energy scale.

The next section describes the calibration procedure.

6.7.2 Electron Calibration

The electrons were generated by converting photons in the beam in a sheet of 0.13 mm copper and 0.08 mm titanium inserted in the beam upstream of the detector hall. To enhance the photon content of the beam and reduce hadron contamination, we removed the 7.6 cm of lead from the absorbers downstream of the target, and added 71 cm of beryllium. The electron pairs travelled forward along the beam direction until they reached the magnet $AN1$, located at $z = 119$, which split the pair vertically (y). Further downstream at $z = 138$ m, the $AN2$ magnet kicked them horizontally (x), and the analyzing magnet, $AN4$, at $z = 169$ m, gave them each an additional horizontal momentum kick. The magnet currents fixed the ratio of horizontal to vertical momentum kicks, so for any setting the electrons and positrons illuminated a band across the diameter of the glass, as shown in Figure 57. Given the positions and field strengths of the magnets as a function of the current passing through them, the angle of the band on the glass as a function of its angle about the beam axis is given by
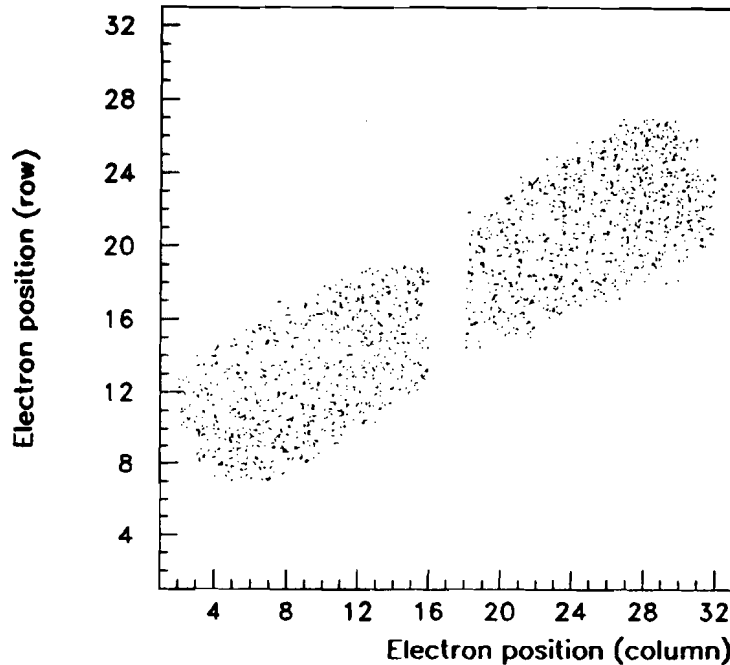
Figure 57. The region of the array illuminated for one set of magnet currents.

$$\tan \theta = \frac{\left(z_{PbG} - z_{AN1}\right)P_{y_{AN1}}}{-\left(z_{PbG} - z_{AN2}\right)P_{x_{AN2}} + \left(z_{PbG} - z_{AN2}\right)P_{x_{AN4}}}$$

$$= \frac{62.1P_{y_{AN1}}}{-43.1P_{x_{AN2}} + 12.2P_{x_{AN4}}} \qquad , \qquad (6.31)$$

where $P_{y_{AN1}}$ and $P_{x_{AN2}}$ are the transverse momenta delivered to the electrons by the magnets $AN1$ and $AN2$ respectively. The momentum p of the electrons or positrons hitting a particular lead glass block was inversely proportional to its distance from the beam hole r, and for any given magnet settings was given by

$$p = \frac{1}{r}\left[\left(62.1P_{y_{AN1}}\right)^2 + \left(-43.1P_{x_{AN2}} + 12.2P_{x_{AN4}}\right)^2\right]^{\frac{1}{2}} . \qquad (6.32)$$

Because of the limitations of the magnet, -0.06 GeV/c $< P_{x_{AN2}} < 0.06$ GeV/c. The transverse momentum kick of the analyzing magnet, $P_{x_{AN4}}$, was always 0.200 GeV/c, the same as during normal polarity running. Because of the finite size of the beams at the glass, about 0.1 m in x and y, for any given set of magnet settings, the momenta of the particles hitting a particular point on the array were spread over several GeV. Furthermore, because electrons originated in both beams, two values of r applied to each point on the glass, and so each point received electrons in two momentum ranges. At most locations, the momentum difference between the two ranges was small or zero; however, immediately above and below the beam holes, the values of r differed significantly, and so the separation between the momentum ranges was proportionately larger. Data at eight different magnet settings were required to cover the entire face of the array with electrons or positrons, with all eight settings chosen to keep the momentum at fixed r constant. Additional groups of settings were used to vary the electron momenta.

The electrons were triggered using the standard $\pi^+\pi^-$ trigger. With 10^{11} protons hitting the target, about 50,000 triggers were generated per 22 second spill, of which, because of dead time, 10,000 were written to tape. A single calibration run provided the gains for the analysis described in the

thesis. It consisted of 16 tapes of data, each containing data from 150,000 triggers, with eight tapes in each of two momentum ranges. In the lower momentum range, electrons varied between 2 GeV/c in the outer blocks of the array up to about 40 GeV/c in the blocks bordering the beam holes, while in the higher range, the electrons varied between 4 GeV/c and 80 GeV/c. In general, the energies of the electrons hitting any particular block were well matched to the energy of photons hitting it in the $\pi^0\pi^0$ data. The calibration run took about six hours to complete.

Data Selection Criteria

Analysis of the electron data consisted of track reconstruction and cluster finding, followed by selection criteria chosen to provide an unbiased sample of well-reconstructed electron tracks, matched with isolated showers. Because the momenta are determined by the horizontal bend angle of the tracks, it was of particular concern that the track segments on both sides of the analyzing magnet be well reconstructed in the x view. To ensure this, it was required that there be no missing hits for the x tracks, and that the sum of distances of the hits in two planes in each chamber be consistent with the chamber cell size in both x and y. Cuts were applied on the χ^2 of the upstream and downstream segments of the fit tracks in the x view and on the full track in the y view, and, at the 2.5σ level, on the distance separating the upstream and downstream x track segments extrapolated into the center of the analyzing magnet. Finally, it was required that the sum of x momentum components of the two tracks be consistent with zero, as expected for a conversion pair, and that the invariant mass of the e^+e^- pair calculated from the track momenta was less than 3.2 MeV/c^2.

Either one or two electromagnetic showers in the lead glass was required, and several cuts were applied to ensure that their energies would be well measured. First, as in $\pi^0\pi^0$ analysis, clusters were rejected if they hit the glass within 1/2 block of an edge of the array, and the event was rejected if there was significant energy deposit in the Collar Anti, or if either track extrapolated into it. Next, it was required that the centers of the electron showers be separated by at least 30 cm. The cut was applied to the cluster position rather than the more accurately measured extrapolated

track position in order to avoid selection criteria depending on the track trajectories, and therefore their measured momenta. Fusion cuts were important to eliminate bremsstrahlung photons which landed on top of the electrons in the lead glass. These cuts, described in greater detail in the chapter on $\pi^0\pi^0$ reconstruction, looked for clusters whose shape was inconsistent with a single shower, and cut less than 0.1% of the candidate electrons. Additional fused clusters were rejected by requiring that the extrapolated track position agree with the center position of the cluster within 3σ. Finally, the very few out of time events were identified and rejected using the Adders. Once the clusters were found, no cuts were applied which depended on the measured energies of the showers.

Hadrons were rejected using the MU1 counter bank, as were electrons which fired the scintillator backing the lead mask. Finally, it was required that the trigger fall within a narrow time window. After all of these rather tight cuts, about 50% of the electrons originally written to tape survived.

In order to streamline calibration, data for electrons passing all cuts were saved in condensed files, in which the electron momentum and impact position in the lead glass were recorded as well as the number of ADC counts in each block in a twenty-five block region around the associated cluster center. The ambient intensity at the time of the trigger and the time elapsed since the previous trigger were also recorded. The computer time required to fully analyze the condensed files was about 1400 seconds per million accepted electrons on the Cyber 875 where the analysis was done, so multiple passes through the data were quite feasible.

Determination of Block Gains and Absorptions

The purpose of the calibration was to extract the gain g_i and effective absorption per radiation length α_i of all of the blocks in the array. To do this, we compared the observed cluster energy E_m, calculated as described earlier, with the momentum p of the corresponding track. Recall that the track momentum resolution averaged about 1%, and that the uncertainty in the absolute momentum scale was <0.1%. The magnitude of E_m/p is deter-

mined by the gains of the nine block participating in the shower, and its momentum dependence is therefore determined by the absorption α of the central block:

$$\frac{E_m}{p} = C(p,\alpha,L) \quad . \tag{6.33}$$

Figure 58 a plot of E_m/p versus p for all the electrons which hit a typical block near the center of the array, exhibits the the steep rise at low momenta characteristic of the earlier plots of $C(E,\alpha,\ell)$.

To determine the gains and absorptions of the blocks, we fit E_m/p as a function of p. The most direct way of doing this would be to simultaneously

Electron momentum (GeV / c)
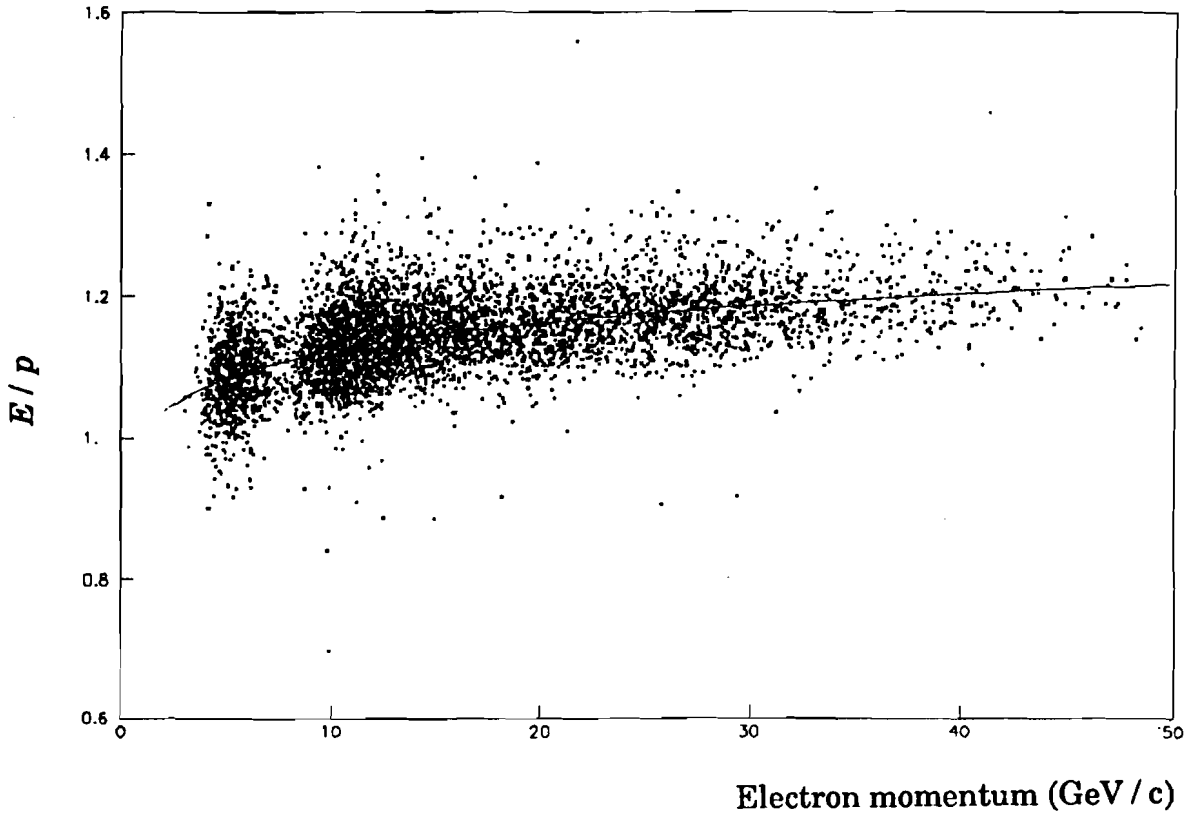
Figure 58. The ratio E/p as a function of momentum for all calibration electrons in one of the blocks near the center of the array. The line indicates the expected nonlinearity.

fit the value of E_m/p of each of the 1.3 million electrons for the $2N$ gain corrections and absorptions; however, for $N = 804$, this approach is problematic. Instead, we fit all the showers centered on the ith block for its gain g_i and absorption coefficient α_i, neglecting possible errors in the gains of the neighboring blocks. After using the results of the fit to update the gain of the ith block, we move to the next, $(i+1)^{th}$, block, and fit for its gain g_{i+1} and absorption α_{i+1}, making the same assumptions. To determine all the gains and absorptions with the desired accuracy, a few parts in ten thousand, we had to iterate through all the blocks and events about four times.

Let us consider the fits to the data in each block in more detail. These were simplified by taking advantage of the nearly power law dependence of $C(p,\alpha,L)$ on p. It follows from Equations (6.28) and (6.33) that

$$\left[\frac{E_m}{\left(\frac{C(p,\alpha,L)}{p^{1/\beta-1}} \right)^{\frac{1}{\beta}}} \right]^\beta = p \ . \tag{6.34}$$

For β given by Equation (6.29), the factor in parentheses is close to unity and insensitive to the values of α (and β), (see Figure 55). Thus, the value of β can be determined from a straight line fit to $\ln\left(E_m / \left(C(p,\alpha,L)/p^{1/\beta-1} \right)^{1/\beta} \right)$ versus $\ln(p)$. Figure 59 shows the data in one of the blocks plotted in this way with with resulting fit superimposed. The slope β returned by the fit gives the absorption α_i directly, according to Equation (6.29), while the intercept is the necessary correction to the gain g_i.

The value of α in each block found in this way is shown as a function of the block's distance from the nearest beam (r) in Figure 60. It has the startling feature that while α is almost independent of r for large r, near the pipes it rises by as much as a factor of two. The reason for the rise is radiation damage in the central blocks, which yellowed the glass. The damage was concentrated in the 24 blocks immediately bordering the beam holes and increased with time, affecting the total amount of light absorbed, the shape of the nonlinearity, and the resolution.
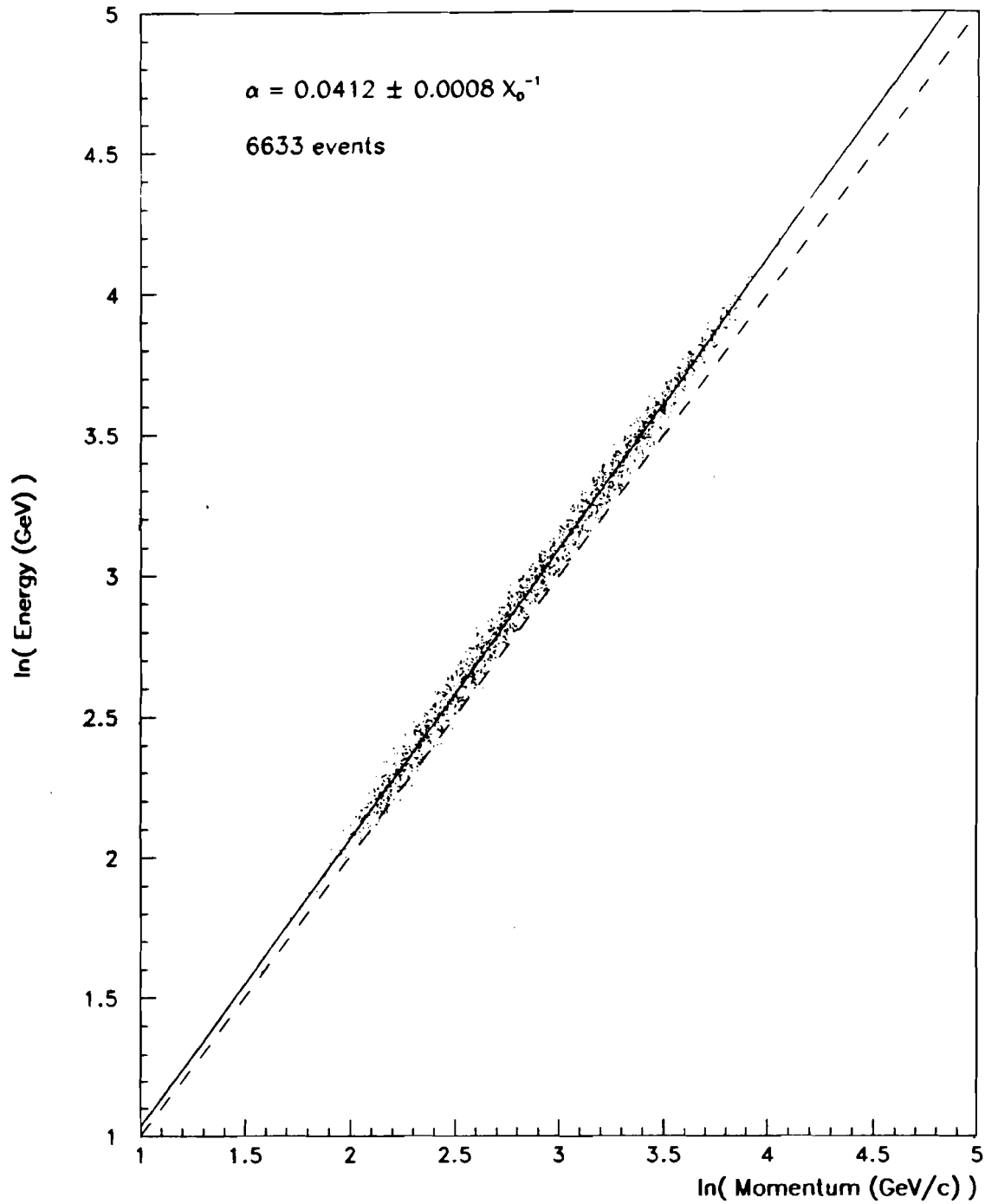
Figure 59. The value of $\ln(E_m)$ versus $\ln(p)$ for electrons in one of the blocks near the center. The slope is a function of the absorption coefficient, α, in the block. If the response were linear the points would lie along the dashed line.

From a study of the deviations of the individual block absorptions from a smooth dependence on r, the root mean square block to block variation of α was 0.0027 X_0^{-1}. For blocks far from the beams, with $r > 0.4$ m, the statistical error on α was comparable to or greater than that, so for these blocks, it was advantageous to fit for the value of α, using the data in Figure in {6.26}, rather than fit for it block by block. In the block by block calibration fits, then, only the gains g_i of these blocks were allowed to vary; their absorption coefficients were taken from the smooth curve superimposed on Figure 60.

Because of the hardware cluster finder, which counted islands of blocks with greater than 1 GeV energy deposit in each, it was important that the array be gain-matched within the 10% energy resolution of the device. Figure 61 shows the distribution of gains at the time of the calibration. The width of the distribution is ± 3.7%. The tail on the low side of the distribution is due to "pipe blocks" whose gains had been reduced by radia-
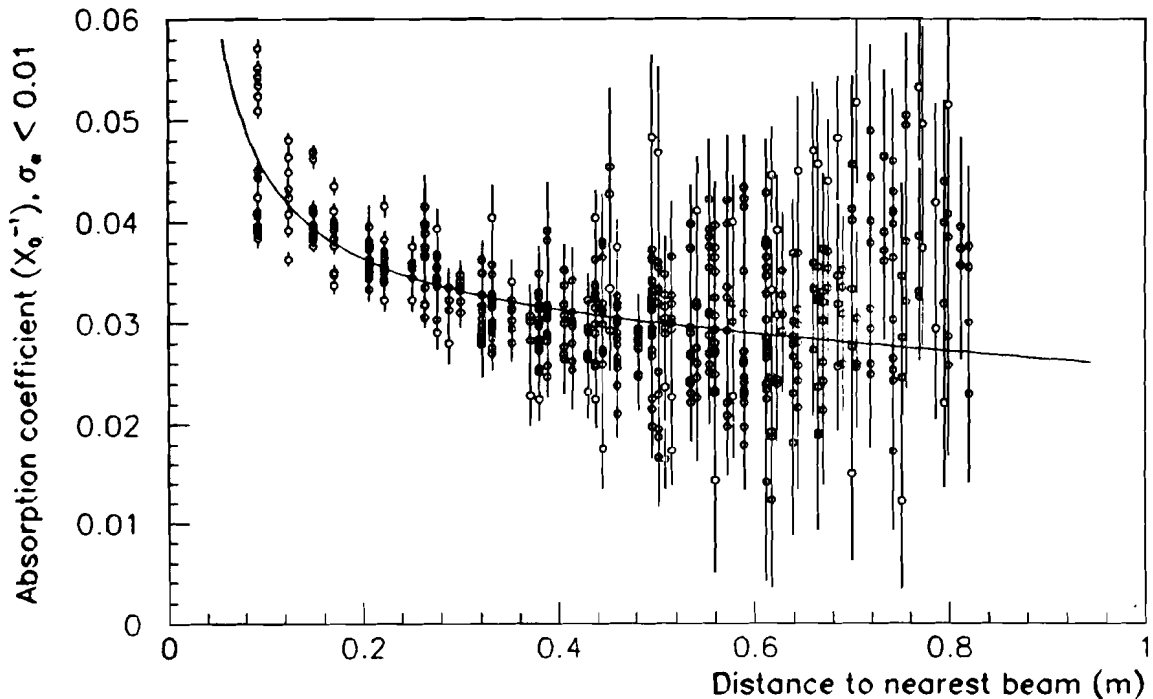
Figure 60. The value of α determined for each block with adequate statistics as a function of its distance from the nearest beam, with a fit to the distribution superimposed.

tion damage. During the run, this distribution was used to gain-match the blocks by adjusting their PMT voltages. The radiation damage evident in some blocks had occurred since the voltage adjustment one week earlier.

6.7.3 Calibration Results

Figure 62 shows E/p versus momentum for all electrons in the calibration run using the extracted gains. Below 40 GeV/c, the deviations from unity, though statistically significant, are less than ~0.2%. The largest deviations are in the 10-20 GeV/c bins, where the ADCs switch from low to high range. The ratio of low to high range gain was determined for each channel in bench tests before the run, and where necessary, was tuned using information from the flasher.

Above 40 GeV/c, there is a rise in E/p, attributable to bremsstrahlung photons superimposed on the electron cluster. Only bremsstrahlung occurring between the magnets $AN2$ and $AN4$ is important. Photons produced upstream of $AN2$ have negligible x momentum and land on the glass
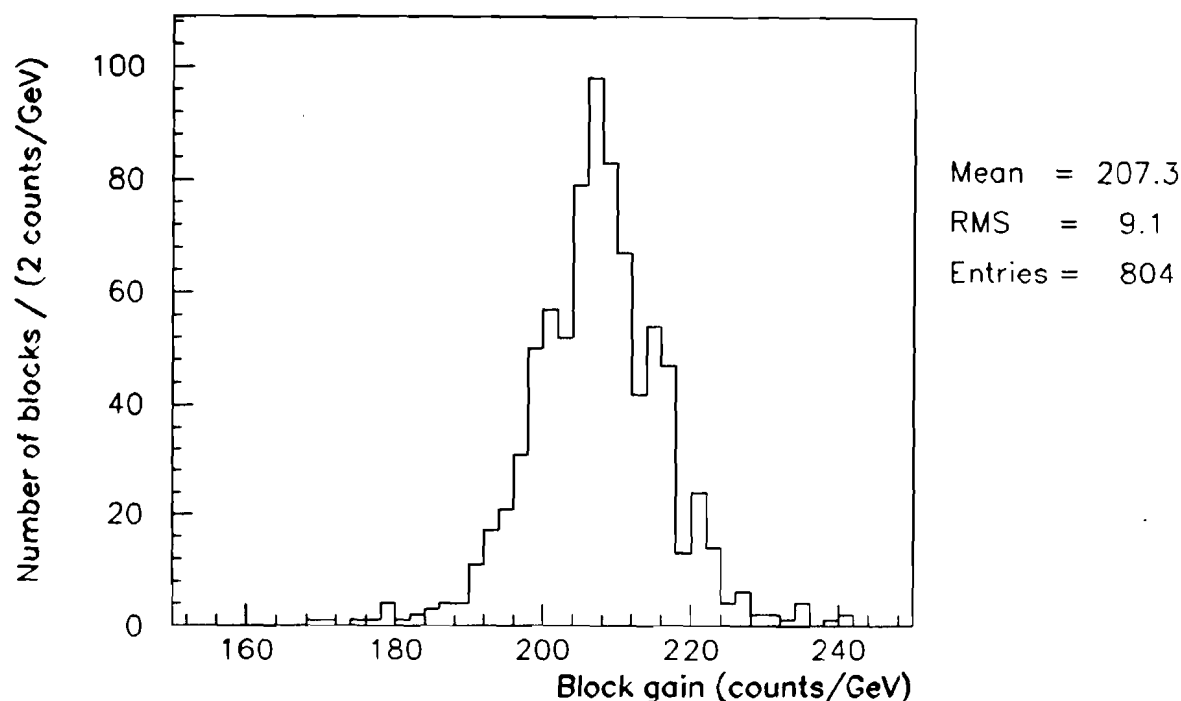
Figure 61. The distribution of gains found in the calibration.

in a vertical stripe down the center, generally far from the electrons. Bremsstrahlung occurring downstream of the analyzing magnet *AN4* also has limited effect on *E/p* because the full electron momentum is measured and the photon is superimposed on the electron in the glass (but see Section 6.8.4). On the other hand, if bremsstrahlung occurs in the vacuum window (0.0025 X_0) or in chamber 1 or 2 (0.003 X_0 each), and the bend angle of the track in the analyzing magnet *AN4* is small, *E/p* will be mismeasured. This is the case for electrons above 40 GeV/c, and we see the consequent rise in *E/p*.

We conclude that predictions from the shower calculations agree within a few tenths of a percent with the electron calibration data at all energies .
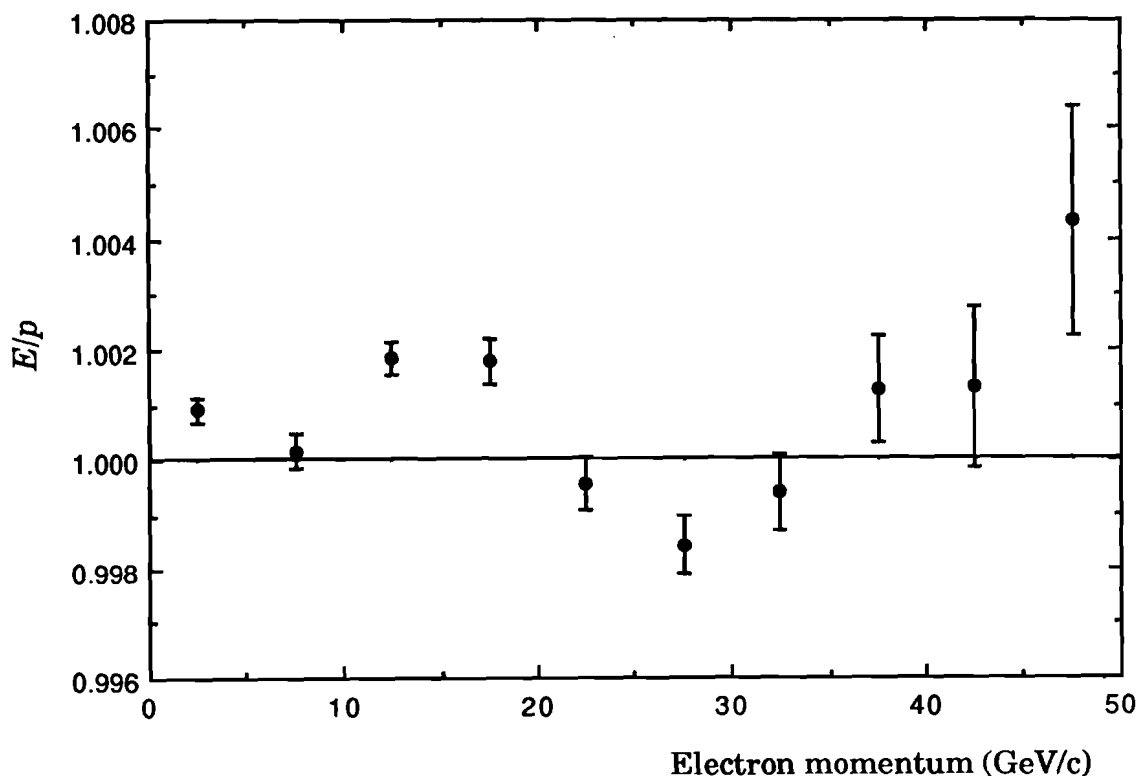
Figure 62. The value of *E/p* as a function of electron momentum, for calibration data.

6.7.4 Time Dependence of the Calibration Constants

The next step in calibration is to track gain drifts using the flash lamp. After normalizing to the average of the 365 blocks with $r > 0.4$ m (where radiation damage was negligible) each flash measured the relative gains of all blocks with an accuracy of 0.7%.

Gain changes from the time of the calibration run to the time of $\pi^0\pi^0$ data collection were tracked by the change in flasher signal size. For approximately every thirtieth tape (about every 12 hours of data taking), the average of all flashes on a single raw data tape, about 350 flashes, was calculated and saved in a file. The fractional change in pulse height in each block between a flasher file from the time of the calibration and from the file nearest the time of the data being analyzed was used to correct its gain. After extrapolating in this manner, the gains were stable within about 0.5% throughout the run. Figure 63 shows the two photon invariant mass for
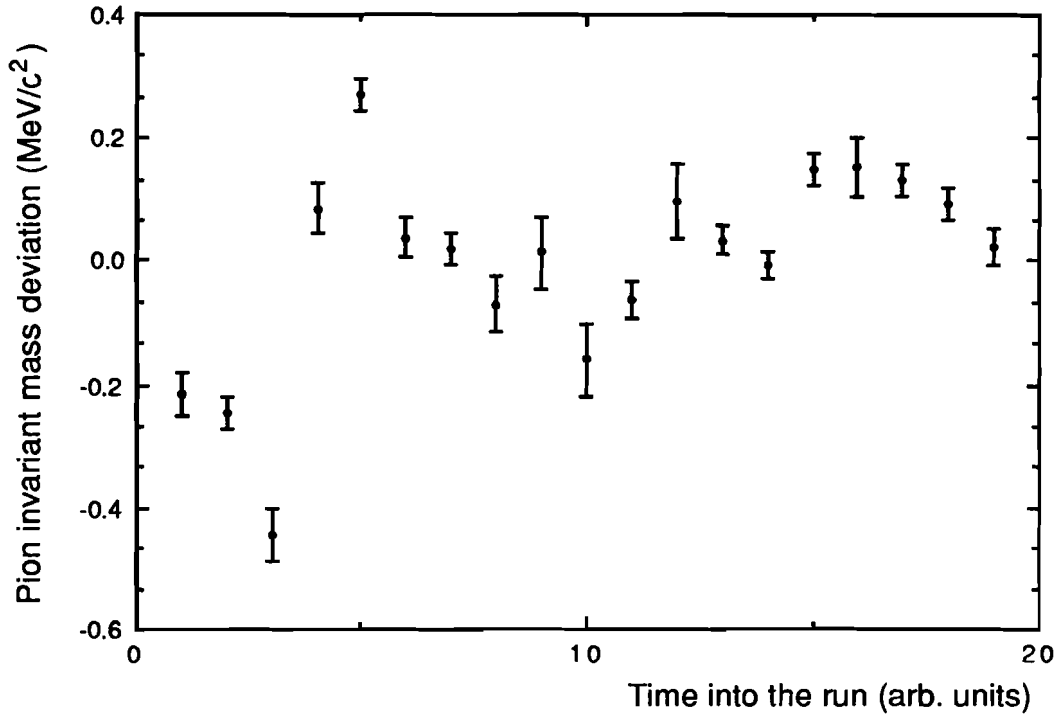
Figure 63. The deviation of $m_{\gamma\gamma}$ from m_π for $K_L \to \pi^+\pi^-\pi^0$ decays as a function of time into the run. Each point corresponds to one of the flasher files used to extrapolate the gains.

$K_L \to \pi^+ \pi^- \pi^0$ decays for the portion of the data associated with each flasher file. The deviation of the invariant mass from the nominal pion mass is proportional to the error in the energies of the photons; thus, the deviations of about 0.5 MeV correspond to gain shifts of about 0.4%. We attributed these to variations in the flasher brightness, and corrected the normalization of each flasher file to eliminate the time dependence. No attempt was made to track time variations in α.

6.8 Application of Calibration Results to the Standard Data

The measure of success of the calibration and shower energy calculation was the resolution and linearity of the electron and photon energies in the real data. Because of interactions of the photons and electrons upstream of the lead glass and radiative decays, as well as contributions to the observed resolution from charged particle tracking, it is most valuable to compare the results with those from a Monte Carlo simulation of the experiment. The Monte Carlo used was an extremely detailed simulation of the full detector, described in detail in Chapter 8. Here we describe simulation of electromagnetic clusters in the glass.

6.8.1 Simulation of Clusters in the Detector Monte Carlo

The signals from electron and photon showers in the lead glass were calculated using the results of the first part of this chapter. The total signal for an electron of energy E was taken from the table $C(E,\alpha,L)$ and then smeared according to a gaussian distribution with sigma given by the table $S(E,\alpha,L)$, using the value of α determined in calibration for the struck block.

The distribution of the energy among the blocks participating in the shower was taken from a library of showers. The library was a collection of 18,529 sample showers taken primarily from electron calibration data (with inhibited readout threshold), binned in E_m and the electron impact point within the block (1 bin = 1/8 × 1/8 block= 0.23 X_0 × 0.23 X_0). Below 4 GeV, where fewer electron clusters were available, the library was supplemented

by 10,000 EGS simulated showers corrected for the difference from calibration data in radial leakage (see Figure 54). When the Monte Carlo simulated an electron shower, a cluster was chosen at random from the appropriate energy and position bin of the library, the block energies were scaled to give the correct total energy, and, using the gains of the participating blocks determined in the calibration, the correct number of ADC counts was planted in each. After applying the 5 count readout threshold, the number of counts in each block was recorded in the same format as the data.

Photons converted in the glass, and the showers of the two electrons were separately treated in the above manner. Their energies were separately smeared, and two showers were taken from the library. Each block was assigned the sum of the counts from the two showers, and then the readout threshold was applied. The electrons composing photon showers could have arbitrarily small energies, and called for the very low energy clusters in the library.

6.8.2 Electrons from $K \rightarrow \pi e \nu$ Decay

We now have the tools to study the calibration results in the data. We first look at electrons from $K_L \rightarrow \pi^{\pm} e^{\mp} \nu$ decays, for which the deviation from unity of the ratio of energy to momentum, $E/p-1$, is plotted in Figure 64 for the data and Monte Carlo. The means of the distributions are 0.9974 and 0.9970 for the data and Monte Carlo respectively, and their widths are 2.8% and 2.7%. The larger width of the data is due to small tails visible two decades below the peak; the full width at half maximum is slightly less for the data than the Monte Carlo. The overall agreement of the widths suggests that the shower model included the important contributions to the resolution.

Figure 65 shows $<E/p>$ as a function of electron momentum. The shape of data and Monte Carlo are similar to one another. Above about 40 GeV/c the value of $<E/p>$ rises by about 0.4% in both the data and Monte Carlo due to extra energy contributed to electron showers by radiative and bremsstrahlung photons, as described above. At very low momenta, $<E/p>$
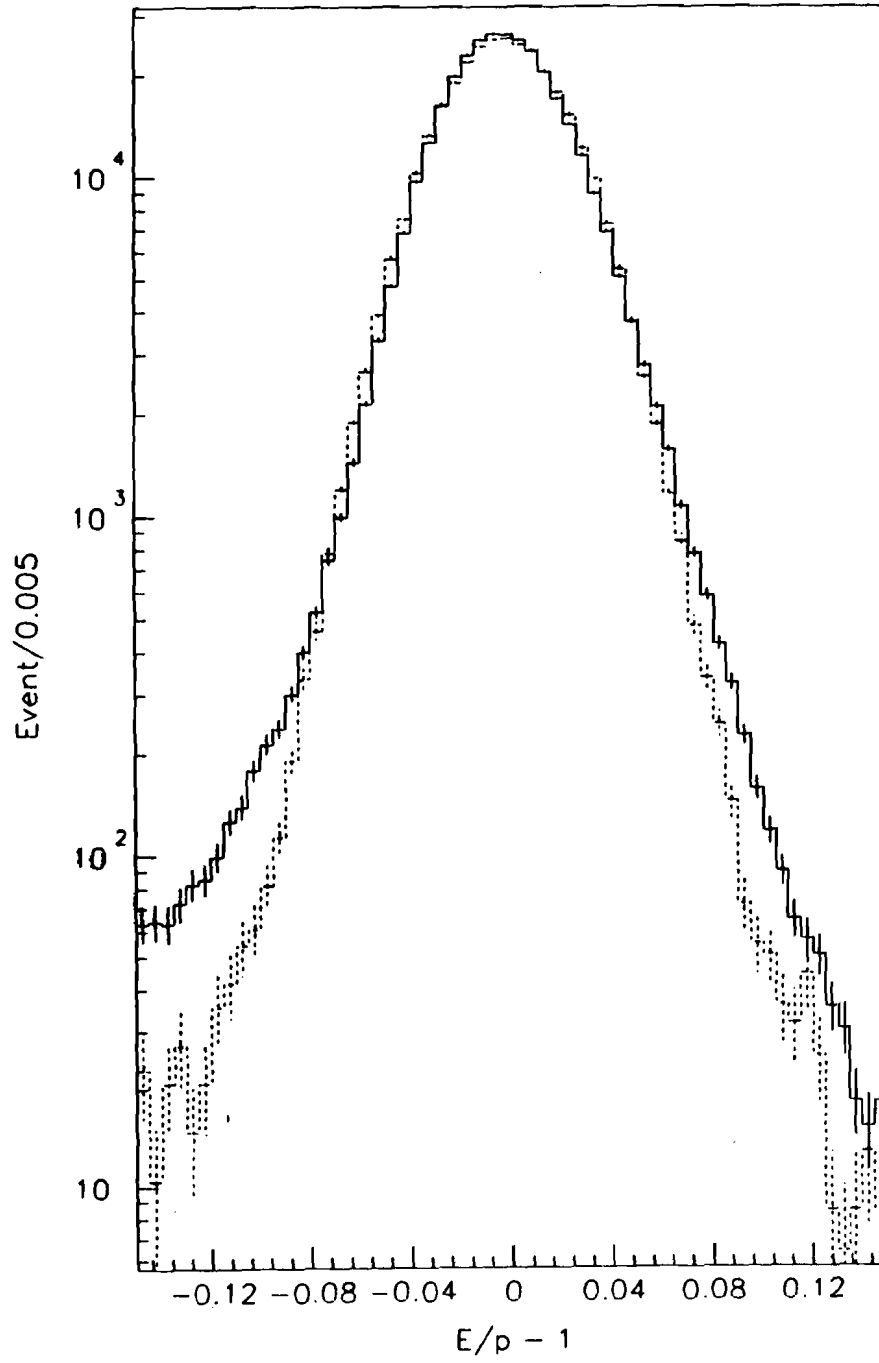
Figure 64. The distribution of E/p-1 for electrons from $K_L \to \pi^\pm e^\mp \nu$ decays. The solid line is data, the dashed one is Monte Carlo.

is below its average value by 0.2% in both data and Monte Carlo -- we shall see shortly that this is partially due to bremsstrahlung in the B and C counter banks. Apart from these two effects, whose origins are known, E/p is momentum independent within about 0.2% for all energies between 5 and 75 GeV. The absolute energy scale in the data is correct to within 0.1% below 20 GeV and 0.2% above that.

Figure 66 shows the rms widths of the E/p distributions of the data and Monte Carlo as a function of electron momentum. The resolution is best, about 2.6%, for 25 GeV/c electrons. At low momentum the resolution is poorer because of photostatistics. The rise at high momentum is partially due to deteriorating momentum resolution. In addition, higher energy electrons are concentrated in blocks around the beam holes, where the resolution is degraded because of the increased absorption due to radiation damage. As noted above, the rms width of the data is somewhat worse
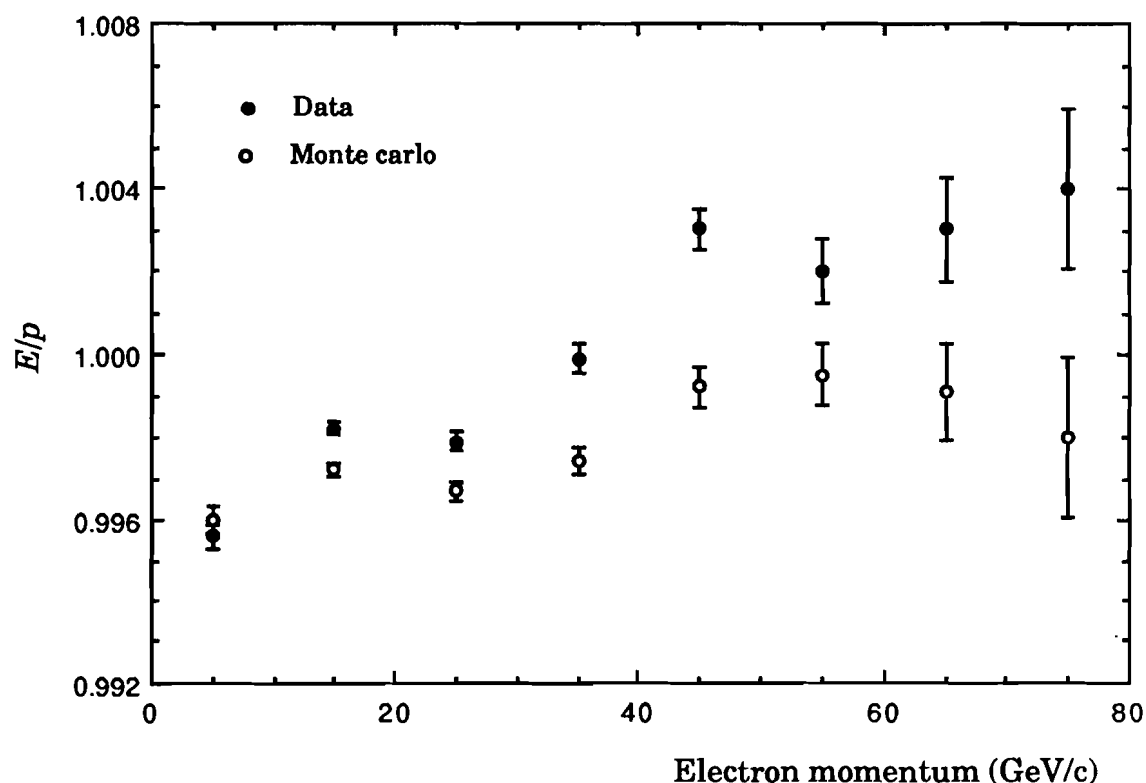
Figure 65. The value of E/p as a function of momentum for electrons from $K_L \to \pi^{\pm} e^{\mp} \nu$ decay in the data and Monte Carlo.

than that of the Monte Carlo, but the difference is small, and almost energy independent. The discrepancy is equivalent to an additional energy smearing of 0.7% to 1% added in quadrature, perhaps arising from uncertainty in the block gains.

6.8.3 Photons from $\pi^+\pi^-\pi^0$ and $\pi^0\pi^0$ decay

Figure 67 shows the two photon invariant mass for $K_L \to \pi^+\pi^-\pi^0$ decays in the data and Monte Carlo, where the energies of all the clusters have been increased by 0.4% to align the peaks. (The origin of most of this error in scale is understood and is described in the following section.) There are small deviations of the Monte Carlo from the data at very low mass, but the overall shapes agree well over four decades. Much of the low side tail common to the data and Monte Carlo is due to mis-tracked events and is not an artifact of photon showers.
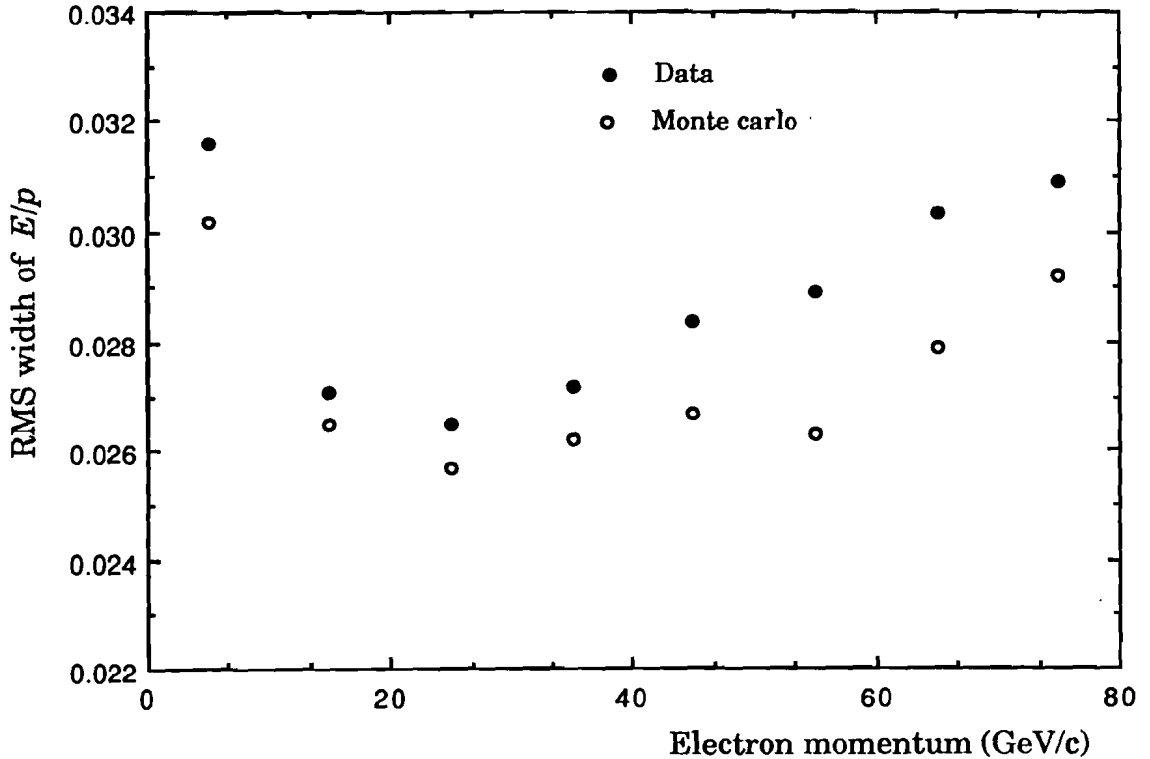
Figure 66. The resolution of E/p as a function of momentum for elec-trons from $K_L \to \pi^\pm e^\mp v$ decay in the data and Monte Carlo.

Reconstruction of the mass and the decay vertex (z) distributions of the $\pi^0\pi^0$ decays will be described in the next chapter; here we focus on the aspects relating to the calibration. First, the distribution of invariant mass $m_{\pi\pi}$ appears in Figure 68. The widths of the data and Monte Carlo distributions are nearly identical, though the shapes of the tails differ. There is an offset between the distributions: in order to align the peaks, we have added 0.4 MeV/c^2 to the masses in the data and subtracted 0.2 MeV/c^2 from those in the Monte Carlo. These discrepancies between the data and Monte Carlo have negligible effect on the data analysis since they are identical for K_S and K_L, but are interesting because they indicate that a small residual non-linearity remains (the mass is insensitive to an overall scale error). The
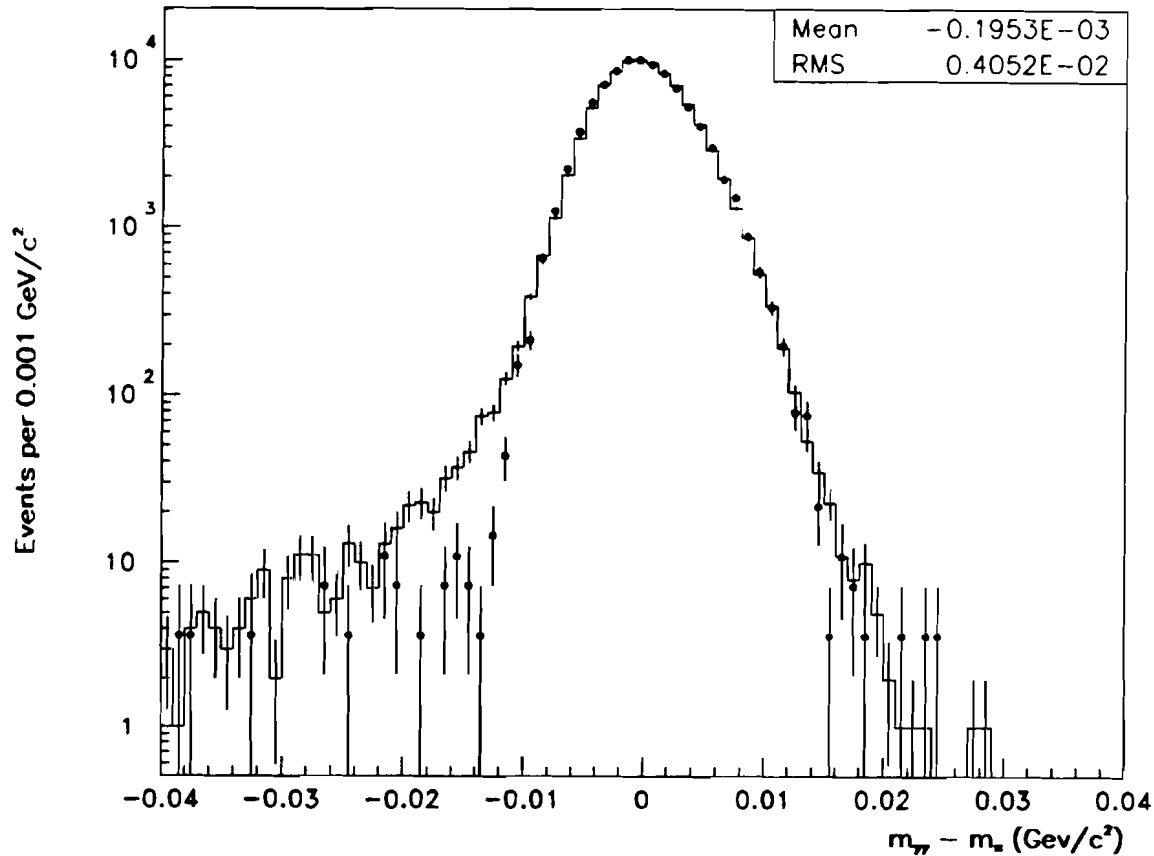
Figure 67. The $\gamma\gamma$ invariant mass distribution for photons produced in $K_L \to \pi^+\pi^-\pi^0$ decay. The histogram represent the data; the solid circles are Monte Carlo.

origins of such a nonlinearity is unknown, though there is some evidence that it arises from errors in the energies of low energy photons.

Finally, we compare the decay vertex distributions of the data and Monte Carlo in Figure 69. These are important to the analysis, and we will return to them in more detail in later chapters. The positions of the distributions depend on knowing the photon energies on an absolute scale, and here they have been increased by 0.5% in the data, mostly to correct for an effect described in the next section. The shape of the upstream edge is sensitive to the photon energy resolution, and is quite accurately reproduced by the Monte Carlo.
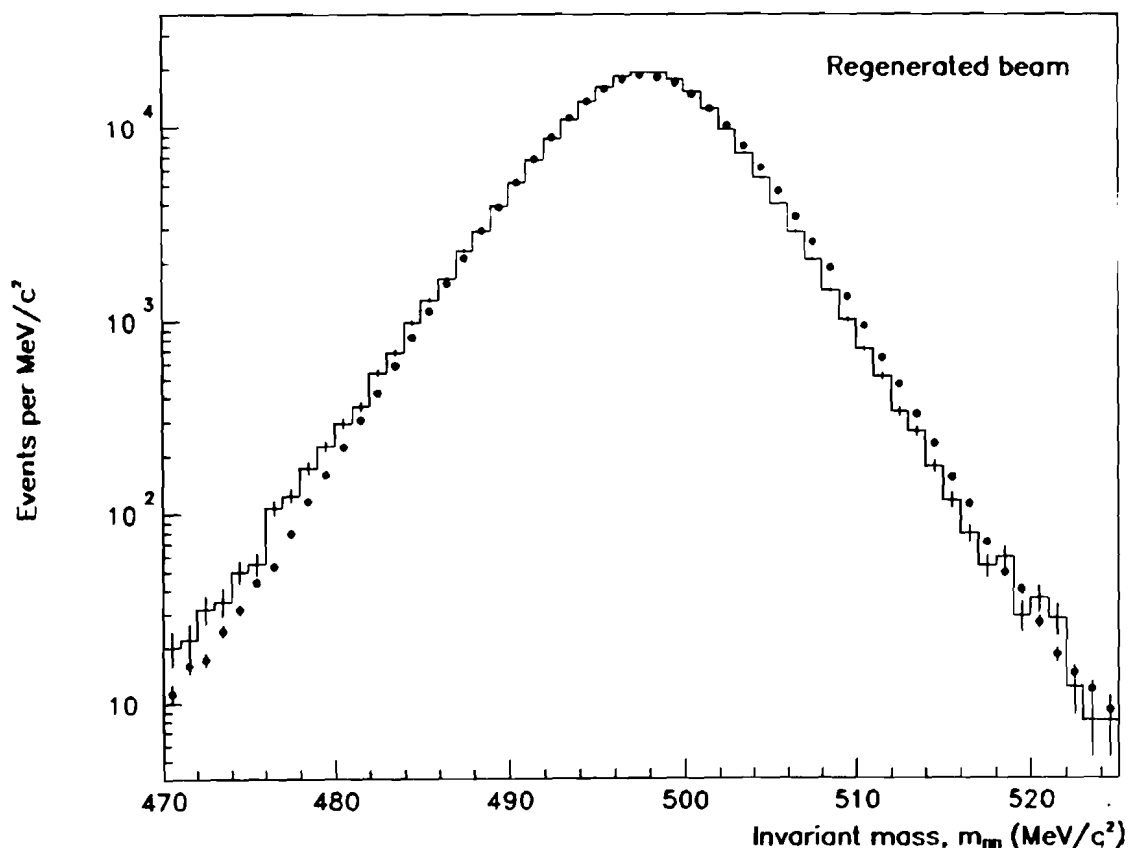
Figure 68. The invariant mass of the four photons from candidate $K_S \rightarrow \pi^0 \pi^0$ decays. The histogram represent the data; the solid circles are Monte Carlo. The data distribution has been shifted +0.4 MeV/c^2 and the Monte Carlo has been shifted −0.2 MeV/c^2.

6.8.4 Further Checks

The model of showers we have described allows us to predict the effects of interactions in the material upstream of the lead glass on the measured energies of the electrons and photons. Besides leading to important corrections, they provide nice independent checks of the model.

We first consider the effect on the photon energies of conversion in the material upstream of the calorimeter. When a photon preconverts, the two electron showers commence immediately at the front face of the lead glass, rather than at some depth within. On the basis of light attenuation alone, we expect the photon signal to decrease on average by the fraction:

$$\alpha t_{avg} \approx 0.039 \quad , \tag{6.34}$$
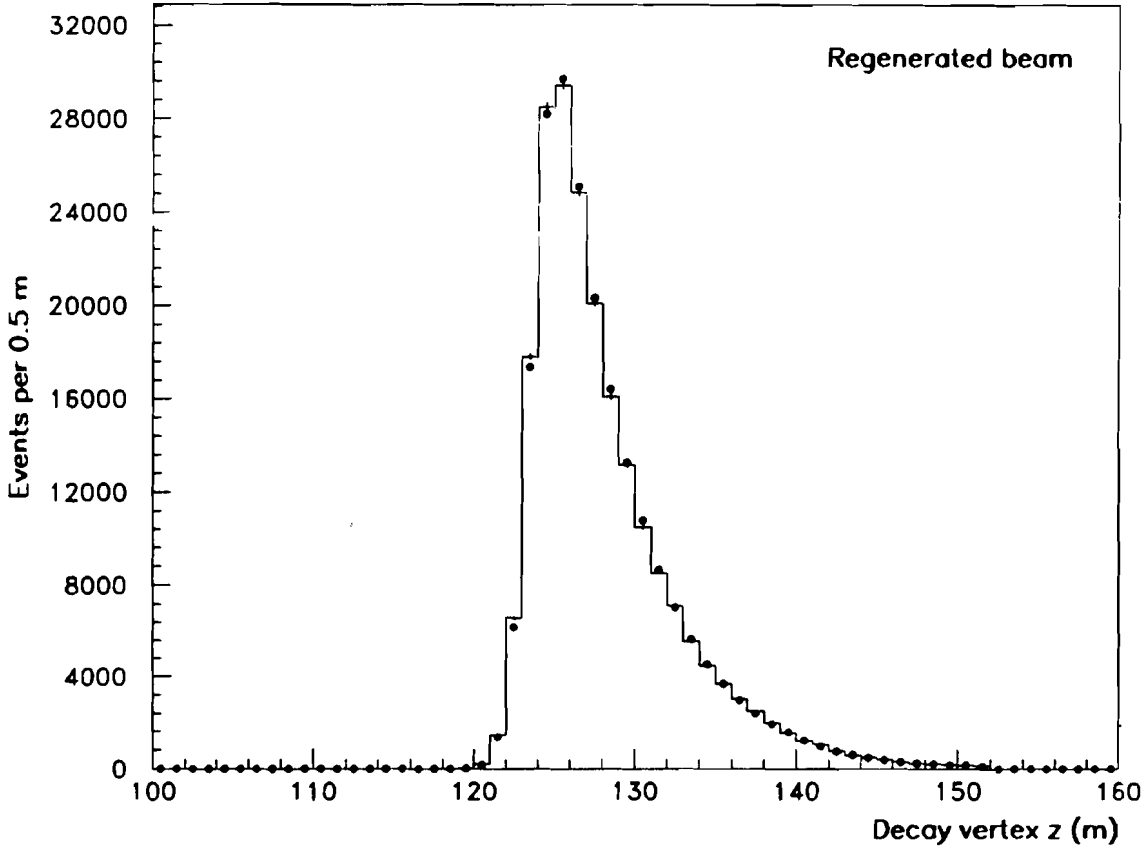
Figure 69. The decay vertex distribution of candidate $K_S \rightarrow \pi^0\pi^0$ decays. The energies of clusters in the data have been increased by about 0.5% to align the upstream edge of the distribution.

where t_{avg} is the average photon conversion depth, 1.29 X_0. Leakage of shower energy out the back of the block reduces the effect by 0.005 to 0.015, depending on the photon energy. In the data, signals in the B bank flagged conversion; the concurrent shift in the value of $m_{\gamma\gamma}$ for $K_L \to \pi^+\pi^-\pi^0$ decays was $(3.0 \pm 0.2)\%$, consistent with expectations.

Similarly, emission of bremsstrahlung photons in the B and C banks affects the measured energies of electrons, even when the electron and bremsstrahlung photon land on top of one another in the lead glass. As shown in Figure 70, this effect reduces E/p by about 0.3% at all momenta. Denoting the fraction of energy imparted to the photon by f, and using the power law approximation to the nonlinearity given by Equations (6.27) and (6.28), the ratio, r, of signals of radiating to non-radiating electrons is

$$r = \frac{R(E,\alpha)(fE)^{1/\beta} - ((1-f)E)^{1/\beta}}{E^{1/\beta}}$$

$$= R(E,\alpha)f^{1/\beta} + (1-f)^{1/\beta} \qquad , \qquad (6.35)$$

where $R(E,\alpha)$ is the electron-photon difference given by Equation (6.15). Bremsstrahlung occurs about 40% of the time in the 0.08 X_0 of the B and C banks, with an average of $f = 0.08$ of the electron energy given to the photon. Since for an energetic electron, $R(E,\alpha) \approx 1.02$, and typically the absorption power $\beta = 0.979$, Equation (6.35) yields $\langle r \rangle \approx 0.998$ averaged over all electrons. At low momenta, the effect is larger because of the momentum dependence of $R(E,\alpha)$.

Use of electrons for calibration neglecting such an effect would lead to a gain error of 0.3% when analyzing photon showers. We made exactly this mistake. All of our photon energies had to be artificially adjusted by about 0.4%, and this effect explains most of that shift.

6.9 Cluster Positions

So far, we have described only extraction of electron and photon energies from the data; however, as discussed in Section 6.1, their positions, which were determined from the distribution of energy among the nine
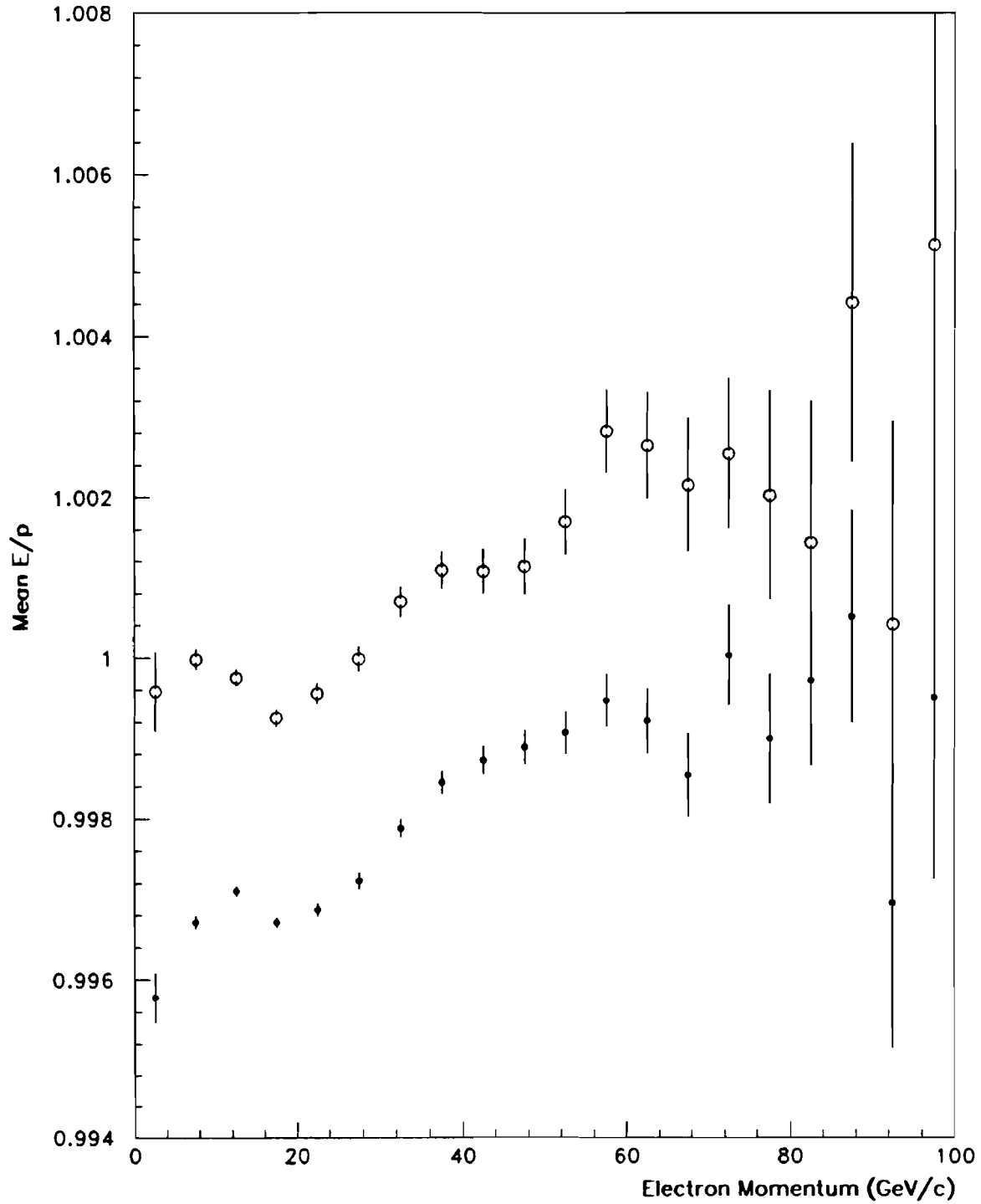
Figure 70. The value of E/p as a function of momentum for electrons from $K_L \to \pi^\pm e^\mp v$ decay as simulated in the Monte Carlo. The open circles represent non-radiating electrons; the solid circles include both radiating and non-radiating electrons.

lead glass blocks participating in the shower, were also important. Figure 71 shows the radial distribution of 1, 8 and 64 GeV showers. In general, they are quite collimated, and for clusters which hit near the center of a block, 85% of the total energy was contained within it. The position was determined from the sharing of energy between the central block and its neighbors. When a photon or electron hit close to the edge of a block, the fraction of energy outside the central block was large and sensitive to the impact point, so position resolution was good. When they hit near the center of a block, energy sharing was less and less sensitive to the position, so resolution was worse.

The horizontal (x) and vertical (y) positions of clusters were determined separately, but the same procedure was followed for both. Consider the technique for finding the x position. The cluster finding algorithm identified the block with the most energy as the central block of the cluster, and the particle was assumed to have hit the glass somewhere within it. To find the x position of the cluster, the energies in the blocks of each of the
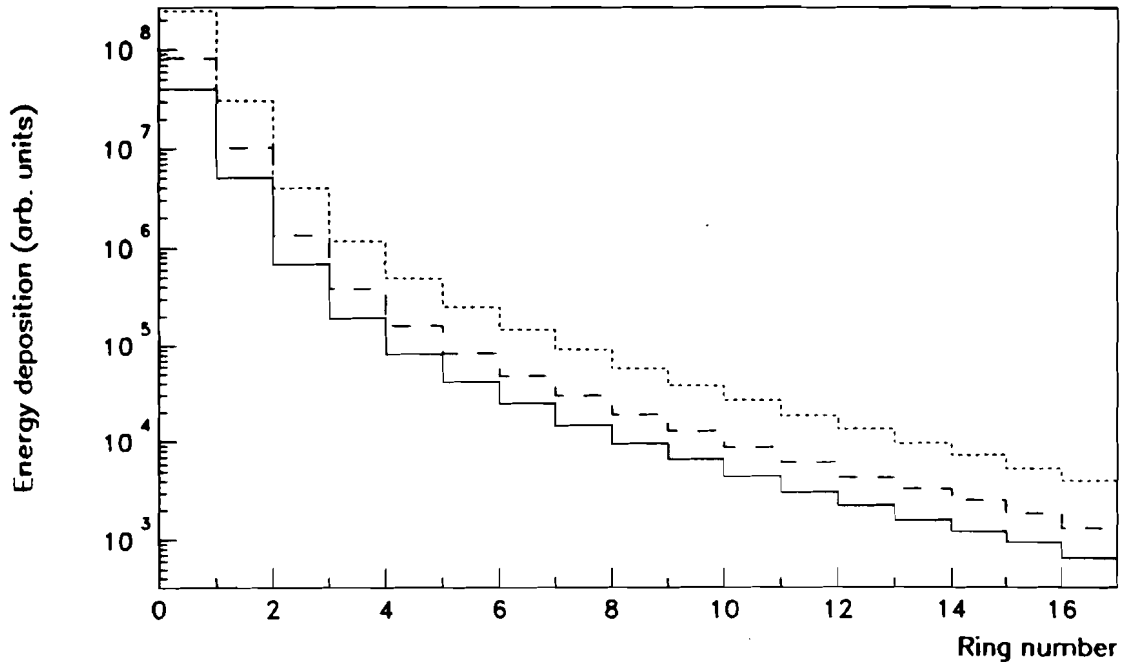
Figure 71. The radial distribution of Cerenkov light production in 1, 8 and 64 GeV electron showers. Each square ring is $0.363\,X_0$ wide.

three columns of the 3×3 block cluster region were summed as shown in Figure 72. Generally, the central column had the most energy, and the side column nearest the impact point had the next most. The position was calculated from the ratio q of energies in the maximum side column to that in the center column. The distribution of this ratio is shown in Figure 73. As anticipated, the most likely values of q are small, corresponding to events in which the central core of energy is mostly contained within the center column.

The function relating the ratio of column energies q to the hit position was extracted by applying the assumption that the clusters in a specially selected data set were uniformly distributed across the block. For these data, the distance in x of the hit from the center of the block related to the ratio q according to

$$x(q) = \frac{h}{2} \frac{\int_0^q N(q')dq'}{\int_0^1 N(q')dq'} \quad , \tag{6.36}$$

where $N(q)dq$ is the distribution of ratios and h is the transverse block size. We approximated the integrals with sums, and generated a table used in

0.2	0.2	
2.7	21.0	0.2
2.1	5.9	

Total column
energy   6.0   27.1   0.2 $q = \dfrac{6.0}{27.1}$

Figure 72. Calculation of the column ratio used to find the x position of the cluster within the central block. The squares show the energy deposits in the lead glass blocks in GeV for a typical photon.

the analysis which gave the value of x corresponding to any value of q. This technique is similar to that used to find the time to distance relation for the cells of the drift chambers.

To find the y positions of clusters, we calculated the ratio of the energies in rows of blocks, rather than columns, and then used the same table relating the energy ratio to hit position that was used for x. Using the ratio of columns (or rows) to calculate the cluster positions, rather than of the central to side blocks alone, reduced coupling of x and y: The sum of energies in columns was almost completely independent of the y position of the clusters, and the sums in rows were independent of their x positions.

The position algorithm described so far gives the distances of the impact point from the nearest edges of the block, but to find the position of each cluster within the general coordinate system, we also needed to know the absolute positions of these edges. The blocks were packed tightly together, but because of variations of about ± 1 mm in their transverse dimensions, their edges could be displaced from their nominal position.
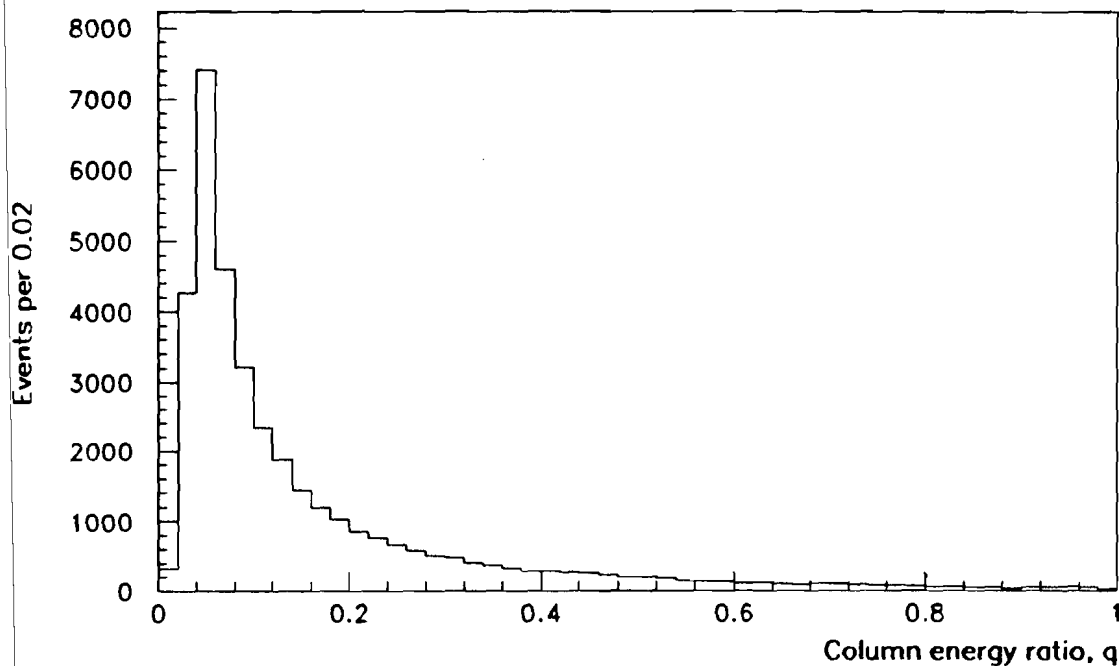
Figure 73. The distribution of the ratio, q, of the sum of energy in the maximum of the two side columns to the sum of energy in the center column.

Before stacking them into an array, the dimensions of the blocks were measured. The dimensions together with the overall offset of each row and column, found by extrapolating electron tracks into the lead glass, determined the location of each block edge. The position algorithm, then, used the ratio of energies to find the distance of the hit from the block edge, and then consulted the lead glass block data bank to find the location of the edges of that block.

The energy deposited in the blocks in principle varied with the incident angle of the electron or photon on the lead glass. To partially account for this, the z position of clusters (i.e., the lead glass) used in the analysis was taken to be 20 cm into the lead glass block, where the bulk of observed light originated.

To determine the position resolution, we compare the positions of electron clusters with that of their extrapolated tracks, which were generally known within 150 μm. As shown in Figure 74, the root mean square width is 2.8 mm. As anticipated, the position resolution increases with the distance of the impact point from the block edge (see Figure 74), rising from ± 1.5 mm at the block edge to ± 4 mm at the block center. The apparent improvement in resolution at the center of the block is an artifact shower fluctuations. In reality the position sensitivity is poorest at the center.

6.10 Conclusions

At the start of the chapter, we argued that the energy and position scales had to be known within ± 0.2% and that their resolutions had to be replicated in the Monte Carlo within ± 1%, added in quadrature. We have seen that the absolute energy scale is known within ± 0.2% at all energies, in the absence of any ad hoc corrections factors. That this error is small and energy independent increases confidence that the absolute energy scale is known within the desired accuracy. Consistent with the results of the previous sections, the energies of photons from $\pi^0 \pi^0$ decays were reduced by 0.3% to account for the bremsstrahlung effect in calibration, and by an additional 0.15% chosen to align the edges of the data and Monte Carlo decay distributions at the regenerator.

146
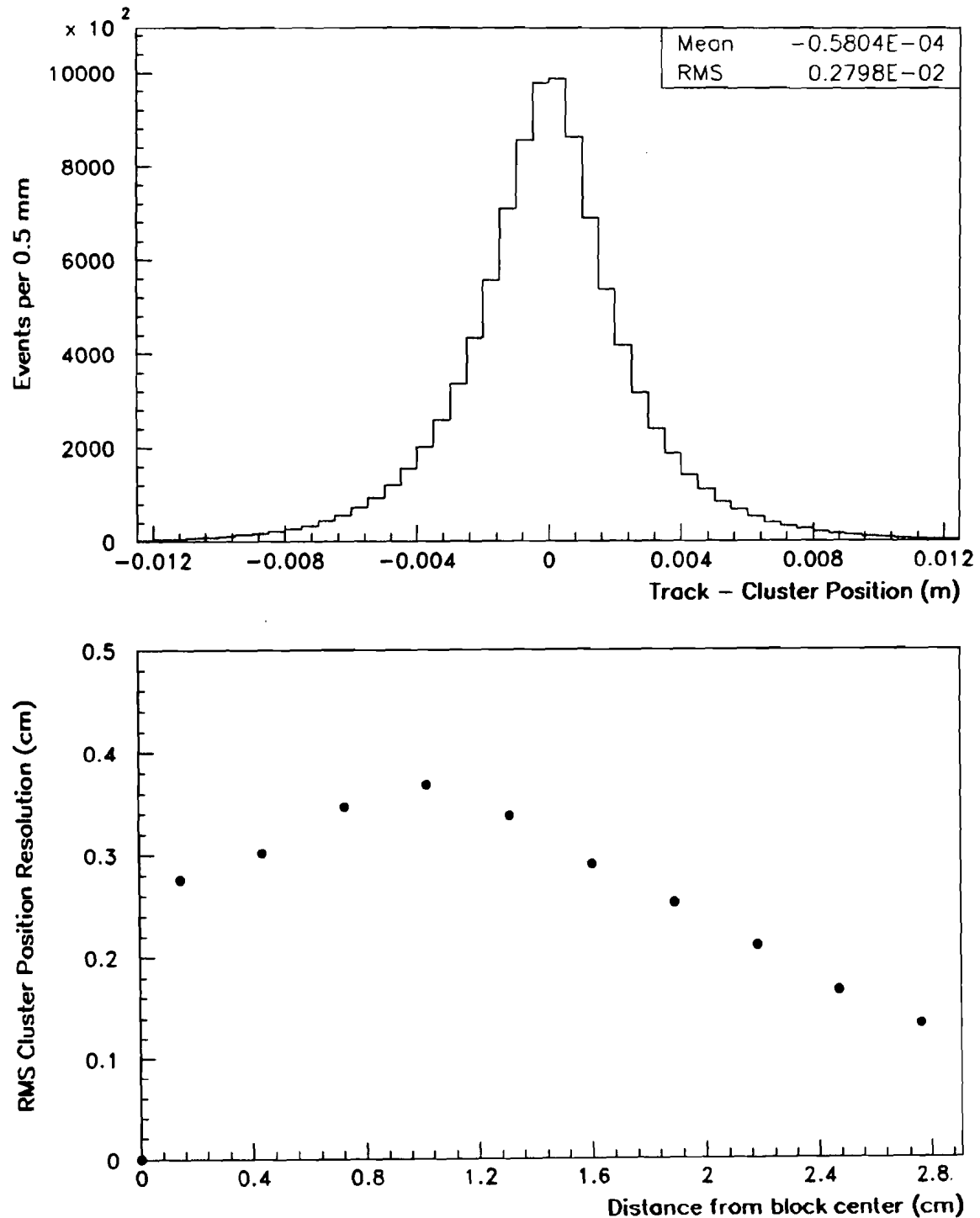
Figure 74. The position resolution of clusters in the lead glass. Plot (a) shows the distribution of the separation between the extrapolated track and cluster positions, and (b) shows the rms width of the distribution of the track and cluster separations as a function of the electron impact point within the lead glass block.

The resolutions are also satisfactory. The position resolution is good, and the energy resolution is close to the intrinsic limit of the calorimeter. The Monte Carlo reproduces them within the desired accuracy at all energies.

We are now prepared to discuss the neutral mode data, the subject of the next chapter. We will return to the energy scale and resolution briefly in Chapter 9, in order to evaluate the effect of the remaining uncertainties on $\text{Re}(\varepsilon'/\varepsilon)$.

CHAPTER 7

ANALYSIS OF THE NEUTRAL DECAYS

7.1 Overview

We now move to discussion of the neutral decays. The stages of the $K_{L,S} \to \pi^0\pi^0$ analysis paralleled those of the $K_{L,S} \to \pi^+\pi^-$ analysis. In the initial analysis of the 1000 raw data tapes, candidate $\pi^0\pi^0$ decays were selected using loose criteria. The resulting data sample, in which the K_L and K_S candidates were intermingled, fit on a tractable 14 magnetic tapes. More refined selection criteria for the $\pi^0\pi^0$ decays were then developed.

Neutral pions decay into two photons 99% of the time. Because the π^0 lifetime is short, the $K_{L,S} \to \pi^0\pi^0$ decays appeared to have four photons originating from a single vertex. If the photons hit the lead glass, then the energies and positions of the resulting clusters allowed reconstruction of the kaon mass and decay position. Additional selection criteria reduced non-$\pi^0\pi^0$ background, which arose primarily from $K_L \to \pi^0\pi^0\pi^0$ decays, and ensured that the observed ratio of K_S to K_L decays was insensitive to the selection criteria. Finally, we estimated the contributions of the remaining backgrounds and of the non-coherent $K_S \to \pi^0\pi^0$ decays to the final data samples.

7.2 Event Reconstruction

As shown Figure 75 the four photon clusters were easily recognizable in the lead glass. The first step of the reconstruction was to determine how the photons were paired into the two π^0's. Given four photons (i,j,k,l), there
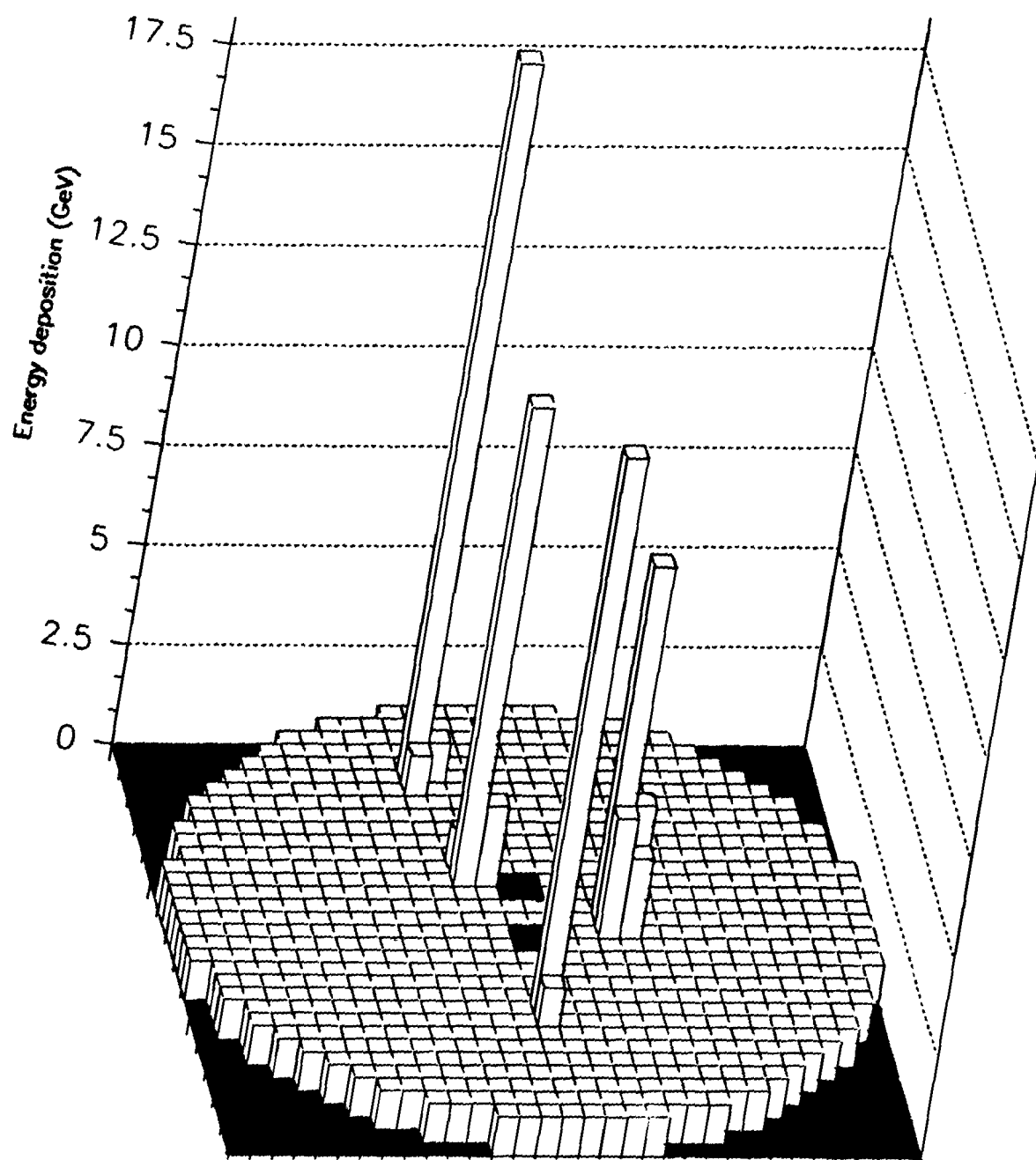
Figure 75. The energy profile of the lead glass array for a typical $\pi^0\pi^0$ decay. The height of each bar represents the energy deposited in that block plus a 1.5 GeV offset.

are three possible ways to pair them: $(i,j)(k,l)$, $(i,k)(j,l)$, and $(i,l)(j,k)$. Assuming that a π^0 decayed into a particular pair of photons, the z position of its decay can be calculated from the cluster energies and positions. This follows simply from kinematics:

$$
\begin{aligned}
m_\pi^2 &= E_\pi^2 - p_\pi^2 \\
&= \left(E_i + E_j\right)^2 - \left|\mathbf{p}_i + \mathbf{p}_j\right|^2 \\
&= 2E_i E_j(1 - \cos\theta)
\end{aligned}
$$

where E_i and E_j and $\mathbf{p}_i$ and $\mathbf{p}_j$ are the photon energies and momenta and θ is the angle between them. Assuming θ is small (for us the maximum value of θ is 0.04 radians) this can be written

$$
m_\pi^2 = \frac{E_i E_j r_{ij}^2}{z_{ij}^2} \quad , \tag{7.1}
$$

where r_{ij} is the separation of the photons in the calorimeter and $z_{ij} = z_{PbG} - z$ is the distance of the decay vertex from the lead glass. Thus,

$$
z_{ij}^2 = \frac{E_i E_j r_{ij}^2}{m_\pi^2} \quad . \tag{7.2}
$$

In reconstructing the neutral decays, we used this relation to pair the photons and find the decay position. For each of the three possible pairings, we calculated the decay vertices of the two π^0s. For the wrong pairing choices, the z's of the π^0's generally differed, while for the right choice they were generally consistent with one another. Operationally, a χ^2 was calculated for each pairing given by

$$
\chi^2 = \frac{\left(z_{ij} - z_{kl}\right)^2}{\sigma_{z_{ij}}^2 + \sigma_{z_{kl}}^2} \tag{7.3}
$$

where the uncertainties on the two pion decay positions, $\sigma_{z_{ij}}$ and $\sigma_{z_{kl}}$, were calculated from the energy and position resolutions of each cluster,

parametrized (pessimistically) by 2% + 6%/$\sqrt{E}$ and the function shown in Figure 74b respectively. For each event, the pairing with the smallest χ^2 was selected. The distributions of the selected χ^2s for decays in the vacuum and regenerated beams are shown in Figure 76 (the technique for identifying beam of origin will be described shortly.) The tail on the distribution is due primarily to $K_L \to \pi^0\pi^0\pi^0$ decays. To eliminate these and other non-$\pi^0\pi^0$ decays, events with $\chi^2 > 4$ were rejected.

The kaon decay vertex, z, was taken to be the weighted average of the two pion vertices. Once z was known, it was easy to calculate the four photon invariant mass, $m_{\pi\pi}$, using

$$m_{\pi\pi}^2 = \sum_{\substack{i=1,4 \\ j=i+1,4}} \frac{E_i E_j r_{ij}^2}{(z_{PbG} - z)^2} \qquad (7.4)$$

which is a simple generalization of Equation (7.1).

For 2% of the $\pi^0\pi^0$ decays the above procedure selected the wrong photon pairing, and to eliminate these we rejected events for which the second best pairing had $\chi^2 < 40$ and invariant mass in the range $0.470 < m_{\pi\pi} < 0.526$ GeV/c². After this cut, virtually no mispaired events remained, while the loss of well-reconstructed $\pi^0\pi^0$ decays was less than 0.5%.

Decays in the upper and lower beams were distinguished by the center of energy of their four photons in the lead glass, given by

$$r_c = \frac{\sum\limits_{i=1,4} E_i r_i}{\sum\limits_{i=1,4} E_i} \qquad (7.5)$$

where r_i is the position vector of the ith cluster in the glass. The center of energy distribution is shown in Figure 77 for $\pi^0\pi^0$ decays (after all other cuts) which occurred while the regenerator was in the upper beam. The two beams are clearly visible, and their relative populations exhibit the ratio of vacuum to regenerated decays. Smearing of the cluster energies and po-
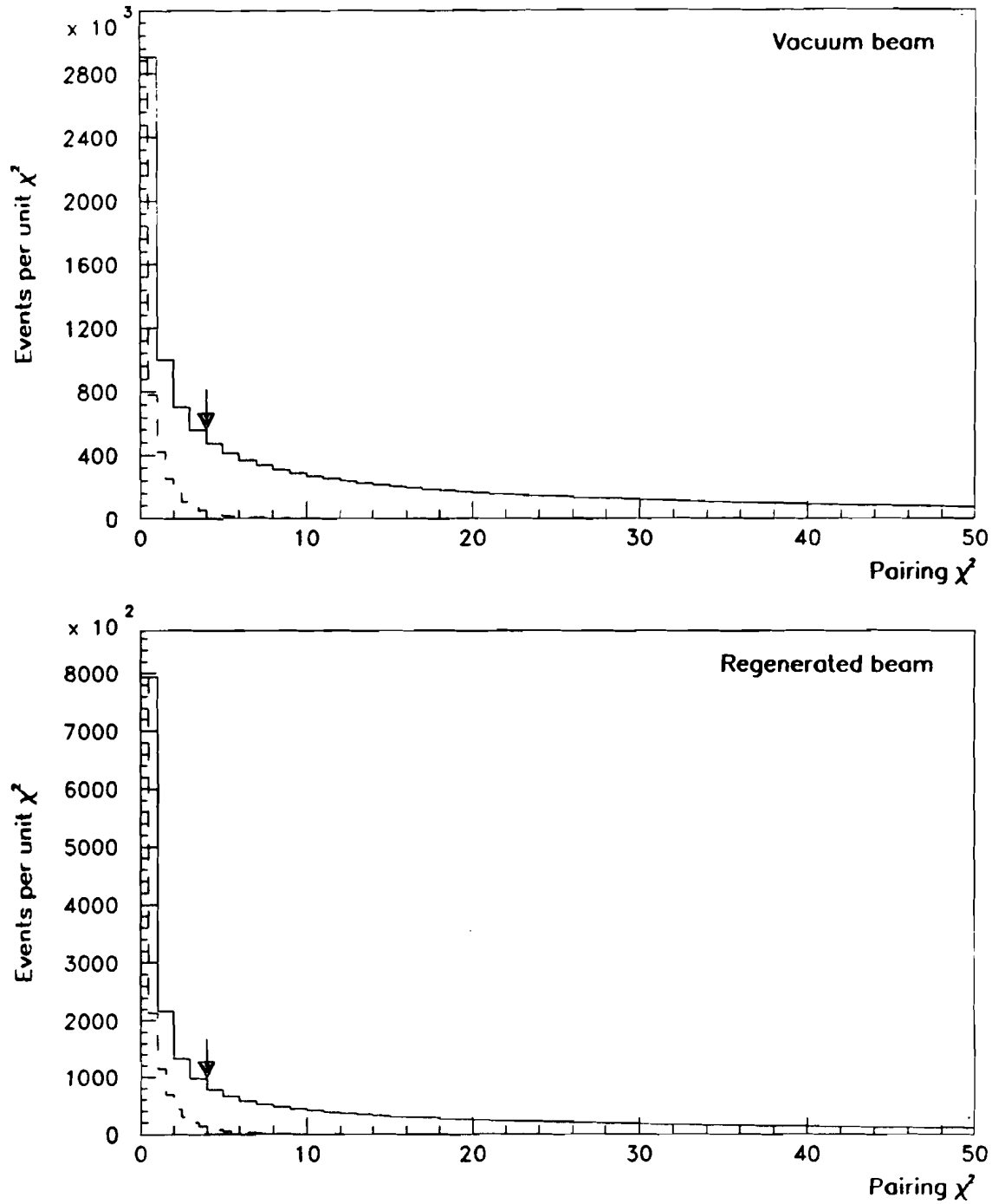
Figure 76. The pairing χ^2 distribution for all four cluster events. The dashed line shows the distribution for $K_S \to \pi^0\pi^0$ decays after all other cuts, and the arrows indicate the position of the cut.
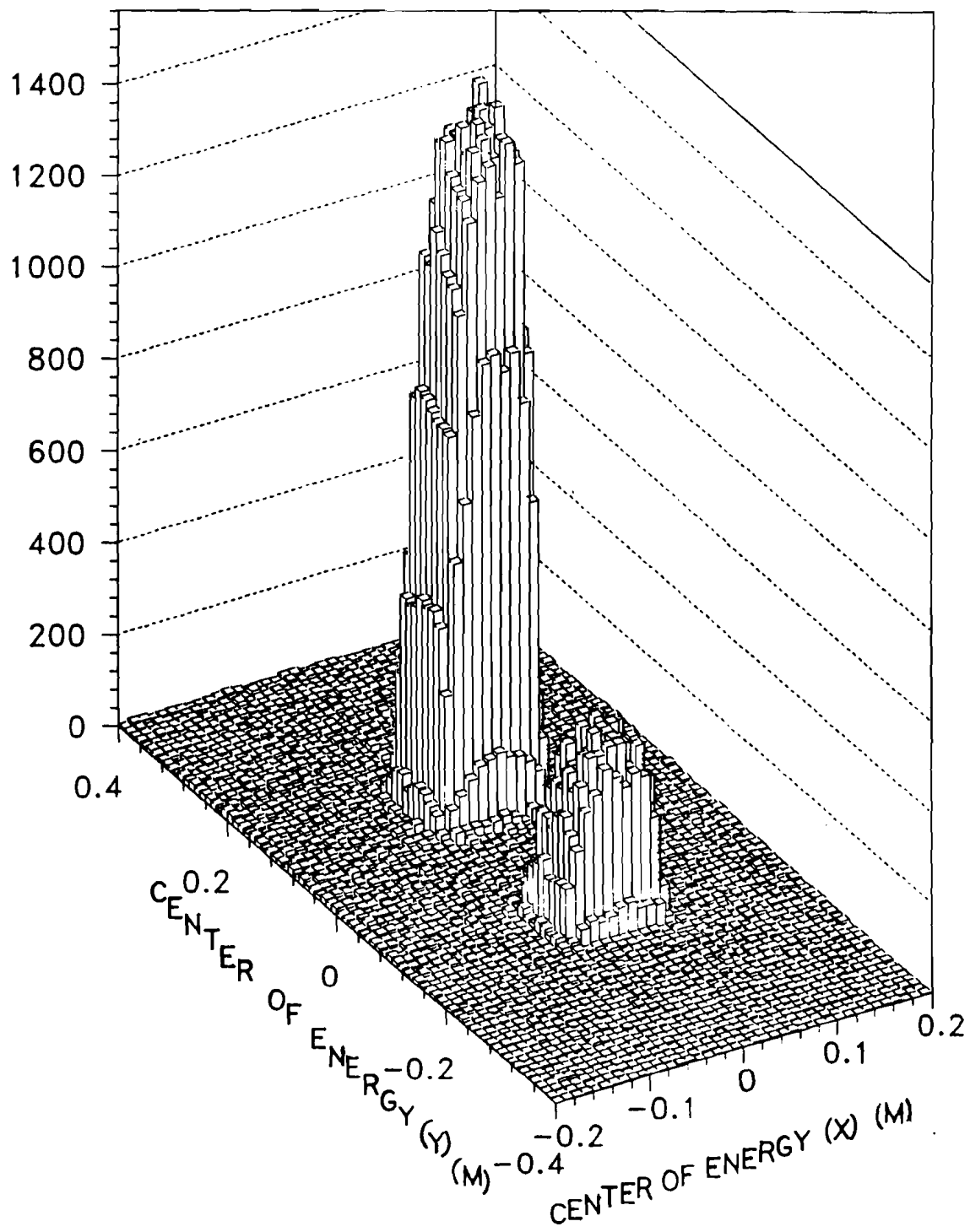
Figure 77. The center of energy of the four photons in the lead glass for reconstructed $\pi^0\pi^0$ decays which occurred while the regenerator lay in the upper beam.

sitions led to a resolution of 0.4 cm for the center of energy, and since the beam separation was 12 cm, the probability of mismeasuring the center of energy so severely that a kaon was assigned to the wrong beam was negligible. Crossover from one beam to another, however, could occur when a kaon scattered heavily in the regenerator and will be treated in detail in the section on non-coherent regeneration. Only events with center of energy within one beam or the other were included in the final data sample, as is shown in Figure 78.

Figure 79 shows the invariant mass distribution, $m_{\pi\pi}$, for decays from the two beams for all recorded four cluster events. The final data sample included events with invariant mass in the range $0.480 < m_{\pi\pi} < 0.516$ GeV/c². The background to the $K_{L,S} \to \pi^0\pi^0$ peaks is due to $K_L \to \pi^0\pi^0\pi^0$ decays with lost or overlapping photons. The are much suppressed for the regenerated beam because the K_L content of the regenerated beam is 6% that of the vacuum beam.

The z distributions of decays in the two beams (vacuum and regenerated) are shown in Figure 80. The final data sample included kaons decaying in the region $120 < z < 137$ m, chosen primarily to reduce sensitivity to any shift in the absolute cluster energy scale as described in Chapter 9. Upstream decays in the K_L beam were choked off by the lead mask and anti counter located at $z = 121.9$ m. The K_L distribution is roughly flat throughout the allowed decay region because there the reconstruction efficiency was largely independent of z. The reconstruction efficiency fell for decays close to the lead glass (located at $z = 181.1$ m) because clusters more frequently overlapped or were lost down the beam holes. The z distribution of regenerated decays has an edge at the scintillator following the lead at the downstream end of the regenerator, which would be perfectly sharp were it not for resolution smearing. The shape of the edge corresponds to resolution on the reconstructed decay vertex of 1.1 m. The mean decay length of kaons in the laboratory frame in this experiment can be seen from the fall of the K_S distribution; it is 3.8 m at 70 GeV.

We have now completed the reconstruction of the neutral kaon decays. Additional cuts that reduced backgrounds are the subject of the next section.
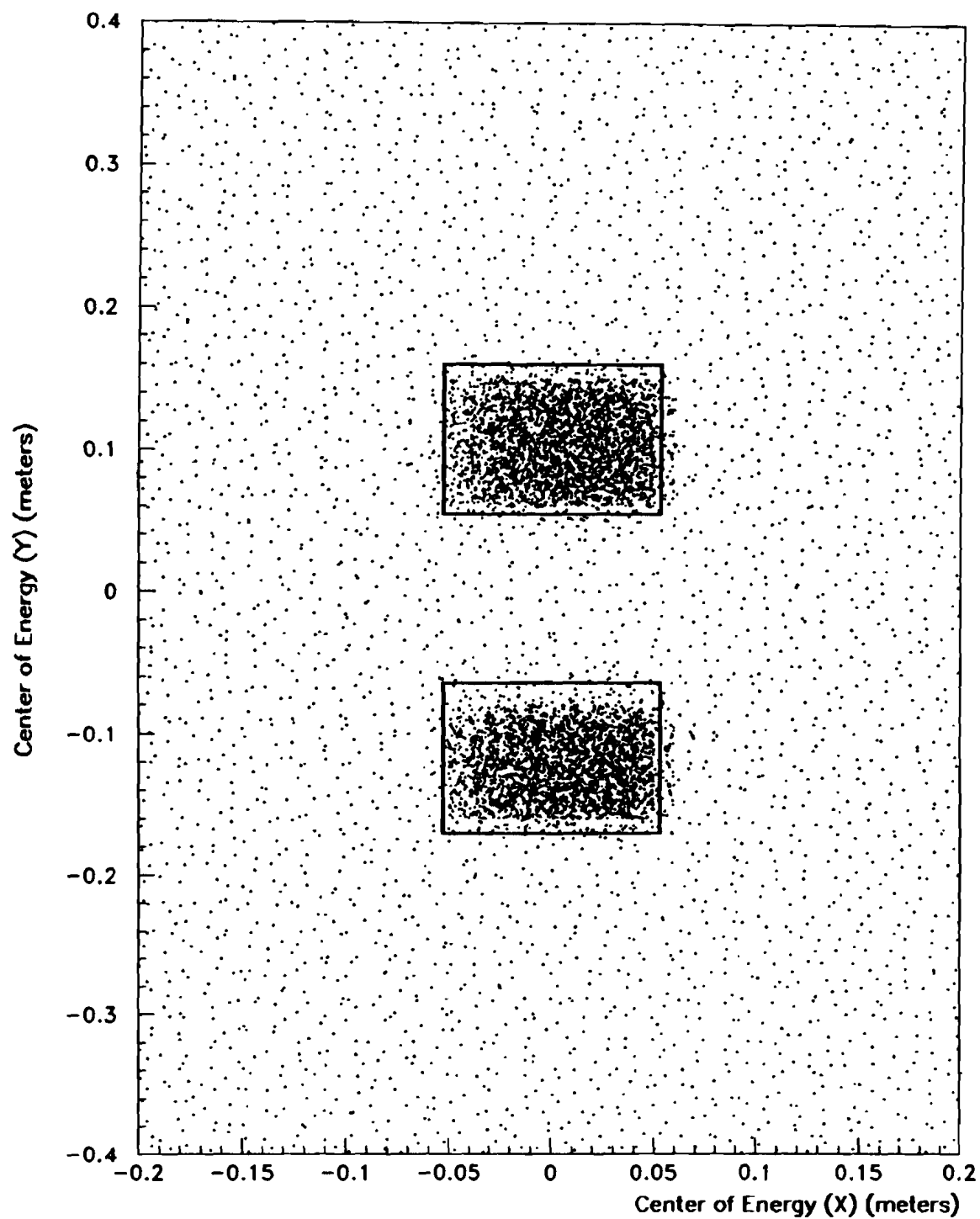
Figure 78. The center of energy of the four photons in the lead glass for all reconstructed $\pi^0\pi^0$ decays. Events outside the boxes were rejected.
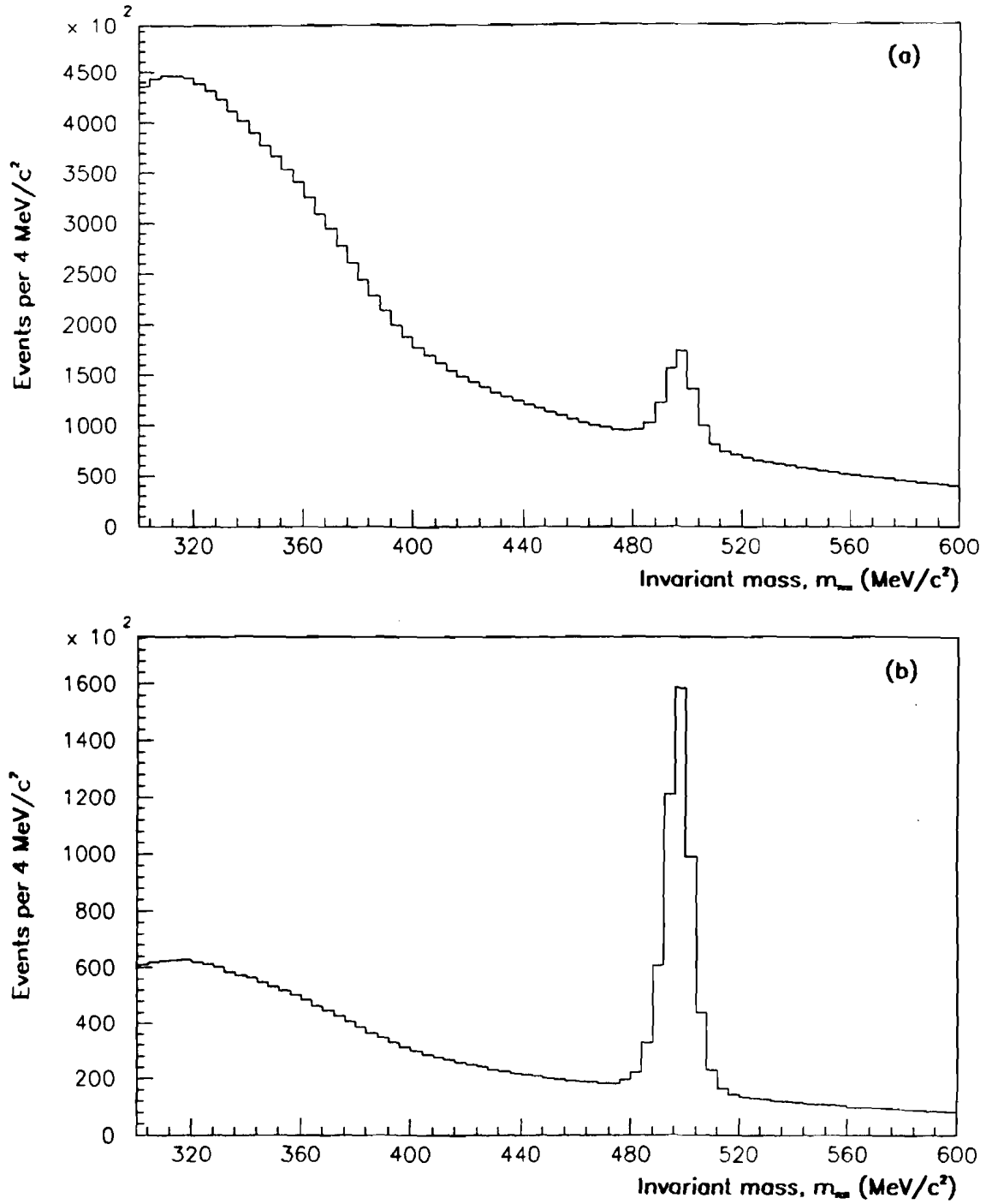
Figure 79. The four photon invariant mass of all four cluster events in (a) the vacuum and (b) the regenerated beam.
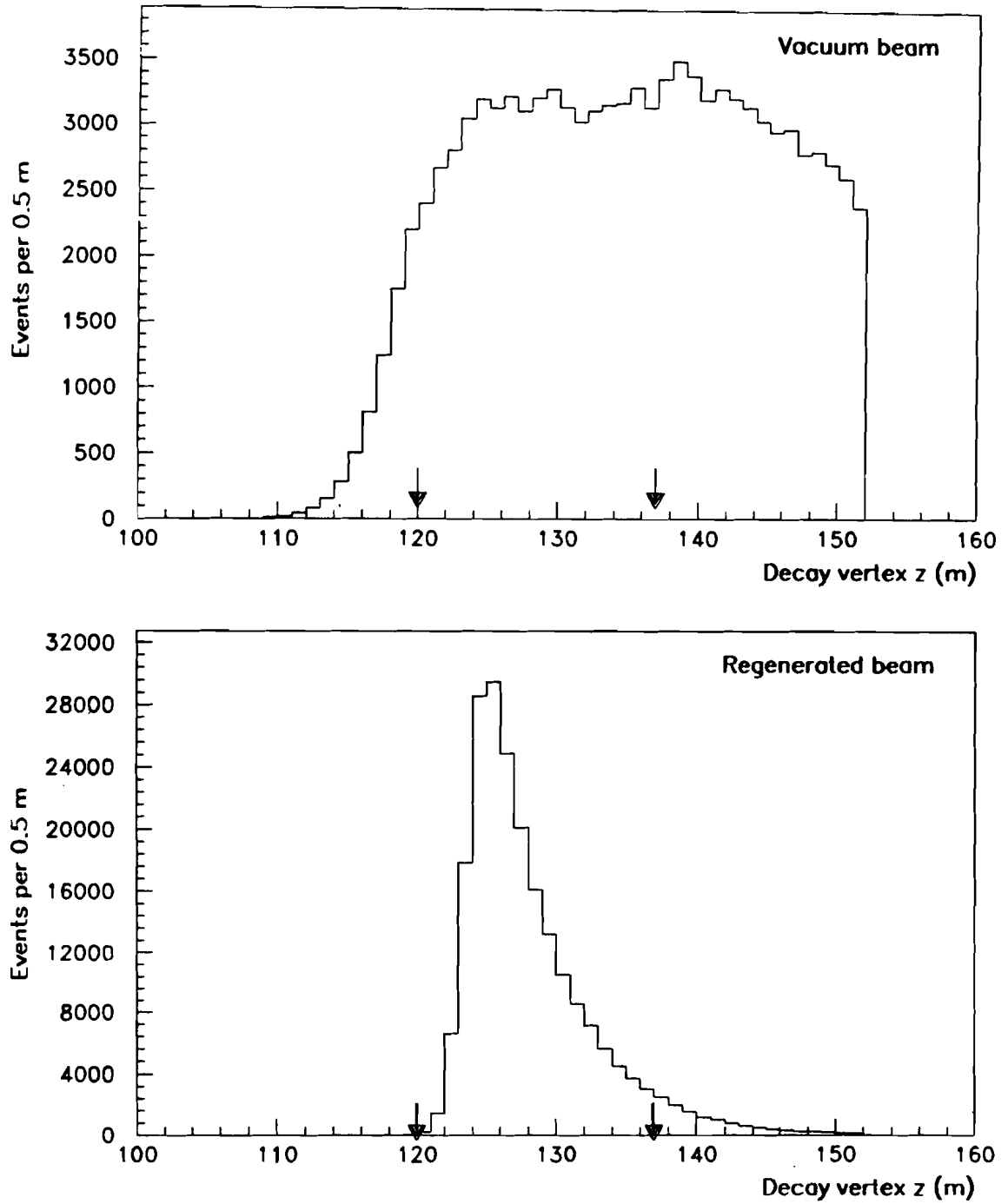
Figure 80. The z distribution of $\pi^0\pi^0$ decays upstream of $z = 154$ m after all other cuts. The arrows indicate the fiducial region.

7.3 Background Rejection

7.3.1 The $K_L \to \pi^0 \pi^0 \pi^0$ Background

The $K_{L,S} \to \pi^0 \pi^0$ decays were not the only source of four cluster events. The plentiful $K_L \to \pi^0 \pi^0 \pi^0$ decays could also leave four clusters if two photons were lost, either because they missed the lead glass and a multitude of veto counters or because their showers overlapped with others in the lead glass. When one or more photons missed the lead glass, the missing energy artificially shifted the reconstructed decay vertex toward the lead glass and displaced the center of energy, typically by a few centimeters. Cuts on z, the mass, and the center of energy therefore selected against these events, but even after these cuts, they represented 4% of the events observed in the vacuum beam at this stage.

Detection of Photons Missing the Calorimeter

To identify photons destined to miss the lead glass and reduce the background, we employed the veto counters which collared the decay and drift volumes at ten locations (see Figure 3). A few of these counters, the Pinching Anti (PA), the Active Lead Mask (AM), the fourth Vacuum Anti (VA4) and Lead Glass Anti (LGA) vetoed events at the trigger level. In the off-line analysis cuts were applied to the others: the Sweeper Anti (SA), the remaining Vacuum Anti counters (VAs 1,2 and 3), and the charged and neutral Decay Region Anti counters (DRAC and DRAN.) For VA1, VA2, VA3 , VA4, LGA, DRAC and DRAN the pulse area integrated over a 30 ns gate was available, while a single bit flagged activity in the SA (see Table 6). To maximize $K_L \to \pi^0 \pi^0 \pi^0$ rejection, it was advantageous to lower the veto thresholds as much as possible, increasing efficiency for very soft photons; however, excessively low thresholds sacrificed good $\pi^0 \pi^0$ decays because of noise. The cut thresholds optimally balanced efficient $K_L \to \pi^0 \pi^0 \pi^0$ background rejection with loss of otherwise good $\pi^0 \pi^0$ decays. Of the photons that missed the lead glass, 94% hit one of these counters, and when they did so, the average veto efficiency was 92%. Most of those that escaped without hitting anything did so between the lead glass and LGA. To avoid distorting

the ratio of K_S to K_L decays, we applied these cuts, like all others, to decays in both beams.

The Back Anti (BA), the multi-layer lead-lucite shower counter covering both beam holes downstream of the lead glass, further identified escaping photons. As described in Chapter 3, it was 28.1 X_0 long in total, and in order to distinguish electrons and photons from hadrons, energy deposition was calculated separately in the first 16 (electromagnetic) and last 8 (hadronic) layers. In the trigger, an event was vetoed if the energy deposit in the electromagnetic section was greater than 5 GeV and in the hadronic section was less than 10 GeV.

Detection of Low Energy and Fused Showers in the Lead Glass

The next major class of cuts eliminated $K_L \to \pi^0\pi^0\pi^0$ background by identifying extra showers in the lead glass which had not been seen, either because they fell below the 1 GeV (per block) energy threshold of the hardware cluster finder (HCF), or because they merged with other nearby clusters. We could not effectively search for the soft clusters using the lead glass signals because the high flux of random particles would have lead to loss of many good events. Instead we searched for extra photons using the Adders (the nine block hardware energy sums), which, because of their short 30 ns gate, were sensitive only to energy deposits that were in-time with the trigger. Events with more than 0.6 GeV in any Adder that was unassociated with any of the four clusters were rejected.

Other cuts identified photon showers which had fused into a single cluster by comparing the transverse distribution of the shower energy with expectations for a single shower. An example of a fused cluster is shown in Figure 81. The HCF would identify only a single shower in the configuration on the right-hand diagram in the figure, but the diagonal 12.0 and 21.1 GeV blocks with the two ~6 GeV blocks nestled next to them identify it as a fusion. Other fusion cuts were devised which recognized clusters which were broader than expected or had excess energy deposit outside the nine block region. Together, the fusion cuts removed almost 80% of the $\pi^0\pi^0\pi^0$ background, while sacrificing only 2% of the good $\pi^0\pi^0$ decays.

7.3.2 Background Due to Interactions of Kaons with Material

Some $\pi^0\pi^0$ decays resulted from interactions of kaons in the trigger plane at 137.8 m (HDRA). Most of these were eliminated by the downstream z cut at 137 m; however, because of the 1.1 m resolution in z, some leaked into the accepted region. Since such events were often accompanied by extra particles, they were reduced by a cut on events with hits in the two scintillator banks immediately upstream of the lead glass (B and C) and twelve or more hits in the drift chamber. This cut also eliminated events in which one of the photons pair-converted somewhere upstream of B and C.

7.4 Fiducial Cuts

It was important to the success of the measurement that the relative reconstruction efficiencies of K_S and K_L decays be well known, and several cuts on the photon positions and energies were applied to ensure this. For both K_L and K_S decays, photons were concentrated near the beams, with a cluster in a block neighboring one of the beam holes about 30% of the time. Energy loss of clusters within 1/2 block of the holes decreased the chances for successful event reconstruction by an amount that would have been difficult to predict since it depended on the details of lateral shower development and shower fluctuations. In order to guarantee that loss on this edge was well-defined, we rejected events with energy deposit in the Collar Anti (CA) (see Figure 19). A loose cut, equivalent to 25 minimum ionizing parti-

	0.2	0.2	
	2.7	21.0	0.2
	2.1	5.9	
		0.2	

$+$

0.5	2.8		
0.7	9.9		

$\rightarrow$

	0.3	0.2	
0.6	5.5	21.1	0.2
0.8	12.0	6.0	
	0.3	0.3	
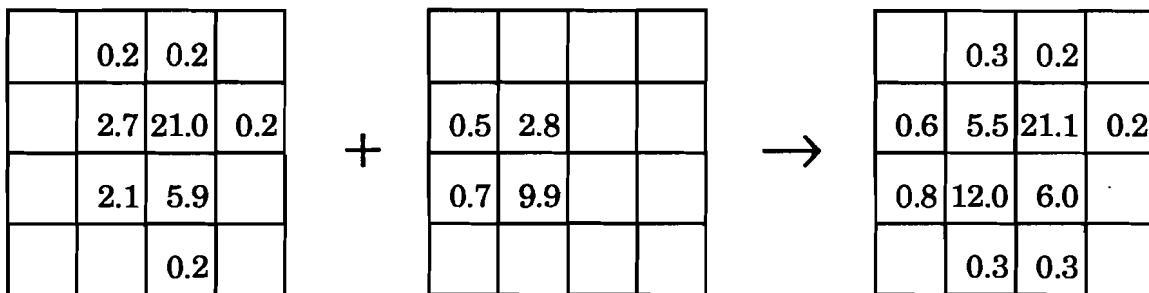
Figure 81. An example of a fused cluster. Each cell represents a lead glass block, and the number within is the energy deposit in GeV (energies below 0.2 GeV are not shown.)

cles in the scintillator, was used in the trigger; this was tightened to 5 minimum ionizing particles off-line. Photons hitting the lead glass outside the CA lost at most 3.5% of their energy, and after corrections, only marginally degraded reconstruction of the event.

Events with clusters very near the outer edge of the array were also in danger of misreconstruction; however, fewer photons landed there (about 1% within 1/2 block of the edge), and their concentration varied slowly with distance from the beam hole and was very similar for K_S and K_L decays, so such events required no special hardware precautions. Events with clusters within 1/2 block of the edge, based on the reconstructed cluster positions, were rejected.

A well-defined lower energy limit on the cluster energies was applied by cutting all those below 1.5 GeV. During data collection, the HCF selected islands of blocks above 1 GeV, but because of variations in the gains of the lead glass blocks of ± 4% and comparable variations in the HCF thresholds, the real level of the threshold varied somewhat across the array and with time into the run. The software threshold made it easier to reproduce the low energy cutoff of the clusters in the Monte Carlo.

7.5 Residual Background Calculation

The invariant mass distribution of events in the two beams after all cuts is shown in Figure 82. The effects of the cuts are summarized in Table 10. The residual background to the K_S decays was 0.02%, due primarily to $K_L \to \pi^0\pi^0\pi^0$ decays of K_L transmitted through the regenerator. The background was larger for the vacuum decays. An exponential fit to the mass distribution above and below the peak, in the mass regions $0.424 < m_{\pi\pi} < 0.460$ GeV/c² and $0.536 < m_{\pi\pi} < 0.572$ GeV/c², found 0.41% background in the signal region. Reproducing the background distribution in a Monte Carlo simulation of $K_L \to \pi^0\pi^0\pi^0$ decays in our detector, however, had the potential to verify that the background was indeed $K_L \to \pi^0\pi^0\pi^0$ decays and to allow us to determine its size more accurately. This job was undertaken using the same Monte Carlo as for the $\pi^0\pi^0$ and $\pi^+\pi^-$ decays, which is the subject of the next chapter. By applying the photon veto and cluster fusion
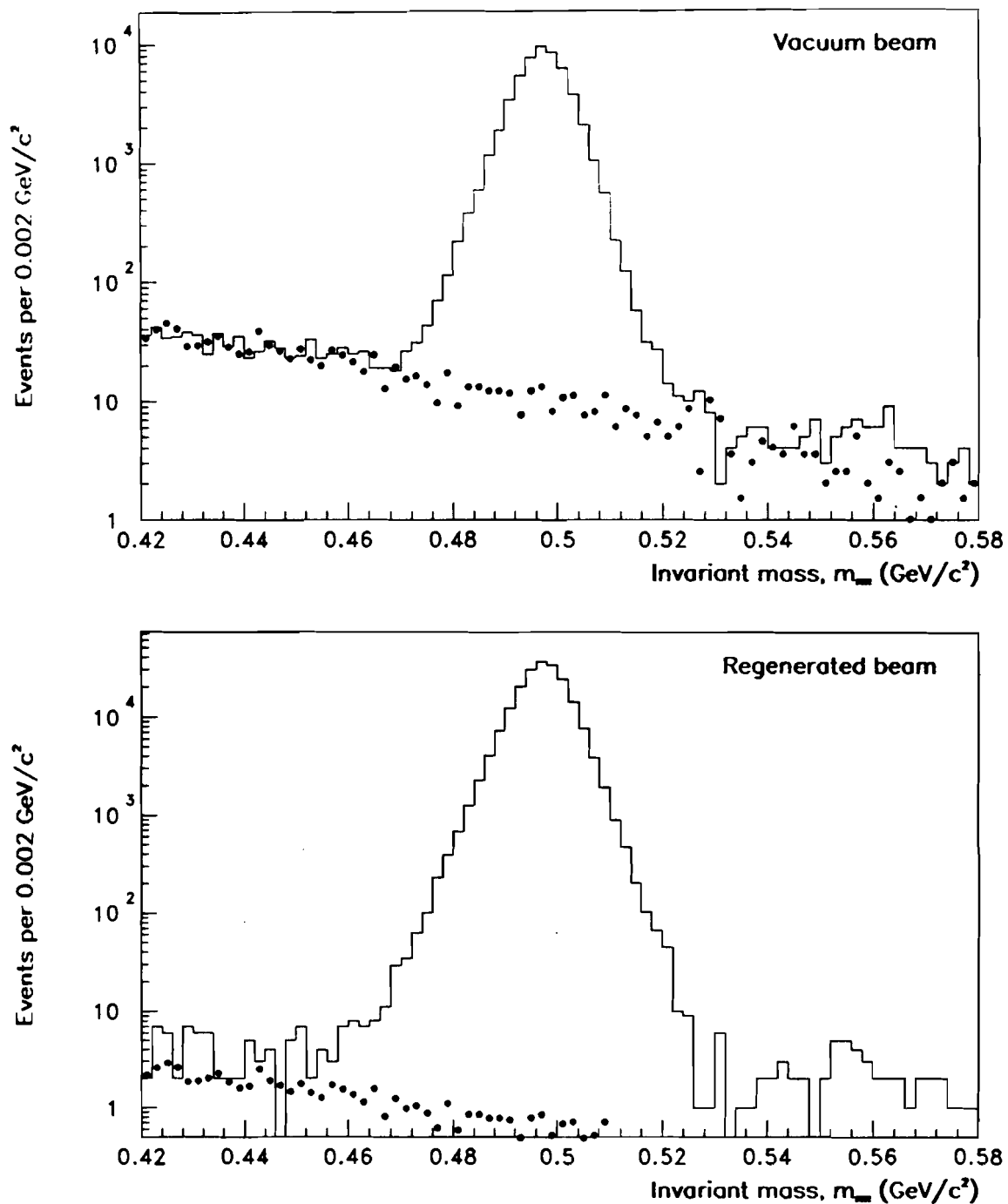
Figure 82. The four photon invariant mass after all cuts, for decays in the vacuum and the regenerated beams. The dots show the $K_L \to \pi^0\pi^0\pi^0$ background predicted by the Monte Carlo.

TABLE 10. The effect of cuts (applied in series) on the $K_{L,s} \to \pi^0\pi^0$ data. The figures apply to events in the accepted mass, decay vertex and kaon energy ranges.

Cut	Coherent $\pi^0\pi^0$ Event Loss	Non $\pi^0\pi^0$ Bkgd. (regenerated)	Non $\pi^0\pi^0$ Bkgd. (vacuum)
None (accepted by trigger)		1.6 %	21 %
Pairing χ^2	4 %	0.4	4.4
Center of Energy	1.6	0.3	4.3
Photon Veto	8.6	0.1	2.3
Fusion	2.1	0.1	0.5
Collar Anti & Outer Edge	6.4	0.1	0.5
Minimum Photon Energy	1.0	0.1	0.5
Extra particles	7.0	0.1	0.4

cuts during event generation, it was feasible to generate the 60 million $K_L \to \pi^0\pi^0\pi^0$ decays required to simulate this small background.

The result is shown superimposed on the $\pi^0\pi^0$ mass plot shown in Figure 82. The shape of the predicted background matches that of the data well. A slight excess in the data is visible above the mass peak. From the decay position of these events, it is known that they arise from interactions in the HDRA; they are expected to contribute a smooth background to the invariant mass distribution. Based on the background subtractions described shortly, they contribute 0.05% of the events within the mass cut.

The normalization of the Monte Carlo to data shown in the plot is absolute: it follows from the absolute $\pi^0\pi^0$ acceptance determined from the Monte Carlo, the ratio of $K_L \to \pi^0\pi^0\pi^0$ to $K_L \to \pi^0\pi^0$ branching fractions, and the number of K_L decays generated by the Monte Carlo. Accuracy of the normalization is limited by the 5% uncertainty in the ratio of branching fractions, but uncertainty in the efficiency of the photon vetoes leads to an additional uncertainty of about 10% on the absolute size of the background. Adjusting the normalization to give the best agreement with the data in the tails of the distribution, we find a background level of $(0.38 \pm 0.07)\%$, where the error is dominated by the statistics of the data and Monte Carlo.

7.6 Inelastically and Diffractively Regenerated Kaons

The value of Re(ε'/ε) was extracted from the numbers of K_L and coherently regenerated K_S decays. As discussed in Chapter 5, decays of K_S produced in diffractive or inelastic regeneration were excluded from the data sample. In the charged mode, subtraction of scattered K_S from the data was small and easy to do using the P_t^2 of the kaon. In the neutral decays, the only information available was the center of energy in the lead glass. Because the kaon's trajectory from the z of the regenerator was unknown, the scattered kaons were less readily identified (see Figure 83) and the subtraction was significantly larger.

Figure 84 shows the event density of the kaons as a function of distance from the center of each beam versus the two pion invariant mass, where the event density was calculated from the number of events lying in square rings about the center of each beam. The $\pi^0\pi^0$ decays are centered
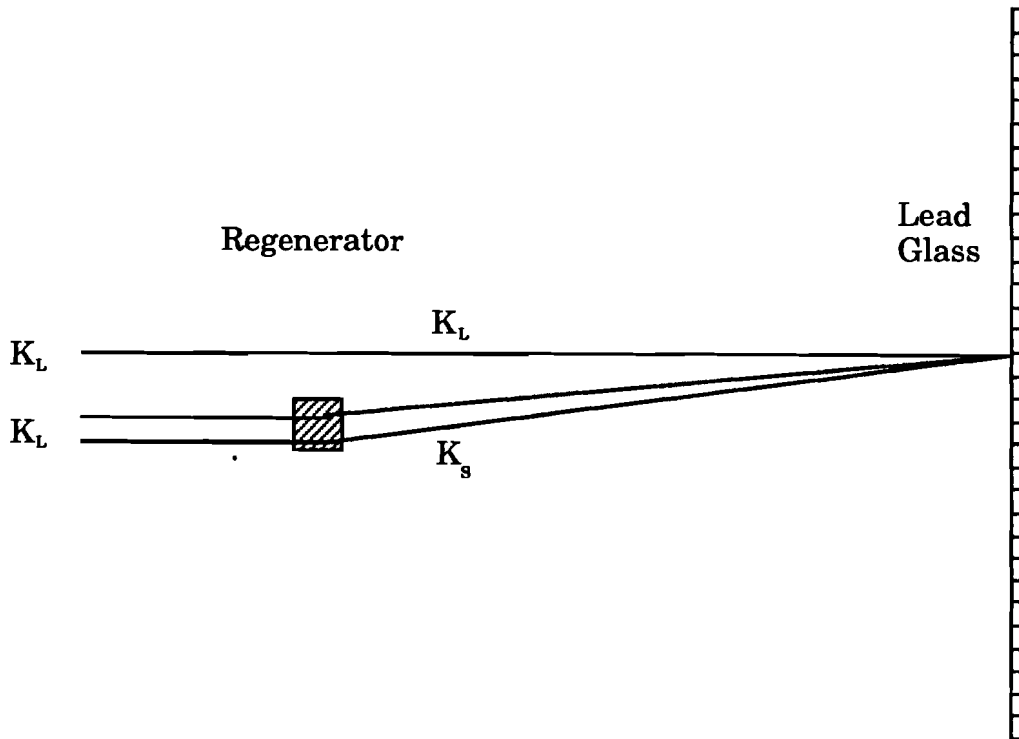
Figure 83. Scattering of K_S into the K_L beam. All three of the kaons shown have different P_t^2, but their centers of energy are the same.

on the kaon mass, with the K_L and the coherent K_S in the peaks at small ring numbers, and the scattered K_S filling the dark bands above. The z distribution of the events in the band (see Figure 85) confirms that they are K_S decays. (The small background from interactions in the trigger plane referred to in Section 7.3.2 is also visible in the figure.) The much smaller $K_L \to \pi^0\pi^0\pi^0$ background is also visible in Figure 84, clustered in the region with low mass and ring number.

To quantify the non-coherent background level, it is convenient to project the contents of the center band as shown in Figure 86. The size of the background can be estimated by extrapolating under the peak. In the regenerated beam it is about 2.6%. In the vacuum beam, while the absolute number of non-coherent events below the K_L peak is smaller than below the K_S peak, the background is fractionally larger, about 4.7%.

As alluded to above, the large background arises because the kaon's position of origin within the beam is unknown: scattered K_S from all locations within the regenerated beam can contribute to every center of energy. However, the P_t^2 distribution is a Green's function of the center of energy distribution, and we can use the P_t^2 distribution determined with the charged decays to predict its size and shape. The rather shallow slope of the non-coherent P_t^2 distribution (see Figure 34) implies that the background will be almost flat under the coherent peak in the $K_S \to \pi^0\pi^0$ sample.

That we can use the charged mode P_t^2 distribution as a Green's function to predict the background in the neutral mode depends the fact that the K_S which decayed to neutral and charged final states were produced in the same regenerator, and that their P_t^2 distributions were therefore the same. The observed P_t^2 distribution also depended on P_t^2 dependent variations in the geometric detection efficiency and on vetoing of inelastic events by the RA and VA; however, calculation of the former was straight-forward, and given the same cuts, the vetoing efficiencies were assured to be the same for the two data sets since they were collected simultaneously.

To take advantage, then, of the P_t^2 distribution observed in the charged data we had first to correct for variations in detection efficiency as a function of P_t^2. Using the Monte Carlo of the experiment described in de-
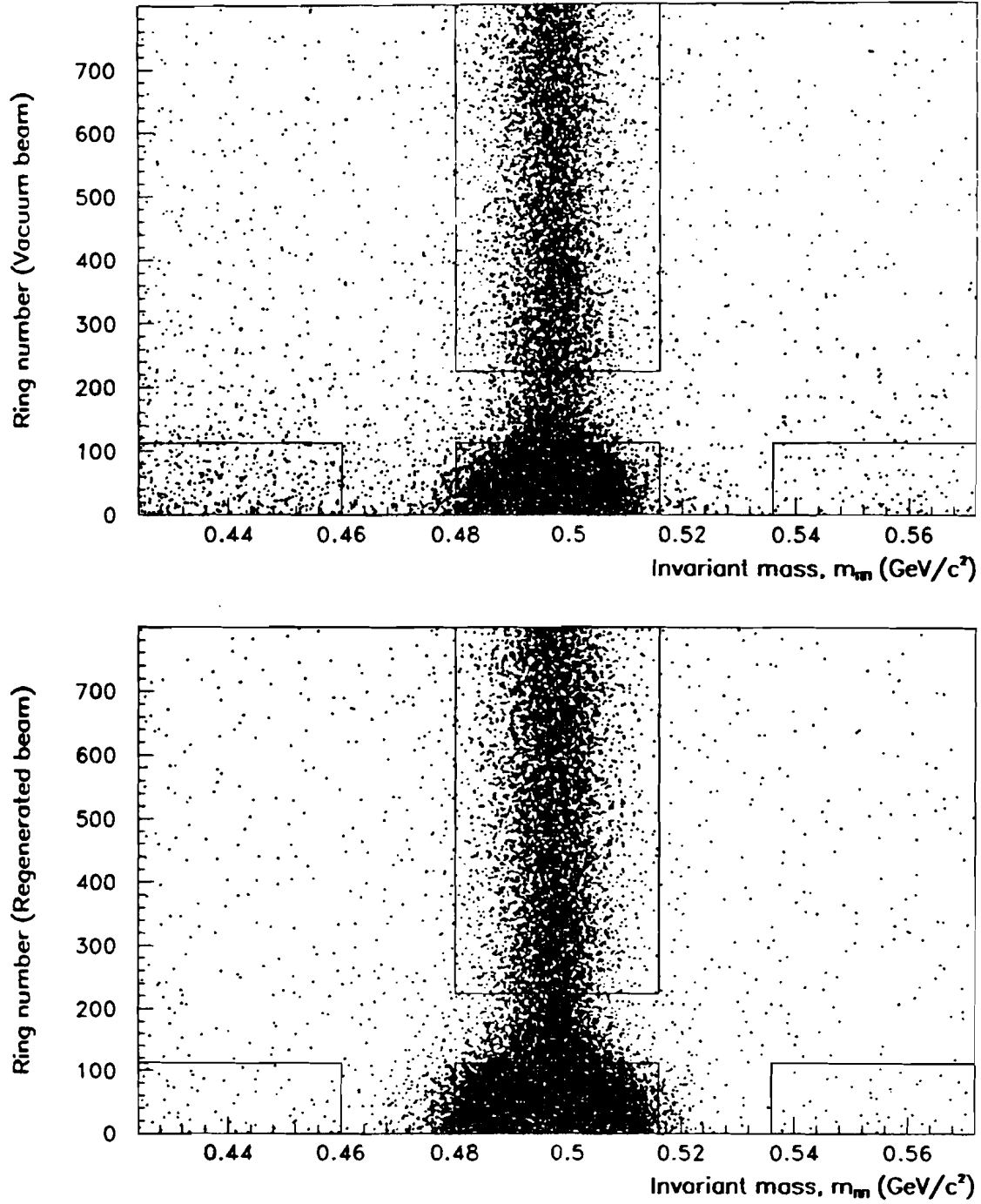
Figure 84. The center of energy ring number versus the $\pi^0\pi^0$ invariant mass. The bounded regions on the sides and at the top are used for normalization of the $\pi^0\pi^0\pi^0$ and non-coherent backgrounds respectively.

tail in Chapter 8, we found that the reconstruction efficiency as a function of P_t^2 was accurately described in each 10 GeV/c kaon momentum bin by a shallow double exponential. After correcting for this, the P_t^2 distribution of the charged decays was the same within statistical errors in all momentum bins, and could be parametrized as

$$\frac{dN}{dP_t^2} dP_t^2 = 3431 e^{-5.2 P_t^2} + 1875 e^{-222.8 P_t^2} \qquad (7.6)$$

as shown in Figure 87. The ratio of non-coherently to coherently scattered K_S in the range $0 < P_t^2 < 1 \; (GeV/c)^2$ was 39.5%.

To predict the size and shape of the non-coherent background in the neutral mode, kaons were generated in the Monte Carlo (see Chapter 8) with the P_t^2 distribution of Equation (7.6), the detector response was simulated, and the events were analyzed with the standard reconstruction program. The resulting center of energy distribution is superimposed on the
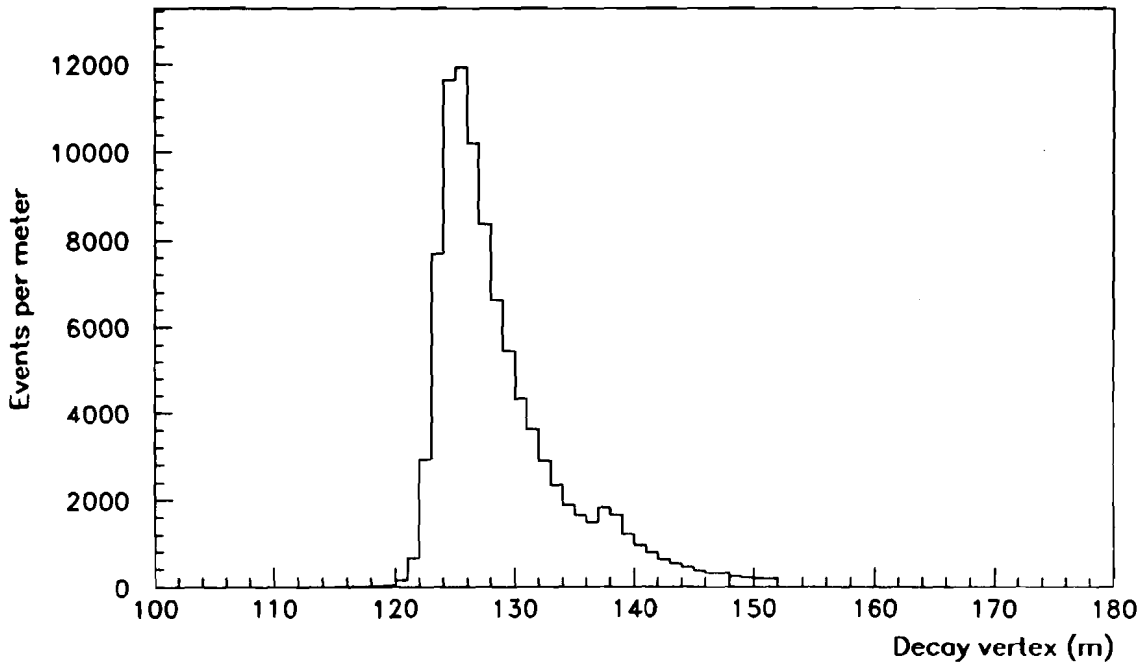
Figure 85. The z distribution of events with center of energy outside the beams.
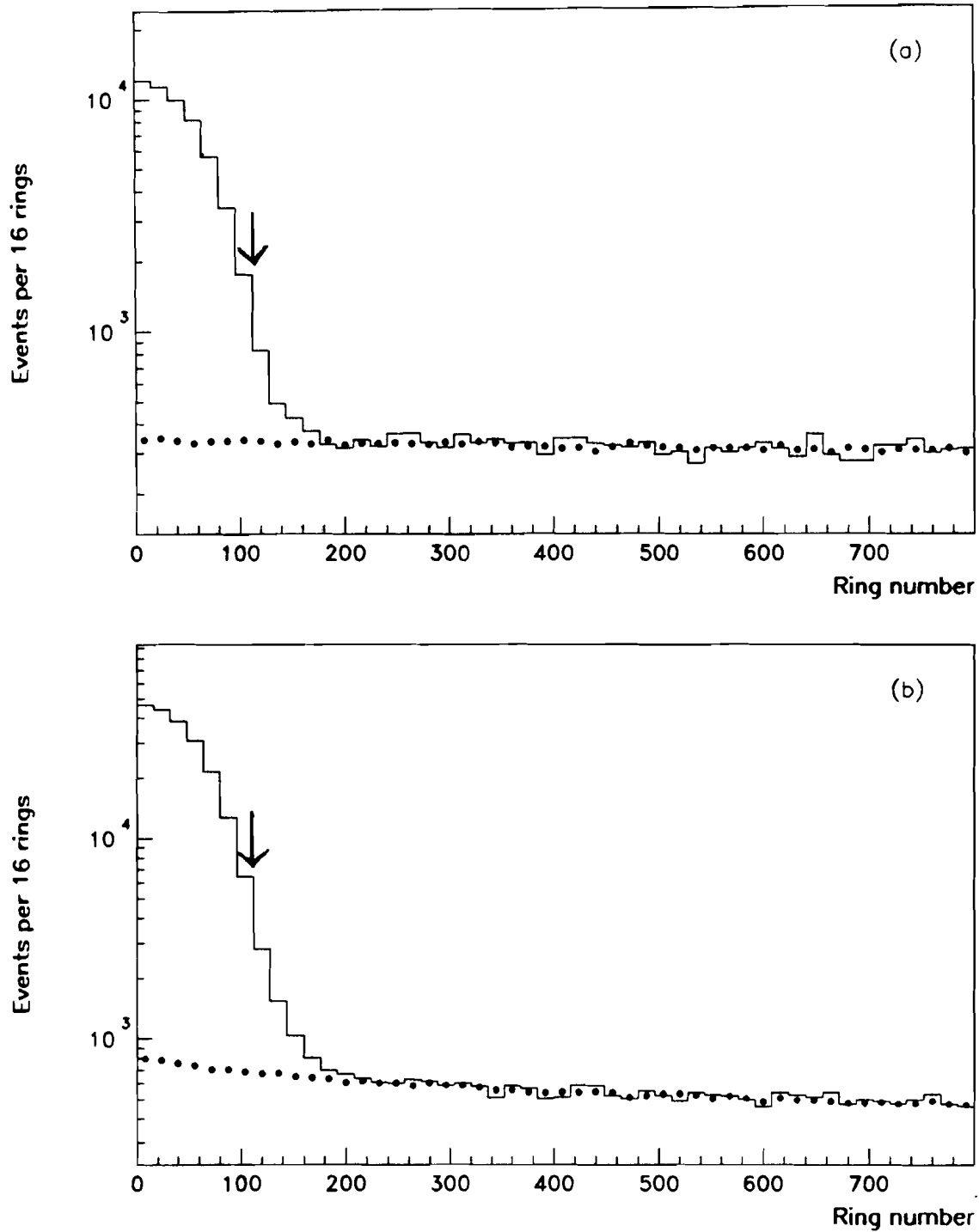
Figure 86. The distribution of events in rings centered on (a) the vacuum and (b) the regenerated beam. The arrows indicate the position of the center of energy cut.
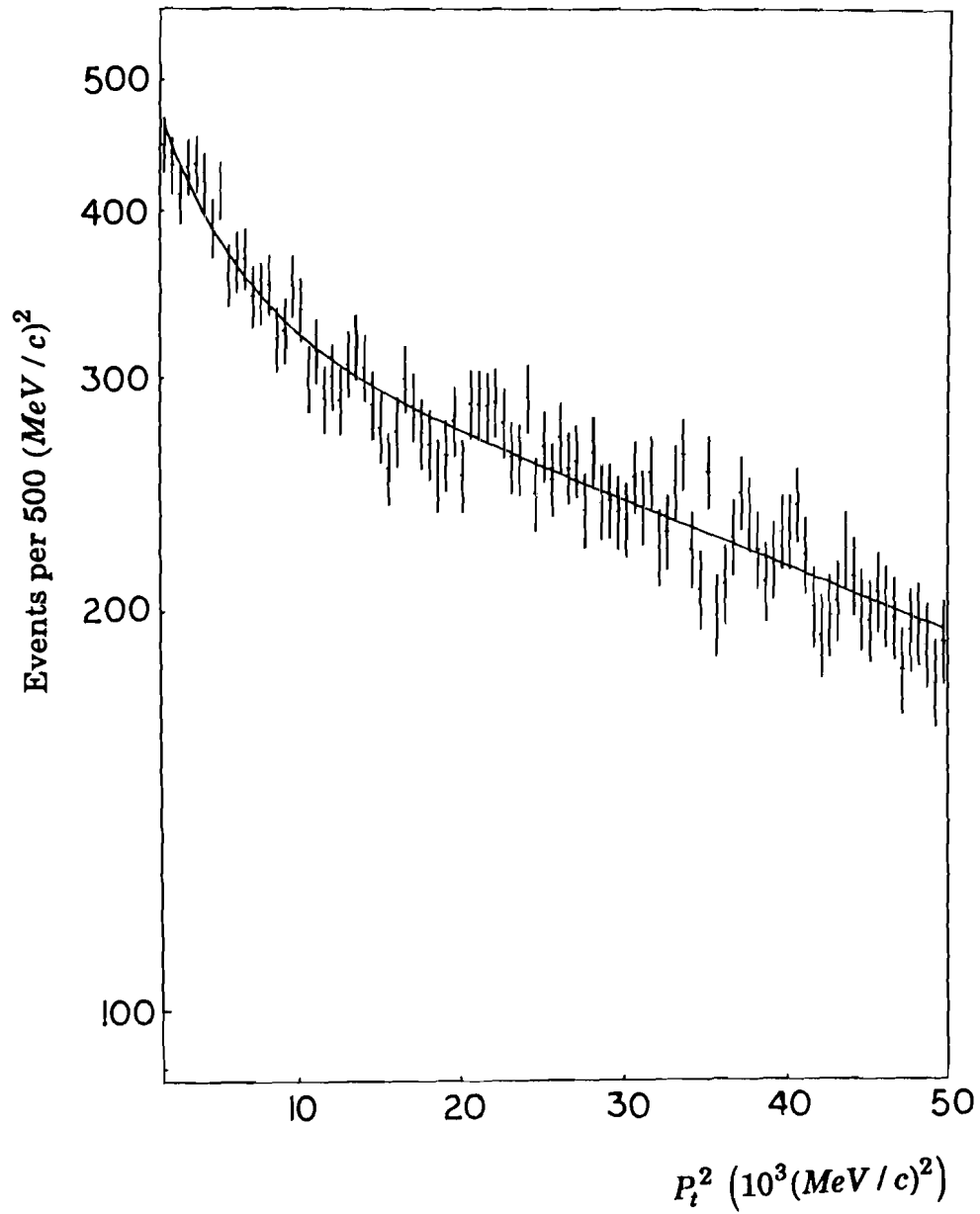
Figure 87. The P_t^2 distribution of the charged decays after acceptance corrections. The line is the fit given in Equation (7.6).

TABLE 11. The backgrounds to the neutral decays and their uncertainties.

Background source	Background level Upper beam (%)	Background level Lower beam (%)
Vacuum Decays:		
$K_L \rightarrow \pi^0\pi^0\pi^0$ & non-kaon	0.36 ± 0.07	0.38 ± 0.07
Non-coherent $K_S \rightarrow \pi^0\pi^0$	4.11 ± 0.12	5.24 ± 0.15
Regenerated Decays:		
Non-coherent $K_S \rightarrow \pi^0\pi^0$	2.66 ± 0.07	2.56 ± 0.07

data in Figure 86. The relative normalization of Monte Carlo to the data is absolute, calculated from the 39.5% non-coherent scattering probability observed in the charged decays. The shape of the distributions is quite flat for both the K_L and K_S beams as anticipated, so the background level is very close to that found by a simple extrapolation under the peak.

The absolute background levels to the K_L data differed for the samples in the upper and lower beams. This arose from the difference in intensity of the two beams: when the regenerator was in the more intense (by 8%) upper beam, the rate of crossover into the vacuum beam increased, and conversely, when the regenerator was down, the flux of scattered K_S was less. We therefore subtracted the backgrounds separately for decays in the upper and lower beams. For each sample, this was done by normalizing the Monte Carlo distribution in ring number to the data between rings 240 and 800, and counting the number of Monte Carlo events in the signal region (ring<112). The results are shown in Table 11.

Uncertainties in the backgrounds were evaluated by varying the subtraction technique. Possible variations in the slope of the exponential fit to the non-coherent tail corresponded to an uncertainty of 0.14% on the vacuum and 0.07% on the regenerated signal. Comparable or smaller variations in the backgrounds were seen when the non-coherent tail region was varied from rings 240 to 800 to rings 320 to 800 or rings 240 to 700, and when the cut on the coherent signal was loosened from 112 to 140.

TABLE 12. The number of $K_{L,S} \to \pi^0\pi^0$ events and the background fractions in each momentum bin.

P_K (GeV/c)	Vacuum beam			Regenerated beam	
	Events	$K_L \to \pi^0\pi^0\pi^0$ & non-kaon	Non-coherent K_S	Events	Non-coherent K_S
40 - 50	5428	0.22 %	2.34 %	18796	1.03 %
50 - 60	8839	0.21	3.32	34418	1.52
60 - 70	9462	0.22	4.64	38193	1.96
70 - 80	8294	0.23	5.19	33370	2.47
80 - 90	6599	0.42	5.78	26681	2.91
90 - 100	5032	0.53	5.41	19226	3.53
100 - 110	3391	0.69	6.33	12938	4.09
110 - 120	2300	0.67	5.33	8248	4.79
120 - 130	1482	0.93	5.50	5033	5.71
130 - 140	874	1.32	5.32	2884	6.32
140 - 150	526	1.26	6.05	1547	7.71
Total	52227	0.38 %	4.66 %	201334	2.62 %

7.7 The Final Data Sample

For the extraction of Re(ε'/ε) the data samples were divided into 10 GeV/c bins of kaon momentum between 40 and 150 GeV/c. The number of events and the background levels in each bin appear in Table 12. The final sample after background subtraction included 49,595 vacuum and 196,019 coherent K_S decays.

This completes selection of the neutral and charged data samples. The remaining ingredient required for extraction of Re(ε'/ε) is the acceptances for the four decay modes.

CHAPTER 8

ACCEPTANCE CORRECTIONS

8.1 Overview

8.1.1 The Purpose of the Acceptance Corrections

$\text{Re}(\varepsilon'/\varepsilon)$ is extracted from the ratio of the four $K_{L,S} \to \pi\pi$ decay rates, which we determine from the number of decays in our final vacuum and regenerated beam samples over fixed momentum (p) and decay vertex (z) intervals, corrected for acceptance. Determination of the acceptance is the subject of this chapter.

The acceptance in a p and z bin actually accounts for two corrections which are conveniently treated together. The first of these is for differences in detection efficiency among the four decay modes. The second correction is for is shuffling of events between p, z bins due to the finite resolution of the detector. The total change in the double ratio of decay rates due to acceptance corrections was 4.5%.

The differences in detection efficiencies for the different decay modes is largely determined by the fraction of photons or pions which are lost because they escape down the beam holes or outside the detector. If the bins were infinitesimally small in p and z, the detection efficiency would be the same for vacuum and regenerated decays to a common final state; however, while each p bin was only 10 GeV/c, because of other considerations discussed shortly, the data were grouped into a single z bin stretching from 120 to 137 m. Over the z bin, the vacuum and regenerated decay distributions differed markedly due to the factor of 600 difference in their lifetimes

(see, for example, Figure 32). The size of the correction was limited, however, because the detection efficiency was nearly uniform as a function of z (see Figure 32 and Figure 80). In addition, the mean decay vertex positions of vacuum and regenerated decays differed by only 1.3 m in the charged mode, and 1.4 m in the neutral, so that we were relatively insensitive to changes in acceptance that were linear in z. To first order at least, knowledge of the acceptance variation within 0.1% per meter determined the correction to the ratio of vacuum and regenerated decays to within 0.2%. We emphasize here that we needed to be concerned only with the relative vacuum and regenerated detection efficiencies; losses common to both, arising, for example, from uniform inefficiency in one of the counter banks, cancelled in the ratio of rates. Nevertheless, uncertainty in the acceptance was ultimately the largest source of systematic uncertainty in the experiment.

The number of events shuffled between p, z bins due to the finite detector resolution depended on the shapes of the p and z distributions at the bin boundaries and on the resolution. Resolution smearing was an issue primarily for neutral decays, because their resolution was about 10 times worse than that of charged decays in both p and z, and about 10% of the neutral events in any momentum bin shuffled over each of its boundaries. However, because the momentum distributions of the decays in the vacuum and regenerated beams were similar, as shown in Figure 88, the fractional change in the number of events in each p bin was roughly the same for decays in the two beams, and so largely cancelled in the ratio.

Resolution smearing in z was more important. With the choice of vertex cuts, about 0.6% of neutral decays in the vacuum beam smeared in or out of the z bin at each boundary, while many fewer events in the regenerated beam were affected. Had we binned the data more finely in z, the corrections due to smearing would have been large because of the very different shapes of the vacuum and regenerated beam decay distributions. This was the most important reason for using a single z bin, rather than many small ones, in spite of the cost of the bigger acceptance corrections.
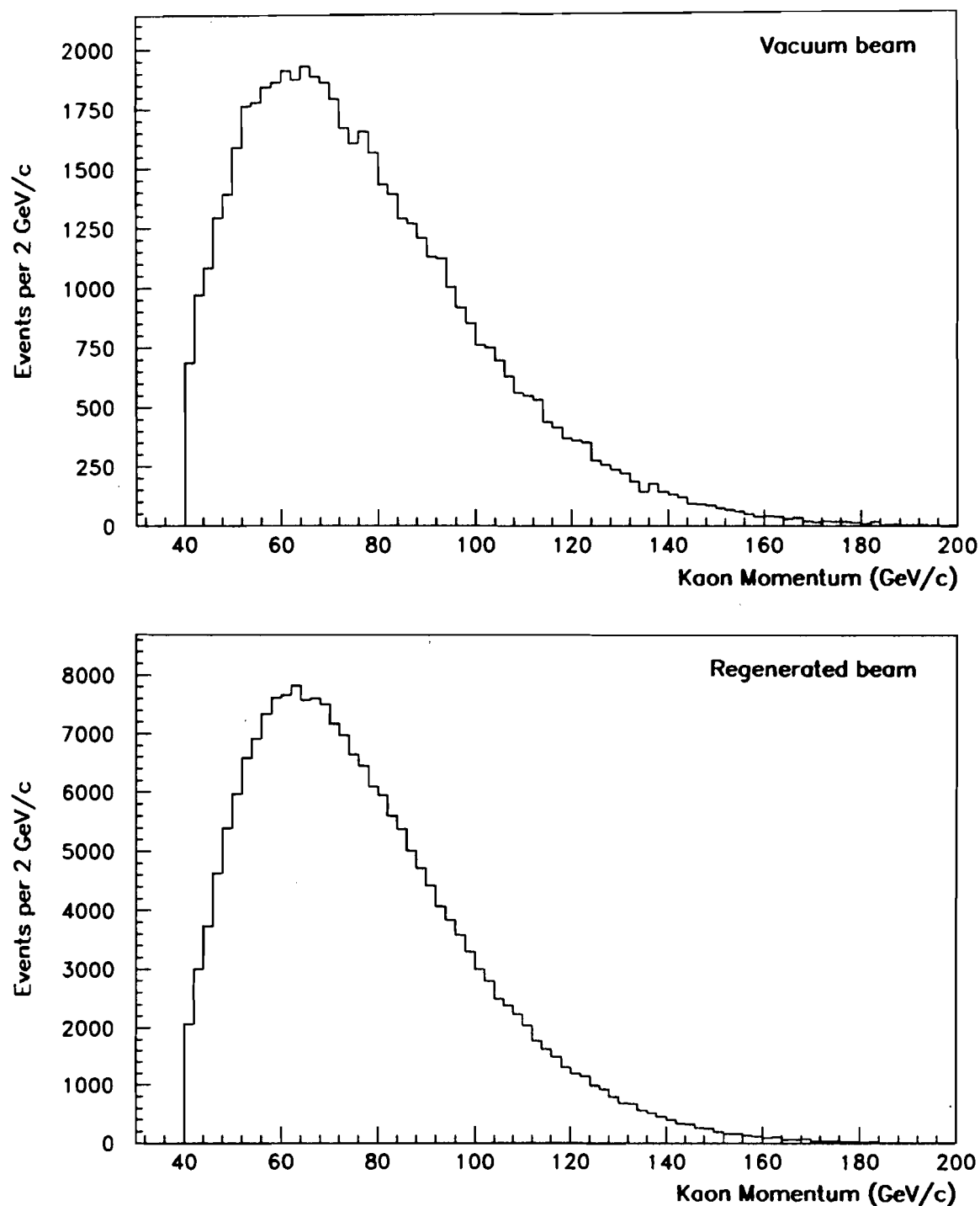
Figure 88. The momentum distributions of neutral decays in the vacuum and regenerated beams.

8.1.2 The Strategy for Calculating Acceptances

To determine our detection efficiency and the effects of smearing, we did a full Monte Carlo simulation of kaons decaying within our apparatus and of the detector's response to the decay particles. To calculate the acceptance for decays in the vacuum beam, we generated kaons in the target, allowed them to propagate through the collimators, scatter and regenerate in the beryllium and lead absorber, and then decay with the appropriate vertex distribution. After their decay products had propagated through the detector, generating signals in the various detector elements, we simulated the trigger, and if the event was accepted, it was written to magnetic tape in the same format as the data, and later analyzed using the same reconstruction programs. The ratio of the number of successfully reconstructed Monte Carlo events satisfying all cuts in each p, z bin (using the reconstructed values of p and z) to the number generated in the same bin was then the acceptance in that bin. The acceptance for decays in the regenerated beam was calculated identically, except that the simulation then included the Shadow Absorber and the regenerator. To avoid errors from possible asymmetries in the upper and lower beams, vacuum and regenerated beam acceptances were calculated separately for each.

Final uncertainty in the acceptance corrections will be evaluated in Section 9.4. It is clear from the outset, however, that the uncertainty hinged on the accuracy of the simulation, which we can assess preliminarily by comparing distributions of various observables in the data and Monte Carlo. If both production spectra and acceptances were perfect, all data and Monte Carlo distributions would be the same within statistical error. Our greatest interest is the decay vertex distribution, because that is where the largest difference between decays in the vacuum and regenerated beams lies; however, comparison of other data and Monte Carlo distributions is useful for revealing problems. For example, if the z resolution for neutral decays were simulated incorrectly, it would be clearly visible in the pairing χ^2 distribution, or if a detector aperture were wrong, it could be obvious in the illumination of pions at that plane, but barely perceptible in

the z distribution itself. Thus, many comparisons of data and Monte Carlo are shown in this chapter, not because they affect the acceptance directly, but because they help evaluate the understanding of the detector response.

In addition to the $\pi\pi$ decay modes, data (and Monte Carlo) were available for the modes $K_L \to \pi^0\pi^0\pi^0$, $K_L \to \pi^\pm e^\mp \nu$ and $K_L \to \pi^+\pi^-\pi^0$. These decays were plentiful, and so allowed high statistics comparisons. Furthermore, because the kinematics of these decays differed from the $\pi\pi$ decay modes, simultaneous agreement between data and Monte Carlo in all modes was evidence that agreement between data and Monte Carlo in the $\pi\pi$ decays was more than coincidental.

8.2 Principles of Kaon Generation and Evolution

Simulation of each event began with production of a kaon in the target, followed by evolution of its wavefunction as the kaon propagated. The latter included both propagation in the evacuated beam pipe and in the absorbers and regenerator, as well as scattering of the kaons in the material. We describe these steps in the following sections, beginning with coherent kaon evolution.

8.2.1 Kaon Evolution

Because interference and regeneration are fundamental to propagation of kaons through vacuum and material, the most natural way to handle kaon propagation is with the full kaon wavefunction. Evidence for these phenomena was visible in the data, not only in the z distribution of the decays downstream of the regenerator, but also in the vacuum beam, where the small K_S amplitude remaining in the beam from the target interfered with the K_L amplitude. We therefore chose to treat the full quantum mechanical wavefunction of the kaon in the Monte Carlo.

At any time t, the total wavefunction could be represented as the sum of K_S and K_L amplitudes, $a_S(t)$ and $a_L(t)$ respectively. Initially, because kaons were produced in the target via the strong interaction, the wavefunction was purely K^0 or $\overline{K}^0$, so that, neglecting CP violation,

$$\begin{pmatrix} a_S(0) \\ a_L(0) \end{pmatrix} = \begin{pmatrix} 1 \\ 1 \end{pmatrix} \text{ for } K^0, \text{ and } \begin{pmatrix} a_S(0) \\ a_L(0) \end{pmatrix} = \begin{pmatrix} 1 \\ -1 \end{pmatrix} \text{ for } \bar{K}^0 \text{ production.}$$

As the kaon propagated from t to t' (measured in the kaon rest frame), evolution of the amplitudes was given by a 2×2 complex matrix $\mathbf{T}$:

$$\begin{pmatrix} a_S(t') \\ a_L(t') \end{pmatrix} = \begin{pmatrix} T_{SS} & T_{SL} \\ T_{LS} & T_{LL} \end{pmatrix} \begin{pmatrix} a_S(t) \\ a_L(t) \end{pmatrix}.$$

In a vacuum, the diagonal elements of $\mathbf{T}$ were

$$T_{SS} = e^{-(im_S + \Gamma_S/2)t} \text{ and } T_{LL} = e^{-(im_L + \Gamma_L/2)t}$$

and the off-diagonal elements vanished. In a medium, $\mathbf{T}$ also included the K^0 and $\bar{K}^0$ forward scattering amplitudes and phases.

The Monte Carlo handled evolution through the evacuated beam pipes and the evolution and forward scattering in material in this way, using the appropriate geometry and scattering amplitudes of the target, upstream absorbers, and the regenerator. Thus the Monte Carlo reproduced absorption and coherent regeneration in all of these.

The decay probability at any time t, $N(t)$, for each final state was then related to the K_L and K_S amplitudes by

$$N_{\pi\pi}(t) = |a_S(t) + \eta a_L(t)|^2$$

$$N_{\pi\pi\pi}(t) = |\eta a_S(t) + a_L(t)|^2$$

$$N_{\pi^- e^+ \nu}(t) = \frac{1}{|1 + \varepsilon|} |a_S(t) + a_L(t)|^2$$

$$N_{\pi^+ e^- \nu}(t) = \frac{1}{|1 - \varepsilon|} |a_S(t) - a_L(t)|^2 \quad,$$

where η and ε are the parameters of CP violation, for which the Particle Data Group values were more than sufficiently precise. Once transformed from the kaon rest frame to the laboratory, these expressions gave the correct p and z dependence of the decay distributions. In the Monte Carlo, a

K^0 or $\overline{K}^0$was generated for each event, and the decay distribution of each mode was the incoherent sum of their contributions.

8.2.2 The Production Spectrum

We now take a step back to consider the production spectra of the kaons in the target, which had to be provided to the Monte Carlo. While the production spectra of the K^0 and $\overline{K}^0$ by protons on a fixed target have not been measured directly, those of the K^+ and K^- have, and since kaon production is dominated by the strong interaction, the results for K^+ and K^- can be related to the production of K^0 and $\overline{K}^0$ on the basis of their quark content. One finds

$$N_{K^0} = \frac{1}{2}\left(N_{K^+} + N_{K^-}\right)$$
$$N_{\overline{K}^0} = N_{K^-}$$

where the N_K are the kaon production distributions.

For the K^+ and K^- production spectra, we used results for 400 GeV protons on a beryllium target [37], parametrized by Malensek [38] as

$$\frac{d\sigma}{dpd\theta} = \sin\theta\,\frac{B}{400}\,\frac{X(1-X)^A\left(1+5e^{-DX}\right)}{\left(1+q^2/M^2\right)^4} \tag{8.1}$$

where X is the ratio of kaon to proton energies, p is the total kaon momentum in GeV/c, q is its transverse momentum, also in GeV/c, and θ is the production angle. The parameters A, B, M^2 and D are given by

	A	B	$M^2\,(GeV/c)^2$	D
K^+	2.924	14.15	1.164	19.89
K^-	6.107	12.33	1.098	12.78

In addition, an overall multiplicative factor of

$$\left(1+w_1 p + w_2 p^2 + w_3 p^3 + w_4 p^4\right)$$

with

$$w_1 = 6.033 \times 10^{-3} \ (\mathrm{GeV}/\mathrm{c})^{-1}$$

$$w_2 = -4.283 \times 10^{-6} \ (\mathrm{GeV}/\mathrm{c})^{-2}$$

$$w_3 = -1.016 \times 10^{-7} \ (\mathrm{GeV}/\mathrm{c})^{-3}$$

$$w_4 = 1.802 \times 10^{-10} \ (\mathrm{GeV}/\mathrm{c})^{-4} \ ,$$

plotted in Figure 89, was required to duplicate the spectrum observed in the data.

Utilization of the angular dependence of the spectrum yielded the correct correlations between each kaon's momentum and its position within the beams. The value of θ, and therefore q, was determined by the orientation and solid angle of the collimator with respect to the proton beam. In the x plane, θ varied by $\pm$ 370 μradians about the average of 5.3 mradians, leading to 10% momentum variation across the beam. Similar variations were present in y. In that case, a 600 μradian angle of the proton beam with respect to the collimator axis lead to a difference of 0.6 GeV/c in the mean momentum of kaons detected in the upper and lower beams.
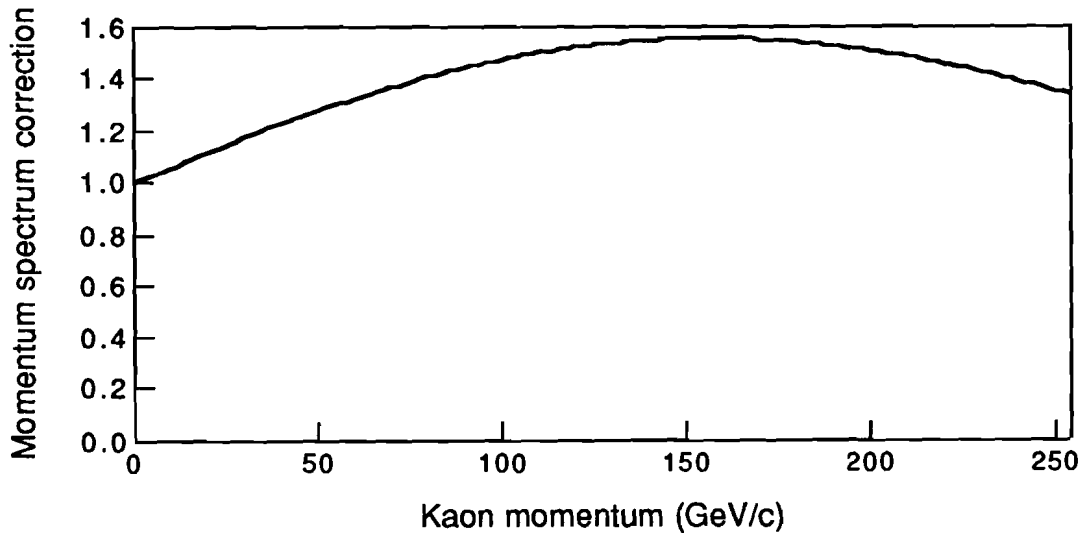
Figure 89. The correction to the Malensek spectrum required to reproduce the data.

8.2.3 Scattering of the Kaons

In addition to evolution of the K_L and K_S amplitudes through vacuum and in forward scattering, it was also necessary to treat scattering in the upstream absorber and in the regenerator.

Recall that there were two upstream absorbers in the experiment. The first of these was made of lead and beryllium and was common to both beams, while the second, composed of 18 inches of beryllium, lay in the same beam as the regenerator. About 0.1% of the $K_L \to \pi^0\pi^0$ events passing all cuts had scattered in the absorbers from the regenerated into the vacuum beam. The Monte Carlo considered only single elastic scattering in each absorber, the parameters for which were taken from Reference [39]. The probability of scattering was 17.8% and 8.6% in the lead and beryllium of the common absorber respectively, and 7.8% in the beryllium of the Shadow Absorber. The transverse momentum distribution of the scattered kaons was given by

$$\frac{d\sigma}{dt} \propto e^{-Bt} \quad ,$$

where t is the squared transverse momentum of the kaon and for the constant B we used 55 $(\text{GeV/c})^{-2}$ for beryllium and 400 $(\text{GeV/c})^{-2}$ for lead.

As discussed in Chapters 5 and 7, after cuts on the RA and VAs to eliminate inelastic interactions, inelastic or diffractive scattering occurred in the regenerator 39.5% of the time (with $P_t^2 < 1 \ (\text{GeV/c})^2$), contributing a significant background to the $\pi^0\pi^0$ signals. As described in Chapter 7, the Monte Carlo simulated both coherent and non-coherent $K_S \to \pi^0\pi^0$ decays, with the P_t^2 distribution for the non-coherently scattered kaons given in Equation (7.7). This was useful for the background subtraction, and also simplified comparison of data and Monte Carlo distributions since the non-coherent events were present in both. Non-coherent events were easily rejected from the charged mode sample and were not simulated in the Monte Carlo.

8.2.4 Procedural Overview

The overall procedure for event generation was as follows. First, a kaon was produced with an appropriate momentum aimed toward the collimator. If it successfully passed through either the upper or lower hole of the collimator, then the upstream absorber and regenerator were placed at random in the upper or lower beam. If the kaon and regenerator lay in different beams, the event was counted as a vacuum event; otherwise it was counted as a regenerated event.

Monte Carlo samples could thus be generated separately for the vacuum and regenerated beams by immediately discarding events when the regenerator was not in the desired position, or generated together by including all events. In the latter case, use of the correct values of η and the forward scattering amplitudes in the absorber and regenerator naturally lead to the correct ratio of decays in the vacuum and regenerated beams (within the few percent error of the scattering amplitudes used in the Monte Carlo). For this analysis, separate vacuum and regenerated samples were used for the charged modes, while for the neutral modes decays in the vacuum and regenerated beams were generated together for convenience in the background subtraction.

8.3 Details of the Simulation

So far we have discussed generation of the kaons themselves. The rest of the Monte Carlo simulated the decay products in the detector, including their interaction in the material and the generation of signals in the detector elements. These are treated in the following sections.

8.3.1 Passage of Particles through the Detector

Once the kaon had decayed, the Monte Carlo traced the decay products through the detector apparatus. Each time a particle passed through a counter bank, the vacuum window, drift chamber or some other material, then it could scatter, pair-produce, or emit a bremsstrahlung photon as appropriate. Secondary photons and electrons were traced through the

remainder of the detector in the same way as the primaries, fully capable of further interaction. Photon and electron trajectories terminated when they hit the lead glass or one of the photon veto counters, while charged pions terminated when they hit the muon filter or decayed in flight. Muons, which could be produced in pion decay, continued to the plane of the muon veto. No attempt was made to simulate hadron showers: pions were treated as minimum ionizing particles throughout.

8.3.2 Detector Response

The detector components included the drift chambers, the lead glass calorimeter, the scintillator banks, and the lead-lucite and lead-scintillator counters. Signal production in each of these is described in the following sections, with the exception of the lead glass, which was already treated in detail in Chapter 6. For events satisfying the trigger, the detector signals were recorded on magnetic tape in the same format as the data.

The Drift Chambers

When a charged particle passed through a chamber, at each plane the arrival time of the hit at the nearest sense wire was calculated using the distance of the particle from the wire and the known time-to-distance relationship. If a second particle passed through the same cell, then we duplicated the TDC response including its deadtime.

To account for inefficiencies in the chambers, about 1% of the hits on the outer wire planes of each chamber and 3% of the hits on the inner wire planes were discarded, using the efficiency of each determined from muon data. Hits on one of the nine missing or dead wires were also eliminated.

The Scintillation Banks

The scintillation counter signals consisted either of a single latch bit or of the integrated pulse area. For counter banks for which a latch bit was set, the efficiencies for minimum ionizing particles were taken from the muon data. The electrons produced in photon conversions in the B or C bank fired the latch only if the conversion occurred early sufficiently in the scintillator.

The Lead-Lucite Counters, the Lead-Scintillator Counters, and the Sweeper Anti

The ADC signals of the photon vetoes were simulated using their gains and resolutions. In the case of the Sweeper Anti, the beam pipe provided the high-Z material, and the amount of material the photons passed through varied with the angle of the their trajectory with respect to the beam axis. In this case the response as a function of the photon energy and angle was determined using an EGS [33] simulation of photon showers.

8.3.3 Detector Alignment

It was important to the geometric acceptance to know the exact location of each component of the apparatus, including the target and collimators and the detector elements themselves.

The z-positions of the detector elements, to which we were relatively insensitive, were known adequately, within a millimeter, from surveys. Their transverse offsets were determined using pions and electrons from $K_L \to \pi^{\pm} e^{\mp} v$ decays, with a typical accuracy of 0.3 mm. For counters important to the trigger, the T, V, B and C banks, offsets were determined not only for the counter banks as a whole, but also for the individual scintillator staves: the effects of the occasional narrow gaps or overlaps among them were thus accounted for.

8.4 Comparisons of Data and Monte Carlo

The major components of the Monte Carlo have now been described, so we can check the results by comparing a variety of data and Monte Carlo distributions. We begin with the charged decays $K_{L,S} \to \pi^+ \pi^-$, and for higher statistics comparisons, $K_L \to \pi^{\pm} e^{\mp} v$. Following these will be the neutral decays $K_{L,S} \to \pi^0 \pi^0$ and $K_L \to \pi^0 \pi^0 \pi^0$.

The number of Monte Carlo events generated ensured that the statistical error of the Monte Carlo would be small compared to that of the data. In the charged mode, the ratio of Monte Carlo to data sample sizes was 12.2 for decays in the vacuum beam and 5.4 for decays in the regenerated beam.

In the neutral mode, where vacuum and regenerated Monte Carlo samples were generated simultaneously, the ratio was 7.2 for both. In the plots shown in this chapter, the vertical axis represents the number of events in the data, while the Monte Carlo samples have been scaled to have the same total area as the data. Below many of the overlaid plots is a window displaying the ratio of Monte Carlo to data events in each bin. If the Monte Carlo were perfect, this ratio would always be equal to unity within the errors shown, which represent the combined statistical uncertainties of the data and Monte Carlo.

8.4.1 The Charged Decays

The overall acceptance of the charged mode decays was 50.4% for decays in the vacuum beam and 50.6% for decays in the regenerated beam. Most of the events that were lost escaped down the beam holes or outside the detector volume. Thus, the acceptance was almost entirely determined by the positions of the detector elements with respect to the beam. These determined the fraction of events satisfying the left-right and up-down requirements imposed on the pions in the trigger, and also the fraction of pions escaping from the fiducial volume of the detector. Detector inefficiencies and our ability to reconstruct overlapping tracks also contributed to a lesser degree. Each component will be discussed in the following sections.

The shapes of the distributions we will compare also depended on the momentum spectrum of the generated kaons; however, because of the good resolution in the charged mode, agreement of the spectra had little impact on the acceptances themselves in any p-bin. As described in Section 8.2, the momentum spectrum in the Monte Carlo was tuned so that it reproduced the momentum spectrum observed in the data, as shown in Figure 90 and Figure 91 for the vacuum and regenerated beams respectively. Confirmation (and evidence that the tuning had not obscured an acceptance error) came from the neutral data, which, because it was collected at the same time as the charged data, had necessarily resulted from same spectrum. The neutral mode distributions will be discussed in Section 8.4.2.
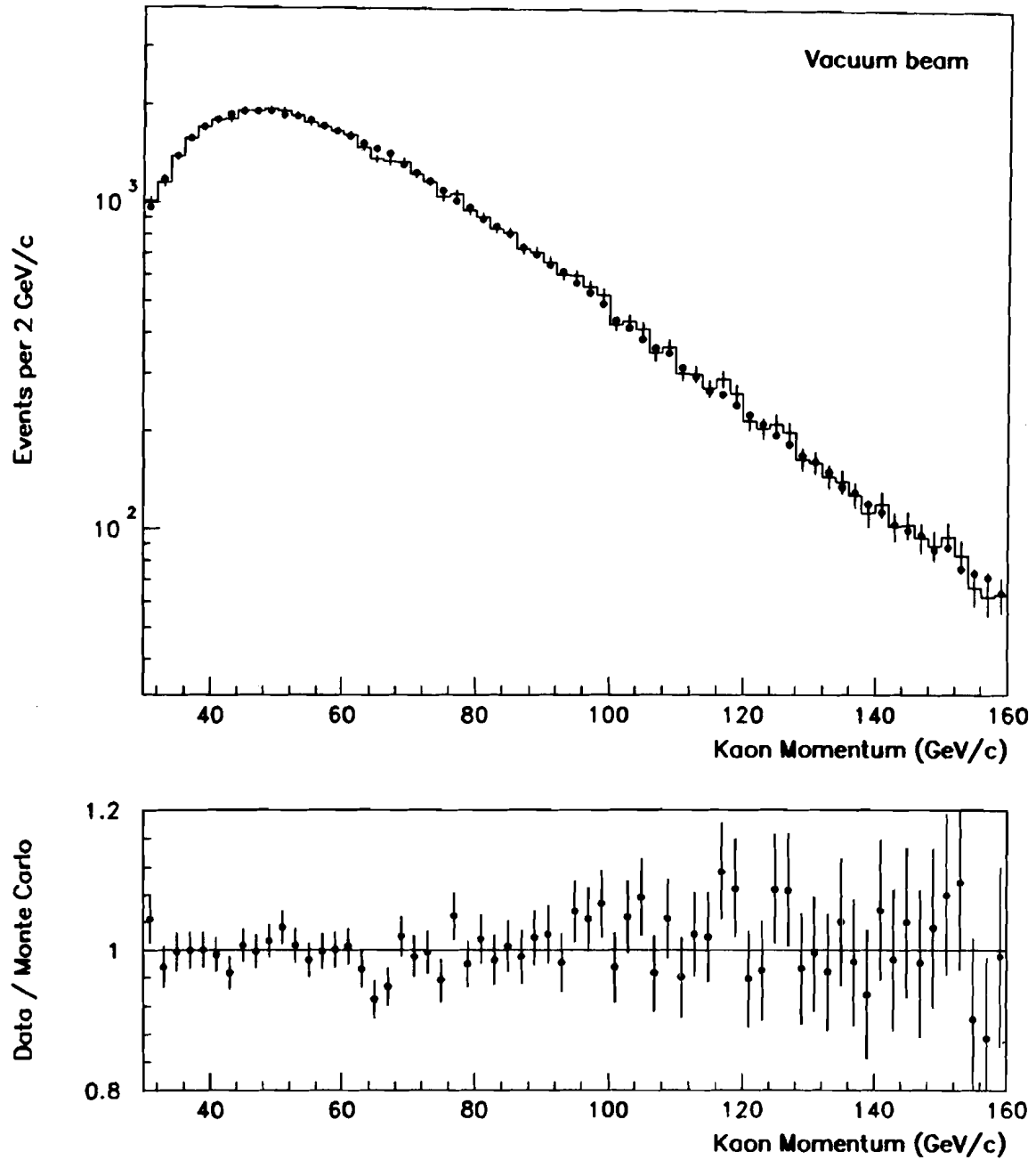
Figure 90. The kaon momentum distribution of observed $K_L \to \pi^+\pi^-$ decays. The histogram represents the data; the dots are Monte Carlo.
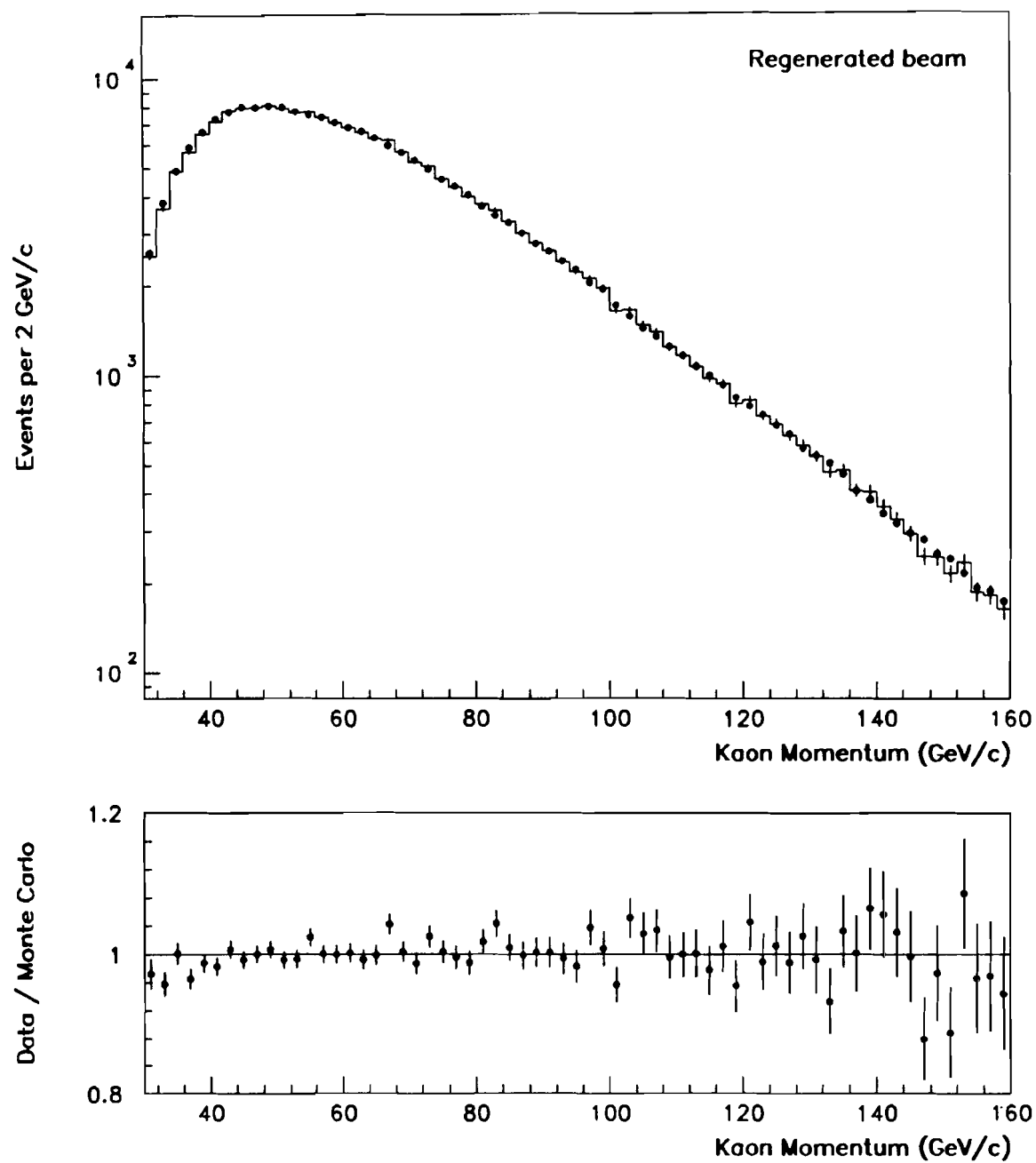
Figure 91. The kaon momentum distribution of observed $K_S \to \pi^+\pi^-$ decays. The histogram represents the data; the dots are Monte Carlo.

Detector Apertures and the Beam Shape

The effect of the beam hole and fiducial volume cuts as well as pion loss at other apertures depended on the position of each detector element with respect to the two beams. The most significant apertures were the trigger plane, the vacuum window, and the beam holes through the lead glass. As described in Section 8.3.3, the positions of all the relevant apertures were known to a fraction of a millimeter from studies with $K_L \rightarrow \pi^{\pm}e^{\mp}\nu$ decays, adequate precision for the acceptances. It remained to determine the beam position.

The beam position and shape were determined by the alignment of the target and collimation train, a schematic of which appears in Figure 2. The collimator offsets could not be measured directly with the data, so instead, we adjusted them to match the Monte Carlo beam shapes to the data. The tuned parameters were the x and y offsets and rotations of the upstream and downstream ends of the two-hole collimator, and the offsets of the adjustable and slab collimators. The result is shown for the y projection in Figure 92. The intensities of the upper and lower beams were not adjusted, leading to a difference in the relative heights of the peaks on the data and Monte Carlo, but the shapes of both beams agree well. The difference in the mean x positions of the beams in the data and Monte Carlo was also small, 0.3 mm, and their widths were the same within 0.2 mm. Although the fine structure of the beams was well simulated by the Monte Carlo, this was unnecessary for the acceptance corrections. We shall return to this point shortly.

To test the apertures, we compare the spatial distribution of pions in the Monte Carlo and the data. Figures 93 and 94 show the x projection of pion tracks extrapolated to the trigger plane, or "illumination" at the trigger plane, for decays in the regenerated and vacuum beams. At this plane, which is relatively near the kaon decay positions, the distribution is sharply peaked around the beams at the center. In the regenerated beam, about 0.002% of the pions lie within a centimeter of the counter edge, implying that a small shift in the position of the edge would lead to a completely negligible increase in the number of undetected pions. In the vacuum beam
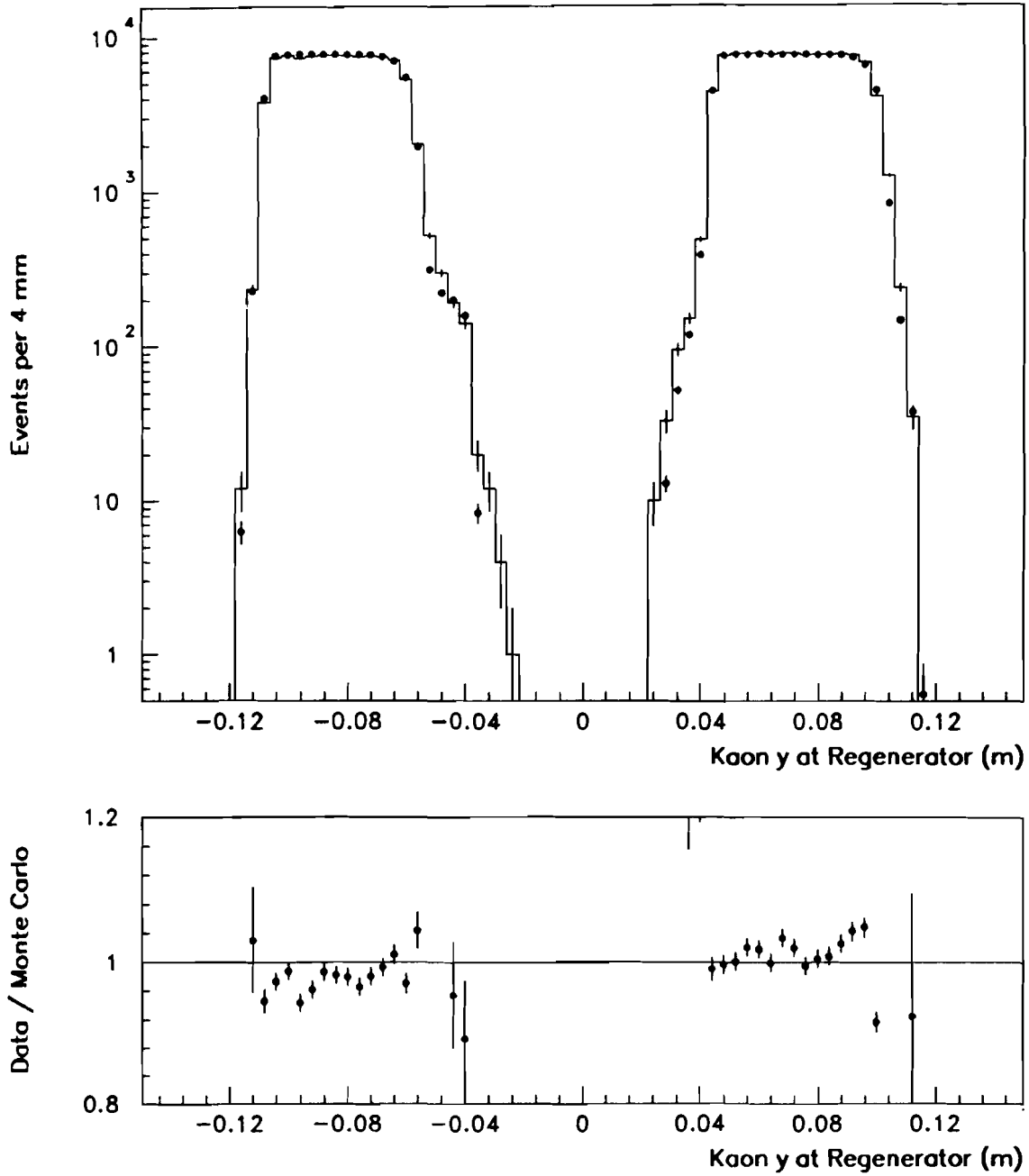
Figure 92. The y position of K_S decaying to $\pi^+\pi^-$ extrapolated to the z of the regenerator. The histogram represents the data; the dots are Monte Carlo.
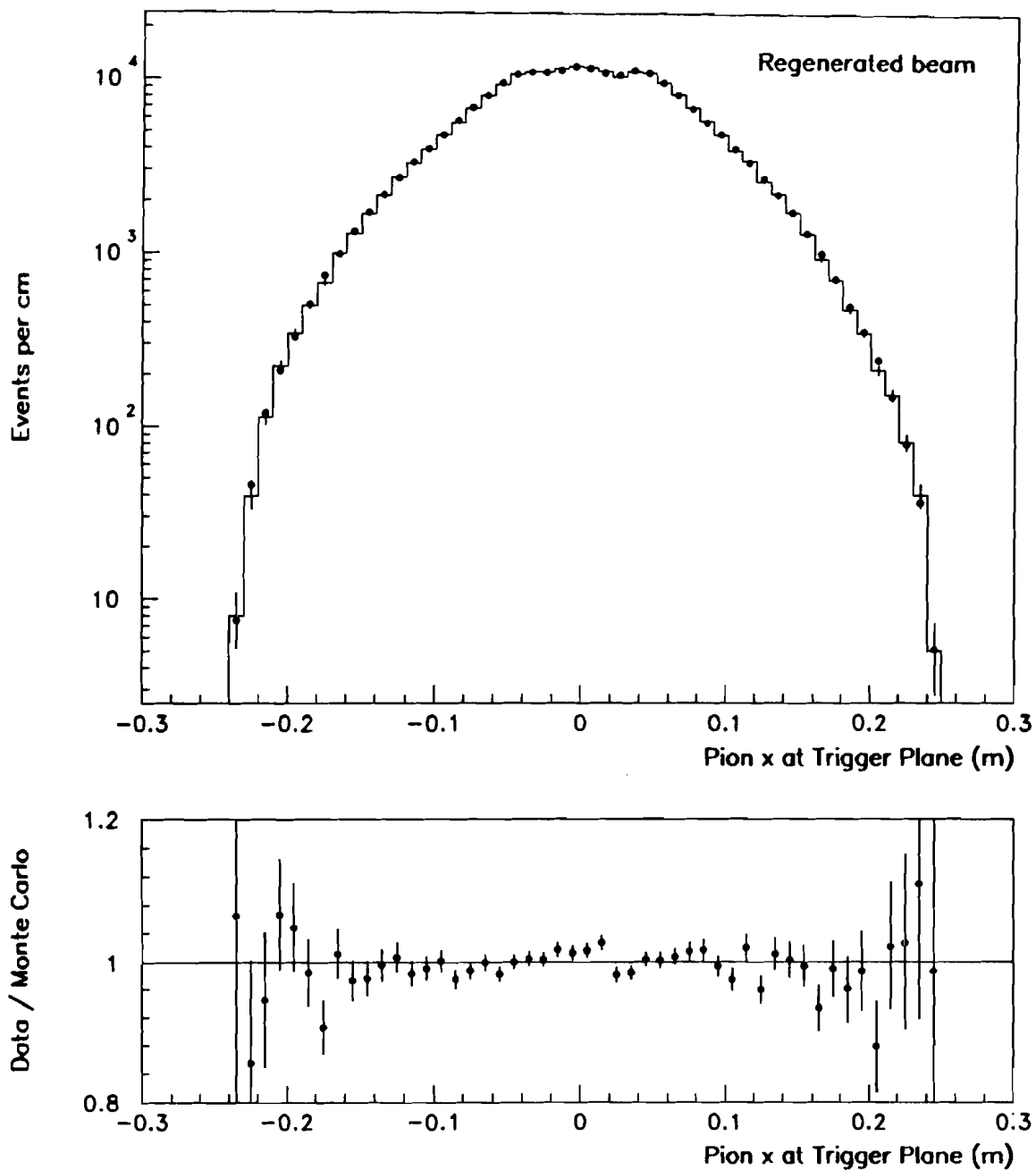
Figure 93. The spatial distribution of pion tracks at the trigger plane projected into the x plane for $\pi^+\pi^-$ decays in the regenerated beam. The histogram represents the data; the dots are Monte Carlo.
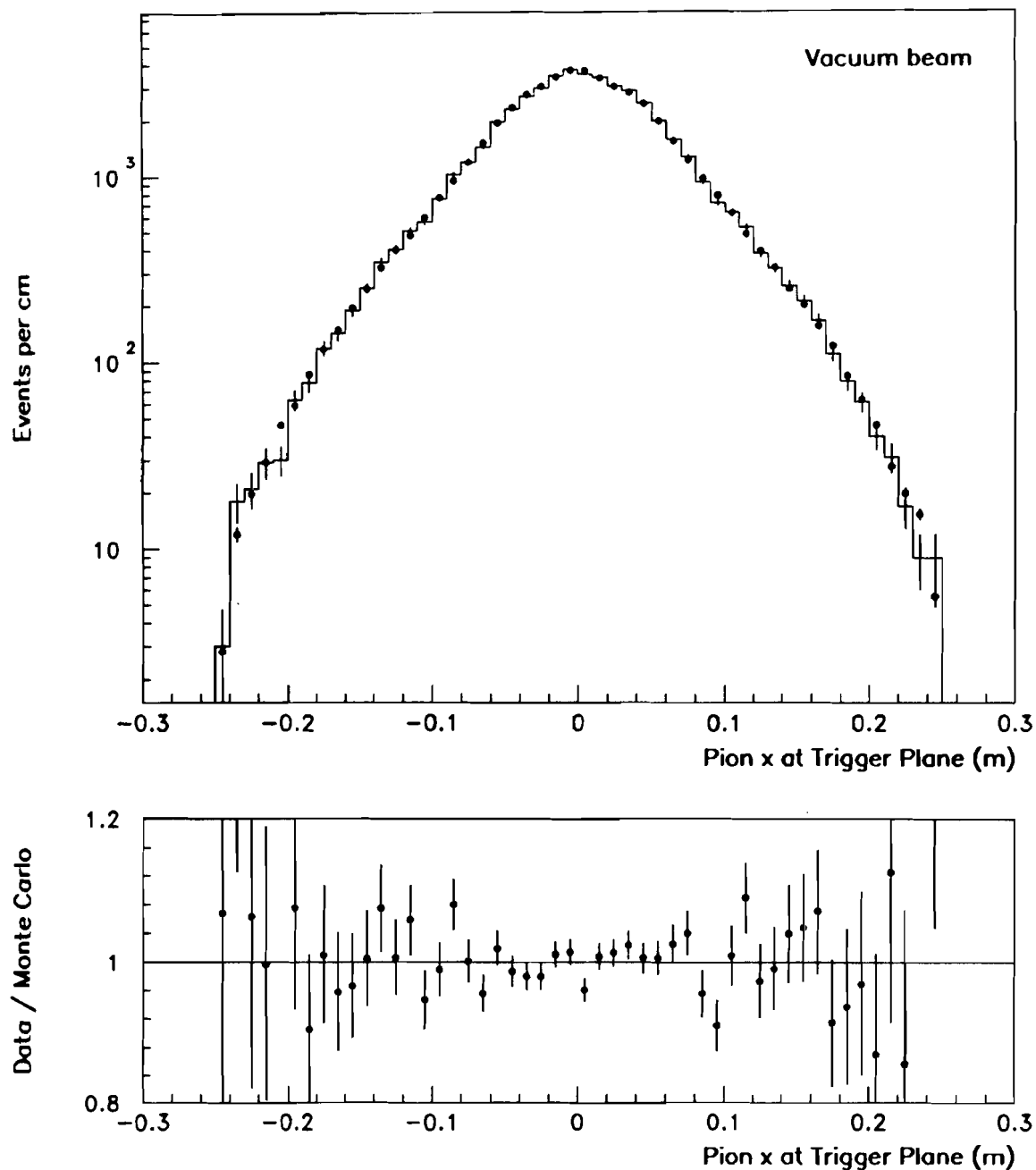
Figure 94. The spatial distribution of pion tracks at the trigger plane projected into the x plane for $\pi^+\pi^-$ decays in the vacuum beam. The histogram represents the data; the dots are Monte Carlo.

0.006% of pions lie within the same 1 cm region near the edge of the counter. The tiny difference reflects the similarity in illuminations of the vacuum and regenerated beam decays, which allows small errors in the alignment to cancel in the ratio of vacuum to regenerated acceptances.

Another major aperture is at the plane of the lead glass calorimeter, where 30% of pions are cut because they lie outside the calorimeter or point at the Collar Anti or down one of the beam holes. The y projection of pions at the lead glass is shown in Figure 95 for regenerated decays in the top beam. Overall, the illumination peaks around the beam, with small dips due to the beam hole cuts. Within errors, the effect of the beam hole cuts is the same in the data and Monte Carlo.

An anecdote will illustrate the approach toward Monte Carlo development, and give a sense of the power of the double beam technique in cancelling even rather gross errors in the beam shapes and apertures. At one stage of development, the Monte Carlo illuminations of tracks projected to Chambers 1 and 2 extended a centimeter beyond the data illuminations on the beam left edge. Investigation showed that an aluminum box supporting the helium bag between Chambers 1 and 2 was obstructing some wide angle pions. Incorporating it into the Monte Carlo resolved the discrepancy with the data, but had negligible effect on the ratio of decays in the two beams.

Detector Efficiencies

The next important contributors to the detection efficiency were variations in the efficiencies of the counter banks across their surfaces. Uniform inefficiencies could not affect the acceptance ratio because vacuum and regenerated decays were collected simultaneously, and so experienced the same inefficiencies.

Non-uniform inefficiencies were studied with muons and $K_L \to \pi^\pm e^\mp \nu$ decays, as well as with $K_{L,S} \to \pi^+\pi^-$ illuminations. The only significant inefficiencies found were in the few missing and dead drift chamber wires, one of which can be seen in the x illumination at Chamber 2 (see Figure 96), where, on the positive x side of the distribution the con-
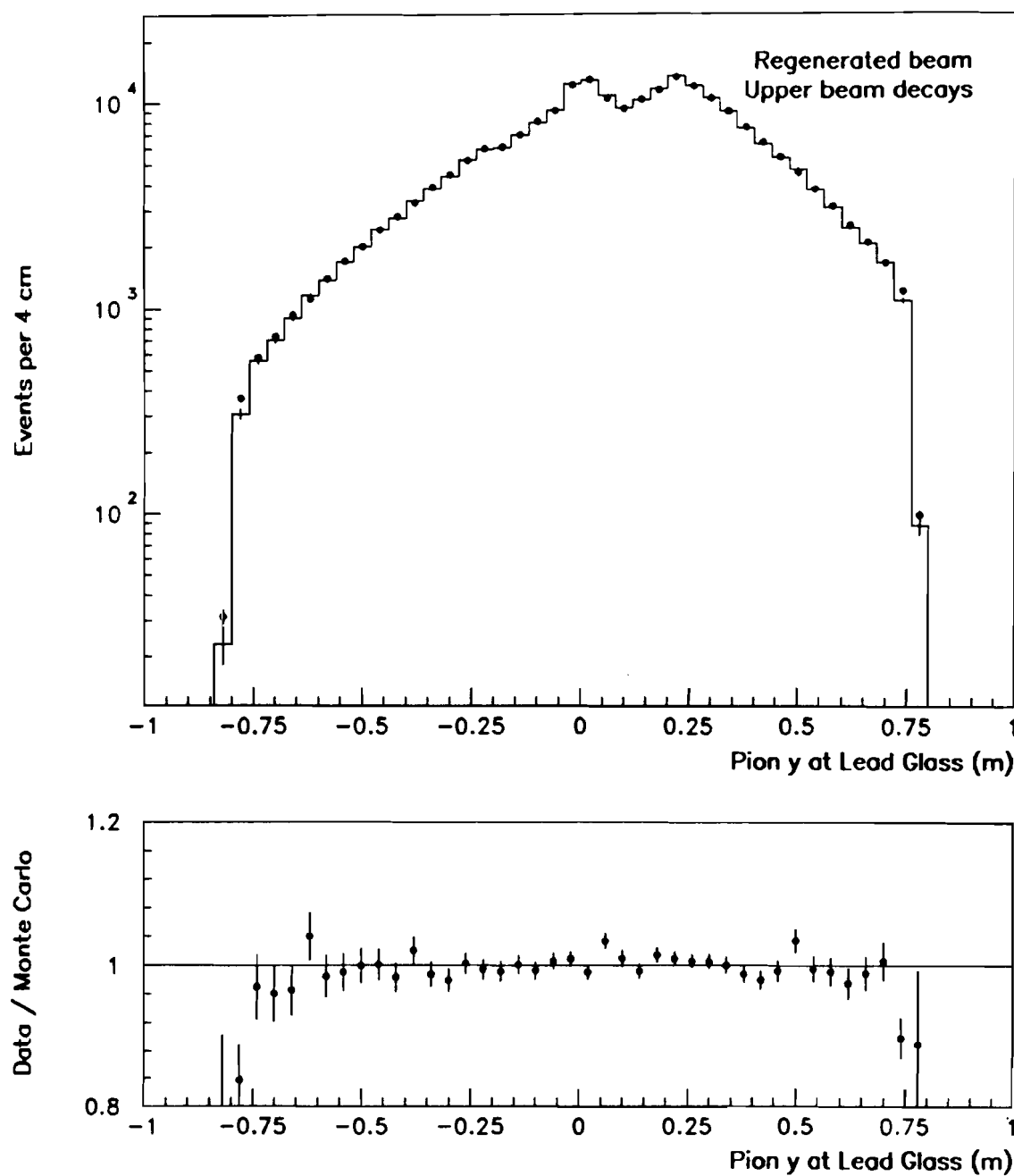
Figure 95. The spatial distribution of pion tracks at the lead glass projected into the y plane for regenerated $\pi^+\pi^-$ decays in the upper beam. The histogram represents the data; the dots are Monte Carlo.
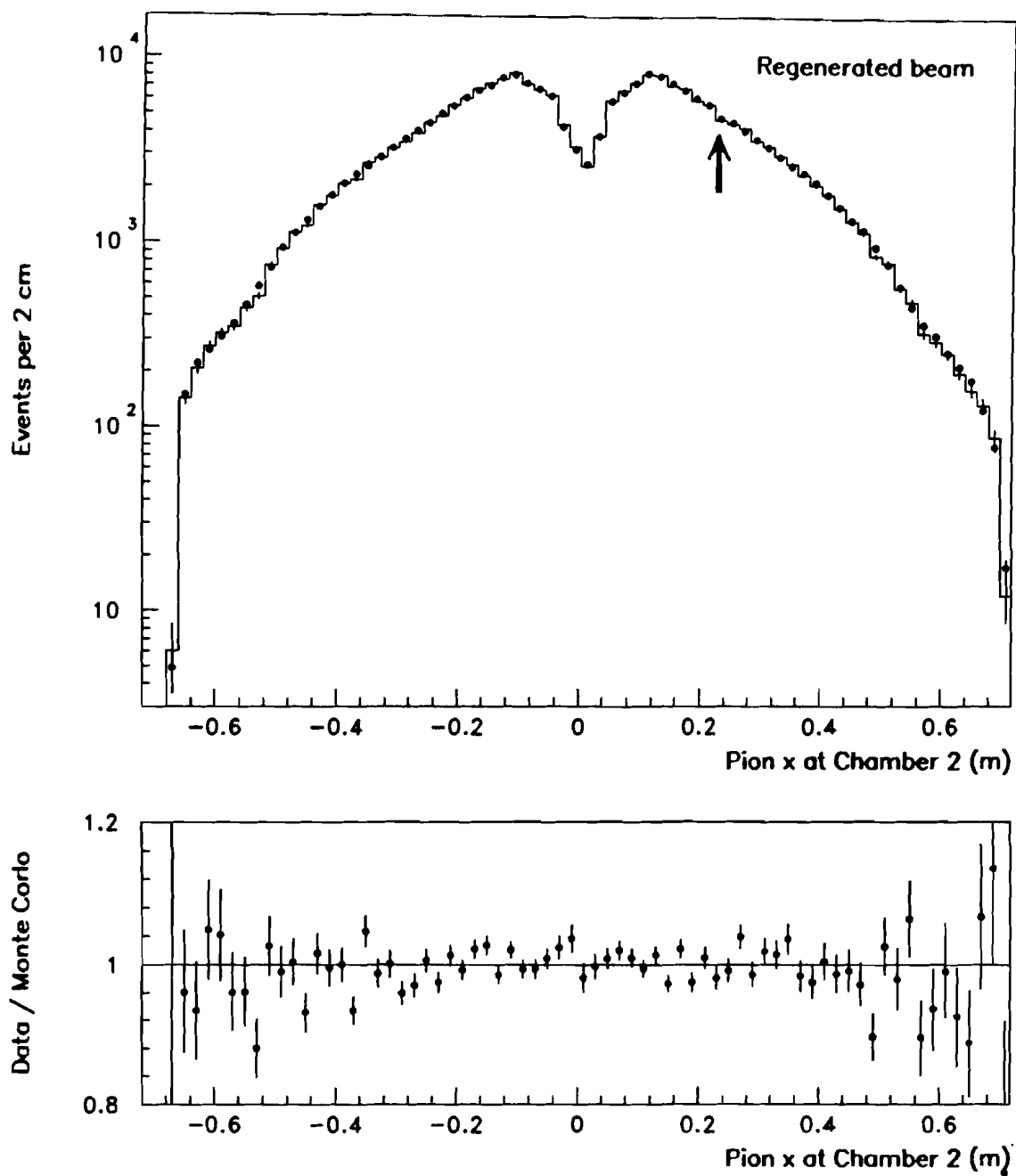
Figure 96. The spatial distribution of pion tracks at Chamber 2 projected into the x plane for $\pi^+\pi^-$ decays in the regenerated beam. The arrow indicates the position of the missing wire. The histogram represents the data; the dots are Monte Carlo.

tents of one histogram channel is abnormally low. Simulation of the missing wire in the Monte Carlo reproduced the dip.

Reconstruction of Overlapping Tracks

A few events were lost because the tracks of the two pions were so close that they could not be distinguished in the chamber system. This could have been important because the probability that the pions would lie close together was slightly higher for vacuum than regenerated beam decays as they decayed further downstream. The trigger requirement that one track lie on each side of Chamber 2 in x, however, eliminated all events with close tracks except those precisely at the center of the beam. In the y view, events with only one reconstructed track were accepted, so sensitivity to reconstruction inefficiencies was less important.

To check that the reconstruction efficiency of nearby tracks was properly handled, we compare the track separation of the data and Monte Carlo in Figure 97. In the data, tracks separated by at least 1 cm (1.6 cell widths) can be resolved. Simulation by the Monte Carlo is nearly perfect.

The Charged Decay Distribution

Of ultimate interest of the simulation of the acceptance as a function of z. Figures 98 and 99 show the overlaid data and Monte Carlo distributions for decays in the vacuum and regenerated beams. In the region of interest, data and Monte Carlo agree within the statistical error: a linear fit to the ratio of data to Monte Carlo in the region $120 < z < 137$ m in the vacuum beam has a slope of $(0.08 \pm 0.10)\%$/m. The comparison is similar in the individual p bins, as shown for example in Figure 100 for the 70 to 80 GeV/c bin, though upstream of $z = 120$ m there is excess data, suggesting an error in the simulation of the active lead mask at $z = 122$ m, which is the defining aperture for the upstream decays. For this bin the slope of the data to Monte Carlo over the fiducial region is $(-0.07 \pm 0.26)\%$/m.

Figure 101 shows the same distribution for the $K_L \to \pi^{\pm} e^{\mp} \nu$ decays, with a factor of 100 more data events than appeared in the $K_L \to \pi^+\pi^-$ sample. The data to Monte Carlo ratio has a slightly negative slope in the region $120 < z < 137$ m of less than 0.1%/m which would have been impossi-
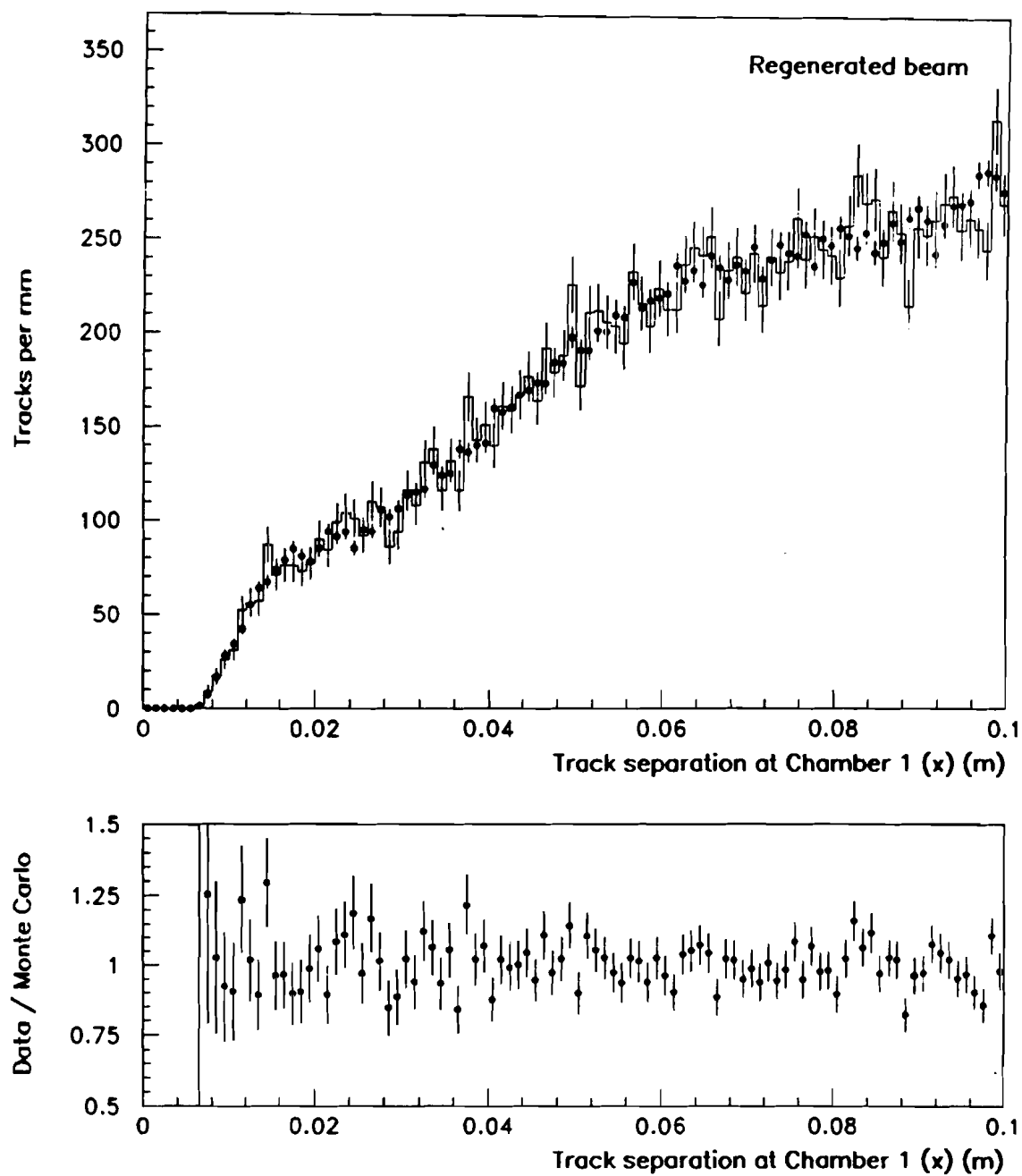
Figure 97. The x separation between hits on the two pion tracks at chamber 1. The histogram represents the data; the dots are Monte Carlo.
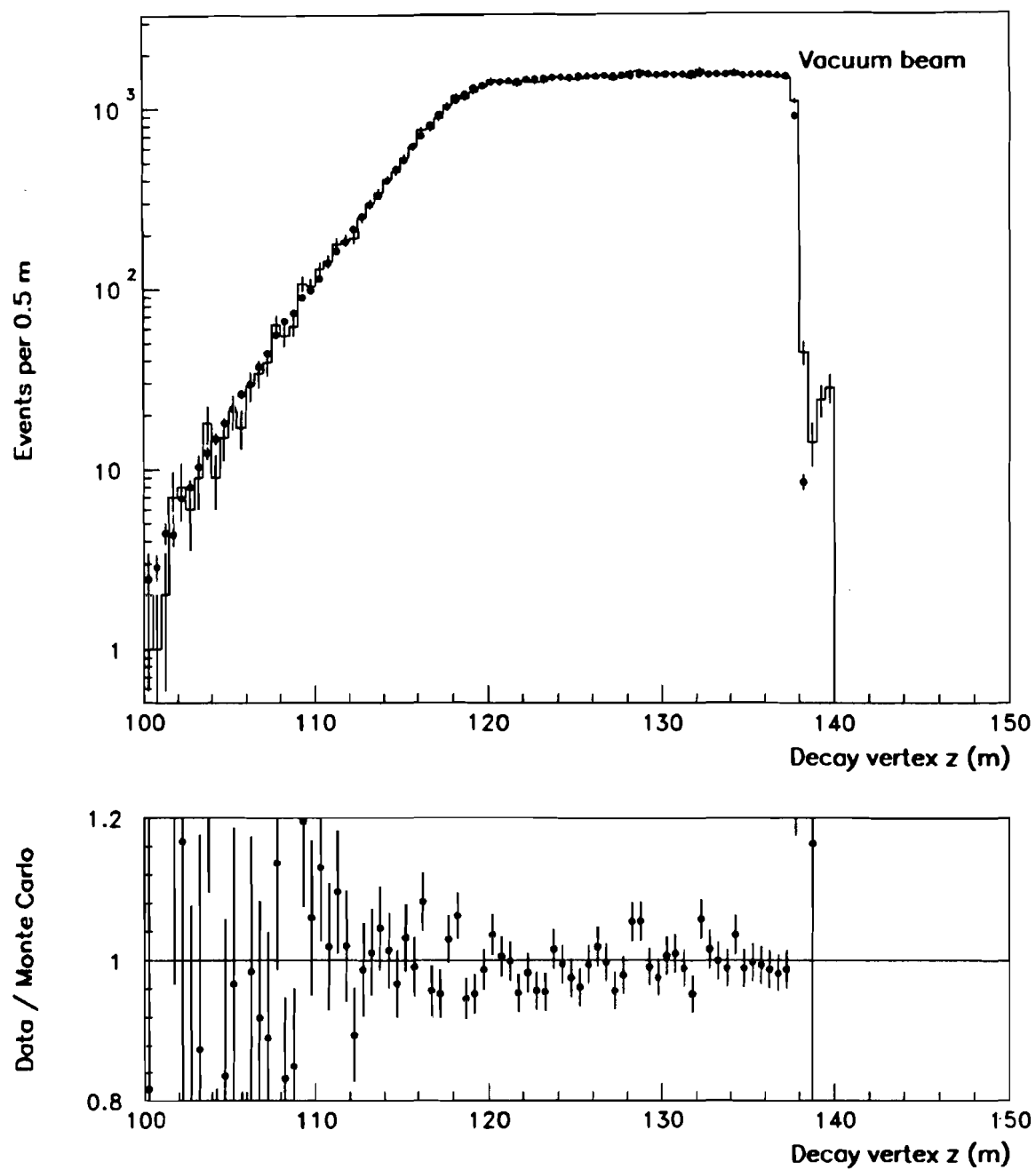
Figure 98. The decay vertex distribution of $K_L \to \pi^+\pi^-$ decays. The histogram represents the data; the dots are Monte Carlo.
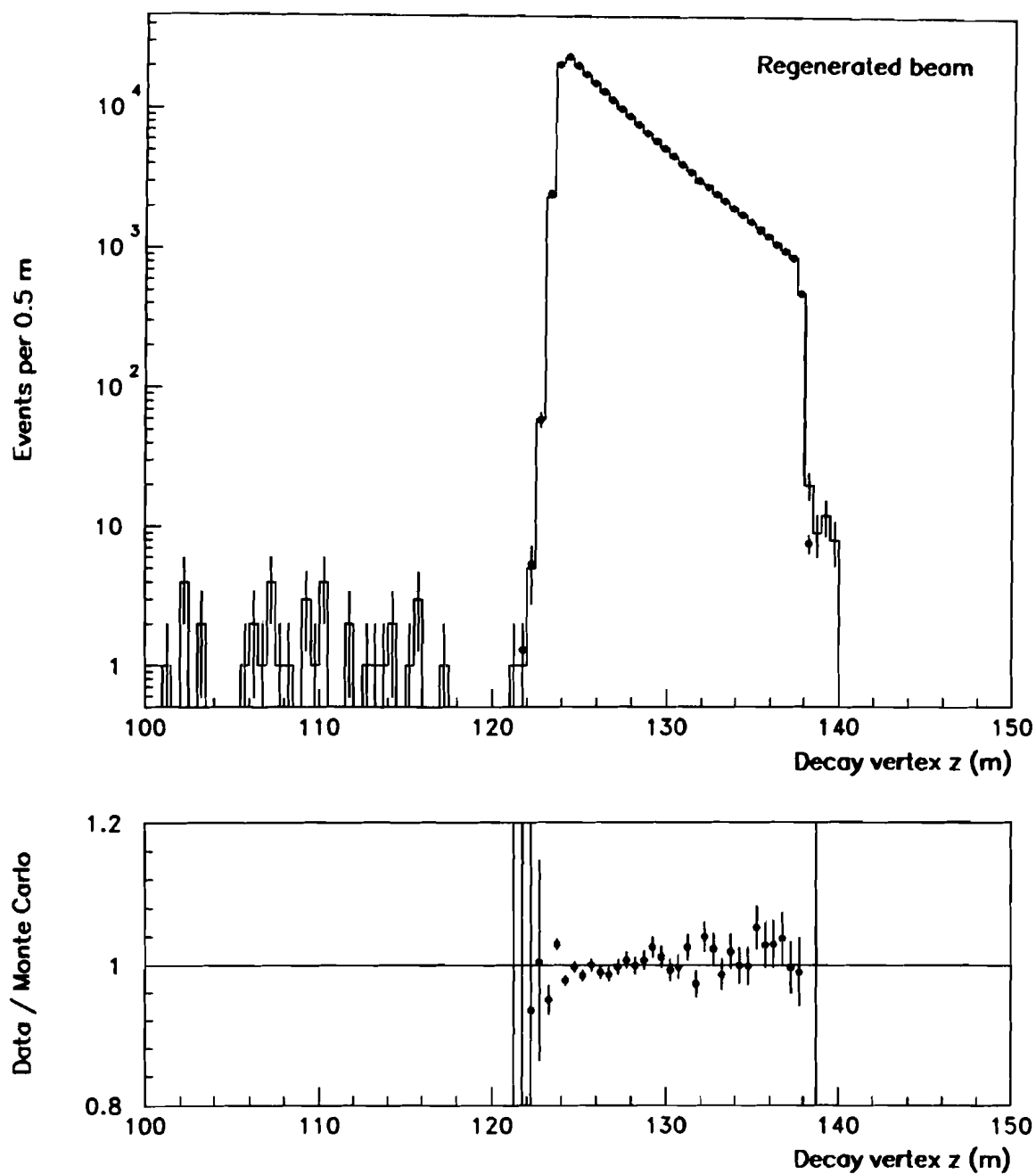
Figure 99. The decay vertex distribution of $K_S \to \pi^+\pi^-$ decays. The histogram represents the data; the dots are Monte Carlo.
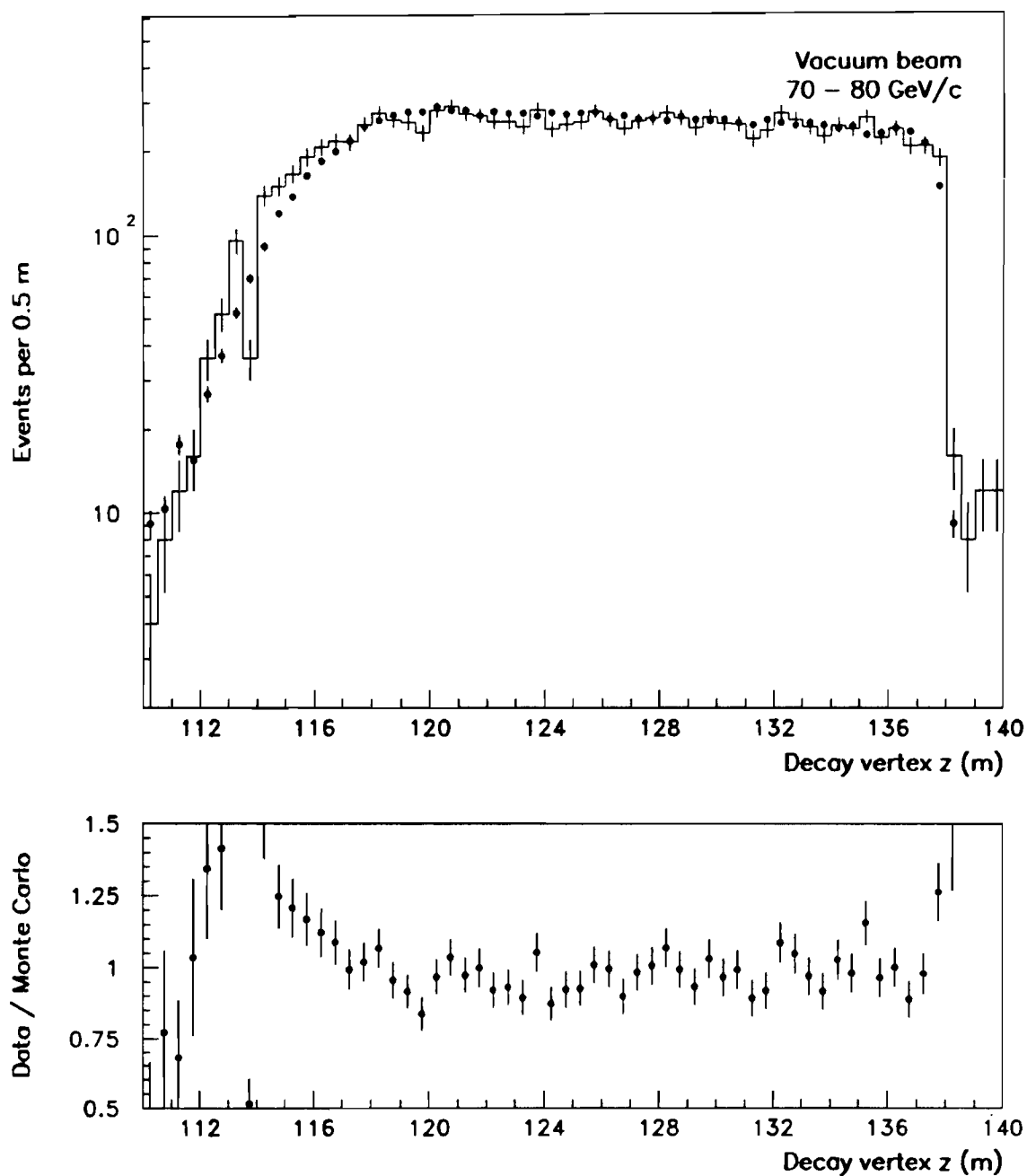
Figure 100. The decay vertex distribution of $K_L \rightarrow \pi^+\pi^-$ decays for kaon momenta between 70 and 80 GeV/c. The histogram represents the data; the dots are Monte Carlo.
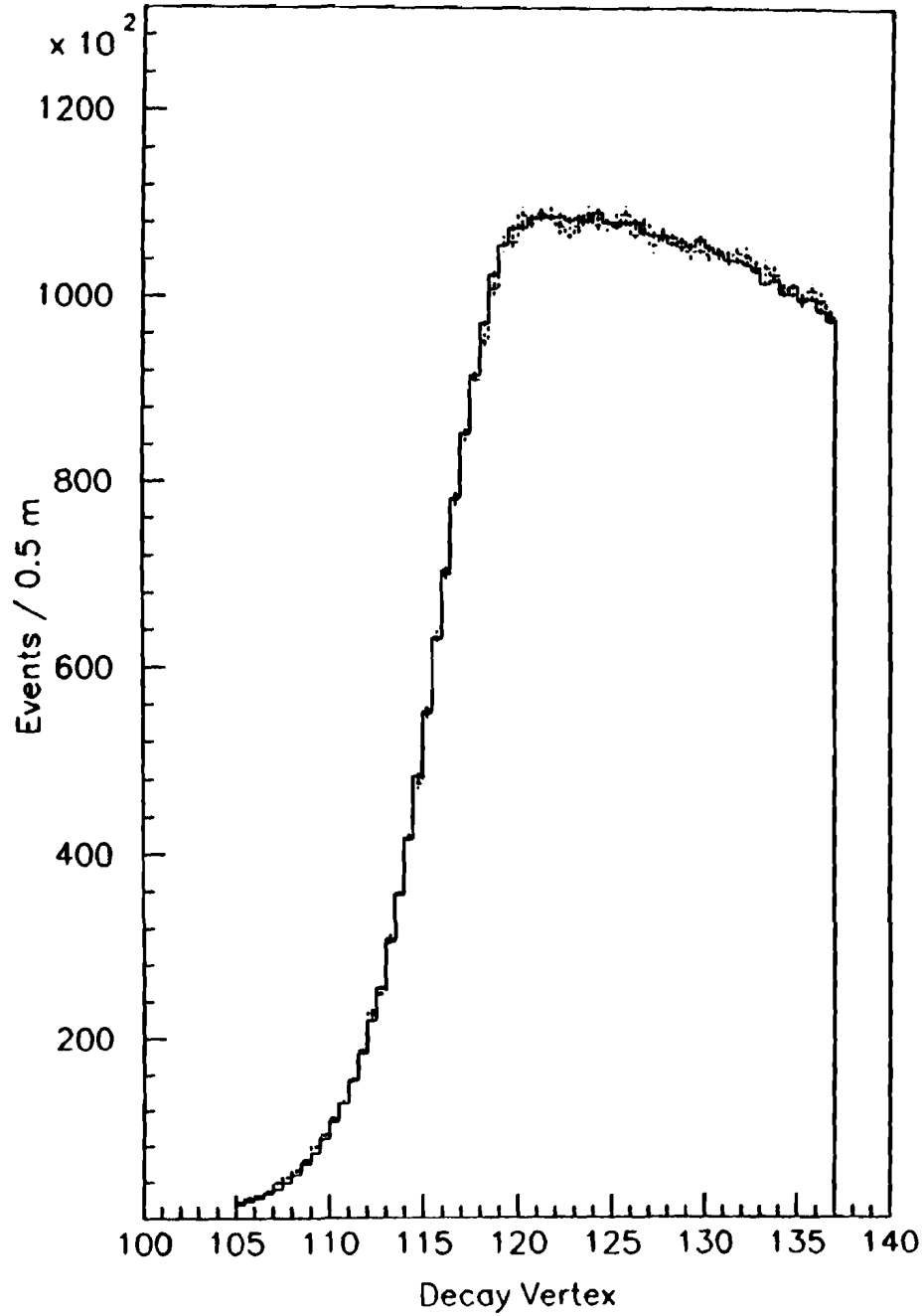
Figure 101. The decay vertex distribution of $K_L \to \pi^{\pm}e^{\mp}v$ decays. The histogram represents the data; the dashed line is the Monte Carlo.

TABLE 13. The acceptance of $K_{L,S} \to \pi^+\pi^-$ decays in each p bin.

Kaon Momentum (GeV/c)	Vacuum Beam Acceptance	Regenerated Beam Acceptance
40 – 50	0.483	0.466
50 – 60	0.569	0.564
60 – 70	0.590	0.595
70 – 80	0.564	0.571
80 – 90	0.520	0.522
90 – 100	0.477	0.480
100 – 110	0.417	0.417
110 – 120	0.378	0.378
120 – 130	0.345	0.344
130 – 140	0.308	0.308
140 – 150	0.273	0.270

ble to see with the $\pi\pi$ decays. This slope corresponds to an error in the double ratio due to acceptance of ~0.1%.

The acceptance of charged decays in the vacuum and regenerated beam is listed for each p bin in Table 13. The acceptance differs by about 0.2% for decays in the upper and lower beams, and they were corrected for separately.

8.4.2 The Neutral Decays

We turn now to the simulation of the $K_{L,S} \to \pi^0\pi^0$ decays. Geometrically, the acceptance was lower for these than for the charged decays because it was a four-body rather than a two-body final state. Overall, it was 18.8% in the vacuum and 18.1% in the regenerated beam.

By far the subtlest part of neutral mode simulation was reproduction of the response of the lead glass calorimeter. The transverse shower shapes determined whether overlapping clusters could be resolved, and therefore the number of identified four cluster events, while the energy response of the calorimeter was essential to the shape of the z distribution because it was the largest source of smearing.

The following sections discuss the geometric and calorimeter-related contributions to the acceptance.

The Geometric Acceptance of Neutral Decays

Geometrically, simulation of the neutral decays was simpler than simulation of the charged: the four photons always travelled in straight lines, and aside from occasional pair-conversion, interacted only in the lead glass calorimeter. Instead of multiple apertures, only the Collar Anti, the HDRA and the outer edge of the lead glass mattered.

Of the apertures, the Collar Anti was more important because of the high concentration of photons around the beam holes, but it was also relatively simple to simulate: its absolute position was known from $K_L \to \pi^{\pm} e^{\mp} v$ data within 0.3 mm, and its veto efficiency for the high energy photons that hit it was 99.8%.

The other important parameters affecting the fraction of events vetoed by the Collar Anti were the positions of the beams, which it cleared by only 5 mm. These were known from the charged mode studies: because they were collected simultaneously, the collimator alignment determined with the charged mode data applied to the neutral as well. The data and Monte Carlo center of energy distributions for $\pi^0 \pi^0$ decays, shown in Figure 102, check this. The means of the x projections of the upper and lower beams in the data and Monte Carlo differ by 0.6 mm and 0.4 mm respectively.

To check the effects of the Collar Anti and the outer lead glass edge, we compare the distributions of photons across the lead glass in the data and Monte Carlo, shown in Figure 103. The large dip at the center is due to the beam holes. The $\pi^0 \pi^0$ distributions agree within the statistical errors.

One other phenomenon affected the number of events lost because of photons in the beam hole region. When very energetic photons hit the lead glass in one of the blocks bordering the beam pipes, some of the shower particles leaked down the holes, and occasionally produced a signal in the Back Anti above its 5 GeV veto threshold. Simulation of the effect with EGS predicted that loss would be negligible for the 92% of photons which are
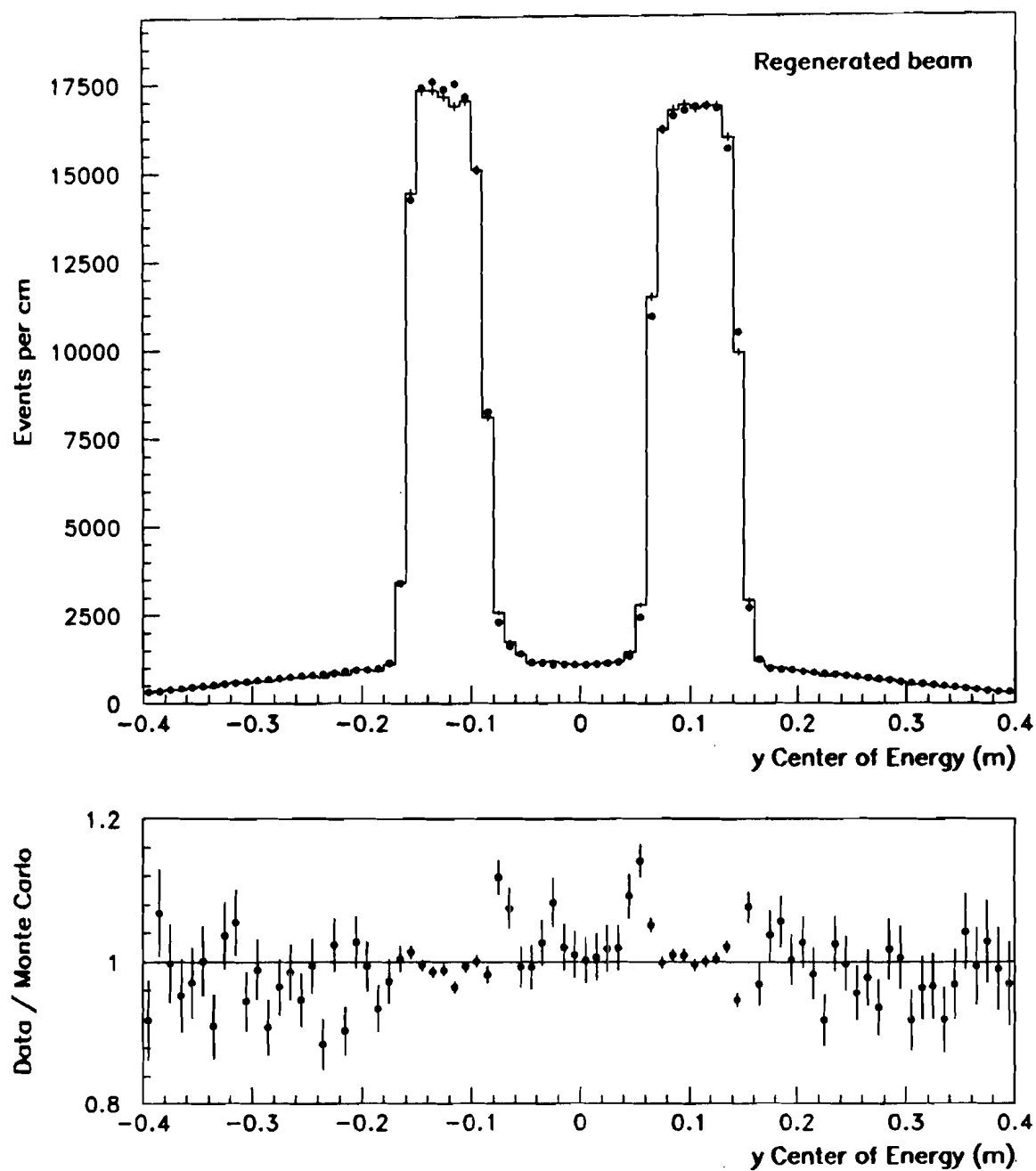
Figure 102. The center of energy distribution of $K_S \rightarrow \pi^0 \pi^0$ decays projected into the y plane. The histogram represents the data; the dots are Monte Carlo.
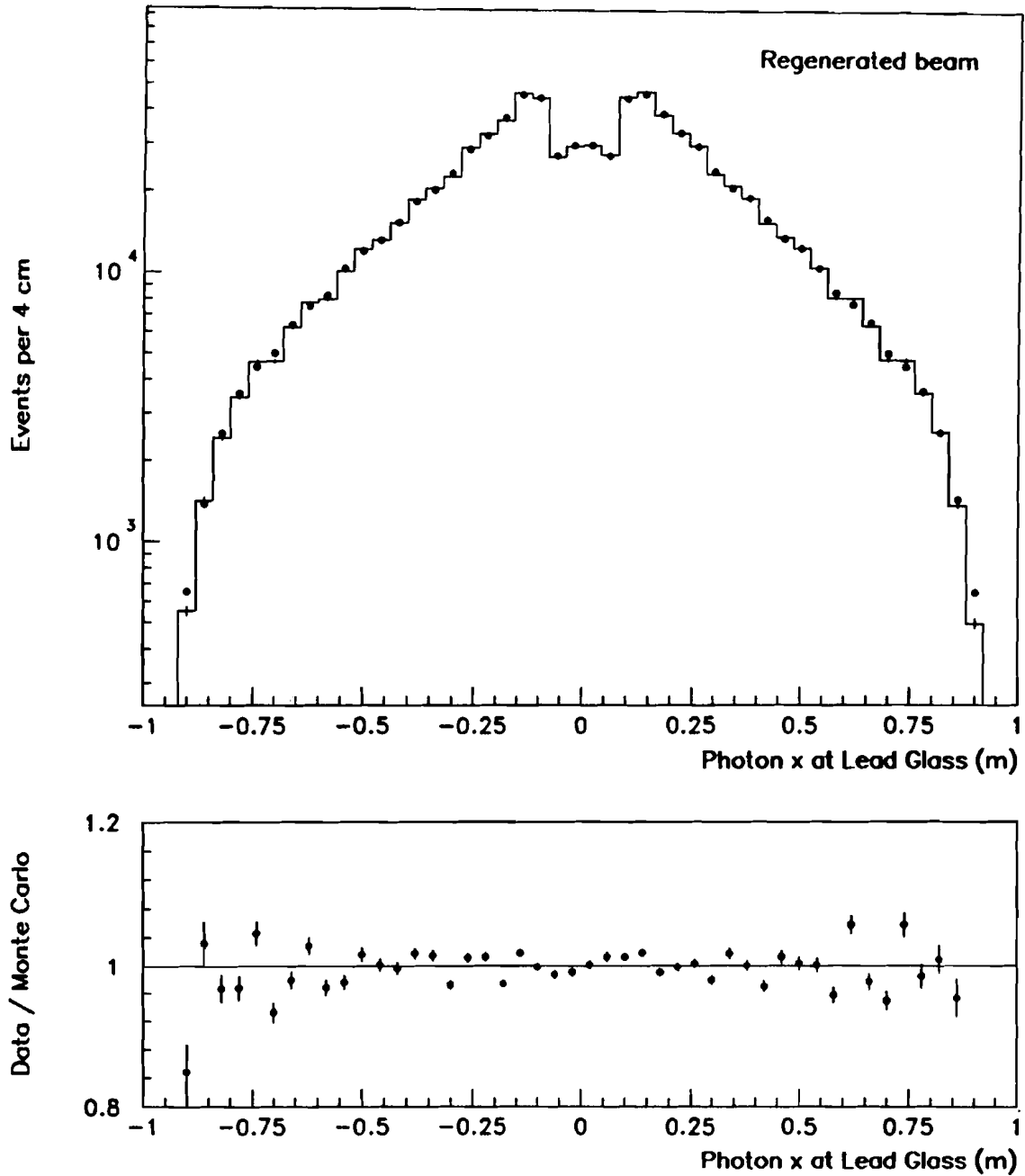
Figure 103. The spatial distribution of photons in the lead glass projected into the x plane for $\pi^0\pi^0$ decays in the regenerated beam. The histogram represents the data; the dots are Monte Carlo.

below 60 GeV, but that above 60 GeV it would increase linearly with energy to 3% at 80 GeV (99% of photons were less than 80 GeV). Thus in the Monte Carlo it was necessary to discard clusters in the blocks surrounding the beam pipes with the probability as a function of energy determined by EGS. Inclusion of the effect changed the acceptances of the vacuum and regenerated decays by 0.04% and 0.03% respectively, leaving their ratio essentially unchanged.

To study the geometric acceptance with greater statistical precision, we turn to the $K_L \to \pi^0\pi^0\pi^0$ decays, about 6 million of which passed all cuts. Their center of energy distributions, shown in Figure 104, agree quite well, though deviations at the edges are statistically significant. In the photon illuminations, shown in Figure 105, discrepancies of 10 to 20% are visible at the very edge of the glass which correspond to errors in the the $K_L \to \pi^0\pi^0\pi^0$ acceptance of roughly 0.05%.

To study the effect of the beam shape errors on the acceptance, events in the $\pi^0\pi^0\pi^0$ data were reweighted to distort their center of energy distribution by a roughly a factor of six more than the discrepancies with the Monte Carlo. Although the illuminations changed slightly, the slope of the z distribution changed by less than 0.004%/m, an utterly negligible amount.

Tests of the Cluster Shape Simulation

The remaining ingredients to the neutral mode simulation all related to the simulation of clusters in lead glass. One component of this was the distribution of the photon cluster energy among the lead glass blocks, which was essential to the acceptance of the four cluster events, primarily because it determined the frequency with which the software cluster finder resolved overlapping clusters. Because of the slight difference in the photon illuminations for decays in the vacuum and regenerated beams, the overlap frequency was slightly different for the two, so a significant error in the transverse shower simulation would lead to an error in the ratio of their acceptances.

As described in Section 6.8.1, showers were culled from the calibration electron data and EGS electromagnetic shower samples to form a library of shower shapes, binned by cluster energy and impact position with-
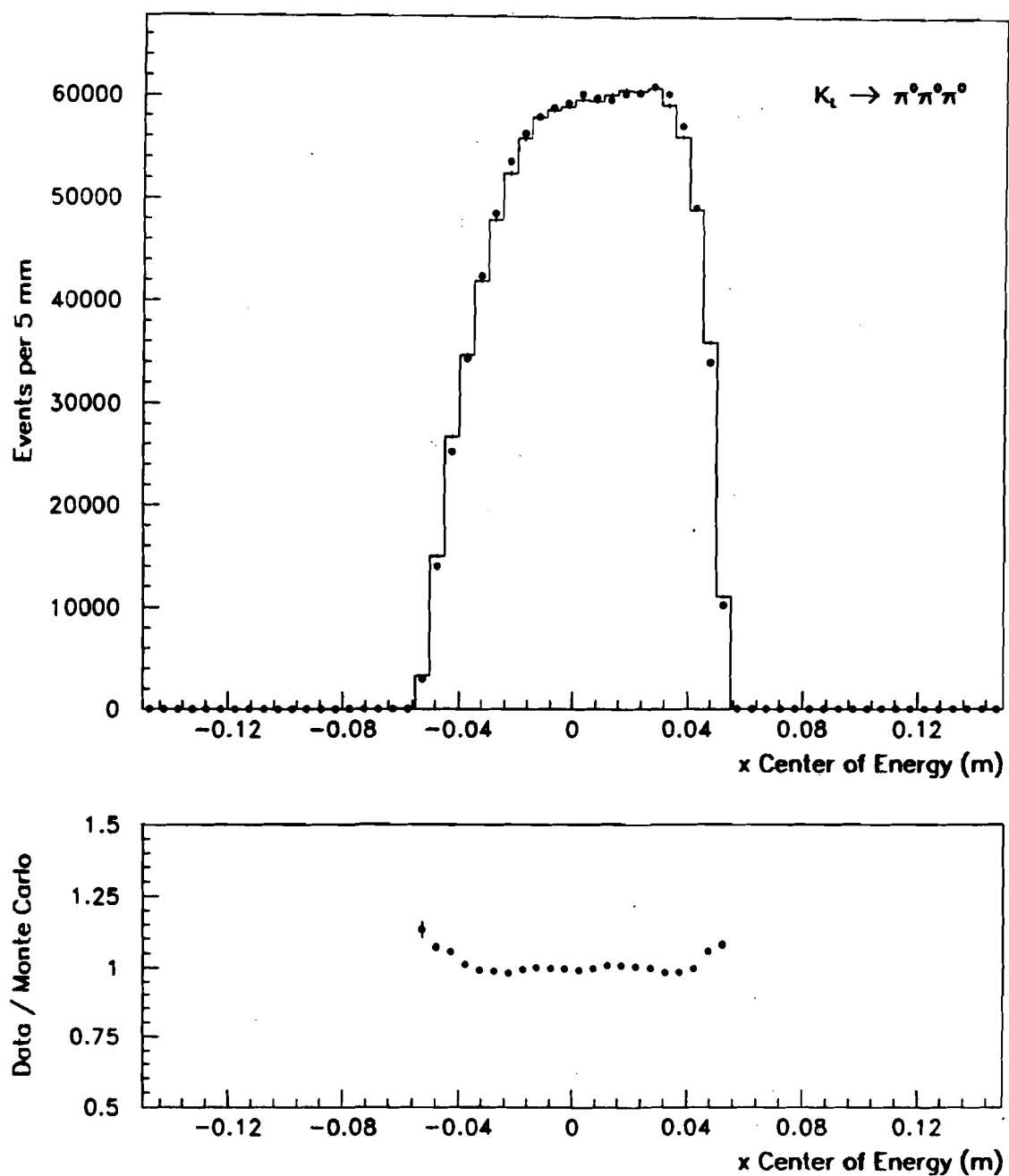
Figure 104. The x center of energy distribution of $K_L \to \pi^0 \pi^0 \pi^0$ decays. The histogram represents the data; the dots are Monte Carlo.
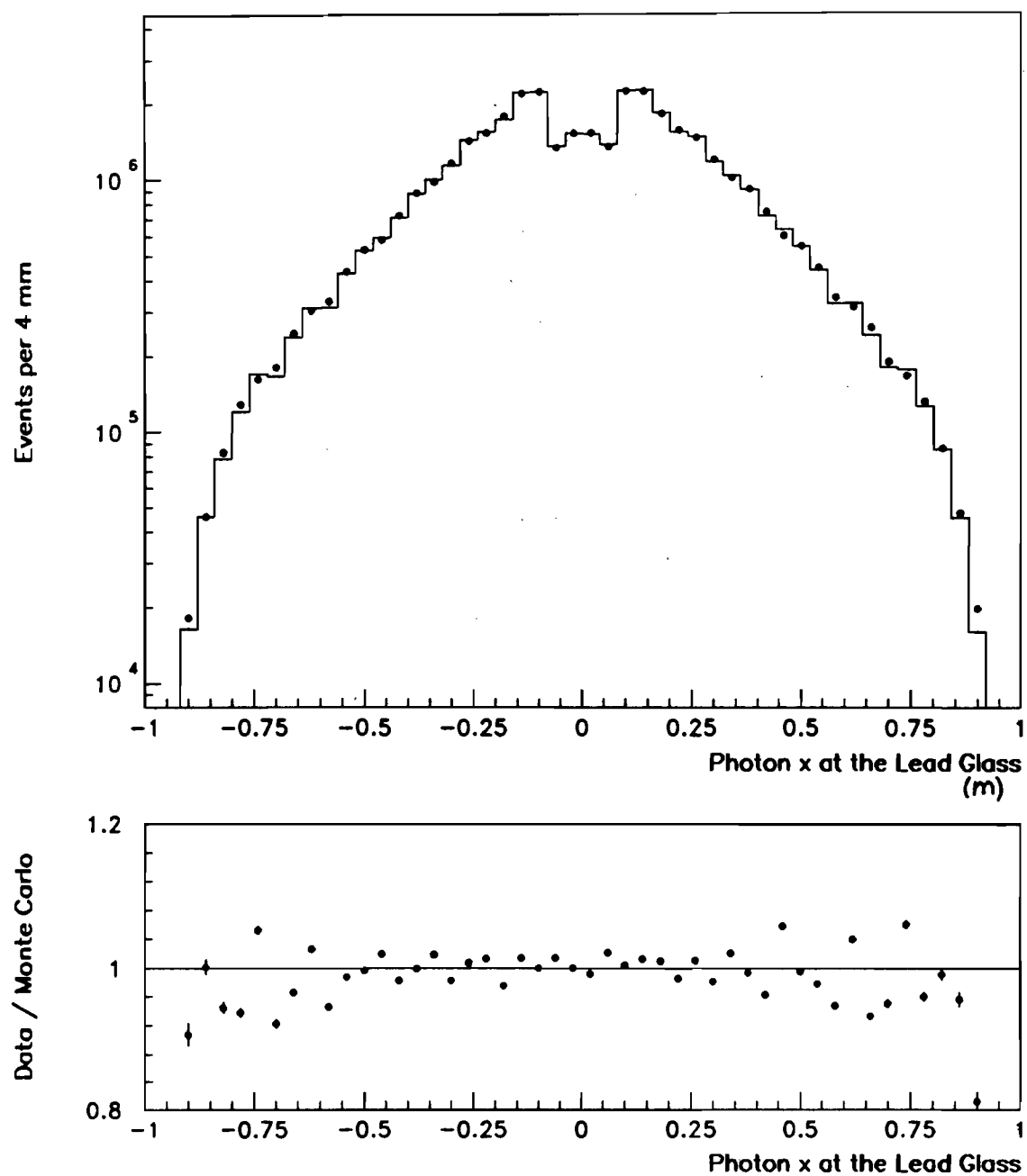
Figure 105. The spatial distribution of photons in the lead glass projected into the x plane for $\pi^0\pi^0\pi^0$ decays. The histogram represents the data; the dots are Monte Carlo.

in the struck lead glass block. For photon showers, which can be modelled as the superposition of the showers of the electron and positron produced in the initial pair-conversion (see Chapter 6), the energy deposits of two electrons in the library with appropriate energies were added.

The overall success of the library is evident in the distribution of cluster separations for accepted $\pi^0\pi^0$ events, shown in Figure 106. Further evidence is the simulation of the $K_L \to \pi^0\pi^0\pi^0$ background to the $K_L \to \pi^0\pi^0$ signal, which was shown in Figure 82. The absolute number of background events, about 85% of which contains at least one fused cluster, was sensitive to resolution of overlapping photon showers.

Tests of the Energy Response

The most difficult part of the simulation of the neutral mode was the energy resolution of the calorimeter, which determined the resolution of the reconstructed momentum and decay vertex. It was simulated using the results of a full EGS shower simulation with light attenuation, which reproduced its non-gaussian features (see Section 6.4).

To check the results, we compare the pairing χ^2 distributions of regenerated decays in the data and Monte Carlo, shown in Figure 107. If the energy resolutions of the Monte Carlo were wrong, the mean value of its χ^2 distribution would differ from the data; however, the observed means are close, 0.842 and 0.840 for one degree of freedom for the data and Monte Carlo respectively. In the corresponding distribution for the $\pi^0\pi^0\pi^0$ decays, shown in Figure 108, the first few bins have slightly fewer events in Monte Carlo than in the data, and the mean of the Monte Carlo distribution is 1.459, 0.015 higher than that of the data. These correspond to differences in the z resolutions of the data and Monte Carlo of 0.6 cm, compared to an average for the $\pi^0\pi^0\pi^0$ decays of 0.8 m.

Many other checks of the resolution, such as the two photon invariant mass distribution for $K_L \to \pi^+\pi^-\pi^0$ decay and the $\pi^0\pi^0$ invariant mass and z distributions, were shown in Chapter 6. All of these indicate that the data and Monte Carlo photon energy resolutions were consistent with one another within about 1% added in quadrature. We will estimate the contri-
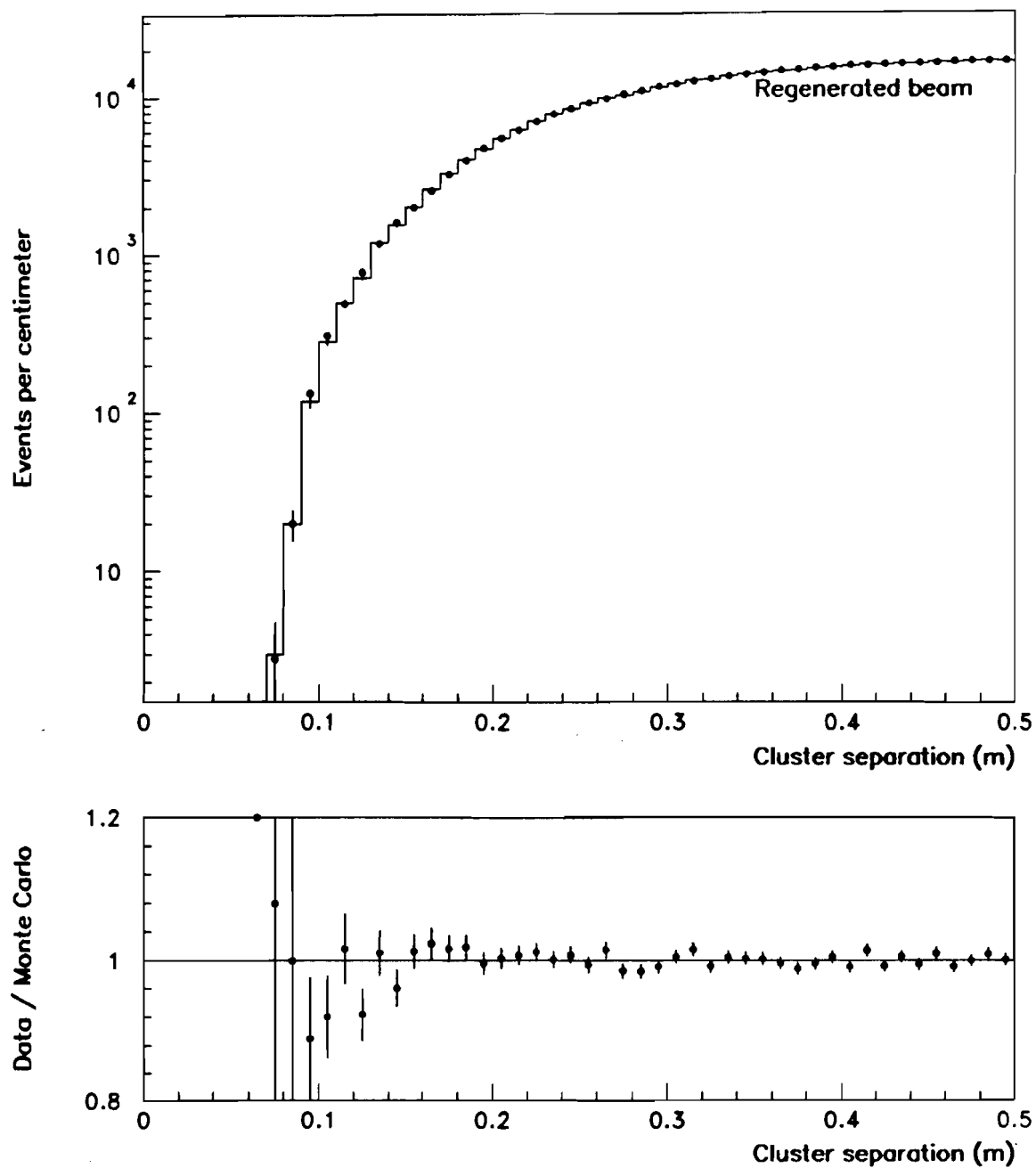
Figure 106. The separation of clusters in accepted $\pi^0\pi^0$ decays in the regenerated beam. The histogram represents the data; the dots are Monte Carlo.
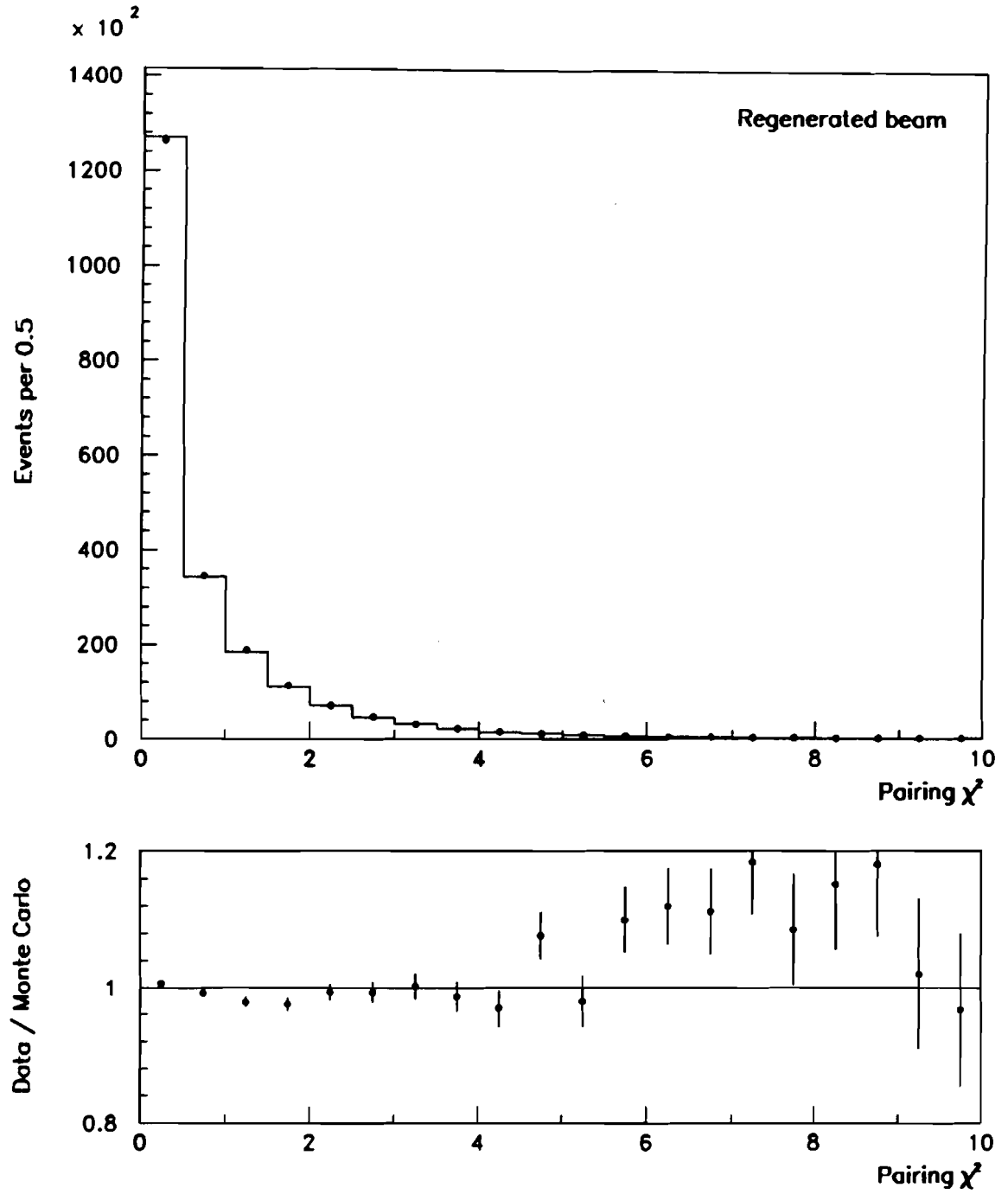
Figure 107. The pairing χ^2 distribution for $K_S \to \pi^0\pi^0$ decays. The histogram represents the data; the dots are Monte Carlo.
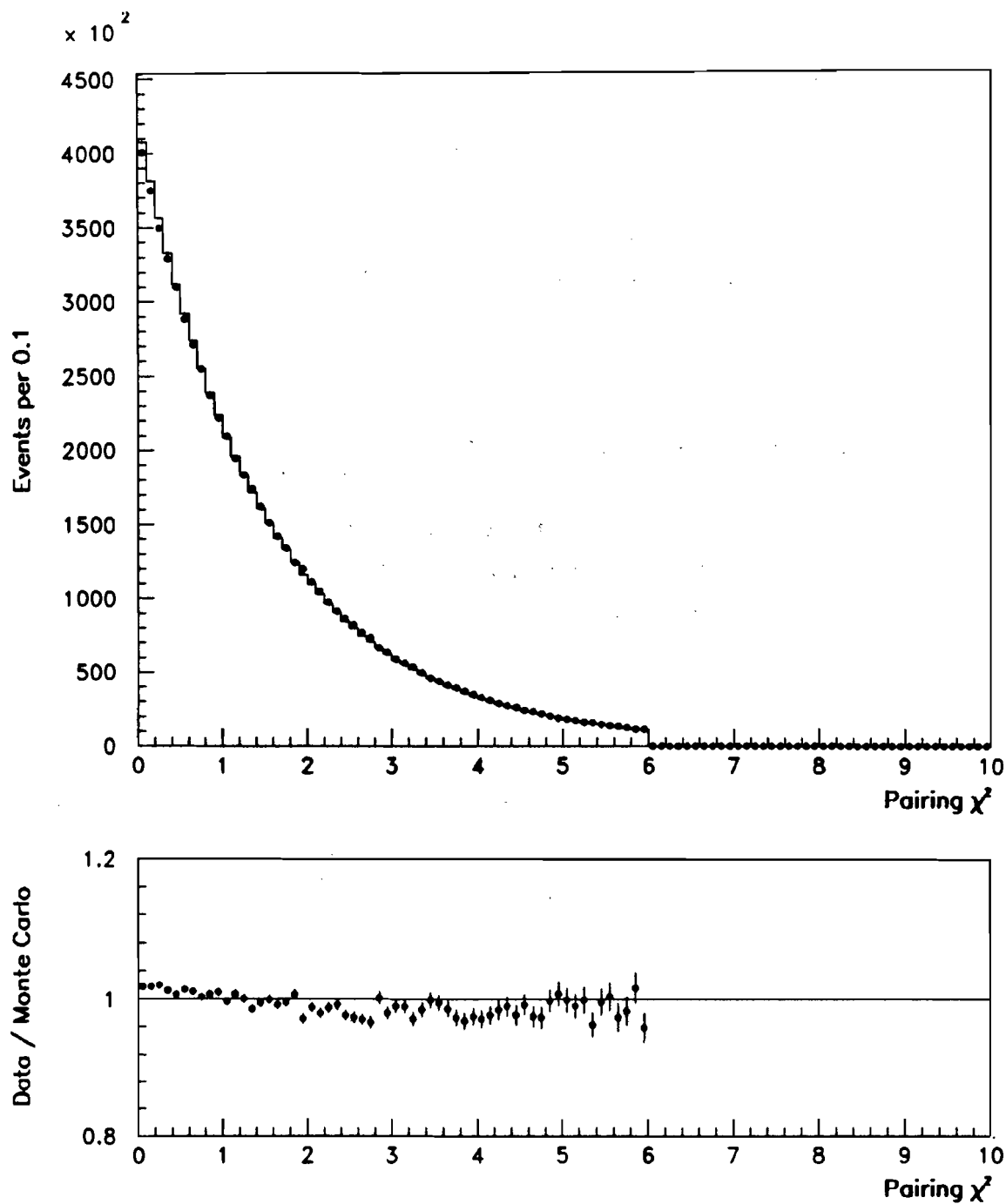
Figure 108. The pairing χ^2 distribution for $K_L \to \pi^0\pi^0\pi^0$ decays. A cut has been made at $\chi^2 = 6$. The histogram represents the data; the dots are Monte Carlo.

bution of uncertainty in the resolution to the final systematic error on the result in Chapter 9.

Other Contributions to the Neutral Mode Acceptance

As described earlier, the same production spectrum was required to reproduce the kaon momentum distributions of both the charged and neutral decays. This is shown in Figures 109 and 110 for neutral decays in the vacuum and regenerated beams respectively. Aside from a possible discrepancy between 40 and 44 GeV/c, the data and Monte Carlo distributions agree in the accepted energy range.

Because the momentum spectrum is sensitive to many sources of event loss, the consistency of the data and Monte Carlo spectra in all four $K_{L,S} \to \pi\pi$ modes is a significant check of the Monte Carlo simulation. For example, it was a discrepancy between the data and Monte Carlo in the neutral mode at kaon momenta above 120 GeV/c that lead to discovery of event loss due to shower leakage into the Back Anti.

The Neutral Mode Decay Distributions

Finally, we show the z distributions of data and Monte Carlo for the vacuum and regenerated beams in Figures 111 and 112. Agreement is good within the statistical errors. The upstream edge of the regenerated beam distribution was produced by the lead at the downstream end of the regenerator. Small differences in the shapes of the data and Monte Carlo are visible, but it is unclear whether these arise from errors in the energy scale or in the resolution or both. Figure 113 shows the data and Monte Carlo in the momentum 70 - 80 GeV/c momentum bin. The excess in the data near $z =$ 138 m is due to interactions in the HDRA, as described in Section 7.3.2. The slope of the data to Monte Carlo ratio over the fiducial region is (0.11 ± 0.24)%/m.

Figure 114 shows the z distribution of $K_L \to \pi^0\pi^0\pi^0$decays. The non-uniformity of the acceptance in z, evident in the large slope of the distributions even in the middle of the decay region, $120 < z < 137$ m, is much greater than for the $K_{L,S} \to \pi^0\pi^0$ decays because of the wider angles of the photons with respect to the beam axis in the six-body decay. At the down-
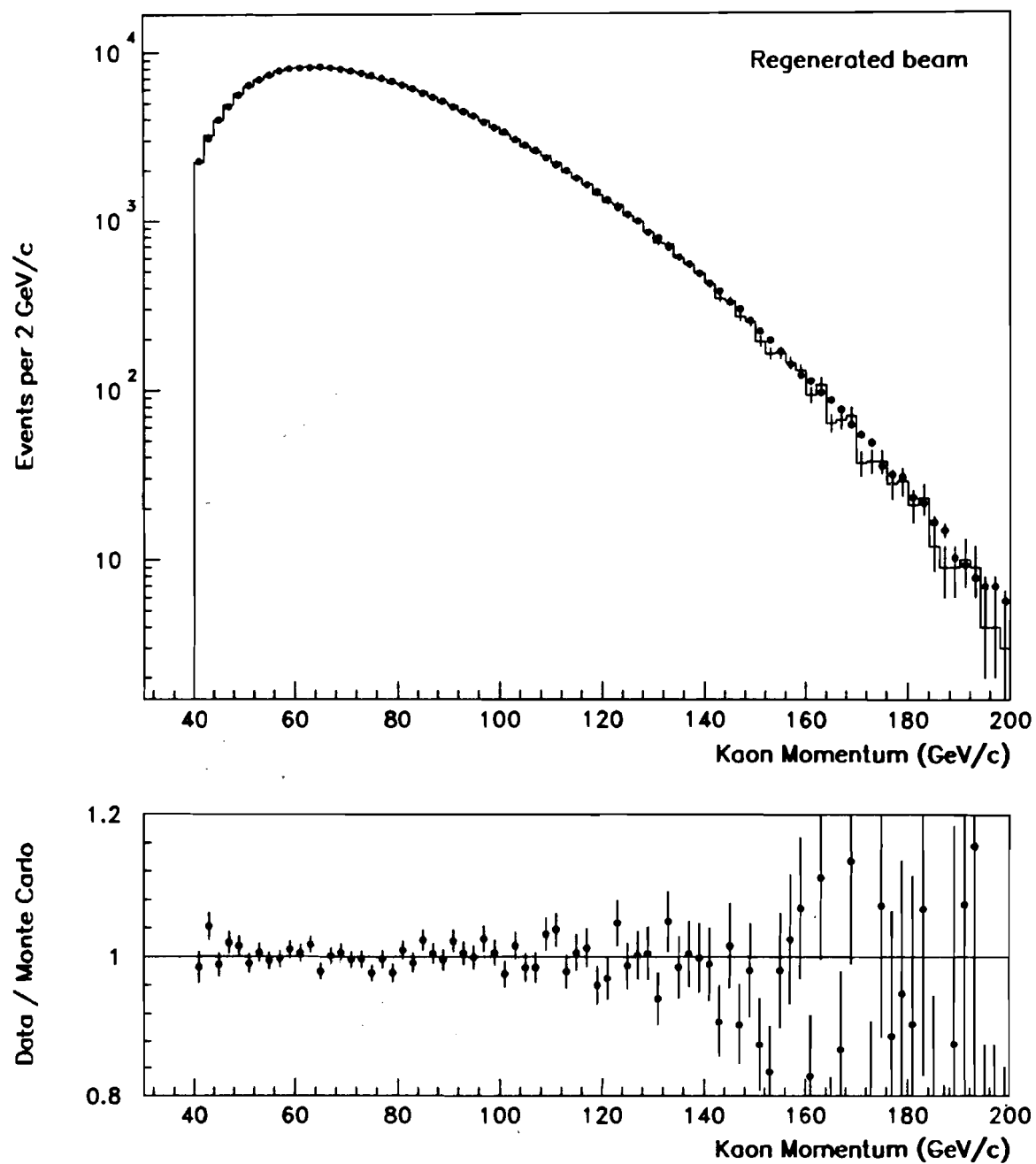
Figure 109. The kaon momentum distribution of observed $K_S \to \pi^0 \pi^0$ decays. The histogram represents the data; the dots are Monte Carlo.
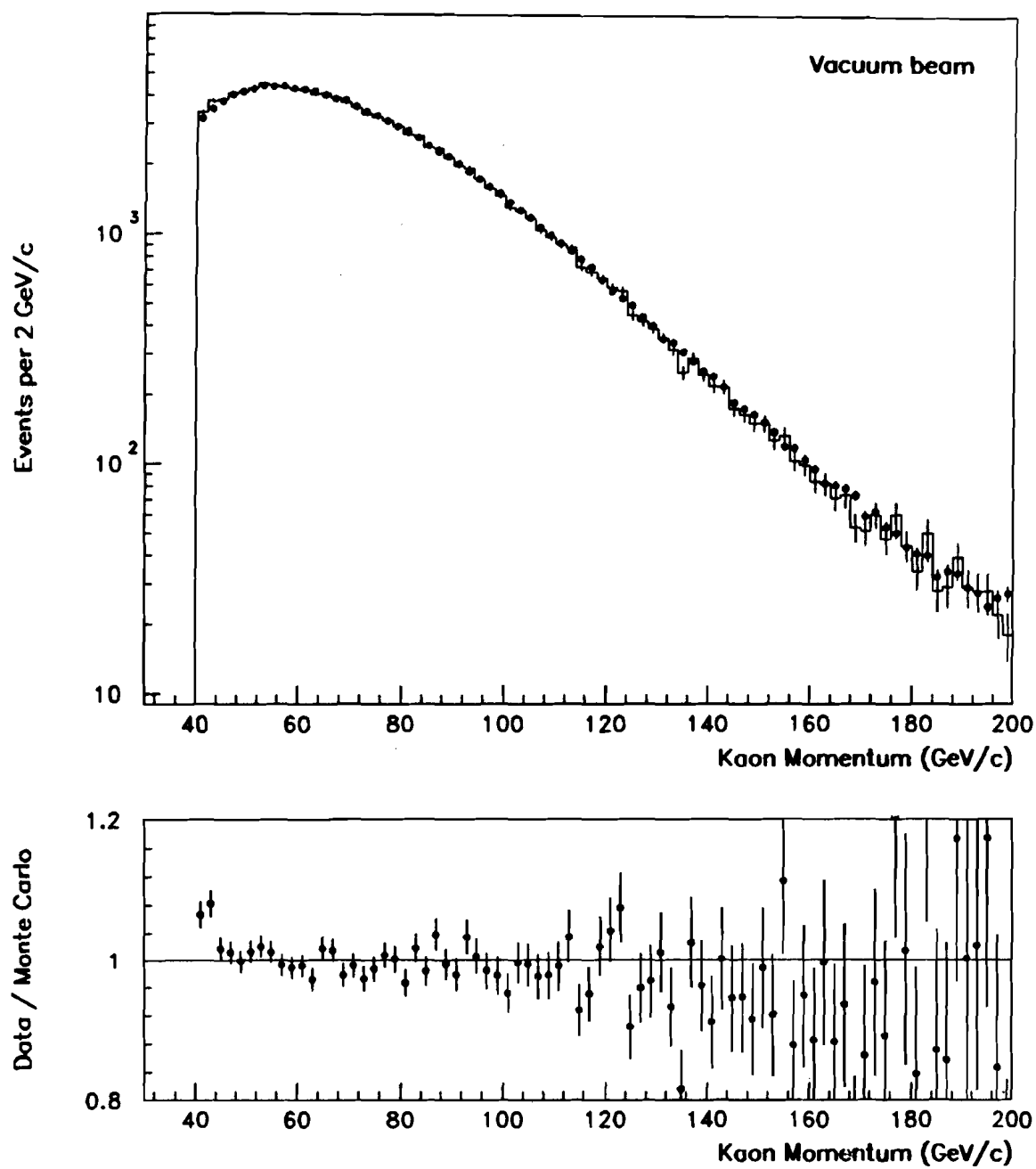
Figure 110. The kaon momentum distribution of observed $K_L \to \pi^0\pi^0$ decays. The histogram represents the data; the dots are Monte Carlo.
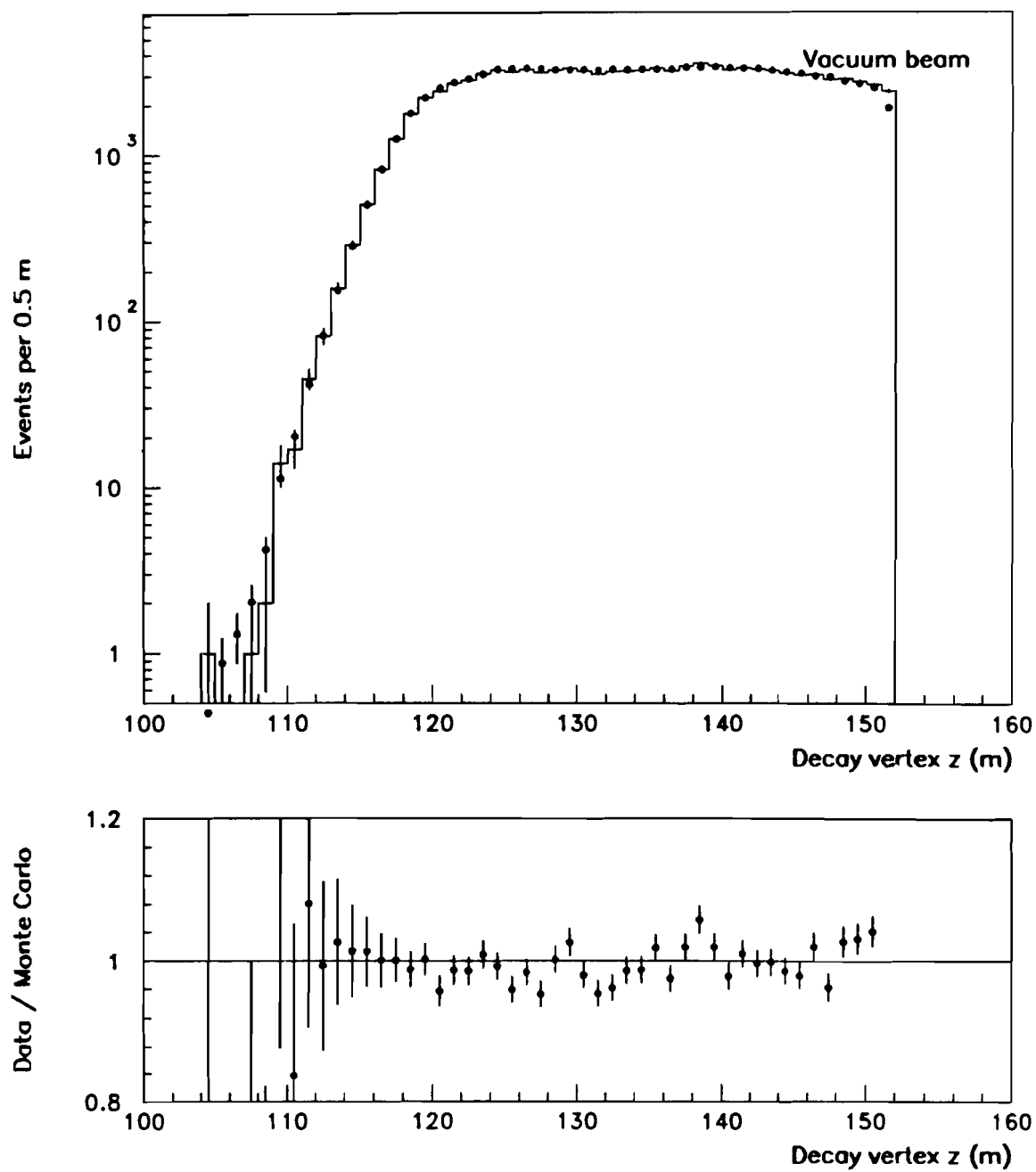
Figure 111. The decay vertex distribution of $K_L \to \pi^0 \pi^0$ decays. The histogram represents the data; the dots are Monte Carlo.
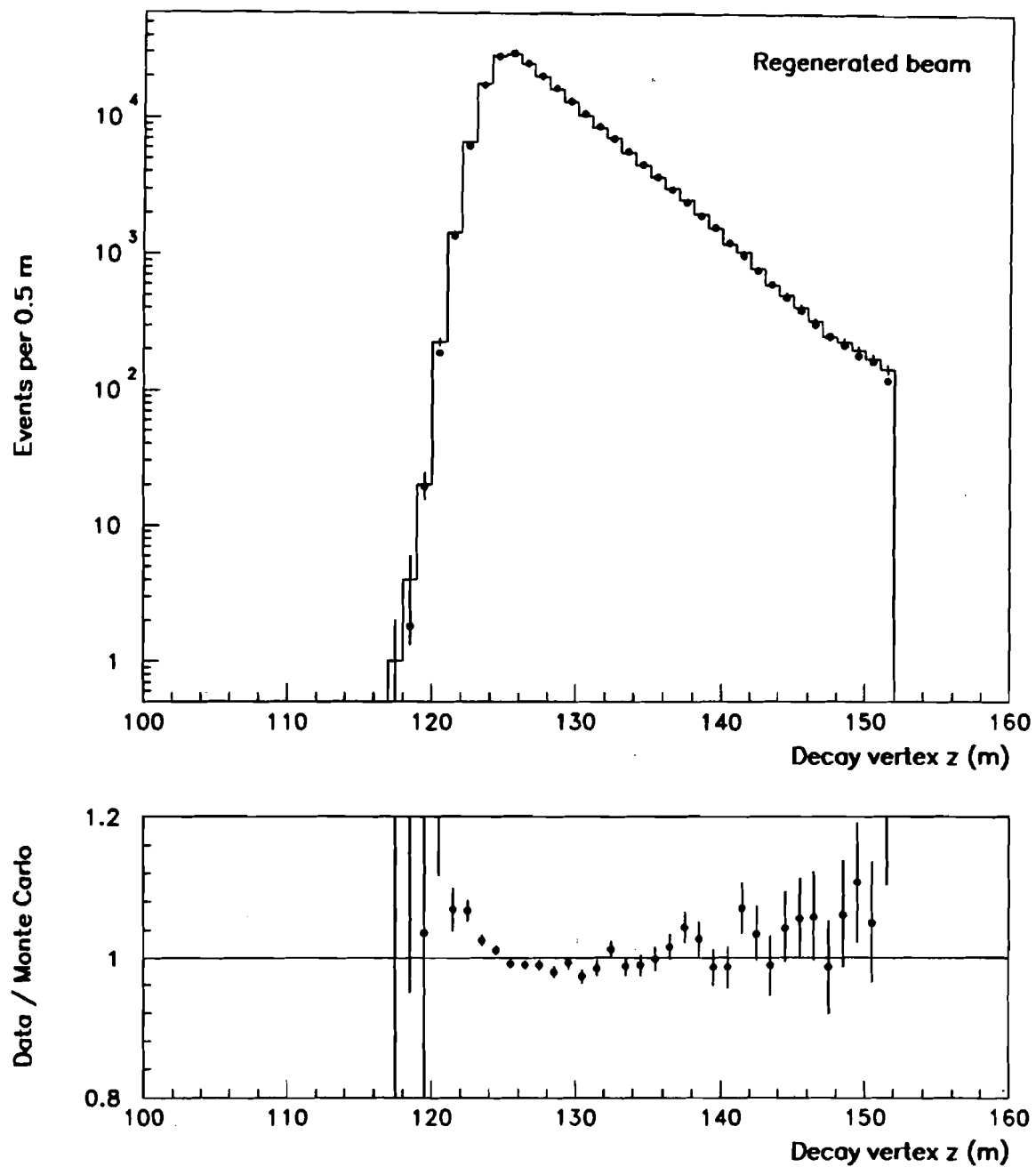
Figure 112. The decay vertex distribution of $K_S \rightarrow \pi^0\pi^0$ decays. The histogram represents the data; the dots are Monte Carlo.
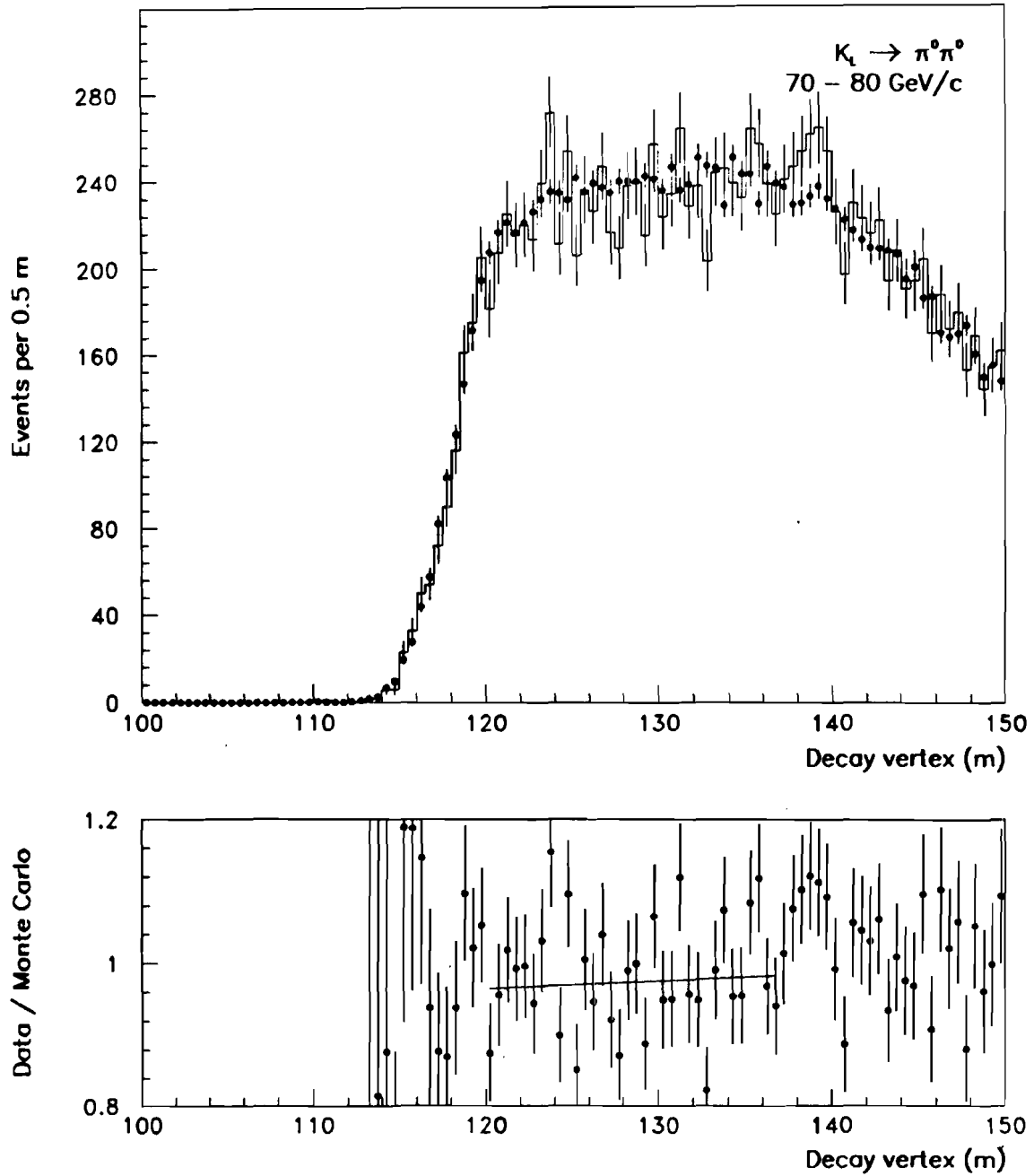
Figure 113. The decay vertex distribution of $K_L \to \pi^0\pi^0$ decays for kaons with momenta between 70 and 80 GeV/c. The short line in the lower window is a fit to their ratio in the fiducial region. The histogram represents the data; the dots are Monte Carlo.
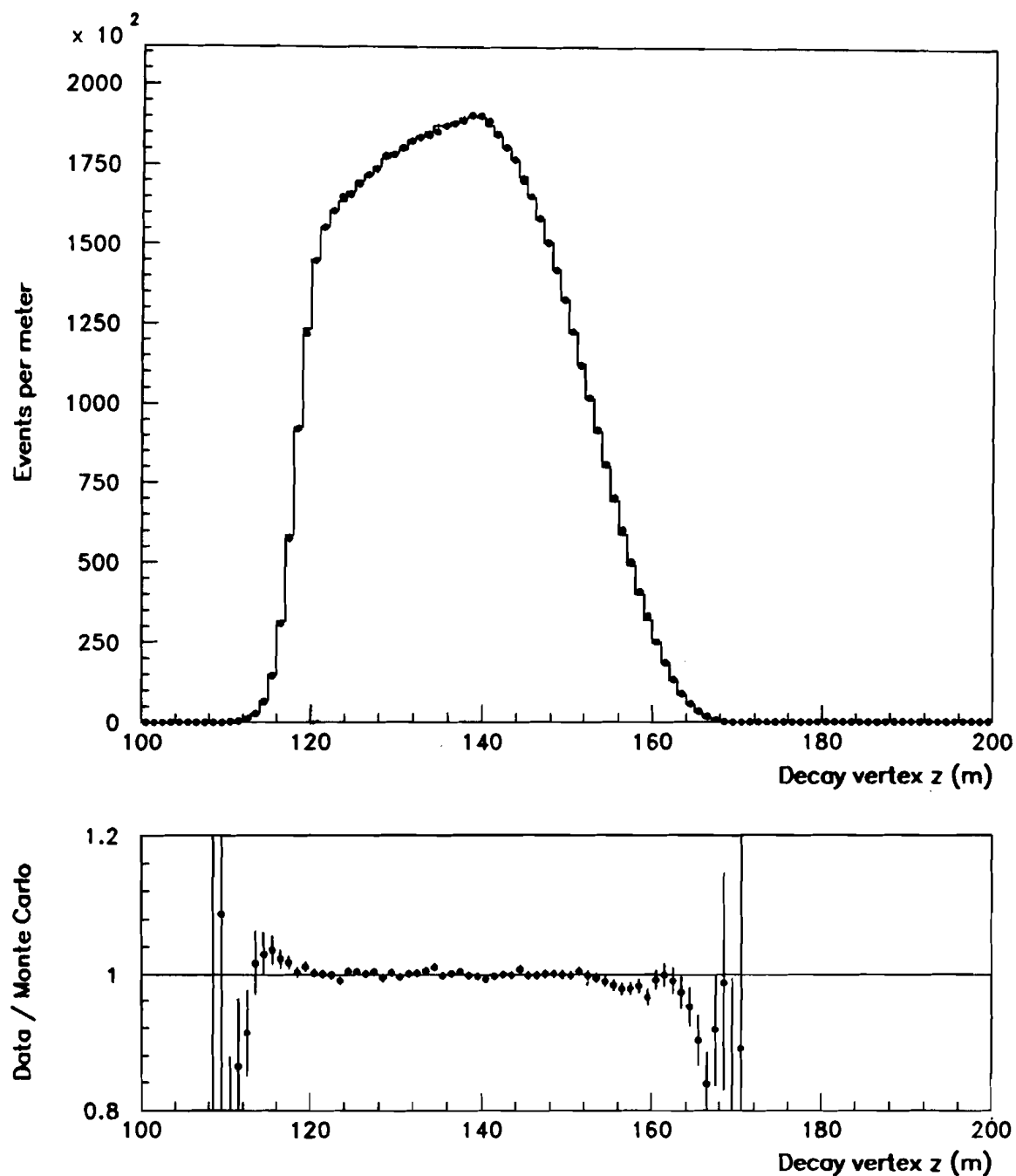
Figure 114. The decay vertex distribution of $K_L \to \pi^0 \pi^0 \pi^0$ decays. The arrow indicates the position of the lead glass calorimeter. The histogram represents the data; the dots are Monte Carlo.

TABLE 14. The acceptance of $K_{L,S} \to \pi^0 \pi^0$ decays in each p bin.

Kaon Momentum (GeV/c)	Vacuum Beam Acceptance	Regenerated Beam Acceptance
40 – 50	0.091	0.072
50 – 60	0.176	0.165
60 – 70	0.236	0.231
70 – 80	0.263	0.264
80 – 90	0.266	0.269
90 – 100	0.250	0.255
100 – 110	0.222	0.228
110 – 120	0.193	0.191
120 – 130	0.150	0.154
130 – 140	0.116	0.119
140 – 150	0.088	0.086

stream end of the distribution, the acceptance drops to zero as the photons escape down the beam holes through the lead glass, or are so tightly clustered about them that they can no longer be resolved. Even so, some events are reconstructed which decay less than 20 m from the lead glass. In this downstream region agreement between data and Monte Carlo is quite good given the complexity of the event topologies in the lead glass. In the region of interest, $120 < z < 137$ m, there are no discrepancies within the small statistical uncertainty. A linear fit over that region indicates that the residual acceptance error is $(0.023 \pm 0.026)\%$/m.[1]

The acceptances of $K_{L,S} \to \pi^0 \pi^0$ decays are listed for each p bin in Table 14. In all bins, the acceptances for decays in the vacuum and regenerated beams are comparable. As for the charged decays, the acceptance was 0.2% higher for decays in the lower beam than for decays in the upper beam, and the acceptance corrections were applied separately for the two.

---

[1] The $K_L \to \pi^0 \pi^0 \pi^0$ decay rate, which is 0.05% per meter at 70 GeV, is included in the Monte Carlo.

8.5 Conclusions

The acceptances of the neutral and charged decays are shown graphically in Figure 115 as a function of p and z. For both the neutral and charged decays, the chief features of the data are successfully reproduced by the Monte Carlo. For the $\pi\pi$ modes, most of the data and Monte Carlo distributions agree with one another within their statistical errors. Where discrepancies are visible in either the $\pi\pi$ or statistically powerful $K_L \to \pi^{\pm} e^{\mp} \nu$ and $K_L \to \pi^0\pi^0\pi^0$ distributions, they generally correspond to acceptance errors of less than 0.1%. Insensitivity of the acceptances to small discrepancies in the Monte Carlo and data distributions is confirmed by the stability of the acceptance ratios even in the face of rather large changes in the Monte Carlo simulation. These qualitative conclusions will be quantified in the following chapter, following a discussion of the extraction of $\mathrm{Re}(\varepsilon'/\varepsilon)$ from the data.
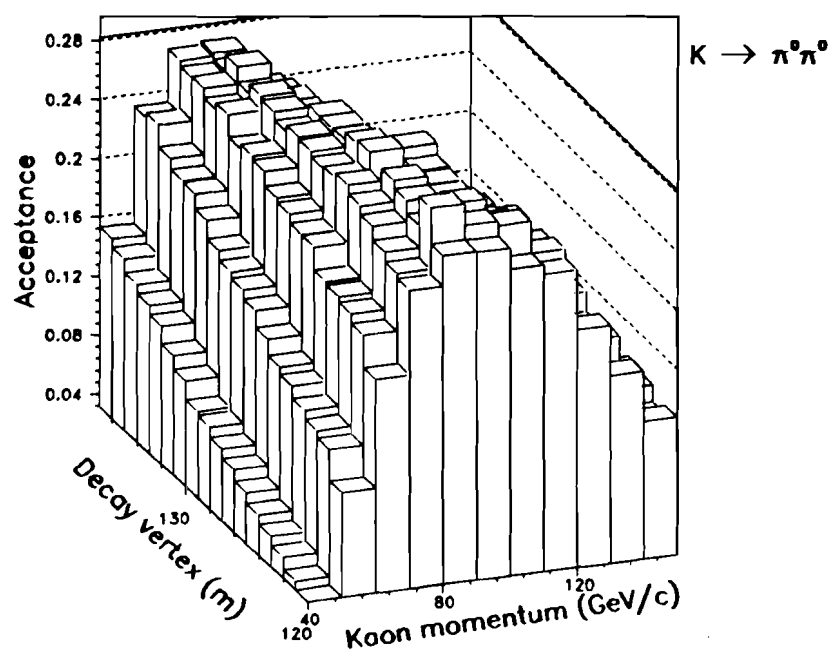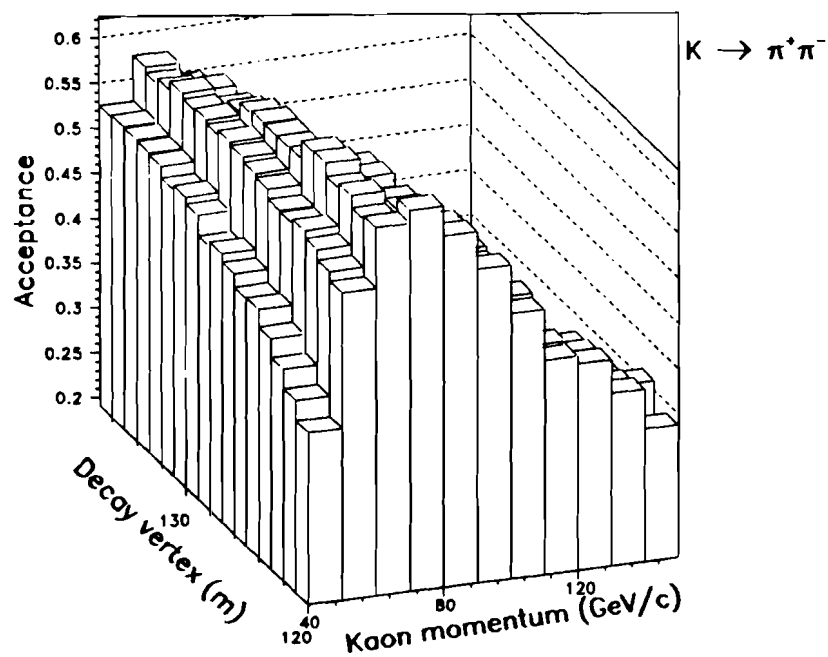
Figure 115. The acceptance as a function of p and z for $K_L \to \pi^+\pi^-$ and $K_L \to \pi^0\pi^0$ decays.

CHAPTER 9

EXTRACTION OF RE(ε'/ε)

9.1 Overview

This chapter treats the procedure used to extract the value of Re(ε'/ε) from the data and evaluate its systematic errors.

9.2 The Final Data Samples

Table 15 summarizes the corrections to the data and the effect of each on the double ratio of decays, R_{+-}/R_{00}. The first correction is for backgrounds, which for the neutral mode are $K_L \to \pi^0\pi^0\pi^0$, the non-coherent $K_S \to \pi^0\pi^0$, and non-kaon decays, and for the charged mode are the $K_L \to \pi^{\pm}e^{\mp}v$ and the non-coherent $K_S \to \pi^+\pi^-$. Subtraction of the backgrounds from the raw data samples changes R_{+-}/R_{00} by 2.5%, primarily because of the large non-coherent K_S contribution in the neutral mode.

Next on the table is a small correction, largely common to the charged and neutral data, for the decays of K_S produced in the target. These K_S were rather rare, and always energetic, since even for a 200 GeV kaon, the upstream end of the decay region was ten K_S lifetimes from the target. Because of interference between the K_S and K_L, they could either add to or subtract from the data sample. The corrections were determined as a function of kaon momentum (p) and vertex position (z) from the ratio of K_S to K_L decay amplitudes in the vacuum beam observed in the Monte Carlo, which as described in Chapter 8, simulated propagation of the full

TABLE 15. Event totals and corrections.

	Neutral	Charged	R_{+-}/R_{00}
Raw events			
K_L	52 227	43 357	
K_S	201 334	178 803	1.0698
Background fractions			
K_L	0.0504	0.0032	
K_S	0.0262	0.0013	1.0454
Target K_S fractions			
K_L	0.0012	0.0010	
K_S	–0.0001	–0.0001	1.0442
Acceptance			
K_L	0.1879	0.5041	
K_S	0.1806	0.5064	0.9998

kaon wave function. As shown in the table, the total correction to the double ratio was only 0.02%, and was insensitive to changes in the relative fractions of K^0 and $\bar{K}^0$ produced in the target. Had the acceptances of the neutral and charged decays been identical, the correction would have vanished completely.

The final correction shown in the table is for acceptance, which as we have already seen, changes the double ratio by 4.5%. At the last stage, the double ratio is nearly unity, indicating that the value of $Re(\varepsilon'/\varepsilon)$ is small. The statistical error on the double ratio of decay rates is $\pm$ 0.8%, equivalent to $\pm$ 0.0014 on $Re(\varepsilon'/\varepsilon)$. Let us now turn to extraction of $Re(\varepsilon'/\varepsilon)$.

9.3 The Fit

9.3.1 The Fitting Procedure

Using Equations (2.1) and (2.2), the number of kaons with momentum p decaying to $\pi\pi$ in the regenerated beam over a proper time interval extending from t_1 to t_2 was given by

$$N_R(\pi\pi) = B_{\pi\pi} f(p) e^{-X}$$

$$\times \int_{t_1}^{t_2} dt \left[|\rho|^2 e^{-\Gamma_S t} + 2|\rho\eta| e^{-(\Gamma_S + \Gamma_L)t/2} \cos(\Delta m t + \phi_\rho - \phi_\eta) + |\eta|^2 e^{-\Gamma_L t} \right] \quad (9.1)$$

and in the vacuum beam was given by

$$N_V(\pi\pi) = B_{\pi\pi} f(p) \int_{t_1}^{t_2} dt |\eta|^2 e^{-\Gamma_L t}. \quad (9.2)$$

where ρ is the regeneration amplitude, $B_{\pi\pi}$ is the K_S branching fraction to the appropriate $\pi\pi$ final state, η represents either η_{+-} or η_{00} as appropriate, and the remaining parameters are as described in Section 2.2. Recall that η_{+-} and η_{00} are related to ε and ε' by the expressions

$$\eta_{+-} = |\varepsilon| e^{i\phi_\varepsilon} \left(1 + \left| \frac{\varepsilon'}{\varepsilon} \right| e^{i(\phi_\varepsilon - \phi_{\varepsilon'})} \right)$$

$$\eta_{00} = |\varepsilon| e^{i\phi_\varepsilon} \left(1 - 2 \left| \frac{\varepsilon'}{\varepsilon} \right| e^{i(\phi_\varepsilon - \phi_{\varepsilon'})} \right) \quad . \quad (9.3)$$

The ratio of decays in the regenerated to vacuum beams was therefore a function of X, Δm, ϕ_ρ, ϕ_η, Γ_S, Γ_L, ε, ε', and ρ. The values of all of these parameters, except ρ and ε', were known from past experiments or were easily determined from our own data. For either the neutral or charged mode the ratio $|\rho/\eta|$ could be extracted from the data by fitting the ratio of Equations (9.1) and (9.2) to the observed ratio of decays in the regenerated to vacuum beams. A simultaneous fit to the two modes with ρ constrained to be the same for both permitted extraction of ε'. The remainder of this section will describe this fit in more detail.

The values of the constants in Equations (9.1), (9.2), and (9.3) are listed in Table 16. The factor e^{-X}, which represents the kaon transmission through the Shadow Absorber and regenerator, was determined to be 0.0638 $\pm$ 0.0007 from the ratio of $K_L \to \pi^+\pi^-\pi^0$ decays observed in the vacuum and regenerated beams, a value confirmed using $K_L \to \pi^0\pi^0\pi^0$ decays.

Some of the properties of the regeneration amplitude ρ provided useful constraints for the fit. For a thick regenerator ρ is given by

$$\rho = \pi i \frac{f(0) - \bar{f}(0)}{k} \Lambda_S N \frac{1 - e^{(i\Delta m/\Gamma_S - 1/2)L/\Lambda_S}}{1/2 - i\Delta m/\Gamma_S} \qquad (9.4)$$

where

$f(0)$ and $\bar{f}(0)$	are the K^0 and $\bar{K}^0$ forward scattering amplitudes;
$k = P_K/\hbar$	is the kaon wave number;
Λ_S	is the K_S decay length;
N	is the density of scatterers;
$\Delta m = m_L - m_S$	is the $K_L - K_S$ mass difference;
$\Gamma_S = \hbar / \tau_S$	is the K_S decay width;
L	is the length of the regenerator.

The value of $\left|\left(f(0) - \bar{f}(0)\right)/k\right|$ has been determined for a variety of materials [24], and is expected to be about 5 mb for 70 GeV kaons on the B_4C molecule. It was observed to have a power law dependence on the kaon momentum of $p^{-0.614 \pm 0.009}$ which is largely independent of the material, consistent with Regge theory predictions.[1] In our fits, we parametrized the regeneration amplitude as

TABLE 16. The constants used in the fit.

Constant	Value
Γ_S	7.38×10^{-12} MeV
Γ_L	1.27×10^{-14} MeV
Δm	3.52×10^{-12} MeV
ϕ_ρ	$126°$
$|\varepsilon|$	2.275×10^{-3}
$\arg\varepsilon$	$44.9°$
$\arg\varepsilon'$	$37.9°$ [18, 19]

[1] From analyticity arguments, the regeneration phase ϕ_ρ and power are related by $\phi_\rho = -\frac{\pi}{2}(2 - \alpha)$. The power is approximately equal to -0.6, hence $\phi_\rho = 126°$.

$$\left| \frac{f(0) - \bar{f}(0)}{k} \right| = A\left(\frac{p}{70 GeV}\right)^{\alpha} . \tag{9.5}$$

In order to extract $\mathrm{Re}(\varepsilon'/\varepsilon)$ we binned the data in momentum and simultaneously fit the charged and neutral data for the regeneration power, α, its magnitude at 70 GeV/c, A, and $\mathrm{Re}(\varepsilon'/\varepsilon)$. The ratio, r, of regenerated to vacuum events corrected for acceptance was calculated for neutral and charged data in each p bin according to

$$r(p) = \sqrt{\frac{\dfrac{N_{Ru}(p)}{\varepsilon_{Ru}(p)} \quad \dfrac{N_{Rd}(p)}{\varepsilon_{Rd}(p)}}{\dfrac{N_{Vu}(p)}{\varepsilon_{Vu}p)} \quad \dfrac{N_{Vd}(p)}{\varepsilon_{Vd}(p)}}} , \tag{9.6}$$

where $N_{Qq}(p)$ is the number of charged or neutral decays in the p bin, $\varepsilon_{Qq}(p)$ is the acceptance, calculated as described in Chapter 8, and the subscripts refer to vacuum ("V") or regenerated ("R") decays in the upper ("u") or lower ("d") beam. Use of the geometric mean to calculate the ratio of regenerated to vacuum decays, rather than the more common arithmetic mean, suppressed biases which could have arisen from asymmetries in the two beams, as we shall see in Section 9.4.1. From the neutral and charged values of $r(p)$ we then calculated the fraction of decays in the vacuum beam for the two modes according to

$$t_{data}{}^{00}(p) = \frac{1}{r^{00}(p) + 1} \tag{9.7}$$

and

$$t_{data}{}^{+-}(p) = \frac{1}{r^{+-}(p) + 1} . \tag{9.8}$$

Given values of A, α, and ε', the expected fraction of decays in the vacuum beam for the two modes could be calculated from the integrals of Equations (9.1) and (9.2). The integrals were evaluated over the proper time

interval corresponding to the z region $120 < z < 137$ m, translated so that $t = 0$ corresponded to the downstream end of the regenerator. The fraction of decays expected in the vacuum beam was given by

$$t_{pred}(p) = \frac{N_V(\pi\pi)}{N_R(\pi\pi) + N_V(\pi\pi)} \ . \tag{9.9}$$

The fit minimized χ^2, defined as

$$\chi^2 = \sum_p \left[\frac{\left(t_{pred}(p) - t_{data}{}^{00}(p)\right)^2}{\sigma_{00}(p)^2} + \frac{\left(t_{pred}(p) - t_{data}{}^{+-}(p)\right)^2}{\sigma_{+-}(p)^2} \right] \tag{9.10}$$

where $\sigma_{00}(p)^2$ and $\sigma_{+-}(p)^2$ were the statistical uncertainties on $t_{data}{}^{00}(p)$ and $t_{data}{}^{+-}(p)$ calculated from the number of data and Monte Carlo events, assuming a binomial distribution for the fraction of decays that originated in the vacuum beam. The data samples were large enough to ensure that a χ^2 fit was appropriate in all momentum bins.

9.3.2 Results of the Fit

We turn now to the results of the simultaneous fit to the charged and neutral data yielding the value of $\text{Re}(\varepsilon'/\varepsilon)$. The data are plotted in Figure 116 with the fit regeneration amplitude superimposed. The power law dependance of $\left|\left(f(0) - \bar{f}(0)\right)/k\right|$ on the kaon momentum was -0.602 ± 0.007, consistent with past experiments, and its magnitude at 70 GeV/c was 5.876 ± 0.013 mb. The value of $\text{Re}(\varepsilon'/\varepsilon)$ was

$$\text{Re}(\varepsilon'/\varepsilon) = -0.0003 \pm 0.0014 \ , \tag{9.11}$$

where the error is statistical, including the contribution from the Monte Carlo. The χ^2 of the fit was 20.1 for 19 degrees of freedom. Plots of the χ^2 contours as a function of the three fit parameters, shown in Figure 117, indicate that a single well-defined minimum exists, and that coupling between $\text{Re}(\varepsilon'/\varepsilon)$ and the parameters of the regeneration amplitude is weak.
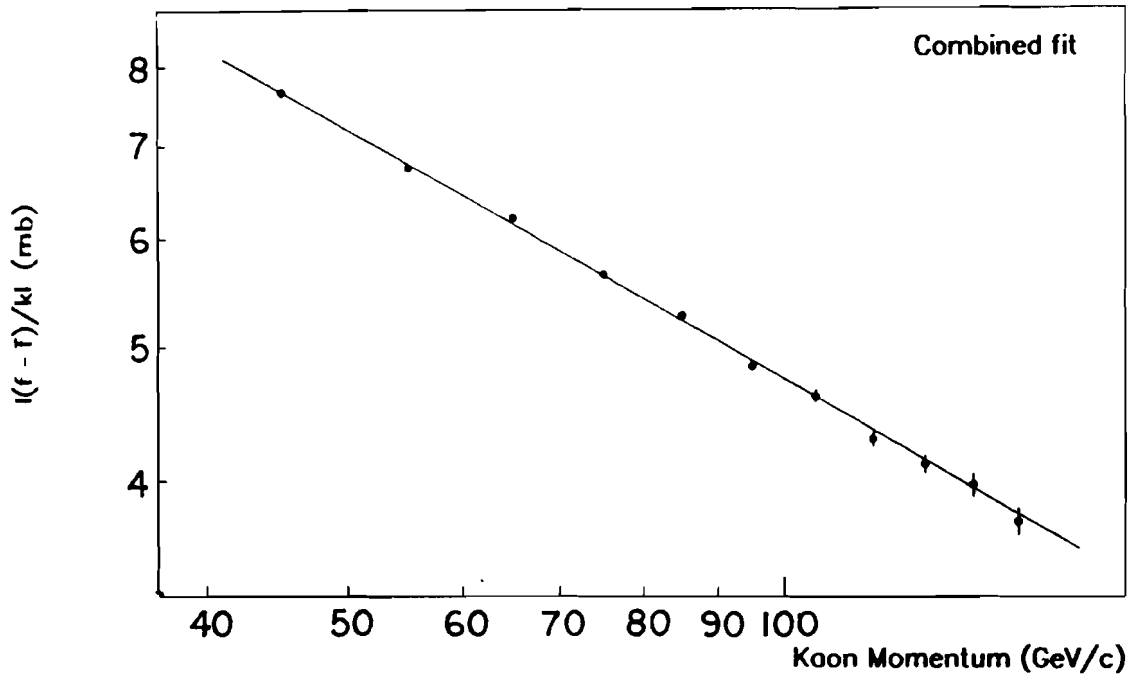
Figure 116. The regeneration amplitude from B₄C as a function of the kaon momentum. The line is the best fit power law.

While use of the power law dependance of $\left|\left(f(0)-\bar{f}(0)\right)/k\right|$ reduced sensitivity to fluctuations in the fit, it was not essential to the result. The results of extracting the value of $\text{Re}(\varepsilon'/\varepsilon)$ separately in each momentum bin without assuming any functional form for the regeneration amplitude are plotted in Figure 118. Within the statistical error the value of $\text{Re}(\varepsilon'/\varepsilon)$ is independent of the kaon momentum, with a χ^2 of 11.7 for 10 degrees of freedom for a constant value. The weighted average is -0.0005 ± 0.0014, very close to the value of $\text{Re}(\varepsilon'/\varepsilon)$ found in the earlier fit.

Tests were done of the sensitivity of the result to the values of constants used in the fit. Several standard deviation changes in the transmission e^{-X} and in the density and position of the regenerator had no measurable effect on $\text{Re}(\varepsilon'/\varepsilon)$. In general, when these changes were made, the magnitude of the regeneration amplitude shifted somewhat to accommodate them, but since the change was common to the neutral and charged
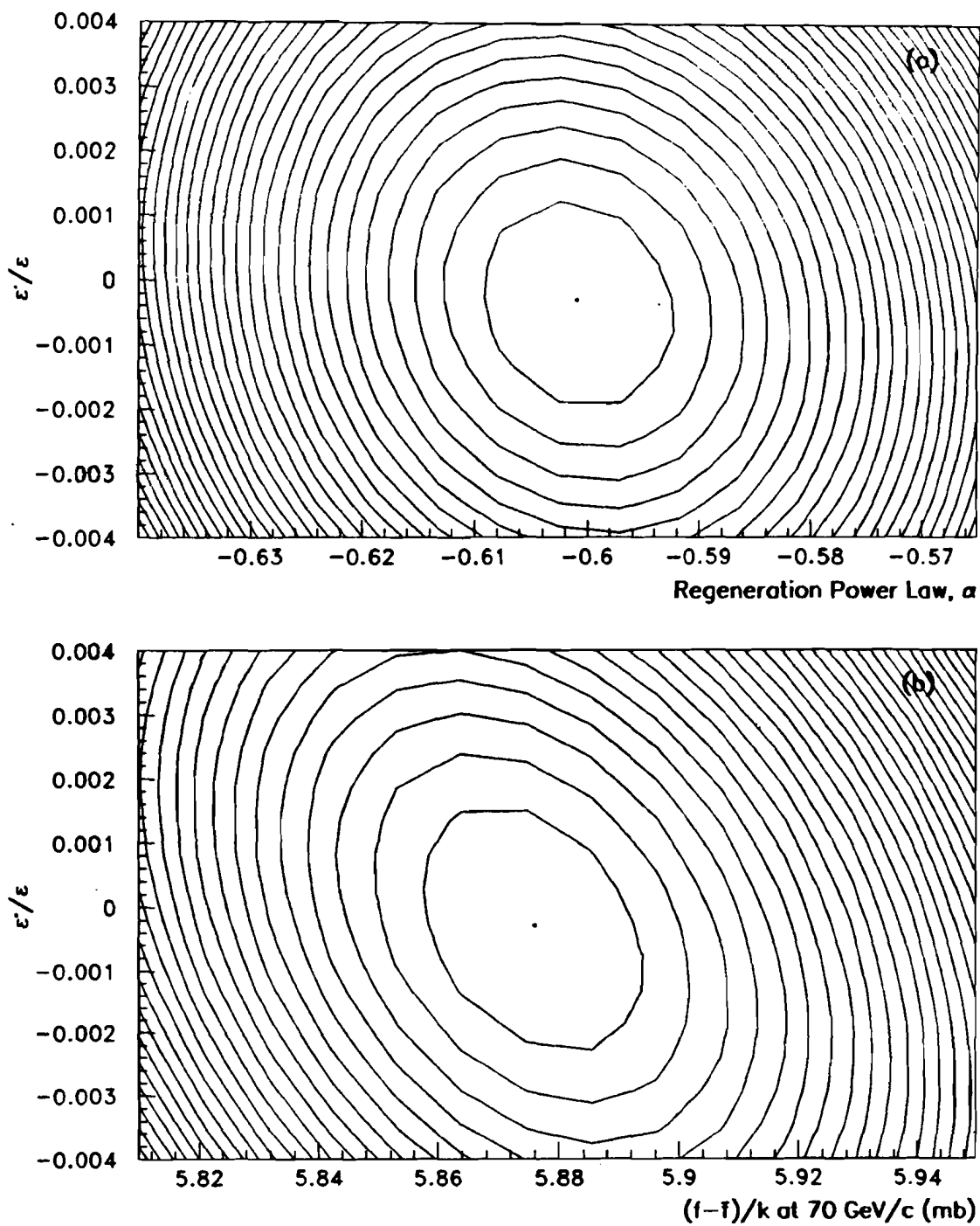
Figure 117. Contours of χ^2 in the $\text{Re}(\varepsilon'/\varepsilon)$ vs regeneration power law plane and in the $\text{Re}(\varepsilon'/\varepsilon)$ vs $\left|\left(f(0)-\bar{f}(0)\right)/k\right|$ at 70 GeV/c plane. The contours correspond to unit increments in χ^2.

modes, the value of Re(ε'/ε) was unaffected. Insensitivity to the changes in the predicted shape of the z distribution, and therefore to a wide variety of systematic errors, was one of the advantages of using the same p and z ranges for the neutral and charged modes.

As a check of the results, we fit for the regeneration power, α, and magnitude at 70 GeV/c, A, in the charged and neutral data separately, fixing the value of Re(ε'/ε) at zero. Since the regeneration amplitude and η always appear in the ratio $|\rho/\eta|$, a non-zero value of Re(ε'/ε) would shift the apparent values of A slightly. The regeneration power laws, however, should be the same. The results are summarized in Table 17, and plotted in Figure 119. The fit values of α are consistent with one another and previous determinations. The close values of A reflect the small value of Re(ε'/ε).
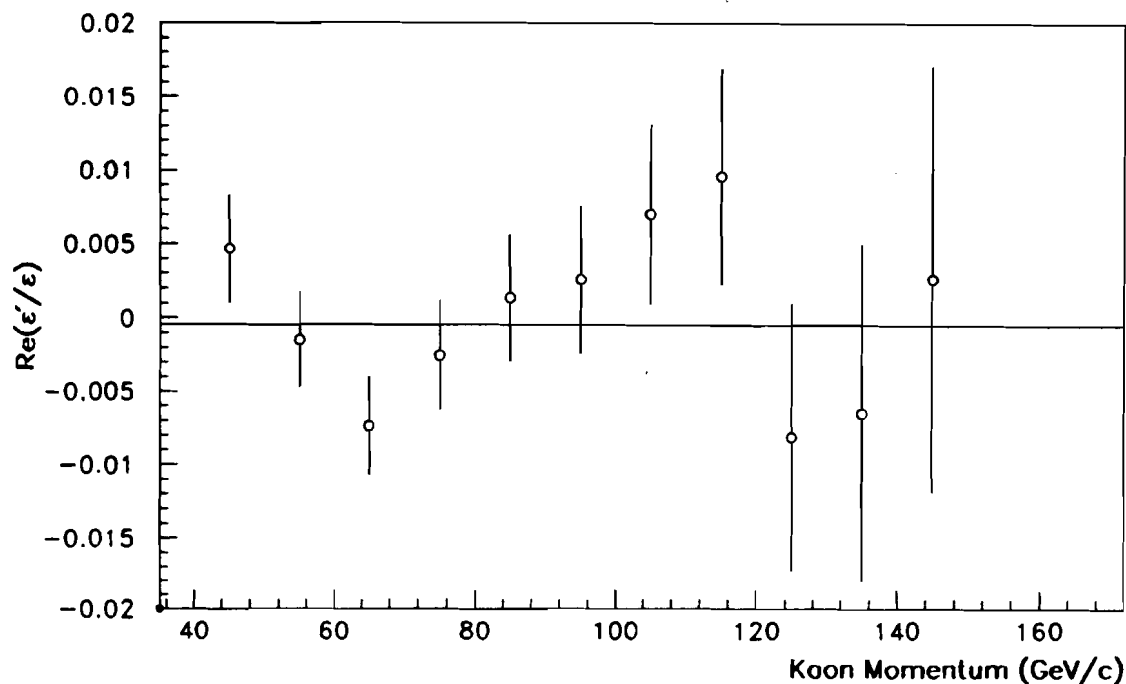
Figure 118. The results of separate determinations of Re(ε'/ε) in each momentum bin. The horizontal line is at the average value of −0.0005. The uncertainty on the average is ±0.0014 and χ^2 is 11.7 for 10 degrees of freedom.
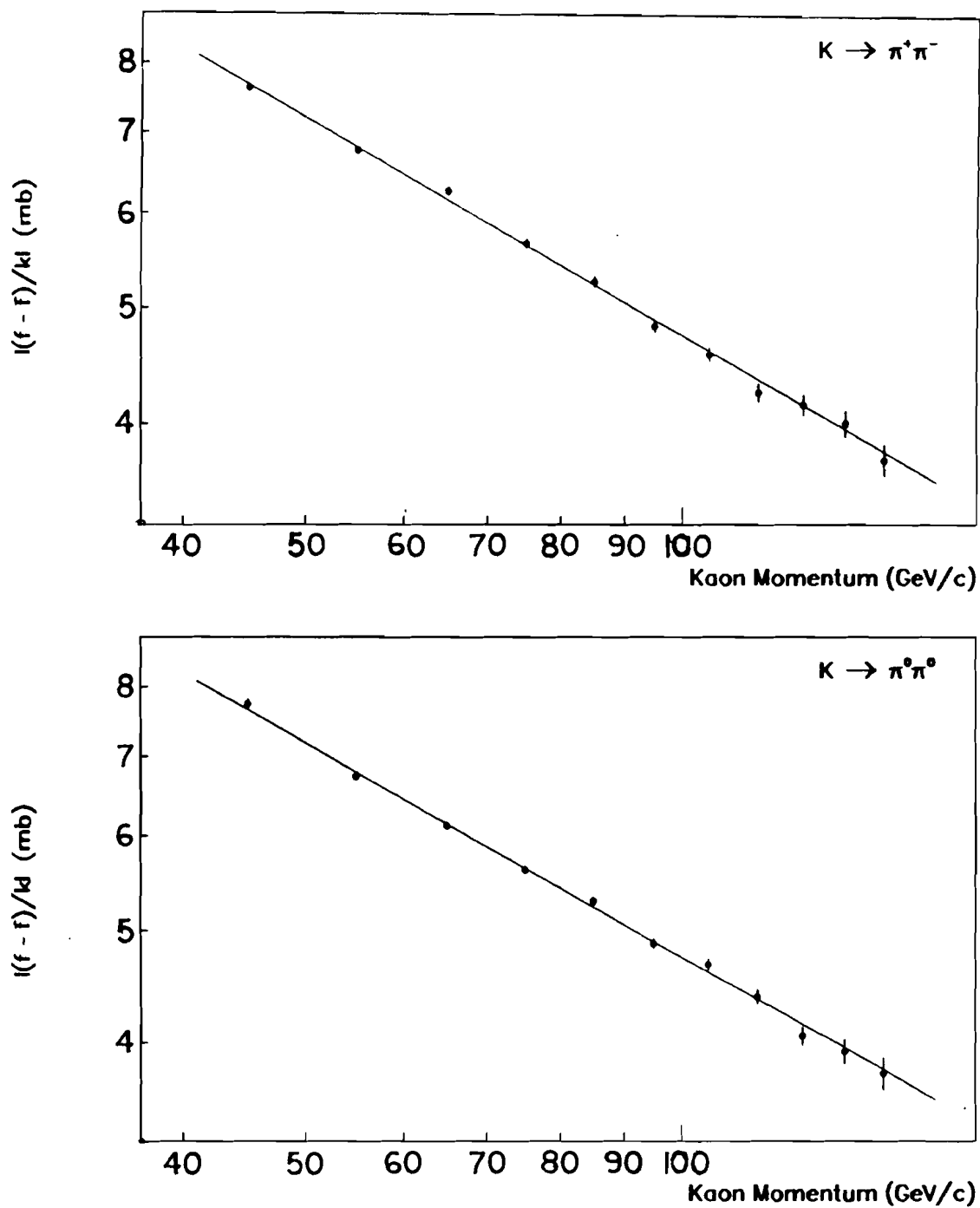
Figure 119. The magnitude of the regeneration amplitude as a function of the kaon momentum as observed in the charged and neutral decays. The lines are fits to the data.

TABLE 17 The results of separate fits for the regeneration power law, α, and magnitude, A, in the neutral and charged data.

	α	A	χ^2 (for 9 d.o.f.)
Charged	-0.602 ± 0.010	$5.878 \pm 0.018\,\mathrm{mb}$	11.5
Neutral	-0.601 ± 0.010	$5.872 \pm 0.018\,\mathrm{mb}$	8.6

9.4 Evaluation of the Systematic Errors

The error reported on $\mathrm{Re}(\varepsilon'/\varepsilon)$ in Equation (9.11) included only the statistical contribution; however, the significance of the result depends on the size of the systematic contributions as well. Systematic errors could arise from asymmetries in the beams, from biases due to rate effects, from uncertainties in the background subtractions, in the calorimeter response, or in the acceptance corrections, and from rate effects. All of these are discussed in the following sections, in ascending order of importance. As a check of the entire procedure as well as a test of the acceptance corrections, the values of the parameters Δm, $\Delta\phi$, and τ_S were extracted from the data. These determinations are discussed in Section 9.4.5.

Since they will be referred to often in what follows, we define more precisely the quantities R_{00} and R_{+-}, the ratio of regenerated to vacuum decays for the neutral and charged modes are given by the following geometric mean:

$$
R = \sqrt{\frac{\left(\sum_p N_{Ru}(p)/\varepsilon_{Ru}(p)\right)\left(\sum_p N_{Rd}(p)/\varepsilon_{Rd}(p)\right)}{\left(\sum_p N_{Vu}(p)/\varepsilon_{Vu}(p)\right)\left(\sum_p N_{Vd}(p)/\varepsilon_{Vd}(p)\right)}}
\tag{9.12}
$$

where the symbols represent the neutral or charged quantities as appropriate. Recall that

$$
\frac{R_{+-}}{R_{00}} \approx \mathbf{R} \equiv 1 - 6\mathrm{Re}\left(\frac{\varepsilon'}{\varepsilon}\right)
\tag{9.13}
$$

so that an an error of 0.1% in R_{+-} or R_{00} corresponds to an error of 0.0002 on $\mathrm{Re}(\varepsilon'/\varepsilon)$.

9.4.1 Beam Asymmetries and the Geometric Mean

In the ideal double beam experiment, the intensity of the two kaon beams would be identical. In this case, the livetimes and detector efficiencies would be independent of the regenerator position. In reality, however, the beam intensities are unlikely to be equal, as for example in this experiment the kaon flux was 8% higher in the upper beam than in the lower, so bias could develop. These biases can be obviated and the elegance of the double beam technique recovered by calculating the geometric mean of decays in the two regenerator configurations as given by Equation (9.6). This section will look at how that comes about.

Let the incident kaon flux in the vacuum beam be I_u and I_d in the upper and lower beams respectively. Now consider the two possible beam configurations: in (a), the regenerator lies in the lower beam; in (b), the regenerator lies in the upper beam. Since most of the particles passing through the detector originated from decays and interactions of the vacuum beam, the higher intensity of the upper beam lead to greater particle flux in configuration (a). One consequence of this was that the detector livetime, or the fraction of good triggers that was actually recorded, was smaller in configuration (a) than in (b). Let us represent the detector livetimes in the two configurations by ℓ_a and ℓ_b.

Detector efficiencies could also depend on the regenerator position, and, unlike the livetimes ℓ_a and ℓ_b, could affect charged and neutral decays differently. Primarily because of inefficiencies of the drift chambers, some charged decays which were well-contained within the detector fiducial volume failed to reconstruct properly. In addition, both neutral and charged events could be lost because of accidental event vetoes by particles produced in inelastic interactions of kaons or neutrons in the regenerator. Both of these losses were intensity dependent, and therefore sensitive to the regenerator configuration. Let us denote the efficiencies (= 1 − (total loss rate)) in the two configurations for the neutral and charged decays by $e_a{}^n$, $e_b{}^n$, $e_a{}^c$

and $e_b{}^c$ respectively. For now, assume that the detector inefficiency in each configuration affected K_S and K_L decays identically. Effects which distinguished between them will be treated in the next section.

Finally, the total exposure of the experiment to beam in the two configurations, f_a and f_b, could be different because of lost spills or time variations in the proton beam intensity.

Now consider the expressions for the number of vacuum and regenerated decays reconstructed in each of the two configurations, shown in Table 18 for the $\pi^0\pi^0$ modes. Based on these, the ratio of reconstructed vacuum to regenerated decays, r_{arith}, is
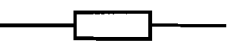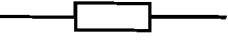
$$r_{arith} = \frac{N_{vu} + N_{vd}}{N_{ru} + N_{rd}}$$

$$= \frac{\left(\ell_a I_u e_a{}^n f_a + \ell_b I_d e_b{}^n f_b\right)|\eta|^2}{\left(\ell_b I_u e_b{}^n f_b + \ell_a I_d e_a{}^n f_a\right)e^{-X}|\rho|^2} \quad . \tag{9.14}$$

The value of R_{00} is thus shifted from its true value of $|\eta|^2/e^{-X}|\rho|^2$.

Next, instead of the arithmetic mean, let us calculate the geometric mean of events in the upper and lower beams, given by

$$r_{geom} = \left[\frac{N_{vu}N_{vd}}{N_{ru}N_{rd}}\right]^{1/2}$$

TABLE 18. The effects of beam asymmetries on the number of neutral decays observed in the vacuum and regenerated beams for the two regenerator configurations. For simplicity, the interference and K_L decay terms have been omitted from the regenerated beam expressions.

Configuration	Beam	Number of $\pi^0\pi^0$ decays observed
Regenerator	(vac.)	$N_{vu} \propto \ell_a I_u e_a{}^n f_a |\eta|^2$
Down (a)	(reg.)	$N_{rd} \propto \ell_a I_d e_a{}^n f_a\, e^{-X}|\rho|^2$
Regenerator	(reg.)	$N_{ru} \propto \ell_b I_u e_b{}^n f_b\, e^{-X}|\rho|^2$
Up (b)	(vac.)	$N_{vd} \propto \ell_b I_d e_b{}^n f_b |\eta|^2$

$$= \left[\frac{\ell_a I_u e_a{}^n f_a \; \ell_b I_d e_b{}^n f_b}{\ell_b I_u e_b{}^n f_b \; \ell_a I_d e_a{}^n f_a} \right]^{1/2} \frac{|\eta|^2}{e^{-X}|\rho|^2}$$

$$= \frac{|\eta|^2}{e^{-X}|\rho|^2} \; . \tag{9.15}$$

When the geometric mean is used, all the asymmetries cancel in the ratio of vacuum to regenerated decays. Use of the geometric rather than the arithmetic mean shifted R_{00} and R_{+-} by 0.12% and 0.18% respectively, consistent with the values of the parameters discussed above. The shift in the charged mode was slightly higher because of the rate dependence of the chamber efficiencies. The change in the double ratio was equal to the difference between the neutral and charged mode shifts, or 0.06%.

It is interesting to consider the case in which a single beam is used, with the regenerator (or target) periodically moved in and out. Then, only the terms depending on the two regenerator configurations would be relevant. It follows that, with the obvious notation, the measured ratio of $\pi^0 \pi^0$ rates would be:

$$r_{onebeam} = \frac{N_v}{N_r}$$

$$= \frac{\ell_a e_a{}^n f_a}{\ell_b e_b{}^n f_b} \frac{|\eta|^2}{e^{-X}|\rho|^2} \; , \tag{9.16}$$

so that bias is possible. If neutral and charged decays were collected simultaneously, the double ratio would be

$$\mathbf{R}_{onebeam} = \frac{\dfrac{\ell_a e_a{}^n f_a}{\ell_b e_b{}^n f_b} \dfrac{|\eta_{00}|^2}{e^{-X}|\rho|^2}}{\dfrac{\ell_a e_a{}^c f_a}{\ell_b e_b{}^c f_b} \dfrac{|\eta_{+-}|^2}{e^{-X}|\rho|^2}}$$

$$= \frac{e_a{}^n e_b{}^c \; |\eta_{00}|^2}{e_b{}^n e_a{}^c \; |\eta_{+-}|^2} \tag{9.17}$$

reducing, but not eliminating, the bias. More disparate particle fluxes of the two configurations would amplify the effect. Protection from this bias is the heart of the double beam technique.

9.4.2 Accidentals and Rate Effects

The previous section discussed variations in reconstruction efficiency which at any time affected K_S and K_L decays in the same way. In this section, we investigate effects which could distinguish between them. The invariant mass distributions K_S and K_L decays, which were almost identical in shape over many decades, as shown in Figures 120 and 121, suggest that the detector resolutions were the same for the two, but we must be sure that other biases were absent.
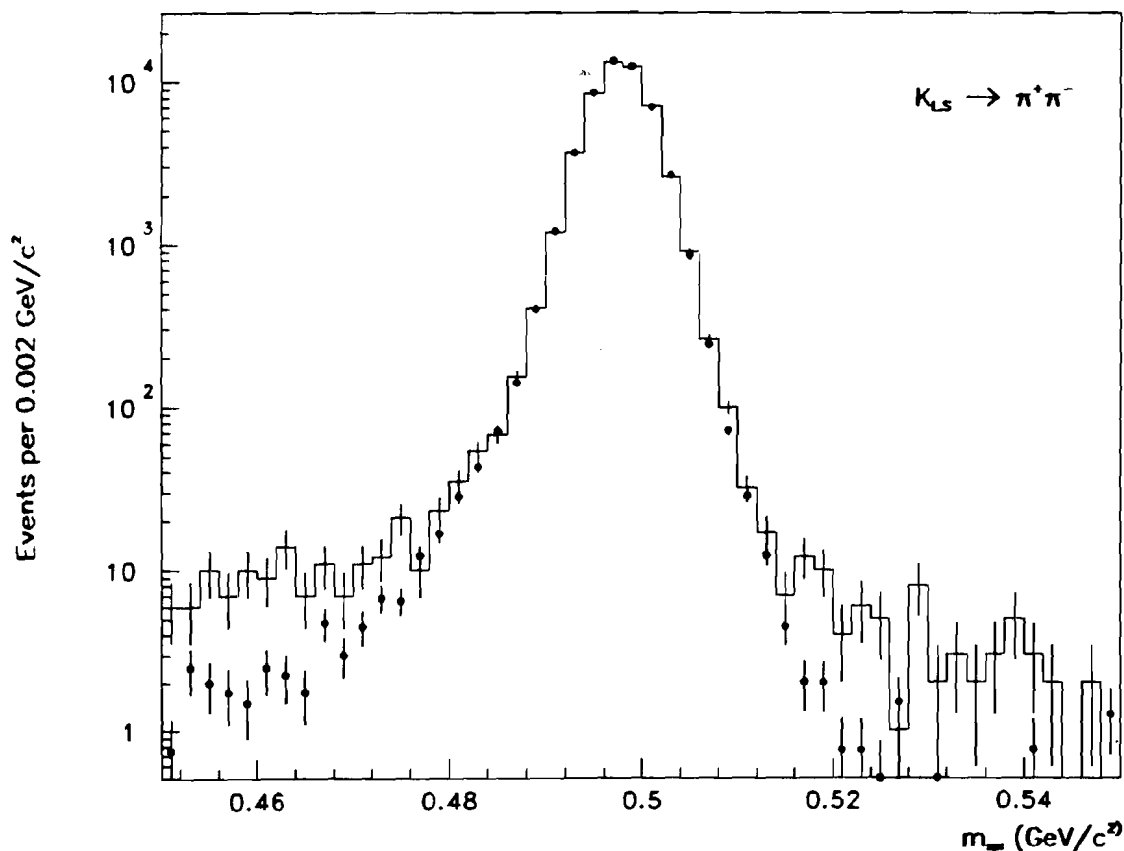
Figure 120. The superimposed invariant mass distributions of K_S and K_L decays to $\pi^+\pi^-$. The histogram represents the decays in the vacuum beam, while the solid circles represent those in the regenerated beam.

How could asymmetries come about? The extra particle flux concentrated around the vacuum beam was the main feature which distinguished it from the regenerated beam. It could lead to asymmetric losses either because of extra particles passing through the detector that overlapped good tracks or clusters and lead to misreconstruction, or, for the charged decays, because of changes in the trigger efficiency or chamber wire efficiencies in regions where the flux was high.

To study losses due to these effects we could look for variations in the ratio of reconstructed vacuum to regenerated decays as a function of the instantaneous rate, which was recorded with each event as described in Section 4.3. As a function of time into the run the beam intensity changed
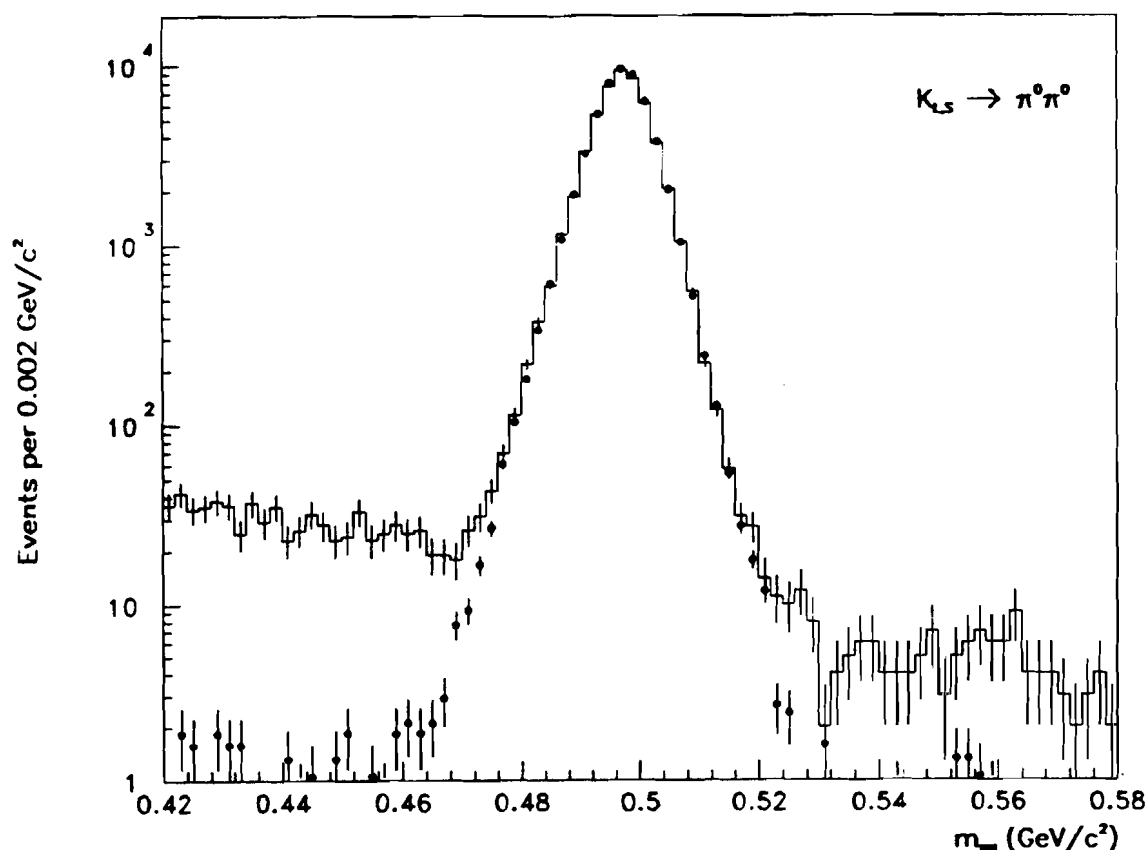
Figure 121. The superimposed invariant mass distributions of K_S and K_L decays to $\pi^0\pi^0$. The histogram represents the decays in the vacuum beam, while the solid circles represent those in the regenerated beam.

by about 30%, as shown in Figure 122, as machine conditions varied and we optimized the running conditions. Within the statistical errors, the ratio of K_S to K_L decays is constant throughout the run in both modes. The statistical power of the plot, however, is insufficient to guarantee that rate dependent effects were less than the desired 0.2%, and so further studies are necessary.

The rate dependent effects that could have biased us fell naturally into two separate categories. The first category included those arising from localized changes in detector efficiency which were correlated (or anti-correlated) with the position of the regenerator. Of these, the most dangerous would be a change in the drift chamber efficiencies or in the efficiencies of the scintillation counters used in the trigger. By design, the staves of the T counter bank were oriented vertically, covering the full height of the trigger plane with a photomultiplier tube at each end (see Figure 9). In addition, the trigger was based on the analog sum of all the photomultiplier signals. These two measures much reduced bias due to possible rate sensitivity of the phototubes or discriminators. The rates in the B and C bank were relatively low, about 1 Mhz over the entire plane, so their efficiencies were always high, over 99.9%, allowing negligible room for bias. Like the T bank, a single discriminator formed their trigger signals.

What about the drift chamber wires? The efficiencies of the wires in one of the chamber planes are overlaid in the top plot of Figure 123 for low and high intensity data, where the difference in the mean intensities of the two samples is about a factor of two. An overall efficiency drop of about 0.2% is evident at the higher beam intensities, except for a set of wires near the middle, where the degradation is larger, about 0.5%, because of a particularly rate sensitive signal amplifier card. Efficiency plots of the same wires for the two regenerator configurations (lower plot), however, are the same, indicating that no bias exists. The other wire planes' efficiencies were less rate sensitive, and were similarly independent of the regenerator position.

In the neutral mode, the only detector used in the trigger or reconstruction was the lead glass calorimeter, which was essentially 100% efficient for photons in our energy range. Although there were small rate de-
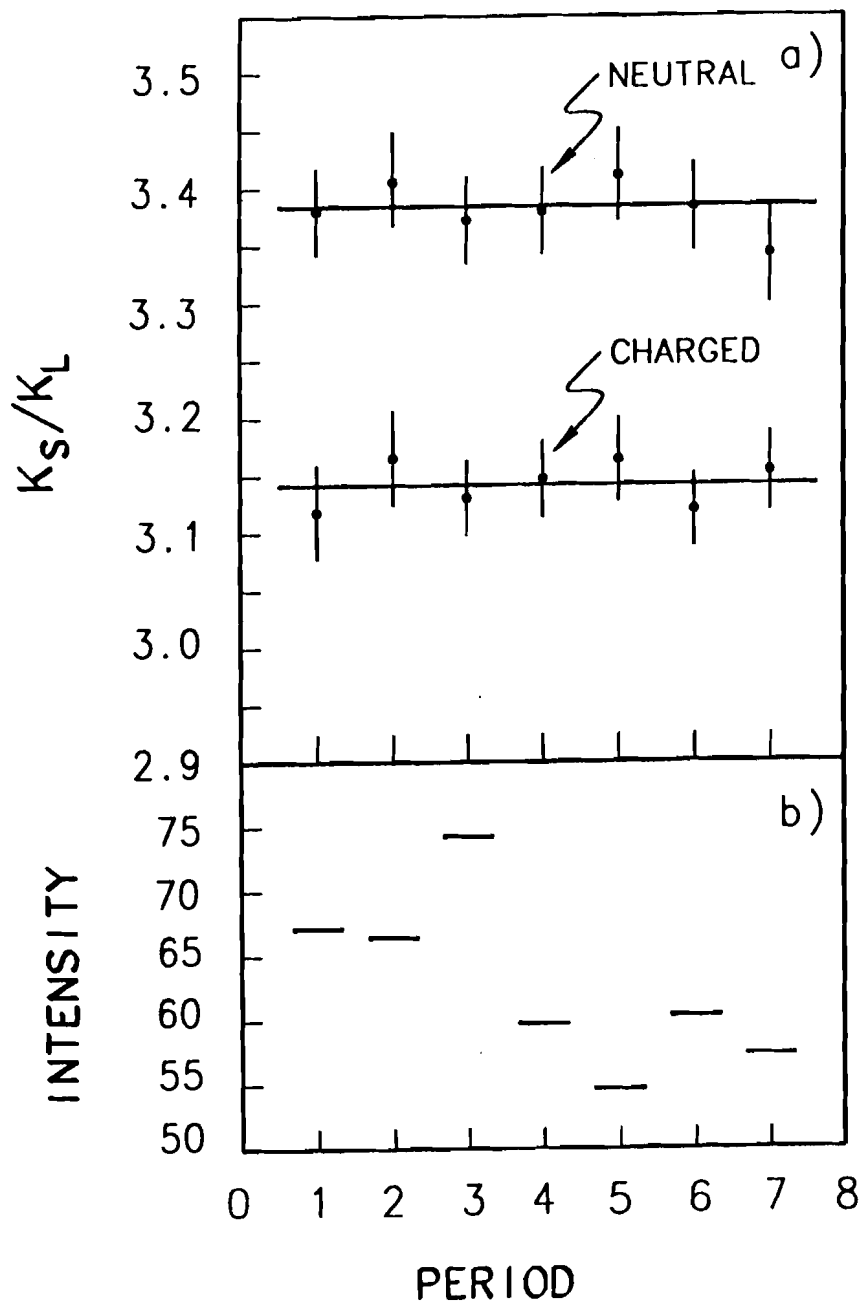
Figure 122. Stability of R_{+-} and R_{00} as a function of time into the run. Plot (a) shows the ratio of regenerated to vacuum decays in the neutral and charged mode in each of seven periods; (b) shows the corresponding average beam intensities. The charged and neutral ratios could be slightly correlated since arithmetic mean rather than the geometric mean was used to make the plot.
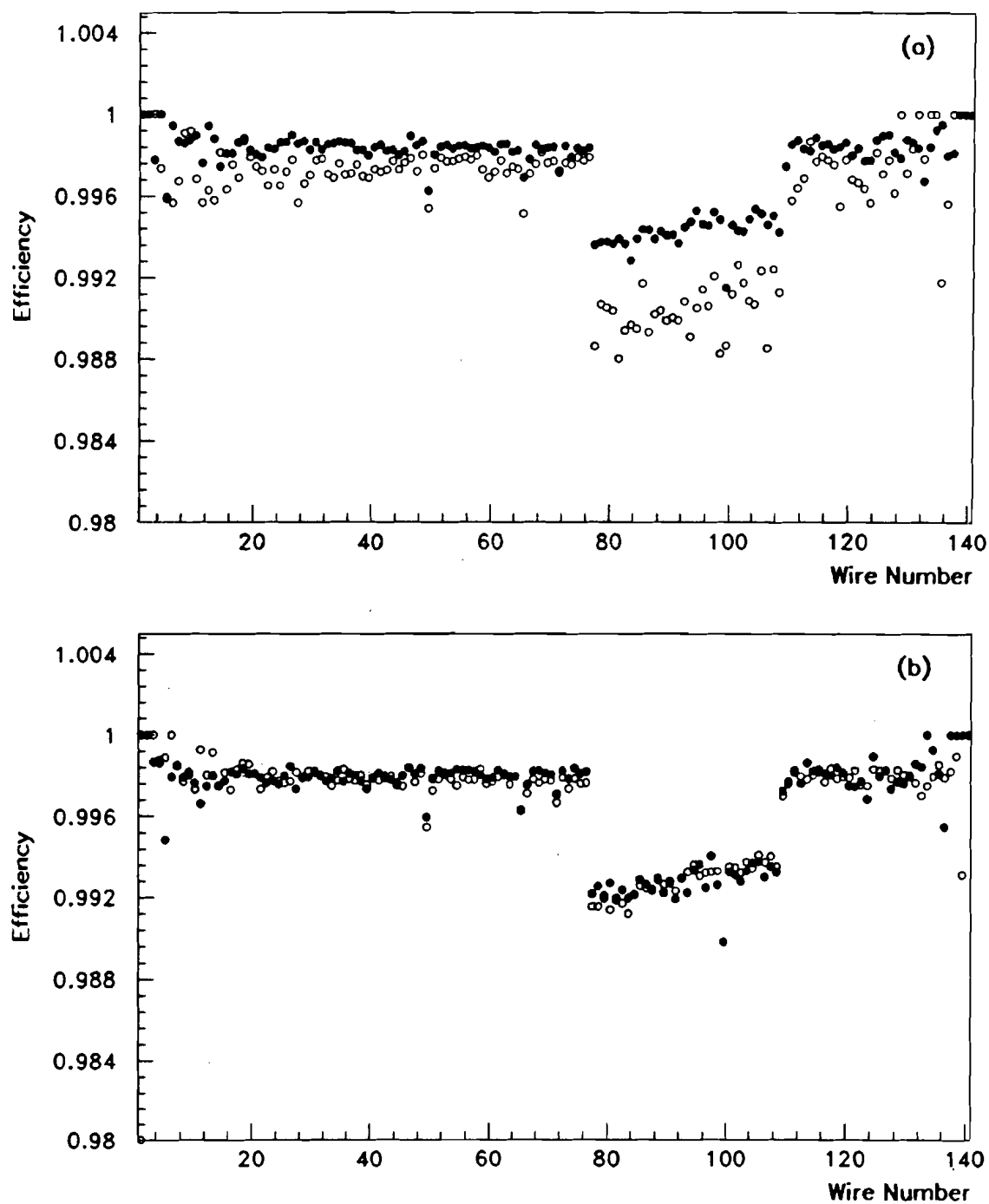
Figure 123. The efficiencies of each wire in downstream *y* plane of drift chamber 4. Plot (a) shows the efficiencies during low intensity (solid circles) and high intensity (open circles) running; (b) shows the average efficiencies when the regenerator was up (solid circles) and down (open circles).

pendent shifts in the ADC pedestals, the maximum excursion was only 10 MeV per block, too small to cause any significant bias.

The second category of rate dependent event loss arises from extra random particles passing through the detector at about the same time as the kaon decays. From studies discussed shortly, it was known that 2.7% of the time a random particle struck the lead glass and left a cluster within a few nanoseconds of the photons from a kaon decay. On average, there were 8.5 extra chamber hits, and an extra in-time track (i.e., a track that would satisfy the sum of distances cut) 0.3% of the time. Bias was possible because the extra hits and clusters were concentrated around the vacuum beam.

To determine the relative loss of K_S and K_L decays, the decrease in reconstruction efficiency was determined for each mode when extra hits and clusters were superimposed on the otherwise clean Monte Carlo events. A special data set of "accidental" events recorded during the run along with the normal $\pi\pi$ data provided the extra clusters and hits. These events were triggered by a coincidence in two scintillation counters aimed at the target and beam dump as shown in Figure 124; therefore, they sampled the detector under exactly the same conditions as the $\pi\pi$ data, and in particular, had the same instantaneous intensity distribution. Like the $\pi\pi$
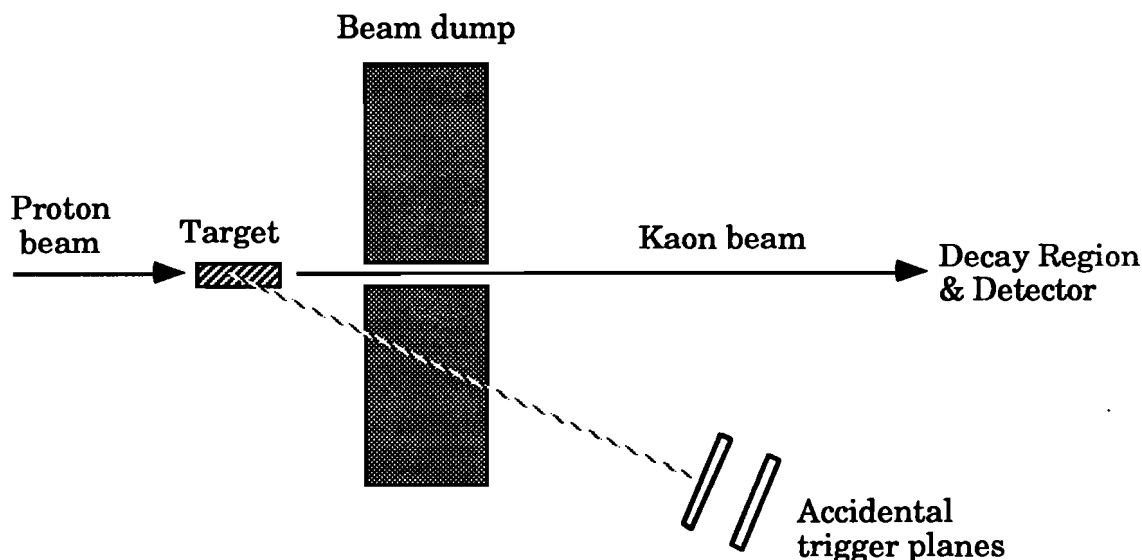
Figure 124. A schematic representation of the accidental trigger apparatus.

triggers, the accidental trigger was timed to the Fermilab RF signal.

In the Monte Carlo study, the signals in the counter banks observed in one of the accidental events were added to those in the Monte Carlo as it was generated. The TDC responses were simulated in detail, including dead-time effects. Care was taken that the regenerator position was the same for the accidental and Monte Carlo events. Once the signals had been overlaid, the trigger logic was simulated, and acceptable events were written to tape and analyzed in the usual way.

The activity in the accidental events closely duplicated that in the $\pi\pi$ events written to tape: for example, energy deposits in the MU1 counter bank, in which we expect no signal for $\pi^0\pi^0$ events, were similar for the $\pi^0\pi^0$ samples and the accidental triggers. The χ^2 distributions of the reconstructed tracks, which deteriorated somewhat with the instantaneous beam intensity in the data, showed the same behavior in the overlaid Monte Carlo events, as illustrated in Figure 125 (the instantaneous beam intensity was recorded with the accidental as well as the $\pi\pi$ triggers).

When the accidentals were added to the charged events, about 9% of the events were trivially lost to vetoes by the RA or muon filter. The reconstruction efficiency for the remaining events dropped by about 10%. Of the events that were lost, in 4.7% the wrong number of tracks was found, and in 3.6% the reconstructed tracks failed the track quality cuts. In remaining events the tracks did not meet at a vertex or overlapped in x at the lead glass,[1] or the event failed the P_t^2 cut. The losses were the same for decays in the regenerated and vacuum beams: accidentals changed the ratio R_{+-} by $(-0.04 \pm 0.07)\%$.

When the accidental events were overlaid on the neutral decays, the non-trivial loss was about 4%. Of these, about 3.55% were lost because of one or more extra clusters in the lead glass and 0.38% were lost because the pairing χ^2 was poor. The change in the ratio of regenerated to vacuum events was within the statistical error of the study, again $(-0.04 \pm 0.07)\%$.

---

[1] Normally events with nearby tracks in x are lost by the left-right Chamber 2 requirement of the trigger. In these events, the two pions passed through the chamber on one side and a random particle passed through the other, so the trigger requirement was artificially satisfied.

Other studies were done to test the results from the accidental over-lays. In particular, it was possible that the fraction of tracks surviving the cuts on the track χ^2, matching of the upstream and downstream segments, and the two-track distance of closest approach might be sensitive to local activity in the chambers; however, when these cuts were loosened by a factor of two, R_{+-} changed by only -0.09%.

From all these studies, we concluded that the error on the double ratio was less than 0.07% due to asymmetry in the neutral decays and less than 0.07% due to asymmetry in the charged decays. The combined error on the double ratio R_{+-}/R_{00} is $\pm 0.10\%$.
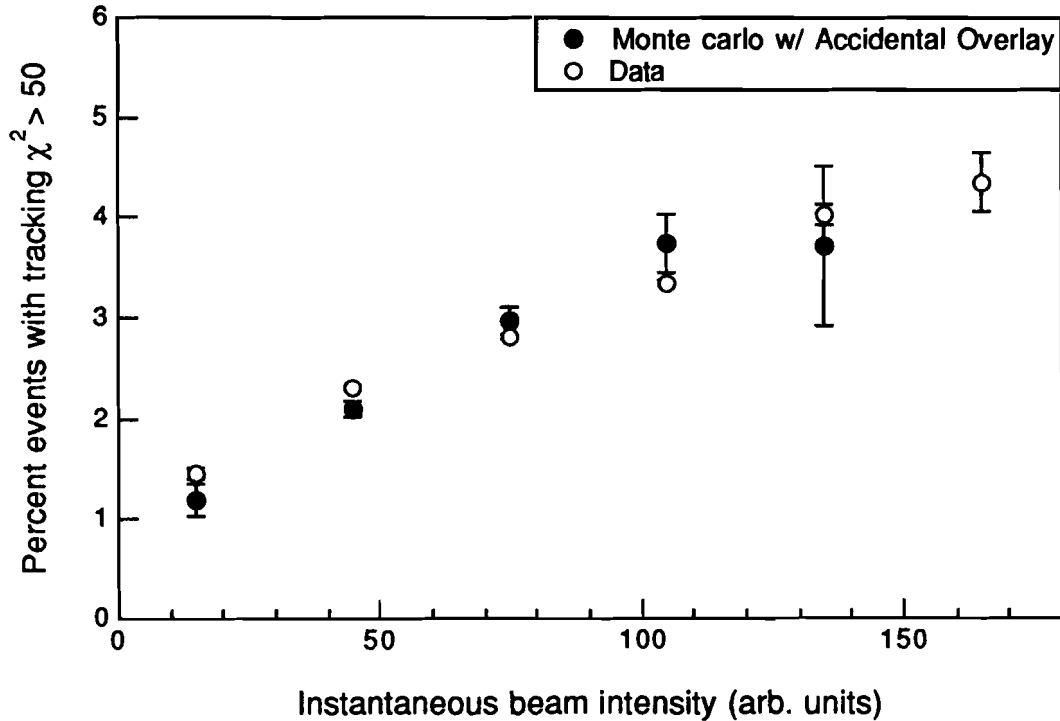
Figure 125. The percent of $K_L \to \pi^\pm e^\mp v$ decays with at least one track with $\chi^2 > 50$ as a function of beam intensity as observed in the data and in the Monte Carlo with accidentals superimposed. A constant offset of 9.3 due to δ-rays (which are not simulated in the Monte Carlo) was subtracted from the points representing the data.

9.4.3 Background Subtractions

The backgrounds were summarized in Tables 8 and 12, and their uncertainties were described there.

Of the backgrounds, the largest by far were the non-coherent K_S contributions to the neutral decays. Because they are not obviously independent of one another, it is worth discussing this before combining their uncertainties. In the systematic studies described in Chapter 7, the evidence was that the backgrounds of the vacuum and regenerated decays were either uncorrelated, or positively correlated, so that the change in backgrounds partially cancelled in the ratio of vacuum to regenerated decays. For example, when the background was normalized directly using the non-coherent tail, rather than the more intricate method described in Chapter 7, the background to the vacuum and regenerated decays increased by 0.09% and 0.03% respectively, so that the ratio of signals in the two beams changed by only 0.06%. Since shifts in the backgrounds tended to cancel in the ratio in this study and others, we believe that adding them in quadrature is a conservative, approach.

The errors on the other backgrounds are all small and independent of one another. The combined error due to all backgrounds is then 0.18%, where we have added in quadrature.

9.4.4 Energy Scale and Resolution

The Origin of Sensitivity to the Calibration

As discussed in Section 6.1, the fit for $\mathrm{Re}(\varepsilon'/\varepsilon)$ was done by comparing the predicted number of events over the z range in each p bin with the number actually observed. It was therefore important to count the number of events over the z interval accurately. The result depended on knowing the the position of the decays with respect to the boundaries of the fiducial region. For the K_S decays, the region $120 \text{ m} < z < 137 \text{ m}$ included nearly all events, so a 7 cm shift in the decay distribution would have been required to change the size of the data sample by 0.1%. For the K_L decays a shift in z was more important because many events lay near the boundaries of the

fiducial region. For example, if the z distribution were shifted 4 cm downstream, 0.2% of the K_L decays would enter the data sample at the upstream end.

For the charged decays, the systematic uncertainty on the z vertex positions was about 5 mm due to uncertainty in alignment of the drift chambers, and it was determined with nearly the same precision by comparing the positions of the edges of z vertex distributions of the data and Monte Carlo where they cut off sharply at the trigger plane. The resulting systematic error on R_{+-}/R_{00} was negligible.

The situation was different for the neutral decays. As discussed in Section 6.1, the position of the decay distribution depended on the photon energies measured in the lead glass calorimeter. An error of 0.1% in their absolute energies shifted the positions of decays at the center of the decay region by 4 cm. In this section, we will discuss how the z distributions of the data and Monte Carlo were aligned and will determine the size of the systematic error due to any residual misalignment.

Closely related to this is the question of reproduction of the decay vertex resolution in the data by the Monte Carlo. This will limit the precision with which we can align the data and Monte Carlo, and also, as discussed in Section 8.1.1, is a potential source of systematic error in its own right since the number of events in our samples depended on smearing of events over the boundaries of the decay region.

Finally, for a calorimeter with many elements, one overall energy scale does not tell the whole story; rather, there are as many energy scales as there are lead glass blocks. So to test the energy scale, one must also study sensitivity to changes in the energy scale not just of the array as a whole, but also of individual regions of the array. Some of these tests are also described.

Estimating the Uncertainty in the Energy Scale and Resolution

In order to align the data and Monte Carlo decay distributions, the energies of the photons in the data were adjusted to yield the same mean decay vertex position as the Monte Carlo for regenerated decays. The

TABLE 19. The adjustment to the photon energies
applied in each kaon energy bin.

Kaon Energy (GeV)	Photon energy correction factor
45	0.9940
55	0.9947
65	0.9952
75	0.9958
85	0.9964
95	0.9960
105	0.9956
115	0.9953
125	0.9949
135	0.9945
145	0.9942

adjustment varied slightly with the kaon energy, as shown in Table 19, but on average was about 0.5%. It was consistent in size with the residual errors in scale seen in other distributions such as the invariant mass of π^0's from $K_L \to \pi^+\pi^-\pi^0$ decays, and its origin is largely understood (see Section 6.8.4).

The uncertainty in the energy scale arose from uncertainties in tuning the z distributions. Even after alignment, small discrepancies were visible in the edge (see Figure 112); however, it was unclear whether these were due to errors in the energy scale or in the resolution of the calorimeter. Nevertheless, shifting the energy scale by 0.1% (6 cm at the regenerator edge) or more lead to clear discrepancies in the z distributions, and so we concluded that this was the upper limit on the residual error.

No tuning was done to the energy resolution to change the shape of the z distribution. The uncertainty on the resolution was determined by further smearing the energies of the photons in the data or the Monte Carlo and comparing the resulting distributions. When photon energies in the Monte Carlo were smeared by 1% (in quadrature) beyond their usual resolution, agreement between the shapes of the z distributions changed only

slightly, while smearing the energies in the data by 1% seriously degraded agreement (see Figure 126). Thus, the resolution error was asymmetric, and further comparisons indicated that it lay in the range from −1.5% to 0.5%, where a positive (negative) resolution error implies better resolution in the data (Monte Carlo). Overlays of other distributions, such as E/p (Figure 64) and the π^0 mass (Figure 67), were consistent with residual resolution errors in this range.

Estimating the Systematic error due to Energy Scale and Resolution

It now remains to calculate the effect of such errors on the ratio of regenerated to vacuum events. The change in R_{00} as a function of the shift in the energy scale, shown in Figure 127, is approximately linear. The uncertainty in R_{00} corresponding to the 0.1% uncertainty in the energy scale is −0.03%.

This insensitivity to the energy scale was due to a judicious choice of the fiducial region. Under a small shift in the energy scale, the same number of vacuum events enters the decay region at the upstream end as leaves it at the downstream end. A shift in the energy scale changed the z position of upstream decays by about 50% more than it did downstream decays since they were 50% further from the lead glass. Thus, perfect cancellation would occur if the number of events in the bins neighboring the upstream cut was 2/3 the number in the bins neighboring the downstream cut. Cuts at 120 and 137 m realize this condition; this was the primary reason for their location. Had the upstream cut been located at $z = 110$ m, the error on $\mathrm{Re}(\varepsilon'/\varepsilon)$ due to uncertainty in the energy scale would have been a factor of ten greater.

Sensitivity to the resolution uncertainty was greater than sensitivity to the energy scale. The dependence of R_{00} on the additional smearing of the data or Monte Carlo is shown in Figure 128. The residual uncertainty on the smearing corresponds to an uncertainty in R_{00} of about 0.15%. This sensitivity also depended on the z cut, and would have been minimized if the distribution near the upstream cut had been flat or sparsely populated.
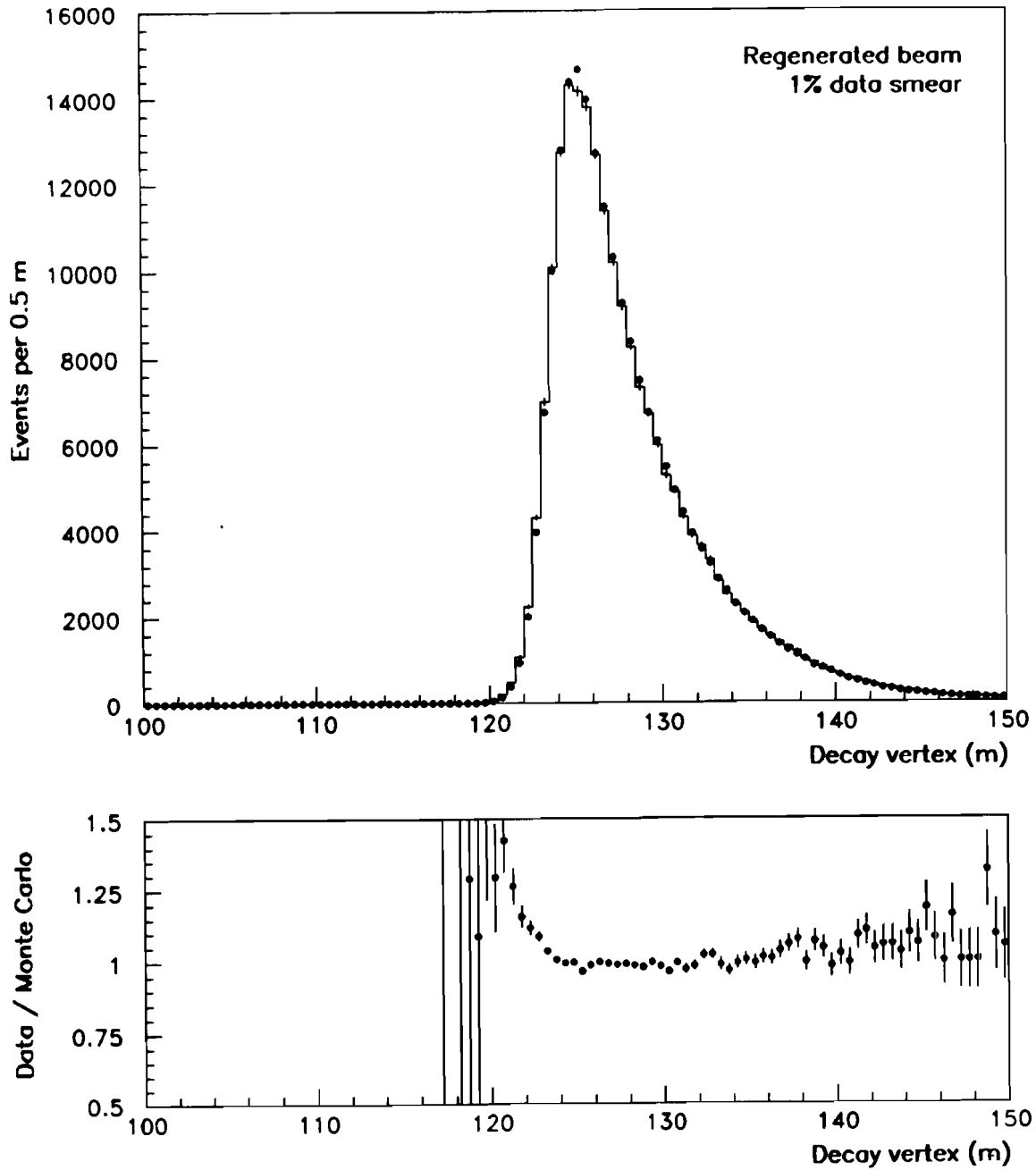
Figure 126. The z distribution of $K_S \rightarrow \pi^0 \pi^0$ decays for Monte Carlo and resolution smeared data. The histogram represents the data with the cluster energies smeared by 1%, while the solid circles are the Monte Carlo. For comparison with unsmeared data, see Figure 112 (note the change in scale of the lower window).
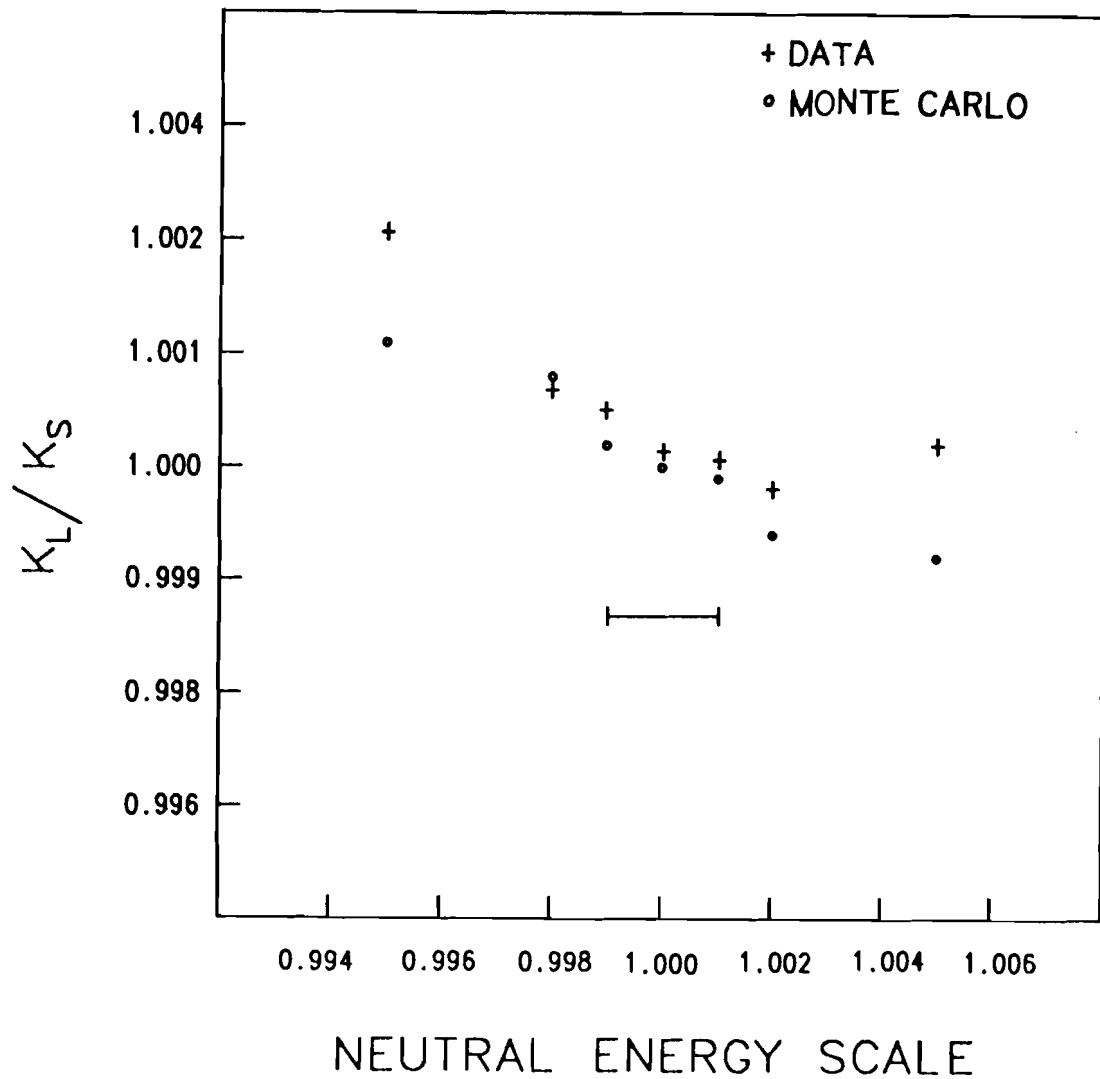
Figure 127. The ratio of vacuum to regenerated beam decays as a function of the energy scale adjustment applied to the data, where 1.0 corresponds to the standard adjustment. The horizontal bar represents the residual uncertainty in the energy scale.

In addition to overall errors in the energy scale or resolution, other calibration errors were possible. To test whether the result was sensitive to these, a variety of studies were done in which we artificially corrupted the photon energies and varied the cuts sensitive to the calibration. The results of the studies are tabulated in Table 20. From these studies and the sensitivity to the overall energy scale and resolution, we assigned a systematic error of 0.2% on the double ratio due to uncertainty in the calibration.

9.4.5 Uncertainty in the Acceptance Corrections

The acceptance corrections were the largest source of systematic error. Fortunately, many tools were available to assess their uncertainties. The discrepancies in the overlays of the data and Monte Carlo illuminations shown in Chapter 8 suggested that the systematic errors on R_{00} and
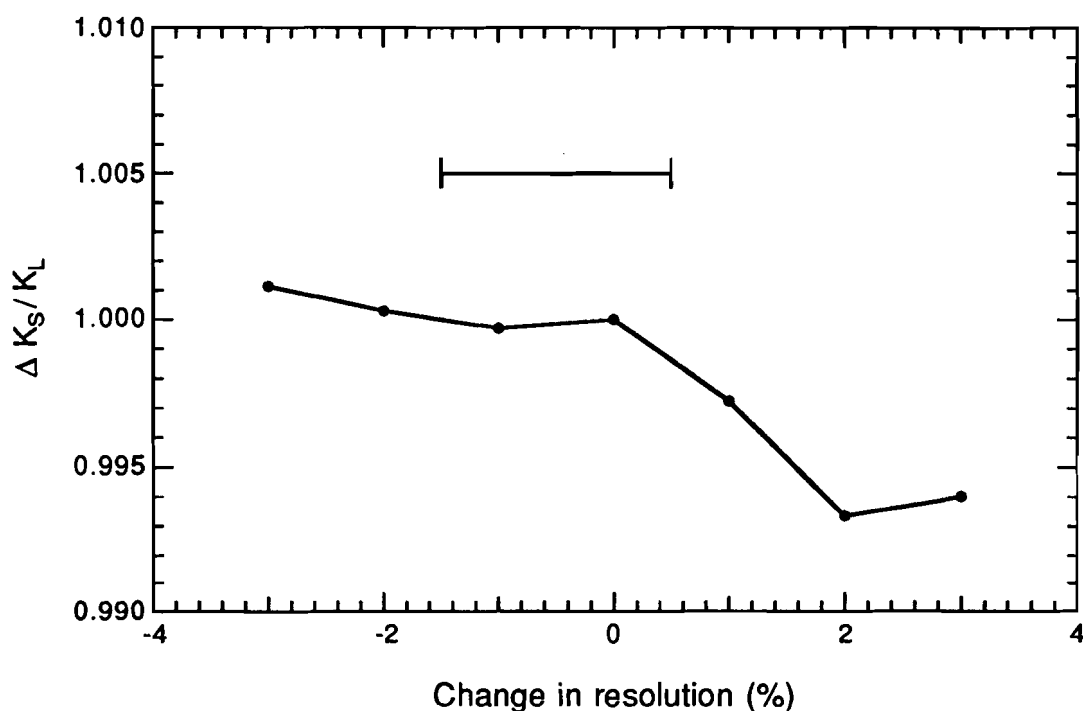
Figure 128. The value of R_{00} as a function of the resolution error. The points corresponding to negative (positive) smearing were obtained by smearing the Monte Carlo (data). The bar indicates the uncertainty in the resolution.

TABLE 20. The sensitivity of R_{00} to changes in the photon energies.

Change to Photon Energies	Change in R_{00} (%)
Decrease by 2% the energies of photons hitting a block adjacent to one of the beam pipes	-0.05
Increase by 20 MeV the energies of photons in the upper half of the array & decrease by 20 MeV those in the lower half	-0.09
Increase by 0.2% the energies of photons in the upper half of the array & decrease by 0.2% those in the lower half	-0.11
Increase by 0.4% the energies of all photons below 8 GeV	-0.14
Use the same energy adjustment in all p bins (see Table 19)	-0.01

R_{+-} due to acceptance were a few tenths of a percent or less. In the following sections we will describe further acceptance checks. After that, we will report on fits for Δm, the K_S lifetime and the phase difference between η_{+-} and η_{00} which also check the acceptances.

The Charged Acceptances

In the first check of the acceptance for charged decays, we measured the ratio of data to Monte Carlo events as a function of z in each p bin. The slopes of straight lines fit to the ratio over the region $120 < z < 137$ m, plotted in Figure 129 as a function of the kaon momentum, were consistent with no acceptance error, though the highest momentum bin deviated somewhat. From the mean value of $(0.08 \pm 0.09)\%$/m and the 1.3 m difference in the mean decay positions of vacuum and regenerated decays, the estimated error on R_{+-} was $\pm (0.11 \pm 0.12)\%$.

Unfortunately, the statistical uncertainty on the slopes was comparable to the size of the systematic error we were looking for. This inspired a similar test which took advantage of the immense statistical power of the
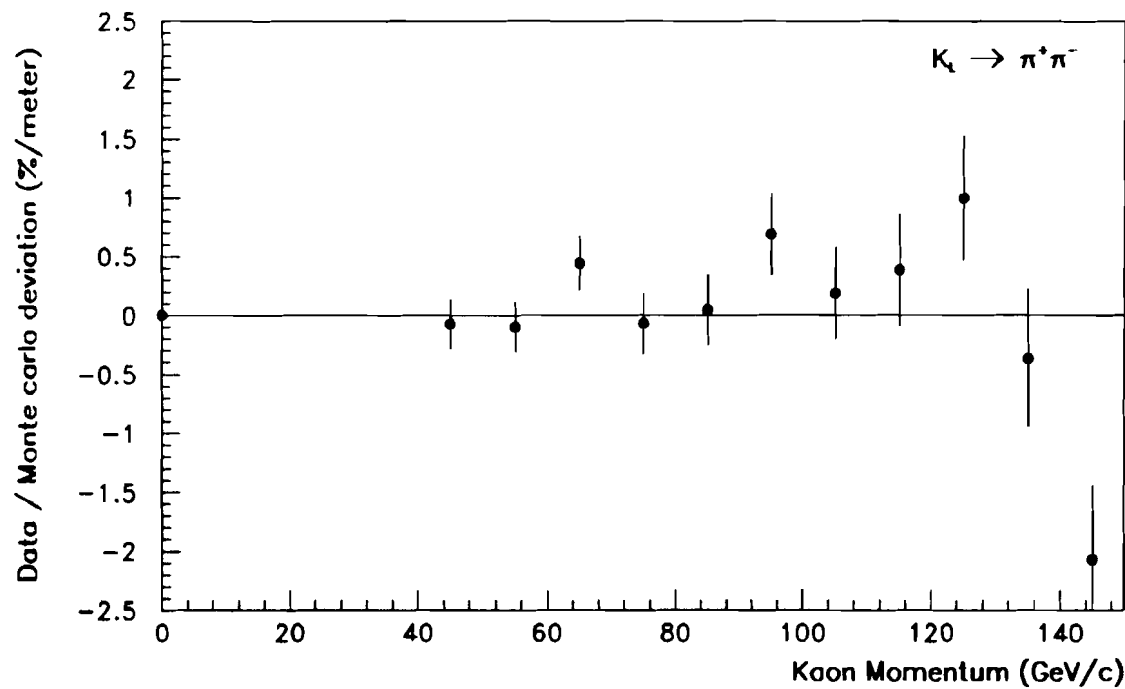
Figure 129. The slope of lines fit to the ratio of data and Monte Carlo decay vertex distributions as a function of the kaon momentum bin for $K_{L,S} \to \pi^+\pi^-$ decays.

$K_L \to \pi^+ e^\mp \nu$ data sample. The test used the deviation between the $K_L \to \pi^+ e^\mp \nu$ data and Monte Carlo decay vertex distributions to correct the $\pi\pi$ acceptance error as a function of p and z. Although the kinematics, and therefore the acceptance errors, of the $K_L \to \pi^+ e^\mp \nu$ decays are not identical to these of the $\pi\pi$ decays, they are similar, so the effect of the corrections was a good indicator of the acceptance error. When the corrections were made, the value of R changed by −0.05%.

In another test, the fit was repeated with the data divided into small z bins. Because the variation in acceptance was small within each bin, the acceptance corrections to the regenerated and vacuum decays nearly cancelled. Thus the fit should yield the same answer as before, but with much reduced sensitivity to acceptance errors. We found that R changed by

–0.28%, consistent with the unbinned value within the increased statistical error.[1]

We also studied the effect on Re(ε'/ε) when cuts were varied: changes in the z range (± 2 m), in the minimum track momentum (7 to 10 GeV/c) and removal of the mask aperture cut (3 mm increase in the aperture size) all changed **R** by less than ±0.1%. Furthermore, as described in Chapter 8, changes in the apertures, momentum spectrum and targeting angle used in the Monte Carlo typically changed the ratio of K_S to K_L decays by 0.1% or less.

The Neutral Acceptances

The tests of the neutral mode acceptances paralleled those of the charged mode. The slopes of straight line fits to the ratio of data and Monte Carlo decay vertex distributions in each p bin are shown in Figure 130. Their weighted average of (0.038 ± 0.096)%/m together with the 1.4 m difference in the mean regenerated and vacuum z distributions suggest a systematic error on R_{+-} due to acceptance of ± (0.05 ± 0.13)%.

Again we must turn to a higher statistics mode for a more significant test, in this case the $K_L \to \pi^0\pi^0\pi^0$ data sample. When the deviations of the $\pi^0\pi^0\pi^0$ Monte Carlo from the data were used to modify the acceptances of the $\pi^0\pi^0$ modes as a function of z in each momentum bin (see Figure 114 for the momentum averaged deviations), the value of R_{00} changed by 0.08%. As in the corresponding charged mode study, these errors were not expected to be identical to the acceptance errors in the $\pi\pi$ decays (or we would have made even better use of them), but they are a good indicator of their size.

Fitting for the result in 2 m z bins was less valuable for the neutral decays than the charged because of increased sensitivity to the energy scale and resolution, which added a systematic uncertainty of 0.7% on R_{00}.

---

[1] To estimate the statistical error expected on the result when the small bins were used, we serially substituted four independent monte carlo samples for the data in the fit, and looked at the purely statistical fluctuations in the result. (When a single z bin was used in this study, fluctuations were consistent with the calculated statistical error.)
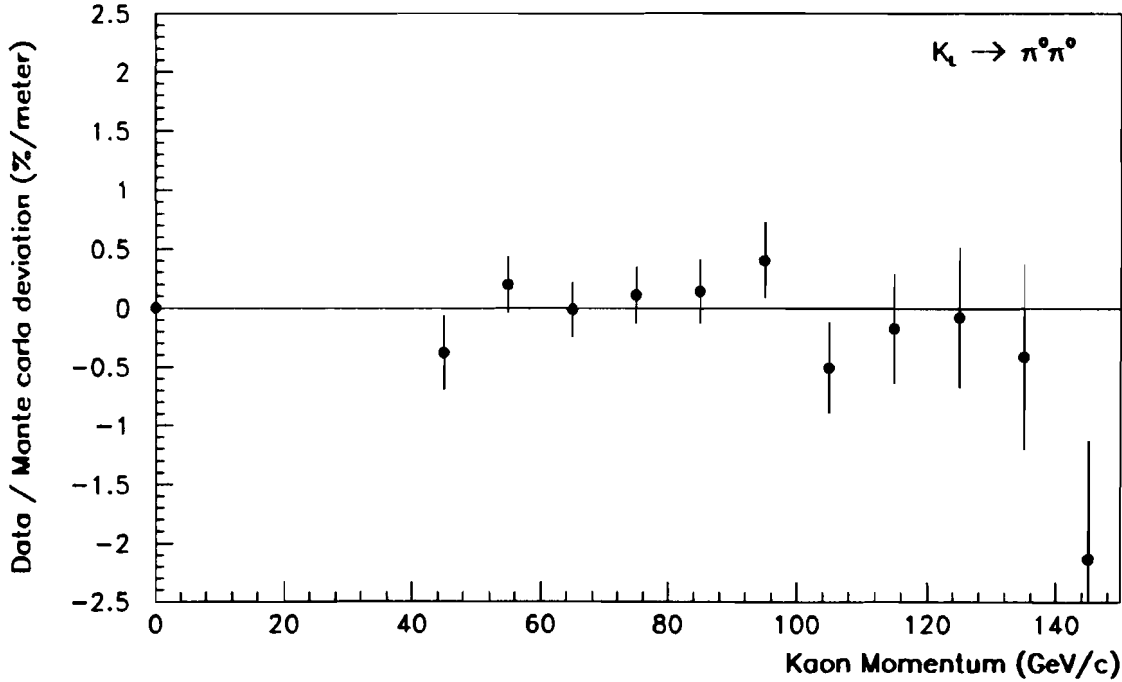
Figure 130. The slopes of lines fit to the ratio of data and Monte Carlo decay vertex distributions for $K_L \to \pi^0 \pi^0$ decays in each p bin.

Within that error, no change in $\mathrm{Re}(\varepsilon'/\varepsilon)$ was observed when the data were binned in z.

Many studies of the neutral acceptance were done in which apertures or analysis cuts were varied, and the results of those which tested the most sensitive aspects of the analysis are summarized in Table 21. Increasing the minimum cluster energy and applying a minimum cluster separation cut of 3 blocks both tested the sensitivity to the cluster energy reconstruction and the HCF thresholds. The cuts around the Collar-Anti, which effectively increased its size by 1 mm on all sides, tested the acceptance around the most sensitive aperture. The study of the MU1 cut tested for event loss due to leakage of shower energy out the back of the lead glass, as did requiring that the cluster energies be below 80 GeV.

Fits for Other Physical Parameters

The extraction of $\mathrm{Re}(\varepsilon'/\varepsilon)$ from the data was an intricate procedure. To give us confidence in the results, we extracted the values of other

TABLE 21. The change observed in R_{00} when the $K_{L,S} \rightarrow \pi^0\pi^0$ selection criteria were varied.

Change to Selection Criteria	Change in R_{00} (%)
Raise from 1.5 to 3 GeV the minimum accepted cluster energy	+0.08
Apply a maximum photon energy cut at 80 GeV	+0.06
Require that cluster centers be separated by at least 3 lead glass blocks	+0.13
Change from 2% + 6%/$\sqrt{E}$ to 3% + 5%/$\sqrt{E}$ the photon energy resolutions assumed in calculating the Pairing χ^2	+0.02
Eliminate all events with a photon striking the lead glass within 0.5 mm of the Collar Anti (data only)	+0.06
Eliminate all events with a photon striking the lead glass within 0.5 mm of the Collar Anti (data and Monte Carlo)	+0.01
Tighten by a factor of two the cut on MU1 activity	+0.04

parameters of kaon decay from the data using the same procedure. The values to which we were sensitive were the $K_L - K_S$ mass difference Δm, the K_S lifetime τ_S, and the phase difference between η_{00} and η_{+-}, $\Delta\phi$.

The extraction of $\Delta\phi$ has been published elsewhere [15]; its value was $-0.3° \pm 2.4°$ (stat.) $\pm 1.2°$ (syst.), consistent with expectations from CPT conservation.

Like $\Delta\phi$, the value of Δm depended on the shape of the decay distribution downstream of the regenerator. In the neutral and charged mode fits we found $(0.532\pm0.013)\times10^{10}\hbar$ sec and $(0.535\pm0.013)\times10^{10}\hbar$ sec respectively, both consistent with the PDG value [13] of $(0.5349\pm0.0022)\times10^{10}\hbar$ sec.

The final fit was for the K_S lifetime. Of all the fits, that for τ_S was most sensitive to acceptance corrections. We found values of $(0.8913\pm0.0027)\times10^{-10}$ sec from the neutral and $(0.8891\pm0.0029)\times10^{-10}$

sec from the charged fits, again consistent with one another and with the PDG value of $(0.8922 \pm 0.0020) \times 10^{-10}$ sec. The statistical uncertainties of the fits were equivalent to a precision of 0.05%/m on the kaon loss due to decay. Within this error the result was consistent with the PDG value, indicating that the error on the acceptance correction was of the order of 0.05%/m or less in each mode.

From the above studies, including the overlays, the stability of the acceptance ratios throughout the long development of the Monte Carlo, the studies with the high statistics modes, the agreement in the shapes of the z distributions of the data and Monte Carlo for both modes, and finally the accuracy of the value of τ_S, we conclude that the systematic errors on R_{+-}/R_{00} due to uncertainties in the charged and neutral mode acceptances were less than 0.18% each. A correlated error in the neutral and charged acceptances would cancel in their ratio, so we can safely combine their acceptances uncertainties in quadrature. The combined systematic error due to acceptance is then $\pm 0.25\%$ on R_{+-}/R_{00}.

9.5 The Result

The systematic errors are listed in Table 22. Added in quadrature, the total is $\pm 0.38\%$ on the double ratio R_{+-}/R_{00}, corresponding to ± 0.0006 on $\mathrm{Re}(\varepsilon'/\varepsilon)$. The final result is then

$$\mathrm{Re}(\varepsilon'/\varepsilon) = -0.0003 \pm 0.0014 \,(\text{stat.}) \pm 0.0006 \,(\text{syst.}) \qquad (9.18)$$

Combining the statistical and systematic errors in quadrature yields a total error of ± 0.0015.

This result is consistent with zero, and as such, it provides no evidence for direct CP violation, consistent with predictions of the superweak models. The next chapter will consider the implications of this result for the Standard Model. First, however, we compare this result with those of previous experiments.

The result is displayed along with those of past experiments in Figure 131. The only other result with comparable precision is the NA31 experiment at CERN, which found $\mathrm{Re}(\varepsilon'/\varepsilon) = 0.0033 \pm 0.0007 \,(\text{stat.}) \pm 0.0008$

TABLE 22. Summary of the systematic uncertainties in R_{+-}/R_{00}.

Source of Systematic Uncertainty		Uncertainty on R_{+-}/R_{00} (%)
Background subtractions		0.18%
Energy scale and resolution		0.20
Acceptance corrections		0.25
Rate effects		0.10
	Total	0.38%

(syst.), with a total error of ± 0.0011. The difference in the errors of the two experiments is due to the difference in the sizes of the data samples.

The central values of the two experiments differ by about two standard deviations, and their implications are rather different. The NA31 result provides a three standard deviation signal for direct CP violation. The result presented in this thesis implies that if direct CP violation occurs, it is a smaller effect than the one seen by NA31.

A two standard deviation difference is expected between two experimental results about 10% of the time, and the difference in these two results could be a statistical fluctuation; however, the techniques of the two experiments, and therefore the possible systematic effects, are quite different, and it is possible that one of these is responsible.

The NA31 technique differs from the one reported here principally in the following ways:

- They used a single beam which alternated between K_L and K_S approximately every eight hours. The K_L and K_S data were therefore collected separately.

- The K_S source was a target rather than a regenerator.

- The K_S target could be stationed anywhere along the decay volume. By varying its position, the z distributions of K_S and K_L

EXPERIMENT		RESULT (10⁻⁴)	STATISTICAL ERROR	SYSTEMATIC ERROR	COMBINED ERROR
1. YALE-BNL	1985	+17	72	43	83
2. CHICACO-SACLAY	1985	−46	53	24	58
3. E731 TEST	1988	+32	28	12	30
4. NA31	1988	+33	7	8	11
5. E731(20%)	1990	−3	14	6	15
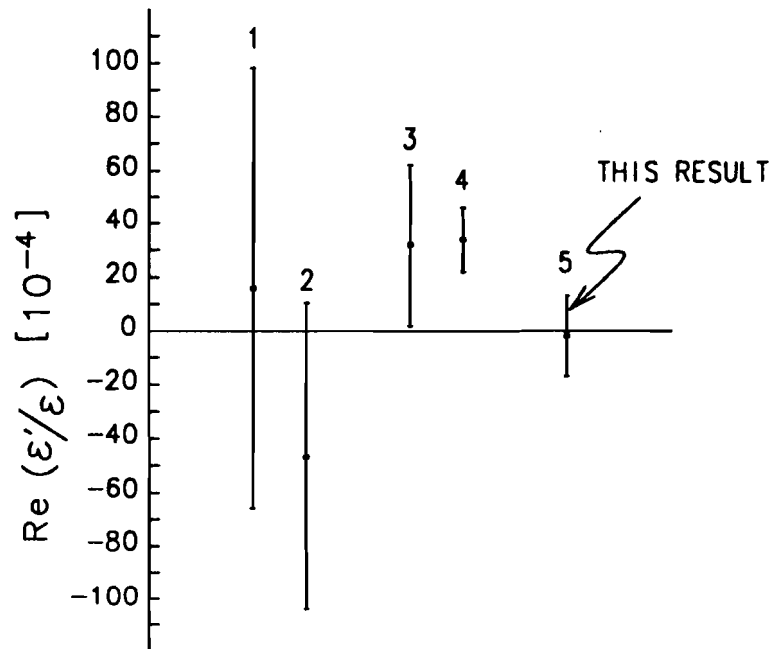
Figure 131. Results of recent determinations of $Re(\varepsilon'/\varepsilon)$.

could in principle have been made quite similar, thus reducing (but not eliminating) the importance of acceptance corrections.

    – No magnet was employed; instead the pion energies were determined with a hadronic calorimeter.

The categories of systematic error are the same for the two experiments: backgrounds, rate effects, energy scale and acceptance. Backgrounds and sensitivity to energy scale were comparable for the two experiments. The contrasts in rate and accidental effects and acceptance corrections are more interesting.

In both experiments, reconstruction of the charged and neutral decays depend on different components of the detector: the chambers and/or hadronic calorimeter for $\pi^+\pi^-$, and the electromagnetic calorimeter for $\pi^0\pi^0$ decays. As shown in Section 9.4.1, sensitivity to drifts and rate effects are inevitable unless decays to the same final state (i.e., those using the same detector components) are observed concurrently. In the NA31 experiment, the hadronic calorimeter response drifted and was intensity dependent, as were the drift chamber and trigger processor efficiencies. No matter how great the precautions taken to ensure the same reconstruction efficiencies for K_L and K_S decays, the fundamental susceptibility to bias remains.

The NA31 experiment used a single beam so they could move the target, thereby reducing acceptance corrections made necessary by the difference in K_L and K_S decay distributions; however, in spite of the presumably uniform decay distributions, they chose to bin the data in z. If the z distribution is non-uniform, use of small bins can amplify sensitivity to errors in energy scale and resolution.

The question of whether the difference in the two results is systematic or statistical will probably be resolved soon. The NA31 group has in hand a data set slightly larger than the last one. Improvements, such as addition of a transition radiation detector and greater similarity between the K_S and K_L momentum spectra, may reduce sensitivity to some systematic effects.

The result reported on in this thesis was based on only 20% of the data collected during the E731 run. The result based on the full data set will have a significantly smaller statistical error and a systematic error equal to or less than the one reported here.

In the next chapter, we will look at the results in the context of the Standard Model, and consider what the forthcoming results might reveal.

CHAPTER 10

DIRECT *CP* VIOLATION IN THE STANDARD MODEL

10.1 Why Search for Direct CP Violation?

Even now, twenty-five years after its discovery, the origins of *CP* violation remain a mystery. So far, *CP*-violating effects have been observed only in the two pion decays of the K_L and in the charge asymmetry of its semi-leptonic decays. Beyond that, we know only that if direct *CP* violation occurs, it is rather rare. The results of this experiment tells us that with 90% confidence $\mathrm{Re}(\varepsilon'/\varepsilon) < 0.0016$, and so, in spite of the NA31 evidence, the existence of direct *CP* violation remains an open question. We know for certain only that there is asymmetric mixing of the *CP* eigenstates, and so far this mechanism accounts for all the *CP*-violating phenomena that have been conclusively observed.

The origins of the asymmetry are unknown. Many models of particle interactions predict the size of *CP*-violating effects. In fact, for new models of particle interactions, consistency of predictions of Δm, ε and ε' with observation is a powerful constraint, and has proved a major stumbling block for many. For example, in one extension of the Standard Model, *CP* violation occurred from the exchange of additional Higgs bosons [40]; however, it predicted that $\mathrm{Re}(\varepsilon'/\varepsilon) \gtrsim 0.007$, which has now been ruled out. Superweak models predict that *CP* violation is observable only in kaon mixing and could therefore be eliminated if direct *CP* violation were detected.

Perhaps the model which one would most like to test through *CP* violation is the Standard Model, which has been extraordinarily successful at

260

describing electroweak physics. So far, no significant discrepancies of any kind have been found between its predictions and the experimental evidence. It is believed, however, to be only a low energy effective theory of a more fundamental theory, and as such it contains many free parameters (19) with no predictions for their values or their origins. One would like very much to discover the more global theory of which it is a manifestation, in which, for example, the values of these parameters could be expressed in terms of more fundamental constants.

If the Standard Model is only an approximation, then at some level there must be phenomena which it cannot explain. Much of the current research in high energy physics is geared either at observation of phenomena that are predicted not to occur, such as forbidden decays, or at determination of the values of the parameters with sufficient precision and redundancy to uncover discrepancies. Determination of $\text{Re}(\varepsilon'/\varepsilon)$ is a powerful tool in the latter effort.

In this Chapter, we will review the predictions of the Standard Model for $\text{Re}(\varepsilon'/\varepsilon)$ and examine the prospects for constraining it further through studies of CP violation.

10.2 The Cabbibo-Kobayashi-Maskawa Matrix

We begin with a brief review of the role of the Cabibbo-Kobayashi-Maskawa (CKM) matrix within the Standard Model. In the Standard Model the effective hamiltonian describing charged current interactions is of the form

$$H_{cc}{}^{eff} = -\frac{G_F}{\sqrt{2}}\left(J^{\mu\dagger}J_\mu\right) \tag{10.1}$$

where

$$J_\ell{}^\mu = \left(\bar{\nu}_e \quad \bar{\nu}_\mu \quad \bar{\nu}_\tau\right)\mathbf{I}_3\gamma^\mu(1-\gamma_5)\begin{pmatrix} e \\ \mu \\ \tau \end{pmatrix} \tag{10.2}$$

is the lepton charged current, with $\mathbf{I_3}$ the 3×3 identity matrix. The charged currents of the quarks can be expressed similarly:

$$J_q{}^\mu = (\bar{u}\quad \bar{c}\quad \bar{t})\;\mathbf{V}\;\gamma^\mu(1-\gamma_5)\begin{pmatrix} d \\ s \\ b \end{pmatrix} \tag{10.3}$$

where $\mathbf{V}$ is a unitary matrix of quark coupling constants of the form

$$\mathbf{V} = \begin{pmatrix} V_{ud} & V_{us} & V_{ub} \\ V_{cd} & V_{cs} & V_{cb} \\ V_{td} & V_{ts} & V_{tb} \end{pmatrix}\,. \tag{10.4}$$

It is straight-forward to show that the Lagrangian is invariant under the CP operation unless

$$\mathbf{V} \neq \mathbf{V}^*\,, \tag{10.5}$$

so $\mathbf{V}$ clearly plays a central role in CP violation in the Standard Model.

The requirement that $\mathbf{V}$ be imaginary for CP violation to occur has several immediate consequences. First, a 3×3 matrix is the smallest which can have complex elements that cannot be eliminated by changing the quark phases, and is therefore the smallest one that can provide CP violation. Interestingly, the desire to incorporate CP violation into the Standard Model was Kobayashi and Maskawa's motivation for introducing the third quark generation even before its discovery [41]. Similarly, no element of $\mathbf{V}$ may vanish, or quark rephasing could again eliminate the complex components. This in turn implies that neither the u-type nor the d-type quark masses can be degenerate [9].

An arbitrary unitary 3×3 matrix may be expressed in terms of three rotation angles and a complex phase, and many equivalent parametrizations of the CKM matrix have been proposed. The standard version is [13]

$$\mathbf{V} = \begin{pmatrix} c_{12}c_{13} & s_{12}c_{13} & s_{13}e^{-i\delta} \\ -s_{12}c_{23}-c_{12}s_{23}s_{13}e^{i\delta} & c_{12}c_{23}-s_{12}s_{23}s_{13}e^{i\delta} & s_{23}c_{13} \\ s_{12}s_{23}-c_{12}c_{23}s_{13}e^{i\delta} & -c_{12}s_{23}-s_{12}c_{23}s_{13}e^{i\delta} & c_{23}c_{13} \end{pmatrix} \tag{10.6}$$

where s_{ij} represents $\sin\theta_{ij}$ and c_{ij} represents $\cos\theta_{ij}$. Here we adopt the parametrization proposed by Wolfenstein [42]:

$$
\mathbf{V} = \begin{pmatrix}
1 - \frac{1}{2}\lambda^2 & \lambda & A\lambda^3\left(\rho - i\eta + i\eta\frac{1}{2}\lambda^2\right) \\
-\lambda & 1 - \frac{1}{2}\lambda^2 - i\eta A^2\lambda^4 & A\lambda^2\left(1 + i\eta\lambda^2\right) \\
A\lambda^3(1 - \rho - i\eta) & -A\lambda^2 & 1
\end{pmatrix} \quad (10.7)
$$

which satisfies the unitarity constraint to order λ^4. Since λ is known to be small, about 0.22, it is sufficient for most purposes to retain terms in the matrix elements only up to λ^3.

It has been observed that CP-violating effects in the Standard Model are always proportional to the quantity [9, 43, 44]

$$
J = s_{12}s_{23}s_{13}c_{12}c_{23}c_{13}{}^2 \sin\delta. \quad (10.8)
$$

In terms of the Wolfenstein parameters the quantity J is given by

$$
J = A^2\lambda^6\eta \quad (10.9)
$$

and the complex phase δ is given by

$$
\sin\delta = \frac{\eta}{\sqrt{\rho^2 + \eta^2}} \quad . \quad (10.10)
$$

The CP-violating phenomena are the only ones directly sensitive to $\sin\delta$, and so offer the most direct means of determining its value. It could be determined indirectly, however, through precise measurements of the magnitudes of the matrix elements.

The magnitudes of the CKM elements $|V_{ud}|, |V_{us}|, |V_{cs}|$ and $|V_{cb}|$ have been determined from a variety of decay rates, and recently, the endpoint spectrum of leptons produced in semileptonic decays of the B meson has provided information about the ratio $|V_{ub}/V_{cb}|$. Further information on the values of the CKM parameters, and δ in particular, is provided by the magnitude of B-$\overline{B}$ mixing observed by CLEO and ARGUS and the kaon mixing parameter ε. Accurate knowledge of these experimental quantities along

with precise predictions for their values in terms of the elements of V would determine the values of all four of the CKM parameters A, λ, ρ and η.

The predicted value of ε' is also a function of the CKM parameters. It is therefore possible to test the Standard Model by using all the available experimental evidence except $\mathrm{Re}(\varepsilon'/\varepsilon)$ to constrain the CKM matrix, and then comparing the predicted value of $\mathrm{Re}(\varepsilon'/\varepsilon)$ with the experimental result. To first order, the outcome of such a study is well-known: we shall successfully find values of A, λ, ρ and η that are consistent with the experimental data, but their uncertainties will be large. The significance of comparison with $\mathrm{Re}(\varepsilon'/\varepsilon)$ will depend largely on the size of the other theoretical uncertainties in the calculation of ε'.

The program for the remainder of the chapter is as follows. We begin with a discussion of the theoretical calculations of ε', and will look at how the CKM parameters enter the result. We will then fit for the parameters of the CKM matrix constrained by the experimental data, and evaluate the prospects for further constraints on their values in the future through studies of CP violation in the K and B meson systems. Finally, we will use the results of the fit to predict ε' and compare the results with the experimental data. This will allow us to evaluate the potential of ε' to provide rigorous constraints on the Standard Model.

10.3 Calculation of $\mathrm{Re}(\varepsilon'/\varepsilon)$

10.3.1 The Preliminaries

As we saw in Chapter 1, the value of ε' is conveniently expressed in terms of the decay amplitudes to the $I = 0$ and $I = 2$ isospin states of two pions. It is given by

$$
\begin{aligned}
\varepsilon' &= -\frac{\omega}{\sqrt{2}} \frac{\mathrm{Im} A_0}{\mathrm{Re} A_0} \left(1 - \frac{1}{\omega} \frac{\mathrm{Im} A_2}{\mathrm{Im} A_0} \right) e^{i\left(\frac{\pi}{2} + \delta_2 - \delta_0\right)} \\
&= -\frac{\omega}{\sqrt{2}} \left(\frac{\mathrm{Im} A_0}{\mathrm{Re} A_0} - \frac{\mathrm{Im} A_2}{\mathrm{Re} A_2} \right) e^{i\left(\frac{\pi}{2} + \delta_2 - \delta_0\right)}
\end{aligned}
\tag{10.11}
$$

where A_n is the transition amplitude $\langle \pi\pi(I=n)|T|K^0 \rangle$. In our normalization, which is taken from Buras [45], the kaon decay amplitude to the charged pion final state is given by

$$\langle \pi^+\pi^-|H_{eff}{}^{\Delta S=1}|K^0 \rangle = \sqrt{\frac{2}{3}}A_0 e^{i\delta_0} + \sqrt{\frac{1}{3}}A_2 e^{i\delta_2}$$

$$\langle \pi^0\pi^0|H_{eff}{}^{\Delta S=1}|K^0 \rangle = \sqrt{\frac{2}{3}}A_0 e^{i\delta_0} - 2\sqrt{\frac{1}{3}}A_2 e^{i\delta_2} \quad .$$

(10.12)

Experimentally, it is known that

$$\omega = \frac{Re\,A_2}{Re\,A_0} \approx \frac{1}{22}$$

(10.13)

and

$$Re A_0 = 3.3 \times 10^{-7}\,GeV$$

(10.14)

where the first of these expresses the small violation of the $\Delta I = 1/2$ rule. Thus, to calculate $|\varepsilon'|$ it remains only to calculate the imaginary parts of A_0 and A_2.

At energies such that $\mu < m_c$, the effective hamiltonian is given by

$$H_{eff}{}^{|\Delta S|=1} = \frac{G_F}{\sqrt{2}}V_{ud}V_{us}{}^* \sum_i R_i(\mu)Q_i(\mu) \;+\; h.c.$$

(10.15)

where the $Q_i(\mu)$ are a group of eight hadronic operators in the form of four quark current operators, and the $R_i(\mu)$ are their Wilson coefficients where both are evaluated at the energy scale μ. The hamiltonian should be independent of the scales, and so the μ dependences of $R_i(\mu)$ and $Q_i(\mu)$ should cancel.

The hadronic matrix elements $\langle \pi^+\pi^-|Q_i(\mu)|K^0 \rangle$ can be evaluated using the vacuum insertion approach, hadronic sum rules, chiral perturbation theory, $1/N_c$ expansion, or lattice calculations. With the exception of the lattice calculations, all of these techniques are applicable only at scales with $\mu \lesssim 1$ GeV, and none provides an exact solution. Evaluation of the coefficients $R_i(\mu)$ is somewhat more straightforward, at least at high energies,

where asymptotic freedom can be assumed and QCD may be treated perturbatively. For $\mu \lesssim 1\,\text{GeV}$, $\alpha_s \approx 1$ and this assumption fails.

Thus the difficulty emerges. To calculate A_0 accurately, one needs to evaluate the operators and their coefficients at the same value of μ, but there is little, if any, overlap between the regions in which the two may be evaluated accurately. The difficulty is compounded, because, although natural energy scales generally appear in both the low energy and high energy calculations, it is not always obvious that these two energy scales can legitimately be identified with each other. Let us look at the calculations of the operators and their coefficients in a little more detail.

In the $1/N_c$ calculations [45], the hadronic operators are expanded in terms of the number of colors. For large N_c, QCD becomes an effective theory of weakly interacting pseudoscalar mesons with masses below the scale parameter M. If M is large, more mesons must be included, so the calculations are manageable only at scales of 0.6 to 0.8 GeV or below, where only pions and kaons contribute. Calculations of the matrix elements are then done in the large N_c limit using chiral perturbation theory.

Although it is currently believed that several of the $Q_i(\mu)$ may contribute significantly, their relative contributions depend on the values of some of the parameters of the model. In particular, the apparently large mass of the top quark enhances the contribution of some operators which could otherwise have been neglected. We will come back to these later, but first we will treat the "strong penguin" diagram which is the largest contributor to ε' for all values of m_t less than about 200 GeV.

10.3.2 The Strong Penguin Operator

The strong penguin diagram is shown in Figure 132. It corresponds to the operator Q_6, given by

$$Q_6 = -4 \sum_{q=u,d,s} \left(\bar{s}(1+\gamma_5)q \right)\left(\bar{q}(1-\gamma_5)d \right) \;, \tag{10.16}$$

and its value is
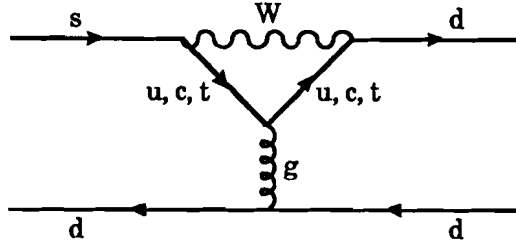
Figure 132. The strong penguin diagram.

$$\langle \pi^+\pi^- |Q_i(\mu)|K^0\rangle = -4f_\pi \left(\frac{m_K^2}{m_s(M)}\right)^2 \frac{\left(m_K^2 - m_\pi^2\right)}{\Lambda_\chi^2} B_6 \quad,$$

where f_π is the pion decay constant, and M is the $1/N_c$ expansion scale. The constant Λ_χ is the scale of the chiral Lagrangian and can be calculated in the $1/N_c$ expansion from the relation [46]

$$\frac{f_K}{f_\pi} = 1 + \frac{m_K^2 - m_\pi^2}{\Lambda_\chi^2} \quad . \tag{10.17}$$

The experimental values of f_K and f_π give $\Lambda_\chi = 1020$ MeV.

The factor B_6 parametrizes the deviation of the true value of $\langle \pi^+\pi^- |Q_6(\mu)|K^0\rangle$ from that found using the vacuum insertion calculation, that is, the calculation done assuming that the vertices are separable so that

$$\langle \pi^+\pi^- |Q_6(\mu)|K^0\rangle = \langle \pi^+\pi^- |0\rangle\langle 0|Q_6(\mu)|K^0\rangle \quad . \tag{10.18}$$

In this case, the $1/N_c$ expansion yields the same result as the vacuum insertion calculation, so that $B_6 = 1$. The success of the $1/N_c$ expansion in explaining the $\Delta I = 1/2$ rule, which stems from enhancement of the real part of A_0, adds to confidence in the prediction.

Unfortunately, not all calculations lead to the same result. Recent lattice calculations have found that $B_6 = 0.5$ [47]. These calculations are difficult, and not yet very reliable; nevertheless, it suggests that the uncertainty in the hadronic matrix elements could be large. Ultimately, lattice

calculations may be the most valuable method for evaluating the hadronic matrix elements, because of all the available techniques they can be done at the highest energy scale, with μ between 1 and 2 GeV, where the Wilson coefficients are known most accurately.

A major feature of the expression for $\langle \pi^+ \pi^- | Q_6(\mu) | K^0 \rangle$ is its quadratic dependence on the mass of the strange quark m_s, which is expected to lie in the range from 125 to 200 MeV/c^2 [48, 49, 50], with values between 150 and 175 MeV/c^2 favored. Variations over the narrower range change the value of the matrix element by 36%.

Now we turn to calculation of the Wilson coefficients. If the top quark mass m_t were small, only the electroweak four-quark operator corresponding to $W^\pm$ exchange, Q_2, would contribute at energy scales near M_W. The hamiltonian would be

$$H_{eff}{}^{\Delta S=1} = \frac{G_F}{\sqrt{2}} \sum_{q=u,c,t} V_{qd} V_{qs}{}^* \; Q_2{}^q(\mu) \tag{10.20}$$

with

$$Q_2{}^q = \bar{s} \gamma_\mu (1 - \gamma_5) q \bar{q} \gamma_\mu (1 - \gamma_5) d \quad . \tag{10.21}$$

From the unitarity of the CKM matrix we know that

$$\sum_{q=u,c,t} V_{qd} V_{qs}{}^* = 0 \quad , \tag{10.22}$$

so that Equation (10.20) can be rewritten

$$H_{eff}{}^{\Delta S=1} = \frac{G_F}{\sqrt{2}} V_{ud} V_{us}{}^* \left((1 - \tau)\left(Q_2{}^u(\mu) - Q_2{}^c(\mu)\right) + \tau\left(Q_2{}^u(\mu) - Q_2{}^t(\mu)\right) \right) \tag{10.23}$$

$$\tau = -\frac{V_{td} V_{ts}{}^*}{V_{ud} V_{us}{}^*} \quad . \tag{10.24}$$

TABLE 23. The value of the Wilson coefficient y_6 as a function of Λ_{QCD} and m_t for $\mu = 1$ GeV. From Ref. [51].

Λ_{QCD} (MeV) m_t (GeV/c^2)	100	200	300
50	−0.051	−0.071	−0.092
75	−0.054	−0.075	−0.097
100	−0.055	−0.077	−0.100
125	−0.057	−0.078	−0.101
150	−0.057	−0.079	−0.103
200	−0.058	−0.080	−0.104
250	−0.059	−0.081	−0.106

The operator coefficients are evaluated using standard renormalization techniques, in which one lowers the energy scale from M_W. As the t, c and b-quark mass thresholds are successively crossed, their contributions are integrated out and one moves from a six quark theory to a five quark theory and so on. At each threshold a new QCD scale, Λ_f is required, and these are chosen so that the running value of α_s is continuous across the thresholds. As the evolution progresses, four-quark current operators other than Q_2 begin to contribute to the hamiltonian, and eventually the low energy hamiltonian of Equation (10.15) is recovered, with the coefficients given by

$$R_i(\mu) = z_i(\mu) + \tau y_i(\mu) \quad . \tag{10.25}$$

The coefficients $z_6(\mu)$ and $y_6(\mu)$ are real, so because we are interested only in the imaginary part of the transition amplitudes, only $y_6(\mu)$ contributes to ε'.

The values of y_6 are shown in Table 23. It is a function of the value of Λ_{QCD} used in renormalization, and, to a lesser degree, m_t. In the calculations which follow, we will take $\Lambda_{QCD} = 200$ MeV and, at least temporarily, $m_t = 100$ GeV/c^2, which give $y_6 = -0.077$. Recall that the hadronic matrix element above was evaluated with μ in the range $0.6 < \mu < 0.8$ GeV. Over this range y_6 varies by about 4%.

We now have everything necessary to calculate the contribution of the strong penguin operator to ε'. We find

$$\left|\frac{\varepsilon'}{\varepsilon}\right|_{QCD\,peng.} = 2\sqrt{3}\,\frac{\omega}{\varepsilon\,Re\,A_0}\,\frac{G_F}{\sqrt{2}}\,Im(V_{td}V_{ts}^*\,)f_\pi\left(\frac{m_K^2}{m_s(M)}\right)^2\frac{\left(m_K^2-m_\pi^2\right)}{\Lambda_\chi^2}\,y_6 B_6$$

$$= (1.06\pm0.35)\times10^{-3}\,\frac{A\lambda^5\eta}{10^{-4}}\left(\frac{150\,MeV\,/\,c^2}{m_s(M)}\right)^2\,, \qquad (10.26)$$

where we have used the experimental value ε = 2.26 x 10^{-3}. The error quoted in the constant term arises from the roughly 30% uncertainty in the parameter B_6 and the 8% uncertainty in y_6 due to lack of knowledge of Λ_{QCD}, where Λ_{QCD} was allowed to vary between 100 and 300 MeV. The factor $A\lambda^5\eta$ (= J) for which the value 10^{-4} is representative, comes from the CKM matrix, and will be discussed in some detail in Section 10.4.2.

10.3.3 Other contributions to ε'

The strong penguin dominates ε', at least for small top quark masses, but other operators also contribute. The largest corrections come from the isospin-breaking mixing of π, η and η' [52], and the electroweak penguin operator, in which the gluon in Figure 132 is replaced by a Z^0 or photon. Both of these generate imaginary parts of A_2. Several other operators also contribute at a lower level.

It is common to express these contributions as corrections to the value of ε' due to the strong penguin operator

$$\varepsilon' = \varepsilon'_{QCD\,peng.}\left(1-\overline{\Omega}\right) \qquad (10.27)$$

where $\overline{\Omega}$ is the sum of the corrections due to the other four-quark operators:

$$\overline{\Omega} = \Omega_{\eta\eta'} + \Omega_{EWP} + \Omega_{27} + \Omega_{octet} + \Omega_p \quad . \qquad (10.28)$$

Recently, special interest has been taken in Ω_{EWP}[51, 53] because it depends strongly on the top quark mass, and for m_t above 100 GeV, significantly suppresses the value of ε'.

The flavor of the calculations of the operators was given above. Here we will only describe the results, which are based on the findings of

References [53] and [51]. The results share many of the uncertainties important to that of $\varepsilon'_{QCD\ peng.}$. There is a B factor associated with each hadronic operator which measures the error introduced by calculating it in the vacuum insertion approximation, but whose value is generally not well known. Often the results of the $1/N_c$ expansion are the same as those using the vacuum insertion approximations, so that $B = 1$; the exceptions are those applying to Ω_{octet} and Ω_{27}, for which they are of order 3 and 0.55 respectively. For consistency with the $\Delta I = 1/2$ rule, B_{octet} should be as large as seven or eight [53]. Lattice calculations may be able to establish the values of the B parameters more firmly in the future. Here we shall use the B values obtained from the $1/N_c$ expansion [51], but the ambiguity should be kept in mind.

Additional uncertainty in the corrections arises from the dependence of the Wilson coefficients on Λ_{QCD} and of some of the hadronic matrix elements on m_s. These dependences are summarized briefly for each operator below, and their values as a function of m_t are plotted in Figure 133.

$\Omega_{\eta\eta'}$: Using the $1/N_c$ expansion, one finds that $\Omega_{\eta\eta'} = 0.27$ [51], while chiral perturbation theory predicts $\Omega_{\eta\eta'} = 0.40 \pm 0.06$ [52]. Here we will use the choice of Ref. [51], $\Omega_{\eta\eta'} = 0.30$. Its value is independent of m_s and Λ_{QCD}.

Ω_{EWP}: This depends strongly on m_t, increasing from -0.1 to 0.95 as m_t rises from 75 to 250 GeV, but is insensitive to m_s and Λ_{QCD}. Preliminary lattice calculations indicate that it could be even more important [54].

Ω_{27}: This enhances the value of ε', ranging between -0.02 to -0.23 as m_t, m_s and Λ_{QCD} vary, increasing in magnitude with m_t, or m_s, and slightly with Λ_{QCD}.

Ω_{octet}: This is insensitive to m_t and Λ_{QCD}, but increases from 0.07 to 0.18 as m_s increases from 125 to 200 MeV, thus reducing the sensitivity of ε' to m_s.

Ω_p: This correction is 0.05, and is insensitive to m_s and Λ_{QCD}.

As m_t ranges between 75 and 250 GeV, the total correction $\overline{\Omega}$ rises from about 0.3 to 1.2. Uncertainty due to Λ_{QCD} is about 15%, while that due to m_s is about 10% for small m_t and negligible for large m_t. For m_t in the range from 100 to 150 GeV, $\overline{\Omega}$ is about 0.5 ± 0.1.

The results of Ref. [51] have been parametrized as a function of m_t for $75 < m_t < 250$ GeV/c^2 [55], and with small adaptations is given by

$$\left|\frac{\varepsilon'}{\varepsilon}\right| = (0.50 \pm 0.16) \times 10^{-3} \left(\frac{150\ MeV/c^2}{m_s}\right)^2 \frac{A^2\lambda^5\eta}{10^{-4}}\left(1 - 0.46\left(\frac{m_t}{100\ GeV/c^2} - 0.7\right)^2\right)$$

(10.29)

where the uncertainty in the constant term is the same as in Equation (10.26).

Including the effect of m_s as is varies between 125 and 200 MeV/c^2, the theoretical uncertainty in the value of $|\varepsilon'/\varepsilon|$ at any fixed value of m_t is about ±55%, apart from the CKM matrix parameters. As we shall see, even with errors of this size, comparison with the experimental results will be
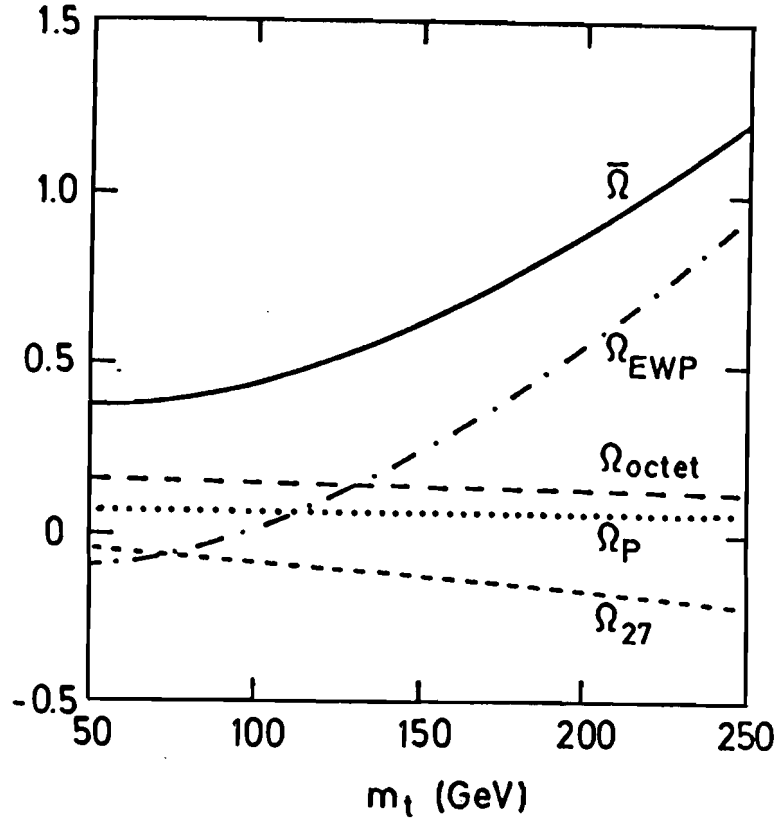
Figure 133. The m_t dependence of the ε' correction factors, for m_s (1 GeV) = 175 MeV/c^2 and Λ_{QCD} =200 MeV. From Ref. [51].

useful. The kind of information provided by the comparison will depend on the values of the CKM parameters. In the next section we will fit for their values from the other (non-ε) experimental data.

10.4 Fits for the Parameters of the CKM Matrix

10.4.1 The Constraints

Four of the elements of the CKM matrix, $|V_{ud}|$, $|V_{us}|$, $|V_{cs}|$ and $|V_{cb}|$, have been determined directly. As shown in Table 24, the first three of these determine the value of the CKM parameter λ, and the last determines of A. Their experimental values, also given in the table, were taken from

TABLE 24. The experimental results constraining the CKM matrix

CKM elt.	Value	CKM and m_t sensitivity	Experimental Source
$|V_{ud}|$	0.9744 ± 0.0014	$1 - \frac{1}{2}\lambda^2$	Nuclear β-decay
$|V_{us}|$	0.220 ± 0.002	λ	$K_L \to \pi^{\pm}e^{\mp}\nu$ and hyperon decay
$|V_{cs}|$	1.00 ± 0.09	$1 - \frac{1}{2}\lambda^2$	Semileptonic D^0 and D^+ decay
$|V_{cb}|$	0.049 ± 0.005	$A\lambda^2$	τ_B; semileptonic B decays
$|V_{ub}/V_{cb}|$	0.10 ± 0.05	$\lambda\left(\rho^2 + \eta^2\right)^{\frac{1}{2}}$	B decays to non-charmed states [57]
$\left(\frac{\Delta m}{\Gamma}\right)_B$	0.64 ± 0.09	$A^2\lambda^6\left((1-\rho)^2 + \eta^2\right)m_t{}^2$	$B^0 - \overline{B}^0$ mixing
$|\varepsilon|$	2.26 ± 0.02	$A^4\lambda^{10}\eta(1-\rho)m_t{}^2$ $(m_t > 100 \text{ GeV/c}^2)$	$K^0 - \overline{K}^0$ mixing
$|\varepsilon'/\varepsilon|$	$(-0.3 \pm 1.5) \times 10^{-3}$ $(\ 3.3 \pm 1.1) \times 10^{-3}$	$A^2\lambda^5\eta f(m_t)$ (See Equation (10.29))	Direct CP violation

Schubert [56], and the errors quoted include both the theoretical and experimental contributions. Together they imply $\lambda = 0.220 \pm 0.002$ and $A = 1.01 \pm 0.10$. The remaining quantities, $|V_{ub}/V_{cb}|$, the magnitude of B^0-$\overline{B}^0$ mixing, and ε, provide information on ρ and η, and are therefore essential to determining the magnitude of the CP-violating effects. They are discussed in slightly more detail below.

The b to u Transitions

The value of $|V_{ub}/V_{cb}|$ has been determined from the momentum distribution of electrons produced in semileptonic decays of the B meson, by fitting the momentum spectrum of leptons with momentum near the kinematic limit for final states including a charmed hadron. The uncertainty in $|V_{ub}/V_{cb}|$ is dominated by that in the momentum distribution assumed for the leptons in the charmed decays; however, the 90% confidence bounds are roughly contained within the range

$$|V_{ub}/V_{cb}| = 0.10 \pm 0.05 \tag{10.30}$$

for all the models considered [57, 58], and we shall use this value in the fits.

Calculation of ε

The expression for ε was given in Equation (1.20). Experimentally, we know that $\Delta m \approx \Delta\Gamma/2$ and $\mathrm{Im}\Gamma_{12} \ll \mathrm{Im}M_{12}$ so we may use the approximate expression

$$\varepsilon = \frac{e^{i\frac{\pi}{4}}}{\sqrt{2}\Delta m} \mathrm{Im}\, M_{12} \quad . \tag{10.31}$$

The value of M_{12} is calculated from the "box" diagrams shown in Figure 134, with the result

$$M_{12} = \frac{G_F{}^2}{12\pi^2} f_K{}^2 m_K B_K M_W{}^2 \left(\lambda_c{}^2 \eta_1 S(x_c) + \lambda_t{}^2 \eta_2 S(x_t) + 2\lambda_c \lambda_t \eta_3 S(x_c, x_t) \right), \tag{10.32}$$

where f_K is the kaon decay constant, equal to 161 MeV, B_K parametrizes the error introduced by using the vacuum insertion approximation, and the factors in parentheses are the contributions of the quark loops, with $\lambda_i = V_{id}^* V_{is}$. The functions $S(x_i)$ and $S(x_i, x_j)$ are given by [59]

$$S(x_i) = x_i F(x_i)$$

$$F(x_i) = \frac{1}{4}\left(1 + \frac{3 - 9x_i}{(x_i - 1)^2} + \frac{6x_i^2 \ln x_i}{(x_i - 1)^3}\right) \tag{10.33}$$

and

$$S(x_i, x_j) = x_i x_j \left[\left(\frac{1}{4} + \frac{3}{2(1 - x_j)} - \frac{3}{4(1 - x_j)^2}\right)\frac{\ln x_j}{x_j - x_i} + (x_i \leftrightarrow x_j) - \frac{3}{4(1 - x_i)(1 - x_j)}\right] \tag{10.34}$$

where

$$x_i = \frac{m_i^2}{M_W^2} . \tag{10.35}$$

The function $F(x_t)$ is unity for $m_i = 0$, 3/4 for $m_i = M_W$ and in the large m_i limit asymptotically approaches 1/4. The constants η_i are QCD corrections to the loop calculations, for which we shall use the values $\eta_1 = 0.85$, $\eta_2 = 0.62$, and $\eta_3 = 0.36$ [51]. The small variations in their values as a function of Λ_{QCD} and the quark masses can safely be neglected.

The value of Δm depends on the real part of the box diagram, but unlike ε, is affected significantly by long distance effects; thus, we use its experimental value, $\Delta m = 3.52 \times 10^{-15}$ GeV/c^2. The value of B_K is uncertain.
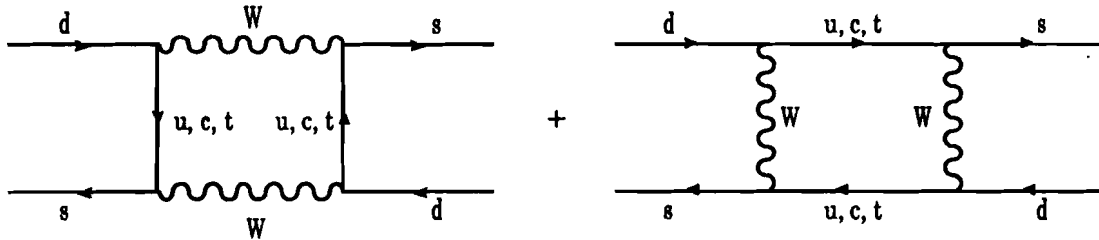
Figure 134. The box diagrams responsible for $K^0 \leftrightarrow \overline{K}^0$ transitions.

Chiral perturbation theory finds $B_K \approx 0.33$ [60] with some uncertainties [61], the $1/N_c$ expansion finds $B_K = 0.67 \pm 0.1$ [45], and hadronic sum rules yield [62] $B_K = 0.58 \pm 0.16$. A recent lattice calculation has found B_K in the range from 0.9 to 1.0 [63]. We shall use $B_K = 0.85 \pm 0.10$.

Numerically, then, Equation (10.32) gives

$$\varepsilon = e^{i\frac{\pi}{4}}\left(32.4 \times 10^3\right)\frac{B_K}{0.85}A^2\lambda^6\eta\left(-\eta_1 S(x_c) + A^2\lambda^4(1-\rho)\eta_2 S(x_t) + \eta_3 S(x_c, x_t)\right)$$

$$(10.36)$$

As shown in Figure 135, in which the contribution of each of the loop terms in the parentheses is plotted function of m_t, the t-quark loop dominates ε for $m_t \geq M_W$. Thus, for all currently allowed values of m_t, ε is approximately given by
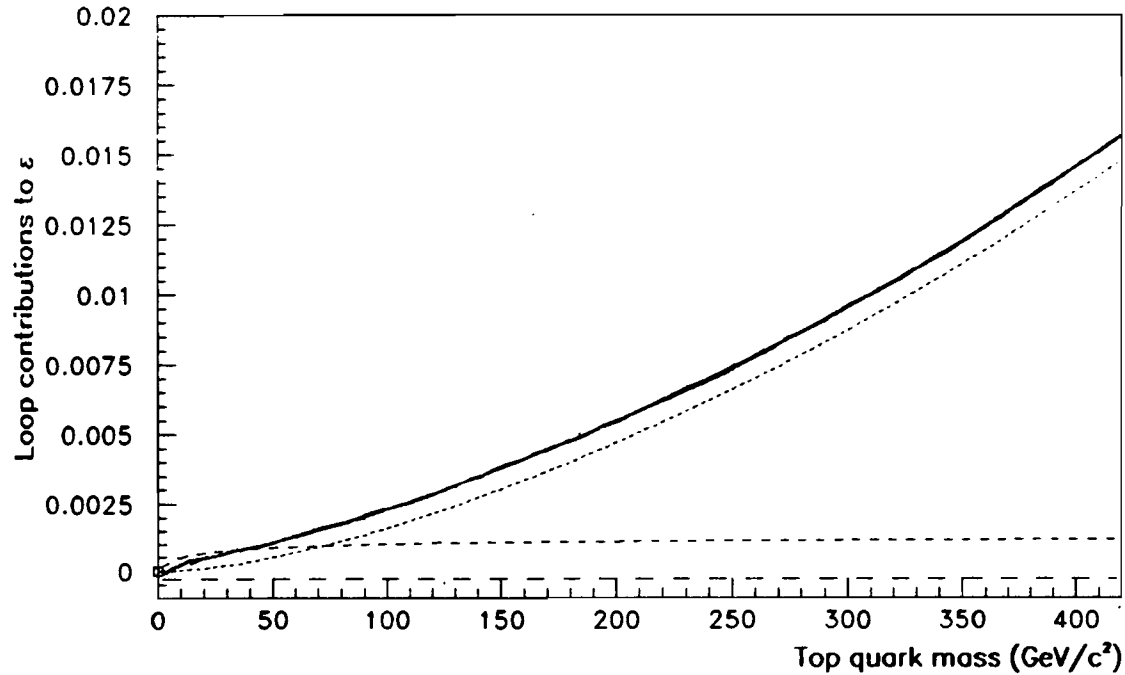
Figure 135. The contributions of the c (long dash), t (dotted) and mixed ct (short dash) loops to ε, and the sum of the three (solid line). The CKM parameters assumed in evaluating the t-loop were $A = 1.0$, $\lambda = 0.22$ and $\rho = 0$.

$$\varepsilon = e^{i\frac{\pi}{4}} \, 3.14 \, \frac{B_K}{0.85} A^4 \lambda^{10} \eta (1-\rho) m_t{}^2 F\!\left(\frac{m_t{}^2}{M_W{}^2}\right) \ . \qquad (10.37)$$

This expression is useful for providing insight into the constraints on the CKM matrix, and we shall return to it shortly; however, the full expression given in (10.36) will be used in the fits.

$B^0 - \overline{B}^0$ Mixing

Mixing in the $B^0 - \overline{B}^0$ system is parametrized by

$$\chi \equiv \frac{\Gamma\!\left(B^0\overline{B}^0 \to B^0B^0\right) + \Gamma\!\left(B^0\overline{B}^0 \to \overline{B}^0\overline{B}^0\right)}{\Gamma\!\left(B^0\overline{B}^0 \to B^0\overline{B}^0\right)}$$

$$= \frac{(\Delta m/\Gamma)_B^2}{2 + (\Delta m/\Gamma)_B^2} \qquad (10.38)$$

The average of results from CLEO [58] and ARGUS [64] yields $\chi = 0.17 \pm 0.04$, implying that

$$\left(\frac{\Delta m}{\Gamma}\right)_B = 0.64 \pm 0.09 \ . \qquad (10.39)$$

In the Standard Model $B^0 - \overline{B}^0$ mixing occurs through the box diagram similar to the one applying to kaons shown in Figure 134. In contrast to such calculations for kaons, here the long distance effects are small because of the large mass of the b-quark. The result is [56]

$$\left(\frac{\Delta m}{\Gamma}\right)_B = \frac{G_F{}^2}{6\pi^2}|V_{td}|^2 m_t{}^2 F\!\left(\frac{m_t{}^2}{M_W{}^2}\right) m_B f_B{}^2 B_B \eta_B \tau_B \qquad (10.40)$$

where f_B is the B-meson decay constant, m_B is its mass, 5.28 GeV/c^2, and τ_B is its lifetime, for which we use the world average value $\tau_B = (1.18 \pm 0.12) \times 10^{-12}$ s [65]. The parameter η_B is a QCD correction factor, equal to 0.85 ± 0.05, and the parameter B_B is the familiar measure of the error induced by using the vacuum insertion approximation, which, follow-

ing Schubert, we shall take to be 0.85 ± 0.10. The function $F(x_t)$ is as given in Equation (10.33).

Of all the above parameters, the most uncertain (aside from m_t) is the decay constant f_B. Using QCD sum rules, one finds that $f_B = 115 \pm 14$ MeV, while the $1/N_c$ expansion predicts that $f_B = f_K$ (= 161 MeV). The non-relativistic static quark model, a phenomenological description of mesons composed of one light and one heavy quark, predicts that the decay constant will scale as [66]

$$\frac{f_{M'}}{f_M} = \left[\frac{m_Q}{m_{Q'}}\right]^{\frac{1}{2}}\left[\frac{\alpha_s(Q')}{\alpha_s(Q)}\right]^{-\frac{6}{33-2n_f}} \tag{10.41}$$

where m_Q and $m_{Q'}$ are the heavy quark masses and f_M and $f_{M'}$ are their respective meson decay constants. The second factor is a QCD correction, with n_f the number of quarks with mass below $m_{Q'}$. The upper limit found by Mark III on f_D of 290 MeV [67] then implies that $f_B < 181$ MeV, where the QCD factor is 1.11. Complete and up-to-date predictions for f_B can be found in Ref. [68]. For our current purposes we will assume the value $f_B = 140 \pm 30$ MeV.

The numerical result is thus

$$\left(\frac{\Delta m}{\Gamma}\right)_B = (0.31 \pm 0.11)GeV^{-2} \, A^2\lambda^6\left((1-\rho)^2 + \eta^2\right)m_t^2 F\left(\frac{m_t^2}{M_W^2}\right) \quad . \tag{10.42}$$

10.4.2 Fit Results

Results of fits for the CKM parameters have been discussed in previous works [55, 56]. In this fit, which is based on that of Ref. [55], the values of A, λ, ρ, η and m_t were allowed to vary to minimize χ^2, where the errors included both the theoretical and experimental contributions. Recall that the first four constraints yielded $\lambda = 0.221 \pm 0.002$ and $A = 1.01 \pm 0.10$. Excluding ε'/ε from the fit, there are three experimental constraints on the

remaining three parameters ρ, η and m_t, so an exact solution can be found. The best fit values are

$$\rho = -0.41^{+0.08}_{-0.06}$$

$$\eta = 0.20^{+0.10}_{-0.08}$$

$$m_t = 116^{+57}_{-28} \ GeV/c^2 \tag{10.43}$$

There is a second minimum with $m_t \approx 415 \ GeV/c^2$, but this solution is less likely both from the quality of the fit and on other experimental grounds: the ratio of W to Z masses suggests that $m_t < 250 \ GeV/c^2$. In the discussion which follows we will therefore focus on the low mass region $89 < m_t < 250$ GeV/c^2, where the lower limit comes from direct searches for the top quark [69].

To gain intuition about the relationships between these quantities we turn to the "unitarity" triangle. One of the unitarity conditions of the CKM matrix is

$$V_{ub}^* \ V_{ud} + V_{cb}^* \ V_{cd} + V_{tb}^* \ V_{td} = 0 \quad . \tag{10.44}$$

Using $V_{ud} \approx 1$ and $V_{tb}^* \approx 1$, this can be rewritten as

$$\frac{V_{ub}^*}{A\lambda^3} + \frac{V_{td}}{A\lambda^3} \approx 1 \quad . \tag{10.45}$$

This relationship can be represented as a "unitarity" triangle in the complex plane defined by ρ and η, as shown in Figure 136. The length of one side (the short one in the diagram) is proportional to $|V_{ub}/V_{cb}|$, and the length of the other non-trivial one is proportional to $\sqrt{(\Delta m/\Gamma)_B}$. The kaon mixing parameter ϵ provides further information on the long leg, since it is essentially proportional to the area of the rectangle with diagonal $|V_{td}|$. The value of ϵ' is proportional to the height of the triangle, η, or, since the base has unit length, its area.[1]

---

[1] It is a general result that the triangles defined by the unitarity relations all have area equal to J, and are therefore proportional to CP-violating amplitudes.
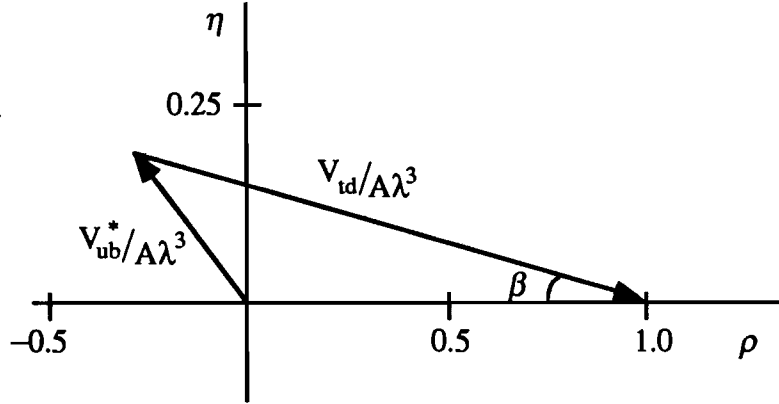
Figure 136. The unitarity triangle.

Unfortunately, the value of $|V_{td}|$ is not well known because both $(\Delta m/\Gamma)_B$ and ε depend strongly on m_t. In the ratio $(\Delta m/\Gamma)_B /\varepsilon$, however, the m_t dependence nearly cancels, with only small deviations arising from the charmed quark loop contributions to ε. This constraint, along with that provided on $\sqrt{\rho^2 + \eta^2}$ by $|V_{ub}/V_{cb}|$, is shown graphically in Figure 137, evalu-
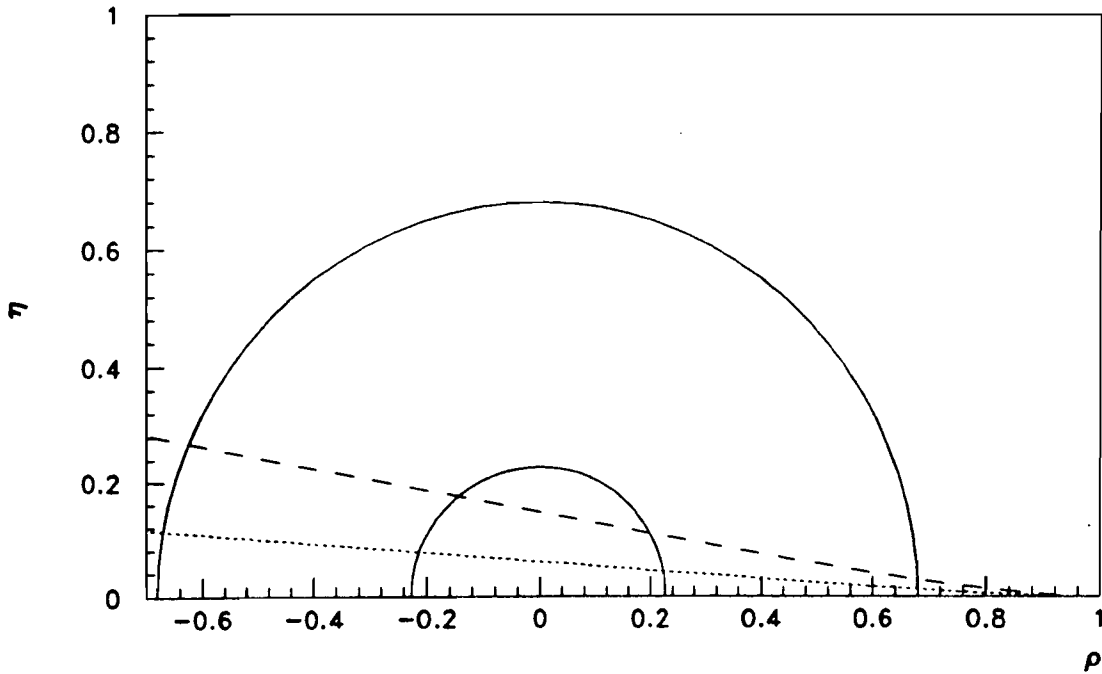
Figure 137. The constraints on ρ and η provided by $|V_{ub}/V_{cb}|$ and $(\Delta m/\Gamma)_B /\varepsilon$.

ated for m_t =116 GeV/c². The two semi-circles are the 90% bounds on $|V_{ub}/V_{cb}|$. The (nearly straight) lines through $(\rho,\eta) = (1,0)$ are the bounds provided by $(\Delta m/\Gamma)_B/\varepsilon$, where the angle they subtend is primarily due to uncertainty in $f_B{}^2$. In general, solutions with small m_t (<250 GeV/c²) are located in the region with $\rho < 0$, while the high m_t solution alluded to above lies in the $\rho > 0$ region. The constraints in that region evaluated with correspondingly high values of m_t are almost the same as those shown in the plot.

We now turn to the more specific problem of determining η, which is the CKM parameter that affects ε'. The range of η favored by the fit is shown as a function of m_t in Figure 138. Because of the ε constraint, which requires that the product $\eta(1-\rho)m_t{}^2$ remain constant, the value of η falls with m_t and its uncertainty is about ±30% at any fixed value of m_t, What can we do to determine its value more accurately? Uncertainty in ρ is currently dominated by m_t and $|V_{ub}/V_{cb}|$, while that in η is dominated by f_B. Until f_B is
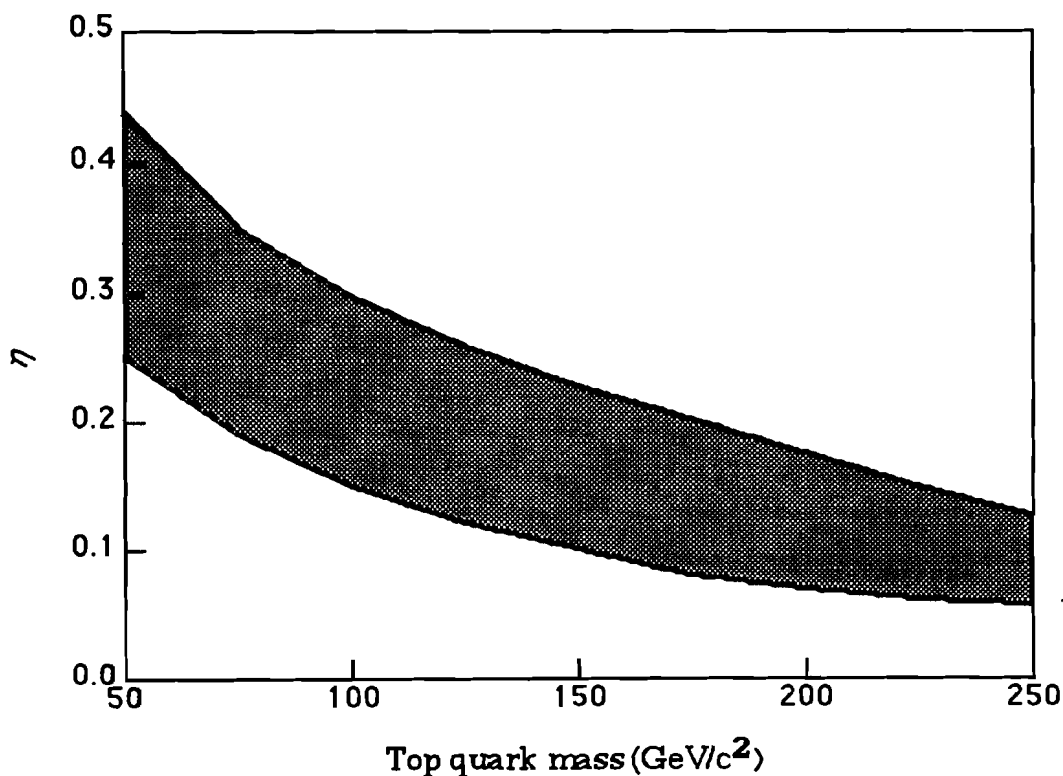
Figure 138. The dependence of η on m_t.

known accurately, even a factor of ten improvement in $|V_{ub}/V_{cb}|$ or B_K will not significantly constrain the value of η. Several other avenues are available for constraining the value of η, all involving new experimental observations.

One such measurement is that of the branching ratio of the $B^\pm \to \tau^\pm v$ decay. Its branching ratio is given by [70]

$$\mathrm{B}\left(B^\pm \to \tau^\pm v\right) = \frac{G_F^2 f_B^2 m_\tau^2 m_B}{8\pi}\left(1 - \frac{m_\tau^2}{m_B^2}\right)|V_{ub}|^2 \tau_B$$

$$= \left(7 \times 10^{-5}\right)\left(\frac{f_B}{140\,MeV}\right)^2 \left|\frac{V_{ub}}{0.005}\right|^2 \qquad (10.46)$$

Since this quantity depends on f_B^2, the ratio $(\Delta m/\Gamma)_B /(\varepsilon\,\mathrm{B}(B^\pm \to \tau^\pm v))$ can be formed which is independent of both f_B^2 and m_t. The dependence on τ_B, another significant source of uncertainty, also cancels. The uncertainty in the experimental values of $(\Delta m/\Gamma)_B$ and ε and in the input parameters B_K, η_B and B_B lead to a total uncertainty in $(\Delta m/\Gamma)_B /(\varepsilon\,\mathrm{BR}(B^\pm \to \tau^\pm v))$ of only $\pm 17\%$. An observation of this decay at the predicted level would thus constrain the values of ρ and η to lie within a narrow range about the the curve shown in Figure 139. Detection of this decay is difficult because of the large combinatoric background; however, even an upper limit of 10^{-4} on the branching ratio would eliminate about one third of the currently allowed region in the ρ , η plane.

Other effects which will constrain the value of η significantly all depend on observation of direct CP violation. One mode which has been studied in depth recently is $K_L \to \pi^0 e^+ e^-$. These decays can be either CP-conserving or CP-violating. The CP-conserving decays proceed through a two photon intermediate state, with an amplitude that will be calculable once the $K_L \to \pi^0 \gamma\gamma$ branching ratio is measured, as has recently been reported [71]. The CP-violating decays proceed through a one photon intermediate state. Like the two pion modes, there is both a "direct" CP-violating contribution and one from "mixing" of the CP eigenstates; however, in contrast to the two pion case, they are expected to be comparable in size. The "mixing" contribution, which can be determined directly by observation of the

$K_S \to \pi^0 e^+ e^-$ decay, is expected to have a branching ratio of about 6 x 10^{-12}. The "direct" contribution is the interesting one: it may be the most accessible window to direct CP violation available. Its branching ratio is known theoretically within 10 to 20%, and is given by [72]

$$\mathrm{B}\left(K_2 \to \pi^0 e^+ e^-\right) = 1.0 \times 10^{-5}\left(\lambda^4 \eta\right)^2 G(m_t)$$

$$= 5.5 \times 10^{-11} \eta^2 G(m_t) \tag{10.47}$$

where $G(m_t)$ is a quadratic function of m_t varying between 0.1 at $m_t = 50$ GeV/c^2 and 1.0 at 200 GeV/c^2. Thus, determination of this branching ratio would give information on the value of η. The current upper limit on this mode is 5.5 x 10^{-9}[73, 74]. Experiments are now in preparation at KEK and FNAL which should have significantly better sensitivity. The challenge is that to provide convincing evidence for direct CP violation, one must observe
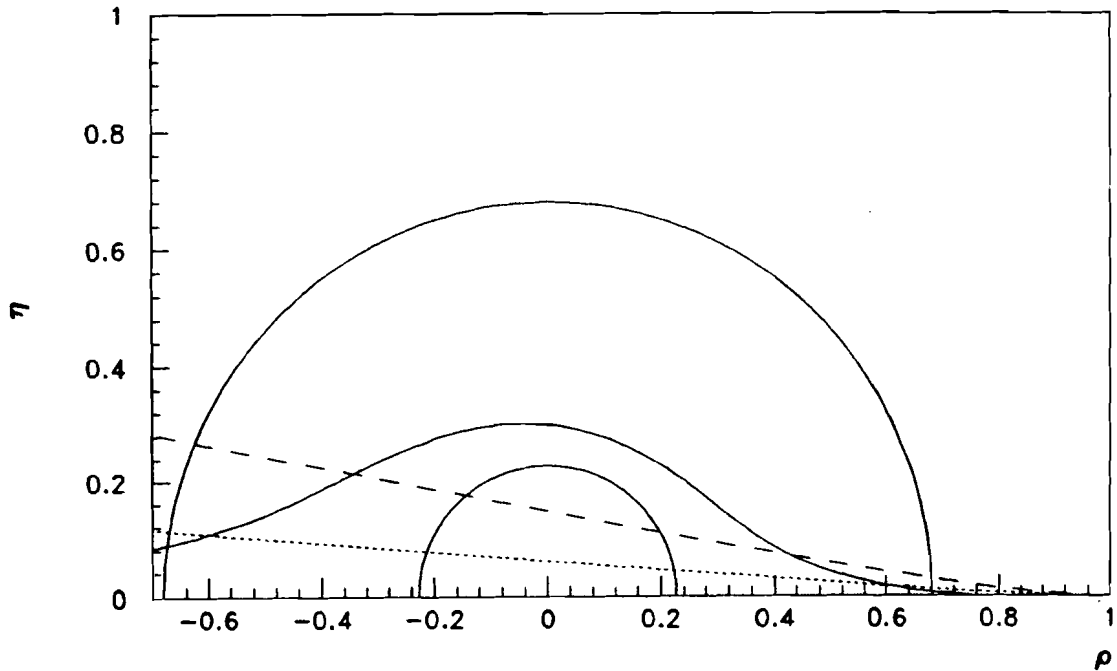
Figure 139. The experimental constraints on ρ and η. All curves are as shown in Figure 137, with the addition of the constraint which would be provided by the ratio $(\Delta m/\Gamma)_B / (\varepsilon\, \mathrm{B}(B^\pm \to \tau^\pm \nu\,))$ if the decay $B^\pm \to \tau^\pm \nu$ were observed at the predicted level.

the interference of the K_1 and K_2 decays, which would require a substantial data sample.

The related mode $K_L \to \pi^0 \nu \bar{\nu}$ is also a potential channel for observation of direct CP violation. Unlike the $\pi^0 e^+ e^-$ mode there is no CP-conserving channel. Furthermore, the CP-violating amplitudes can be predicted accurately since they are related by isopin to the measured $K^+ \to \pi^0 e^+ \nu$ mode. One finds that the branching ratio to the sum of the three neutrino species through the directly CP-violating channel is [75]

$$\mathrm{B}\left(K_L \to \pi^0 \nu \bar{\nu}\right) = 6.2 \times 10^{-5}\left(\lambda^4 \eta\right)^2 H(m_t)$$

$$= 3.3 \times 10^{-10} \eta^2 H(m_t) \qquad (10.48)$$

where $H(m_t)$ increases roughly as $m_t^{2.2}$ from 0.1 at $m_t = 50$ GeV/c^2 to 1.6 at 200 GeV/c^2. The amplitude due to mixing is significantly suppressed by the GIM mechanism, and is nearly negligible, about 5.5×10^{-15} [76]. Because the theoretical calculation is rather certain, observation of this mode, besides being a clean observation of direct CP violation, would directly measure the value of η. The experimental challenge of this mode is formidable because of the missing neutrino information, but preliminary studies indicate that it may be tractable and the feasibility of such an experiment at the Main Injector facility at FNAL is under investigation.

Direct CP violation may also be observed in the $B^0 - \bar{B}^0$ system. Because of the short lifetime of the B^0, it will be difficult to observe the time structure of the interference of the CP-violating decays. The most promising approach is to look for a time-integrated asymmetry in the decays of tagged B^0 and $\bar{B}^0$ decays to a CP eigenstate such as ΨK_S. According to the SLAC study of an asymmetric B-Factory [77], the asymmetry in the ΨK_S mode would determine the angle β (see Figure 136) within 1° after an exposure of 100 fb^{-1}. These estimates are optimistic, and at least ten years are required before the data will be in hand, but clearly a determination of this precision would be a vast improvement on our knowledge, and permit rather stringent tests on the model (besides being exciting in its own right).

10.5 Conclusions

Given the currently allowed range of η, the predicted range of Re(ε'/ε) is plotted as a function of m_t in Figure 140. The upper bound of the shaded region was calculated from the upper limit of $|\varepsilon'/\varepsilon|$ in Equation (10.29) evaluated for $m_s = 125$ MeV/c^2, together with the upper bound of η shown in Figure 138. The lower bound was calculated using the lower limits of each, with $m_s = 200$ MeV/c^2. The shaded area thus represents a conservative estimate of allowed values of Re(ε'/ε), in that the errors due to CKM and the other uncertainties were combined linearly. The value of Re(ε'/ε) falls with m_t as a result of both the electroweak penguin and η, though the latter dominates and, as pointed out in Refs. [53] and [51], vanishes for $m_t \geq 200 \, GeV / c^2$. If the top quark lies in this range, it could be impossible to distinguish experimentally the Standard Model and superweak model
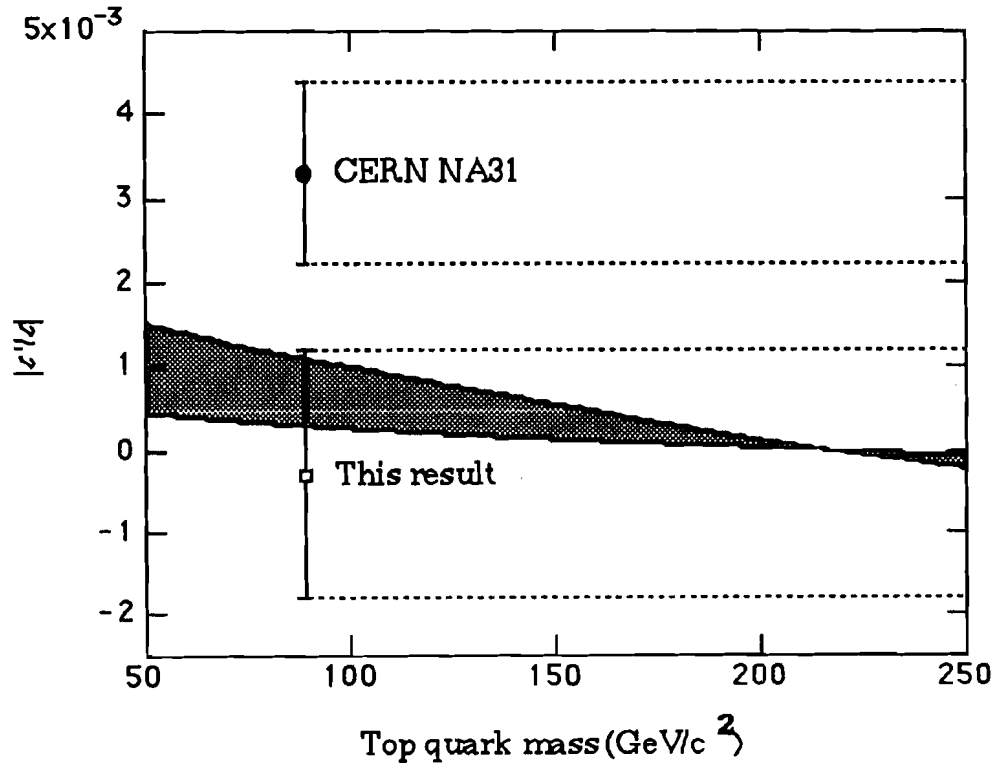
Figure 140. The value of $|\varepsilon'/\varepsilon|$ as a function of m_t. The shaded area is allowed by theory and the other CKM constraints. The solid circle is the result of CERN NA31 and the open square is the result of this experiment.

predictions.

The results of this experiment and of NA31 are also shown in Figure 140. The NA31 value lies somewhat above the Standard Model prediction for all values of m_t, though the discrepancy is less for small m_t. If true, that result could be difficult for the Standard Model to explain. The result of this experiment is consistent with the Standard Model predictions at all m_t. As such, it provides little information either on the value of m_t or on η.

When the experimental error on $\text{Re}(\varepsilon'/\varepsilon)$ decreases a factor of two as expected in the next year, it will significantly constrain the allowed ranges of m_t and η. In conjunction with discovery of the top quark, $\text{Re}(\varepsilon'/\varepsilon)$ could prove to be one of the most rigorous tests of the Standard Model within reach in this decade, providing new information about its parameters, or perhaps, a first indication of the physics beyond.

APPENDIX

This appendix consists of tables of the spatial distribution of Cerenkov light produced in 1, 2.8, 8, 22.6 and 64 GeV/c electromagnetic showers. The results were obtained using the EGS shower Monte Carlo as described in Section 6.3. Each table entry (t, r) gives the fraction of the Cerenkov light produced from depths 0 to t within the square rings 0 to r, where the rings are defined as shown in Figure 141.
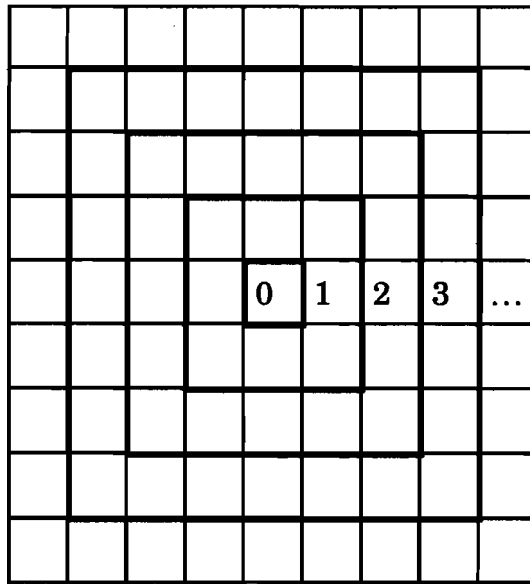
Figure 141. Diagram of the rings used in the tables. Each small square represents a $0.36 \times 0.36 \ X_0^2$ cell; the bold lines demarcate the tabulated rings. Shower impact points were uniformly distributed across the center cell.

TABLE 25. Integrated Cerenkov light production distribution of 1.000 GeV electrons based on 3200 EGS generated showers.

Ring→ Depth↓	0	1	2	3	4	5	6	7	8	9	10	11	12	13	14	15	16	17
0.5 X_0	0.0148	0.0152	0.0153	0.0153	0.0153	0.0154	0.0154	0.0155	0.0155	0.0155	0.0156	0.0156	0.0156	0.0156	0.0157	0.0157	0.0157	0.0158
1.0 X_0	0.0402	0.0443	0.0445	0.0446	0.0447	0.0447	0.0448	0.0449	0.0449	0.0450	0.0450	0.0450	0.0451	0.0451	0.0451	0.0451	0.0451	0.0453
1.5 X_0	0.0765	0.0913	0.0921	0.0923	0.0924	0.0925	0.0926	0.0927	0.0928	0.0928	0.0929	0.0929	0.0930	0.0930	0.0930	0.0931	0.0931	0.0932
2.0 X_0	0.1195	0.1536	0.1555	0.1560	0.1563	0.1564	0.1566	0.1567	0.1568	0.1569	0.1570	0.1571	0.1571	0.1572	0.1572	0.1572	0.1573	0.1575
2.5 X_0	0.1641	0.2254	0.2298	0.2307	0.2312	0.2315	0.2318	0.2320	0.2322	0.2323	0.2324	0.2325	0.2325	0.2326	0.2326	0.2327	0.2327	0.2330
3.0 X_0	0.2054	0.2996	0.3078	0.3096	0.3104	0.3109	0.3113	0.3116	0.3118	0.3120	0.3121	0.3122	0.3123	0.3124	0.3125	0.3125	0.3126	0.3129
3.5 X_0	0.2418	0.3722	0.3856	0.3888	0.3902	0.3910	0.3916	0.3920	0.3923	0.3926	0.3928	0.3929	0.3931	0.3932	0.3932	0.3933	0.3934	0.3937
4.0 X_0	0.2726	0.4397	0.4594	0.4644	0.4665	0.4676	0.4685	0.4691	0.4695	0.4699	0.4701	0.4703	0.4705	0.4706	0.4707	0.4708	0.4709	0.4713
4.5 X_0	0.2972	0.4991	0.5262	0.5334	0.5364	0.5381	0.5393	0.5401	0.5407	0.5411	0.5415	0.5417	0.5419	0.5421	0.5422	0.5423	0.5424	0.5429
5.0 X_0	0.3169	0.5499	0.5849	0.5948	0.5989	0.6012	0.6028	0.6039	0.6046	0.6052	0.6056	0.6060	0.6062	0.6065	0.6066	0.6068	0.6069	0.6075
5.5 X_0	0.3320	0.5923	0.6353	0.6479	0.6534	0.6565	0.6585	0.6600	0.6609	0.6617	0.6622	0.6626	0.6629	0.6631	0.6633	0.6635	0.6637	0.6643
6.0 X_0	0.3438	0.6278	0.6784	0.6940	0.7008	0.7047	0.7073	0.7090	0.7102	0.7111	0.7117	0.7122	0.7126	0.7129	0.7131	0.7133	0.7135	0.7143
6.5 X_0	0.3528	0.6568	0.7147	0.7333	0.7418	0.7466	0.7497	0.7519	0.7533	0.7544	0.7552	0.7557	0.7562	0.7566	0.7569	0.7571	0.7573	0.7582
7.0 X_0	0.3597	0.6800	0.7445	0.7661	0.7761	0.7819	0.7856	0.7882	0.7899	0.7912	0.7922	0.7929	0.7934	0.7938	0.7942	0.7945	0.7947	0.7957
7.5 X_0	0.3651	0.6987	0.7691	0.7935	0.8051	0.8117	0.8161	0.8191	0.8211	0.8226	0.8237	0.8245	0.8251	0.8256	0.8260	0.8263	0.8266	0.8278
8.0 X_0	0.3691	0.7135	0.7889	0.8158	0.8289	0.8364	0.8414	0.8447	0.8470	0.8488	0.8501	0.8510	0.8517	0.8522	0.8527	0.8531	0.8534	0.8547
8.5 X_0	0.3722	0.7256	0.8055	0.8346	0.8491	0.8576	0.8631	0.8668	0.8694	0.8714	0.8729	0.8739	0.8747	0.8753	0.8758	0.8762	0.8765	0.8780
9.0 X_0	0.3745	0.7351	0.8190	0.8502	0.8660	0.8752	0.8813	0.8854	0.8883	0.8906	0.8922	0.8933	0.8942	0.8949	0.8955	0.8959	0.8963	0.8978
9.5 X_0	0.3762	0.7423	0.8297	0.8627	0.8796	0.8896	0.8963	0.9008	0.9039	0.9064	0.9081	0.9094	0.9104	0.9112	0.9118	0.9122	0.9126	0.9143
10.0 X_0	0.3775	0.7481	0.8382	0.8729	0.8908	0.9015	0.9087	0.9136	0.9170	0.9197	0.9216	0.9230	0.9241	0.9249	0.9255	0.9260	0.9265	0.9283
10.5 X_0	0.3785	0.7524	0.8449	0.8811	0.9000	0.9114	0.9192	0.9243	0.9280	0.9309	0.9330	0.9344	0.9356	0.9365	0.9372	0.9377	0.9382	0.9402
11.0 X_0	0.3791	0.7558	0.8501	0.8876	0.9073	0.9193	0.9275	0.9330	0.9369	0.9399	0.9421	0.9437	0.9450	0.9459	0.9466	0.9472	0.9477	0.9498
11.5 X_0	0.3797	0.7584	0.8543	0.8929	0.9134	0.9259	0.9346	0.9404	0.9445	0.9477	0.9501	0.9517	0.9531	0.9541	0.9548	0.9555	0.9560	0.9582
12.0 X_0	0.3801	0.7606	0.8577	0.8972	0.9184	0.9313	0.9403	0.9464	0.9508	0.9542	0.9566	0.9584	0.9598	0.9608	0.9617	0.9623	0.9629	0.9652
12.5 X_0	0.3805	0.7623	0.8604	0.9006	0.9223	0.9356	0.9449	0.9513	0.9558	0.9593	0.9619	0.9638	0.9653	0.9664	0.9672	0.9679	0.9685	0.9710
13.0 X_0	0.3807	0.7635	0.8624	0.9034	0.9256	0.9392	0.9488	0.9554	0.9601	0.9638	0.9664	0.9684	0.9700	0.9711	0.9720	0.9728	0.9733	0.9760
13.5 X_0	0.3808	0.7644	0.8641	0.9055	0.9281	0.9421	0.9519	0.9587	0.9635	0.9673	0.9701	0.9721	0.9737	0.9749	0.9759	0.9767	0.9772	0.9800
14.0 X_0	0.3809	0.7652	0.8654	0.9073	0.9302	0.9445	0.9546	0.9615	0.9664	0.9704	0.9732	0.9753	0.9769	0.9782	0.9792	0.9800	0.9806	0.9835
14.5 X_0	0.3810	0.7658	0.8665	0.9087	0.9320	0.9465	0.9567	0.9638	0.9688	0.9729	0.9758	0.9779	0.9796	0.9809	0.9819	0.9828	0.9834	0.9863

15.0 X_0	0.3811	0.7662	0.8673	0.9098	0.9333	0.9480	0.9585	0.9656	0.9708	0.9749	0.9778	0.9801	0.9818	0.9831	0.9842	0.9851	0.9857	0.9887
15.5 X_0	0.3812	0.7666	0.8680	0.9107	0.9343	0.9492	0.9598	0.9671	0.9723	0.9764	0.9795	0.9817	0.9835	0.9849	0.9860	0.9869	0.9875	0.9906
16.0 X_0	0.3812	0.7668	0.8684	0.9114	0.9352	0.9502	0.9609	0.9683	0.9736	0.9778	0.9809	0.9832	0.9850	0.9864	0.9875	0.9884	0.9891	0.9922
16.5 X_0	0.3813	0.7670	0.8689	0.9120	0.9359	0.9510	0.9618	0.9692	0.9746	0.9789	0.9820	0.9843	0.9862	0.9876	0.9887	0.9896	0.9903	0.9936
17.0 X_0	0.3813	0.7672	0.8692	0.9125	0.9365	0.9516	0.9625	0.9700	0.9754	0.9798	0.9829	0.9853	0.9872	0.9886	0.9897	0.9907	0.9913	0.9947
17.5 X_0	0.3813	0.7673	0.8694	0.9128	0.9369	0.9522	0.9631	0.9706	0.9761	0.9804	0.9836	0.9860	0.9879	0.9893	0.9905	0.9915	0.9922	0.9956
18.0 X_0	0.3814	0.7674	0.8696	0.9131	0.9373	0.9526	0.9636	0.9712	0.9767	0.9810	0.9843	0.9867	0.9886	0.9900	0.9912	0.9922	0.9929	0.9964
18.5 X_0	0.3814	0.7675	0.8697	0.9133	0.9376	0.9529	0.9640	0.9716	0.9771	0.9816	0.9848	0.9872	0.9892	0.9906	0.9918	0.9928	0.9935	0.9970
19.0 X_0	0.3814	0.7676	0.8699	0.9135	0.9378	0.9532	0.9643	0.9719	0.9775	0.9819	0.9852	0.9876	0.9896	0.9911	0.9923	0.9933	0.9940	0.9975
19.5 X_0	0.3814	0.7676	0.8699	0.9136	0.9379	0.9534	0.9645	0.9722	0.9778	0.9822	0.9855	0.9880	0.9899	0.9914	0.9926	0.9936	0.9944	0.9979
20.0 X_0	0.3814	0.7677	0.8700	0.9137	0.9381	0.9536	0.9647	0.9724	0.9780	0.9825	0.9858	0.9883	0.9902	0.9917	0.9929	0.9940	0.9947	0.9983
20.5 X_0	0.3814	0.7677	0.8701	0.9138	0.9382	0.9537	0.9649	0.9726	0.9782	0.9827	0.9860	0.9885	0.9905	0.9920	0.9932	0.9942	0.9950	0.9986
21.0 X_0	0.3814	0.7677	0.8701	0.9139	0.9383	0.9538	0.9650	0.9727	0.9784	0.9829	0.9862	0.9887	0.9907	0.9922	0.9934	0.9945	0.9952	0.9989
21.5 X_0	0.3814	0.7677	0.8702	0.9140	0.9384	0.9539	0.9651	0.9728	0.9785	0.9830	0.9864	0.9889	0.9909	0.9924	0.9936	0.9946	0.9954	0.9991
22.0 X_0	0.3814	0.7677	0.8702	0.9140	0.9384	0.9540	0.9652	0.9729	0.9786	0.9832	0.9865	0.9890	0.9910	0.9925	0.9938	0.9948	0.9955	0.9993
22.5 X_0	0.3814	0.7678	0.8702	0.9140	0.9385	0.9540	0.9652	0.9730	0.9787	0.9832	0.9865	0.9891	0.9911	0.9926	0.9938	0.9949	0.9956	0.9994
23.0 X_0	0.3814	0.7678	0.8702	0.9140	0.9385	0.9541	0.9653	0.9730	0.9787	0.9833	0.9866	0.9891	0.9911	0.9927	0.9939	0.9950	0.9957	0.9995
23.5 X_0	0.3814	0.7678	0.8702	0.9140	0.9385	0.9541	0.9653	0.9730	0.9788	0.9833	0.9867	0.9892	0.9912	0.9927	0.9940	0.9950	0.9958	0.9996
24.0 X_0	0.3814	0.7678	0.8703	0.9141	0.9385	0.9541	0.9654	0.9731	0.9788	0.9834	0.9867	0.9892	0.9913	0.9928	0.9941	0.9951	0.9959	0.9997
24.5 X_0	0.3814	0.7678	0.8703	0.9141	0.9386	0.9542	0.9654	0.9731	0.9789	0.9834	0.9868	0.9893	0.9913	0.9929	0.9941	0.9952	0.9959	0.9997
25.0 X_0	0.3814	0.7678	0.8703	0.9141	0.9386	0.9542	0.9654	0.9732	0.9789	0.9835	0.9868	0.9893	0.9913	0.9929	0.9941	0.9952	0.9960	0.9998
25.5 X_0	0.3814	0.7678	0.8703	0.9141	0.9386	0.9542	0.9654	0.9732	0.9789	0.9835	0.9868	0.9893	0.9914	0.9929	0.9942	0.9952	0.9960	0.9998
26.0 X_0	0.3814	0.7678	0.8703	0.9141	0.9386	0.9542	0.9654	0.9732	0.9789	0.9835	0.9868	0.9894	0.9914	0.9929	0.9942	0.9952	0.9960	0.9998
26.5 X_0	0.3814	0.7678	0.8703	0.9141	0.9386	0.9542	0.9655	0.9732	0.9789	0.9835	0.9869	0.9894	0.9914	0.9930	0.9942	0.9953	0.9960	0.9999
27.0 X_0	0.3814	0.7678	0.8703	0.9141	0.9386	0.9542	0.9655	0.9732	0.9789	0.9835	0.9869	0.9894	0.9914	0.9930	0.9942	0.9953	0.9960	0.9999
27.5 X_0	0.3814	0.7678	0.8703	0.9141	0.9386	0.9542	0.9655	0.9732	0.9789	0.9835	0.9869	0.9894	0.9914	0.9930	0.9942	0.9953	0.9961	0.9999
28.0 X_0	0.3814	0.7678	0.8703	0.9141	0.9386	0.9542	0.9655	0.9732	0.9790	0.9835	0.9869	0.9894	0.9914	0.9930	0.9942	0.9953	0.9961	0.9999
28.5 X_0	0.3814	0.7678	0.8703	0.9141	0.9386	0.9542	0.9655	0.9732	0.9790	0.9835	0.9869	0.9894	0.9915	0.9930	0.9943	0.9953	0.9961	0.9999
29.0 X_0	0.3814	0.7678	0.8703	0.9141	0.9386	0.9542	0.9655	0.9732	0.9790	0.9835	0.9869	0.9894	0.9915	0.9930	0.9943	0.9953	0.9961	0.9999
29.5 X_0	0.3814	0.7678	0.8703	0.9141	0.9386	0.9542	0.9655	0.9732	0.9790	0.9835	0.9869	0.9894	0.9915	0.9930	0.9943	0.9953	0.9961	0.9999
30.0 X_0	0.3814	0.7678	0.8703	0.9141	0.9386	0.9542	0.9655	0.9732	0.9790	0.9836	0.9869	0.9895	0.9915	0.9930	0.9943	0.9953	0.9961	1.0000

TABLE 26. Integrated Cerenkov light production distribution of 2.828 GeV electrons based on 2262 EGS generated showers.

Ring→ / Depth↓	0	1	2	3	4	5	6	7	8	9	10	11	12	13	14	15	16	17
0.5 X_0	0.0056	0.0058	0.0058	0.0058	0.0058	0.0058	0.0059	0.0059	0.0059	0.0059	0.0060	0.0060	0.0060	0.0060	0.0060	0.0060	0.0061	0.0061
1.0 X_0	0.0171	0.0185	0.0186	0.0186	0.0187	0.0187	0.0188	0.0188	0.0188	0.0188	0.0189	0.0189	0.0189	0.0189	0.0190	0.0190	0.0190	0.0191
1.5 X_0	0.0364	0.0421	0.0424	0.0425	0.0426	0.0427	0.0428	0.0428	0.0429	0.0429	0.0429	0.0430	0.0430	0.0430	0.0431	0.0431	0.0431	0.0432
2.0 X_0	0.0632	0.0776	0.0784	0.0787	0.0788	0.0790	0.0791	0.0791	0.0792	0.0793	0.0793	0.0794	0.0794	0.0795	0.0795	0.0795	0.0796	0.0797
2.5 X_0	0.0958	0.1249	0.1269	0.1274	0.1277	0.1279	0.1280	0.1281	0.1282	0.1283	0.1284	0.1285	0.1285	0.1286	0.1286	0.1286	0.1287	0.1289
3.0 X_0	0.1312	0.1810	0.1851	0.1860	0.1865	0.1868	0.1871	0.1872	0.1874	0.1875	0.1876	0.1877	0.1878	0.1878	0.1879	0.1879	0.1880	0.1882
3.5 X_0	0.1672	0.2429	0.2500	0.2518	0.2525	0.2530	0.2534	0.2536	0.2538	0.2540	0.2541	0.2542	0.2543	0.2544	0.2545	0.2545	0.2546	0.2548
4.0 X_0	0.2012	0.3065	0.3178	0.3206	0.3218	0.3225	0.3230	0.3234	0.3237	0.3239	0.3241	0.3242	0.3243	0.3244	0.3245	0.3246	0.3247	0.3250
4.5 X_0	0.2323	0.3688	0.3851	0.3893	0.3912	0.3923	0.3930	0.3935	0.3939	0.3941	0.3944	0.3946	0.3947	0.3949	0.3950	0.3950	0.3951	0.3955
5.0 X_0	0.2600	0.4276	0.4498	0.4558	0.4585	0.4600	0.4610	0.4616	0.4621	0.4625	0.4628	0.4631	0.4633	0.4634	0.4635	0.4637	0.4637	0.4642
5.5 X_0	0.2835	0.4816	0.5105	0.5186	0.5222	0.5243	0.5256	0.5265	0.5271	0.5276	0.5280	0.5283	0.5285	0.5287	0.5289	0.5290	0.5291	0.5296
6.0 X_0	0.3034	0.5297	0.5655	0.5760	0.5807	0.5835	0.5852	0.5863	0.5871	0.5877	0.5881	0.5885	0.5888	0.5891	0.5892	0.5894	0.5895	0.5901
6.5 X_0	0.3195	0.5712	0.6140	0.6270	0.6330	0.6364	0.6385	0.6400	0.6410	0.6417	0.6423	0.6427	0.6431	0.6434	0.6436	0.6438	0.6439	0.6446
7.0 X_0	0.3329	0.6067	0.6564	0.6721	0.6794	0.6836	0.6862	0.6879	0.6892	0.6901	0.6908	0.6913	0.6917	0.6921	0.6923	0.6925	0.6927	0.6935
7.5 X_0	0.3437	0.6368	0.6930	0.7115	0.7202	0.7251	0.7283	0.7304	0.7318	0.7329	0.7337	0.7344	0.7349	0.7353	0.7356	0.7358	0.7360	0.7369
8.0 X_0	0.3523	0.6619	0.7241	0.7453	0.7555	0.7613	0.7649	0.7674	0.7691	0.7704	0.7714	0.7721	0.7727	0.7731	0.7735	0.7737	0.7740	0.7749
8.5 X_0	0.3591	0.6827	0.7504	0.7742	0.7859	0.7926	0.7968	0.7997	0.8017	0.8032	0.8043	0.8051	0.8058	0.8063	0.8067	0.8070	0.8073	0.8084
9.0 X_0	0.3644	0.6998	0.7724	0.7986	0.8118	0.8193	0.8241	0.8275	0.8297	0.8314	0.8326	0.8336	0.8343	0.8349	0.8353	0.8357	0.8360	0.8372
9.5 X_0	0.3685	0.7137	0.7908	0.8193	0.8338	0.8422	0.8476	0.8513	0.8538	0.8557	0.8571	0.8581	0.8590	0.8596	0.8601	0.8605	0.8608	0.8621
10.0 X_0	0.3717	0.7248	0.8058	0.8364	0.8521	0.8613	0.8673	0.8714	0.8742	0.8763	0.8778	0.8790	0.8799	0.8806	0.8811	0.8816	0.8819	0.8834
10.5 X_0	0.3742	0.7339	0.8182	0.8507	0.8676	0.8776	0.8841	0.8885	0.8916	0.8939	0.8956	0.8968	0.8978	0.8986	0.8992	0.8997	0.9000	0.9017
11.0 X_0	0.3761	0.7411	0.8283	0.8625	0.8805	0.8913	0.8982	0.9030	0.9063	0.9088	0.9106	0.9120	0.9131	0.9139	0.9145	0.9150	0.9155	0.9172
11.5 X_0	0.3776	0.7469	0.8364	0.8721	0.8911	0.9025	0.9099	0.9150	0.9185	0.9212	0.9232	0.9246	0.9258	0.9267	0.9274	0.9279	0.9284	0.9303
12.0 X_0	0.3787	0.7515	0.8432	0.8802	0.9000	0.9119	0.9198	0.9252	0.9290	0.9318	0.9339	0.9355	0.9367	0.9377	0.9384	0.9390	0.9394	0.9415
12.5 X_0	0.3797	0.7552	0.8487	0.8868	0.9073	0.9198	0.9280	0.9337	0.9377	0.9407	0.9429	0.9446	0.9459	0.9469	0.9477	0.9483	0.9488	0.9510
13.0 X_0	0.3803	0.7580	0.8530	0.8921	0.9131	0.9261	0.9347	0.9407	0.9448	0.9480	0.9503	0.9521	0.9535	0.9546	0.9554	0.9560	0.9565	0.9588
13.5 X_0	0.3808	0.7602	0.8564	0.8962	0.9179	0.9313	0.9402	0.9464	0.9507	0.9540	0.9565	0.9583	0.9598	0.9609	0.9618	0.9624	0.9630	0.9654
14.0 X_0	0.3812	0.7620	0.8592	0.8997	0.9219	0.9356	0.9449	0.9513	0.9558	0.9592	0.9617	0.9636	0.9651	0.9663	0.9672	0.9679	0.9685	0.9711

14.5 X_0	0.3816	0.7634	0.8615	0.9025	0.9251	0.9392	0.9487	0.9553	0.9600	0.9634	0.9661	0.9681	0.9696	0.9709	0.9718	0.9726	0.9732	0.9758
15.0 X_0	0.3818	0.7646	0.8633	0.9049	0.9279	0.9422	0.9519	0.9587	0.9635	0.9670	0.9698	0.9718	0.9734	0.9747	0.9757	0.9765	0.9771	0.9799
15.5 X_0	0.3820	0.7655	0.8648	0.9068	0.9301	0.9447	0.9546	0.9614	0.9663	0.9700	0.9728	0.9749	0.9766	0.9779	0.9789	0.9797	0.9804	0.9832
16.0 X_0	0.3821	0.7661	0.8659	0.9082	0.9318	0.9466	0.9567	0.9636	0.9687	0.9724	0.9753	0.9775	0.9792	0.9806	0.9816	0.9824	0.9831	0.9860
16.5 X_0	0.3823	0.7667	0.8668	0.9095	0.9332	0.9482	0.9584	0.9655	0.9706	0.9744	0.9774	0.9796	0.9813	0.9827	0.9838	0.9846	0.9853	0.9884
17.0 X_0	0.3824	0.7671	0.8675	0.9104	0.9343	0.9495	0.9598	0.9670	0.9722	0.9761	0.9791	0.9813	0.9831	0.9845	0.9856	0.9865	0.9872	0.9903
17.5 X_0	0.3824	0.7675	0.8681	0.9112	0.9353	0.9505	0.9609	0.9682	0.9735	0.9774	0.9804	0.9827	0.9845	0.9860	0.9871	0.9880	0.9887	0.9919
18.0 X_0	0.3825	0.7677	0.8685	0.9118	0.9360	0.9513	0.9618	0.9692	0.9745	0.9785	0.9816	0.9839	0.9857	0.9873	0.9884	0.9893	0.9900	0.9932
18.5 X_0	0.3825	0.7680	0.8689	0.9123	0.9367	0.9521	0.9626	0.9700	0.9754	0.9794	0.9826	0.9849	0.9868	0.9883	0.9894	0.9903	0.9911	0.9944
19.0 X_0	0.3826	0.7681	0.8692	0.9127	0.9372	0.9526	0.9632	0.9707	0.9761	0.9802	0.9833	0.9857	0.9876	0.9892	0.9903	0.9912	0.9920	0.9954
19.5 X_0	0.3826	0.7683	0.8695	0.9131	0.9376	0.9531	0.9637	0.9713	0.9768	0.9808	0.9840	0.9864	0.9883	0.9899	0.9910	0.9920	0.9927	0.9962
20.0 X_0	0.3826	0.7684	0.8696	0.9133	0.9379	0.9534	0.9641	0.9717	0.9772	0.9813	0.9845	0.9869	0.9889	0.9904	0.9916	0.9925	0.9933	0.9968
20.5 X_0	0.3826	0.7685	0.8698	0.9135	0.9382	0.9538	0.9645	0.9721	0.9776	0.9818	0.9850	0.9874	0.9894	0.9909	0.9921	0.9931	0.9938	0.9973
21.0 X_0	0.3826	0.7685	0.8699	0.9136	0.9383	0.9540	0.9647	0.9723	0.9779	0.9821	0.9853	0.9878	0.9897	0.9913	0.9925	0.9934	0.9942	0.9978
21.5 X_0	0.3826	0.7686	0.8700	0.9138	0.9385	0.9542	0.9650	0.9726	0.9782	0.9824	0.9856	0.9881	0.9900	0.9916	0.9928	0.9938	0.9945	0.9982
22.0 X_0	0.3827	0.7686	0.8700	0.9139	0.9387	0.9544	0.9652	0.9728	0.9784	0.9826	0.9859	0.9883	0.9903	0.9919	0.9931	0.9941	0.9949	0.9985
22.5 X_0	0.3827	0.7686	0.8701	0.9140	0.9388	0.9545	0.9653	0.9730	0.9786	0.9828	0.9861	0.9885	0.9905	0.9921	0.9933	0.9943	0.9951	0.9988
23.0 X_0	0.3827	0.7686	0.8701	0.9140	0.9389	0.9546	0.9654	0.9731	0.9788	0.9830	0.9862	0.9887	0.9907	0.9923	0.9935	0.9945	0.9953	0.9990
23.5 X_0	0.3827	0.7687	0.8702	0.9141	0.9389	0.9547	0.9655	0.9732	0.9789	0.9831	0.9863	0.9888	0.9909	0.9925	0.9937	0.9947	0.9955	0.9992
24.0 X_0	0.3827	0.7687	0.8702	0.9141	0.9390	0.9547	0.9656	0.9733	0.9790	0.9832	0.9864	0.9890	0.9910	0.9926	0.9938	0.9948	0.9956	0.9993
24.5 X_0	0.3827	0.7687	0.8702	0.9141	0.9390	0.9548	0.9657	0.9733	0.9790	0.9832	0.9865	0.9890	0.9911	0.9927	0.9939	0.9949	0.9957	0.9994
25.0 X_0	0.3827	0.7687	0.8702	0.9142	0.9390	0.9548	0.9657	0.9734	0.9791	0.9833	0.9866	0.9891	0.9911	0.9927	0.9940	0.9950	0.9958	0.9995
25.5 X_0	0.3827	0.7687	0.8702	0.9142	0.9391	0.9548	0.9657	0.9734	0.9791	0.9833	0.9866	0.9892	0.9912	0.9928	0.9940	0.9950	0.9958	0.9996
26.0 X_0	0.3827	0.7687	0.8702	0.9142	0.9391	0.9549	0.9658	0.9735	0.9792	0.9834	0.9867	0.9892	0.9913	0.9929	0.9941	0.9951	0.9959	0.9997
26.5 X_0	0.3827	0.7687	0.8703	0.9142	0.9391	0.9549	0.9658	0.9735	0.9792	0.9834	0.9867	0.9893	0.9913	0.9929	0.9941	0.9952	0.9959	0.9997
27.0 X_0	0.3827	0.7687	0.8703	0.9142	0.9391	0.9549	0.9658	0.9735	0.9792	0.9834	0.9867	0.9893	0.9913	0.9930	0.9942	0.9952	0.9960	0.9998
27.5 X_0	0.3827	0.7687	0.8703	0.9142	0.9391	0.9549	0.9658	0.9735	0.9792	0.9835	0.9868	0.9893	0.9913	0.9930	0.9942	0.9952	0.9960	0.9998
28.0 X_0	0.3827	0.7687	0.8703	0.9142	0.9391	0.9549	0.9658	0.9736	0.9793	0.9835	0.9868	0.9893	0.9914	0.9930	0.9942	0.9952	0.9960	0.9998
28.5 X_0	0.3827	0.7687	0.8703	0.9142	0.9391	0.9549	0.9658	0.9736	0.9793	0.9835	0.9868	0.9893	0.9914	0.9930	0.9942	0.9953	0.9961	0.9999
29.0 X_0	0.3827	0.7687	0.8703	0.9142	0.9391	0.9549	0.9659	0.9736	0.9793	0.9835	0.9868	0.9894	0.9914	0.9930	0.9943	0.9953	0.9961	0.9999
29.5 X_0	0.3827	0.7687	0.8703	0.9142	0.9391	0.9549	0.9659	0.9736	0.9793	0.9835	0.9868	0.9894	0.9914	0.9930	0.9943	0.9953	0.9961	0.9999
30.0 X_0	0.3827	0.7687	0.8703	0.9142	0.9391	0.9550	0.9659	0.9736	0.9793	0.9836	0.9869	0.9894	0.9915	0.9931	0.9943	0.9954	0.9962	1.0000

TABLE 27. Integrated Cerenkov light production distribution of 8.000 GeV electrons based on 800 EGS generated showers.

Ring→ Depth↓	0	1	2	3	4	5	6	7	8	9	10	11	12	13	14	15	16	17
0.5 X_0	0.0021	0.0022	0.0022	0.0022	0.0022	0.0022	0.0023	0.0023	0.0023	0.0023	0.0023	0.0023	0.0023	0.0024	0.0024	0.0024	0.0024	0.0024
1.0 X_0	0.0072	0.0078	0.0078	0.0078	0.0078	0.0079	0.0079	0.0079	0.0079	0.0079	0.0080	0.0080	0.0080	0.0080	0.0080	0.0080	0.0080	0.0081
1.5 X_0	0.0167	0.0190	0.0191	0.0192	0.0192	0.0193	0.0193	0.0193	0.0194	0.0194	0.0194	0.0194	0.0195	0.0195	0.0195	0.0195	0.0195	0.0196
2.0 X_0	0.0314	0.0379	0.0383	0.0384	0.0384	0.0385	0.0386	0.0386	0.0387	0.0387	0.0387	0.0388	0.0388	0.0388	0.0388	0.0388	0.0389	0.0390
2.5 X_0	0.0515	0.0656	0.0665	0.0667	0.0669	0.0670	0.0671	0.0671	0.0672	0.0672	0.0673	0.0673	0.0674	0.0674	0.0674	0.0674	0.0675	0.0676
3.0 X_0	0.0765	0.1020	0.1040	0.1044	0.1047	0.1049	0.1050	0.1051	0.1052	0.1053	0.1053	0.1054	0.1054	0.1054	0.1055	0.1055	0.1055	0.1057
3.5 X_0	0.1050	0.1461	0.1497	0.1506	0.1510	0.1513	0.1515	0.1516	0.1518	0.1518	0.1519	0.1520	0.1521	0.1521	0.1521	0.1522	0.1522	0.1524
4.0 X_0	0.1353	0.1966	0.2025	0.2039	0.2046	0.2050	0.2054	0.2056	0.2058	0.2059	0.2060	0.2061	0.2062	0.2062	0.2063	0.2063	0.2064	0.2066
4.5 X_0	0.1661	0.2508	0.2598	0.2621	0.2632	0.2638	0.2643	0.2646	0.2649	0.2650	0.2652	0.2653	0.2654	0.2655	0.2655	0.2656	0.2656	0.2659
5.0 X_0	0.1957	0.3062	0.3191	0.3227	0.3242	0.3251	0.3257	0.3262	0.3265	0.3268	0.3270	0.3271	0.3272	0.3273	0.3274	0.3275	0.3275	0.3279
5.5 X_0	0.2235	0.3612	0.3788	0.3838	0.3859	0.3872	0.3880	0.3886	0.3891	0.3894	0.3896	0.3898	0.3900	0.3901	0.3902	0.3903	0.3904	0.3908
6.0 X_0	0.2486	0.4141	0.4369	0.4437	0.4467	0.4484	0.4495	0.4503	0.4508	0.4512	0.4516	0.4518	0.4520	0.4522	0.4523	0.4524	0.4525	0.4529
6.5 X_0	0.2710	0.4635	0.4922	0.5009	0.5047	0.5069	0.5084	0.5094	0.5101	0.5106	0.5110	0.5113	0.5115	0.5117	0.5119	0.5120	0.5121	0.5127
7.0 X_0	0.2906	0.5091	0.5438	0.5546	0.5596	0.5624	0.5642	0.5655	0.5663	0.5669	0.5675	0.5678	0.5681	0.5684	0.5686	0.5687	0.5688	0.5694
7.5 X_0	0.3075	0.5500	0.5910	0.6042	0.6103	0.6137	0.6160	0.6175	0.6186	0.6194	0.6200	0.6204	0.6208	0.6211	0.6213	0.6215	0.6216	0.6223
8.0 X_0	0.3215	0.5860	0.6331	0.6488	0.6561	0.6603	0.6630	0.6649	0.6662	0.6671	0.6678	0.6683	0.6688	0.6691	0.6694	0.6696	0.6697	0.6706
8.5 X_0	0.3333	0.6173	0.6706	0.6887	0.6974	0.7023	0.7055	0.7077	0.7092	0.7103	0.7111	0.7118	0.7123	0.7126	0.7130	0.7132	0.7134	0.7143
9.0 X_0	0.3430	0.6440	0.7031	0.7236	0.7337	0.7394	0.7431	0.7456	0.7474	0.7487	0.7496	0.7503	0.7509	0.7513	0.7517	0.7520	0.7522	0.7532
9.5 X_0	0.3508	0.6667	0.7311	0.7540	0.7654	0.7719	0.7761	0.7790	0.7811	0.7825	0.7836	0.7844	0.7850	0.7855	0.7859	0.7863	0.7865	0.7877
10.0 X_0	0.3572	0.6858	0.7551	0.7803	0.7929	0.8003	0.8050	0.8083	0.8106	0.8122	0.8134	0.8144	0.8151	0.8157	0.8161	0.8165	0.8167	0.8180
10.5 X_0	0.3625	0.7018	0.7755	0.8029	0.8167	0.8250	0.8302	0.8338	0.8363	0.8381	0.8395	0.8406	0.8413	0.8420	0.8425	0.8429	0.8432	0.8446
11.0 X_0	0.3667	0.7149	0.7926	0.8219	0.8369	0.8458	0.8515	0.8555	0.8584	0.8604	0.8619	0.8630	0.8639	0.8646	0.8651	0.8656	0.8659	0.8675
11.5 X_0	0.3701	0.7259	0.8070	0.8381	0.8542	0.8638	0.8700	0.8743	0.8774	0.8796	0.8812	0.8825	0.8834	0.8842	0.8848	0.8853	0.8856	0.8873
12.0 X_0	0.3728	0.7349	0.8190	0.8517	0.8688	0.8791	0.8858	0.8904	0.8938	0.8961	0.8979	0.8993	0.9003	0.9011	0.9018	0.9023	0.9027	0.9045
12.5 X_0	0.3749	0.7422	0.8290	0.8633	0.8813	0.8923	0.8993	0.9043	0.9079	0.9104	0.9123	0.9138	0.9149	0.9158	0.9165	0.9171	0.9175	0.9194
13.0 X_0	0.3767	0.7481	0.8373	0.8730	0.8917	0.9033	0.9107	0.9160	0.9198	0.9225	0.9245	0.9261	0.9272	0.9282	0.9290	0.9296	0.9300	0.9321
13.5 X_0	0.3779	0.7528	0.8439	0.8808	0.9004	0.9124	0.9203	0.9258	0.9298	0.9327	0.9348	0.9364	0.9377	0.9387	0.9395	0.9402	0.9407	0.9428
14.0 X_0	0.3789	0.7565	0.8493	0.8872	0.9075	0.9200	0.9282	0.9340	0.9382	0.9412	0.9435	0.9452	0.9465	0.9476	0.9485	0.9491	0.9496	0.9519

14.5 X_0	0.3797	0.7596	0.8538	0.8926	0.9134	0.9263	0.9348	0.9409	0.9452	0.9484	0.9508	0.9526	0.9540	0.9551	0.9560	0.9567	0.9572	0.9597
15.0 X_0	0.3803	0.7620	0.8573	0.8970	0.9184	0.9316	0.9404	0.9467	0.9512	0.9546	0.9570	0.9589	0.9603	0.9615	0.9625	0.9632	0.9637	0.9663
15.5 X_0	0.3807	0.7638	0.8602	0.9005	0.9223	0.9359	0.9450	0.9515	0.9561	0.9596	0.9621	0.9641	0.9656	0.9668	0.9678	0.9685	0.9691	0.9717
16.0 X_0	0.3810	0.7653	0.8625	0.9034	0.9256	0.9394	0.9487	0.9554	0.9602	0.9638	0.9664	0.9684	0.9700	0.9712	0.9722	0.9730	0.9736	0.9764
16.5 X_0	0.3813	0.7665	0.8644	0.9058	0.9284	0.9425	0.9520	0.9588	0.9637	0.9674	0.9701	0.9722	0.9738	0.9751	0.9761	0.9769	0.9776	0.9804
17.0 X_0	0.3814	0.7674	0.8659	0.9077	0.9305	0.9449	0.9546	0.9615	0.9665	0.9703	0.9731	0.9752	0.9768	0.9782	0.9793	0.9801	0.9807	0.9837
17.5 X_0	0.3816	0.7681	0.8671	0.9091	0.9322	0.9468	0.9566	0.9637	0.9688	0.9726	0.9755	0.9777	0.9794	0.9807	0.9818	0.9827	0.9834	0.9864
18.0 X_0	0.3817	0.7686	0.8680	0.9103	0.9336	0.9483	0.9582	0.9654	0.9706	0.9745	0.9774	0.9797	0.9814	0.9828	0.9839	0.9848	0.9855	0.9885
18.5 X_0	0.3818	0.7690	0.8687	0.9113	0.9348	0.9496	0.9597	0.9669	0.9722	0.9762	0.9792	0.9815	0.9832	0.9846	0.9858	0.9867	0.9874	0.9905
19.0 X_0	0.3819	0.7693	0.8693	0.9120	0.9357	0.9506	0.9608	0.9681	0.9735	0.9775	0.9805	0.9828	0.9846	0.9861	0.9872	0.9881	0.9888	0.9921
19.5 X_0	0.3819	0.7696	0.8697	0.9126	0.9364	0.9514	0.9617	0.9691	0.9745	0.9786	0.9816	0.9839	0.9857	0.9872	0.9884	0.9893	0.9900	0.9934
20.0 X_0	0.3820	0.7698	0.8701	0.9131	0.9369	0.9521	0.9624	0.9699	0.9753	0.9794	0.9825	0.9849	0.9867	0.9882	0.9894	0.9903	0.9911	0.9944
20.5 X_0	0.3820	0.7699	0.8703	0.9134	0.9374	0.9526	0.9629	0.9705	0.9760	0.9801	0.9832	0.9856	0.9874	0.9889	0.9902	0.9911	0.9918	0.9953
21.0 X_0	0.3820	0.7701	0.8706	0.9138	0.9378	0.9531	0.9635	0.9710	0.9766	0.9807	0.9839	0.9863	0.9881	0.9897	0.9909	0.9918	0.9926	0.9961
21.5 X_0	0.3821	0.7702	0.8708	0.9141	0.9381	0.9534	0.9639	0.9715	0.9771	0.9813	0.9844	0.9869	0.9887	0.9902	0.9915	0.9925	0.9932	0.9967
22.0 X_0	0.3821	0.7703	0.8709	0.9143	0.9384	0.9537	0.9642	0.9719	0.9775	0.9817	0.9849	0.9873	0.9892	0.9907	0.9920	0.9930	0.9937	0.9973
22.5 X_0	0.3821	0.7704	0.8710	0.9145	0.9386	0.9540	0.9645	0.9722	0.9778	0.9820	0.9852	0.9877	0.9896	0.9911	0.9924	0.9934	0.9941	0.9977
23.0 X_0	0.3821	0.7704	0.8711	0.9146	0.9388	0.9542	0.9647	0.9724	0.9780	0.9823	0.9855	0.9880	0.9899	0.9915	0.9927	0.9937	0.9945	0.9981
23.5 X_0	0.3821	0.7704	0.8712	0.9147	0.9389	0.9544	0.9649	0.9726	0.9782	0.9825	0.9857	0.9882	0.9901	0.9917	0.9930	0.9940	0.9947	0.9984
24.0 X_0	0.3821	0.7705	0.8713	0.9148	0.9390	0.9545	0.9650	0.9727	0.9784	0.9827	0.9859	0.9884	0.9903	0.9919	0.9932	0.9942	0.9949	0.9986
24.5 X_0	0.3821	0.7705	0.8713	0.9148	0.9391	0.9546	0.9651	0.9729	0.9785	0.9828	0.9861	0.9886	0.9905	0.9921	0.9934	0.9944	0.9951	0.9989
25.0 X_0	0.3821	0.7705	0.8714	0.9149	0.9391	0.9547	0.9652	0.9730	0.9786	0.9830	0.9862	0.9887	0.9907	0.9922	0.9935	0.9945	0.9953	0.9990
25.5 X_0	0.3821	0.7705	0.8714	0.9149	0.9392	0.9547	0.9653	0.9731	0.9788	0.9831	0.9863	0.9889	0.9908	0.9924	0.9937	0.9947	0.9955	0.9992
26.0 X_0	0.3821	0.7706	0.8714	0.9150	0.9393	0.9548	0.9654	0.9732	0.9789	0.9832	0.9864	0.9890	0.9909	0.9925	0.9938	0.9948	0.9956	0.9994
26.5 X_0	0.3821	0.7706	0.8714	0.9150	0.9393	0.9548	0.9654	0.9732	0.9789	0.9833	0.9865	0.9891	0.9910	0.9926	0.9939	0.9949	0.9957	0.9995
27.0 X_0	0.3821	0.7706	0.8714	0.9150	0.9393	0.9549	0.9655	0.9733	0.9790	0.9833	0.9866	0.9891	0.9911	0.9927	0.9940	0.9950	0.9958	0.9996
27.5 X_0	0.3821	0.7706	0.8715	0.9151	0.9394	0.9549	0.9655	0.9733	0.9790	0.9834	0.9866	0.9892	0.9911	0.9927	0.9940	0.9951	0.9958	0.9996
28.0 X_0	0.3821	0.7706	0.8715	0.9151	0.9394	0.9549	0.9655	0.9733	0.9790	0.9834	0.9867	0.9892	0.9912	0.9928	0.9941	0.9951	0.9959	0.9997
28.5 X_0	0.3822	0.7706	0.8715	0.9151	0.9394	0.9549	0.9656	0.9734	0.9791	0.9834	0.9867	0.9892	0.9912	0.9928	0.9941	0.9951	0.9959	0.9997
29.0 X_0	0.3822	0.7706	0.8715	0.9151	0.9394	0.9549	0.9656	0.9734	0.9791	0.9834	0.9867	0.9893	0.9912	0.9928	0.9941	0.9952	0.9960	0.9998
29.5 X_0	0.3822	0.7706	0.8715	0.9151	0.9394	0.9550	0.9656	0.9734	0.9791	0.9835	0.9867	0.9893	0.9913	0.9929	0.9942	0.9952	0.9960	0.9998
30.0 X_0	0.3822	0.7706	0.8715	0.9151	0.9395	0.9550	0.9656	0.9735	0.9792	0.9836	0.9868	0.9894	0.9914	0.9930	0.9943	0.9953	0.9961	1.0000

TABLE 28. Integrated Cerenkov light production distribution of 22.627 GeV electrons based on 564 EGS generated showers.

Ring→ Depth↓	0	1	2	3	4	5	6	7	8	9	10	11	12	13	14	15	16	17
0.5 X_0	0.0008	0.0008	0.0008	0.0008	0.0008	0.0008	0.0009	0.0009	0.0009	0.0009	0.0009	0.0009	0.0009	0.0009	0.0009	0.0009	0.0009	0.0010
1.0 X_0	0.0030	0.0032	0.0032	0.0032	0.0032	0.0032	0.0033	0.0033	0.0033	0.0033	0.0033	0.0033	0.0033	0.0033	0.0034	0.0034	0.0034	0.0034
1.5 X_0	0.0076	0.0085	0.0086	0.0086	0.0086	0.0086	0.0086	0.0087	0.0087	0.0087	0.0087	0.0087	0.0087	0.0088	0.0088	0.0088	0.0088	0.0089
2.0 X_0	0.0156	0.0183	0.0184	0.0185	0.0185	0.0186	0.0186	0.0186	0.0187	0.0187	0.0187	0.0187	0.0187	0.0188	0.0188	0.0188	0.0188	0.0189
2.5 X_0	0.0278	0.0340	0.0344	0.0345	0.0346	0.0346	0.0347	0.0347	0.0348	0.0348	0.0348	0.0348	0.0349	0.0349	0.0349	0.0349	0.0349	0.0350
3.0 X_0	0.0442	0.0562	0.0571	0.0574	0.0575	0.0576	0.0577	0.0577	0.0578	0.0578	0.0579	0.0579	0.0579	0.0580	0.0580	0.0580	0.0580	0.0582
3.5 X_0	0.0647	0.0857	0.0875	0.0879	0.0882	0.0883	0.0884	0.0885	0.0886	0.0887	0.0887	0.0888	0.0888	0.0888	0.0889	0.0889	0.0889	0.0891
4.0 X_0	0.0887	0.1221	0.1252	0.1260	0.1264	0.1266	0.1268	0.1270	0.1271	0.1272	0.1272	0.1273	0.1273	0.1274	0.1274	0.1275	0.1275	0.1277
4.5 X_0	0.1152	0.1645	0.1696	0.1709	0.1715	0.1719	0.1721	0.1723	0.1725	0.1726	0.1727	0.1728	0.1729	0.1729	0.1730	0.1730	0.1731	0.1733
5.0 X_0	0.1430	0.2111	0.2188	0.2208	0.2218	0.2223	0.2227	0.2230	0.2232	0.2234	0.2235	0.2236	0.2237	0.2238	0.2238	0.2239	0.2239	0.2242
5.5 X_0	0.1708	0.2605	0.2715	0.2745	0.2758	0.2766	0.2772	0.2776	0.2778	0.2781	0.2782	0.2784	0.2785	0.2786	0.2786	0.2787	0.2788	0.2791
6.0 X_0	0.1979	0.3107	0.3258	0.3299	0.3319	0.3329	0.3337	0.3342	0.3346	0.3349	0.3351	0.3353	0.3354	0.3355	0.3356	0.3357	0.3358	0.3361
6.5 X_0	0.2235	0.3605	0.3803	0.3859	0.3886	0.3900	0.3910	0.3917	0.3922	0.3925	0.3928	0.3930	0.3932	0.3934	0.3935	0.3936	0.3936	0.3941
7.0 X_0	0.2470	0.4085	0.4334	0.4408	0.4442	0.4461	0.4474	0.4482	0.4488	0.4493	0.4497	0.4499	0.4502	0.4503	0.4505	0.4506	0.4507	0.4512
7.5 X_0	0.2683	0.4539	0.4842	0.4935	0.4979	0.5003	0.5019	0.5030	0.5038	0.5043	0.5048	0.5051	0.5054	0.5056	0.5057	0.5059	0.5060	0.5066
8.0 X_0	0.2872	0.4960	0.5320	0.5434	0.5489	0.5519	0.5539	0.5552	0.5561	0.5568	0.5573	0.5578	0.5581	0.5583	0.5585	0.5587	0.5588	0.5595
8.5 X_0	0.3039	0.5345	0.5763	0.5900	0.5966	0.6002	0.6026	0.6042	0.6053	0.6061	0.6068	0.6073	0.6077	0.6080	0.6082	0.6084	0.6085	0.6093
9.0 X_0	0.3184	0.5692	0.6168	0.6327	0.6405	0.6449	0.6477	0.6496	0.6509	0.6519	0.6526	0.6532	0.6537	0.6540	0.6543	0.6545	0.6547	0.6555
9.5 X_0	0.3307	0.5997	0.6527	0.6711	0.6801	0.6852	0.6885	0.6907	0.6923	0.6934	0.6943	0.6949	0.6955	0.6959	0.6962	0.6964	0.6966	0.6976
10.0 X_0	0.3411	0.6263	0.6847	0.7054	0.7157	0.7215	0.7253	0.7279	0.7297	0.7310	0.7320	0.7327	0.7333	0.7338	0.7341	0.7344	0.7347	0.7357
10.5 X_0	0.3499	0.6494	0.7128	0.7357	0.7472	0.7538	0.7581	0.7610	0.7631	0.7645	0.7657	0.7665	0.7672	0.7677	0.7681	0.7684	0.7687	0.7699
11.0 X_0	0.3574	0.6695	0.7376	0.7625	0.7753	0.7826	0.7875	0.7907	0.7930	0.7947	0.7959	0.7969	0.7976	0.7982	0.7986	0.7990	0.7993	0.8006
11.5 X_0	0.3636	0.6868	0.7590	0.7860	0.8000	0.8081	0.8134	0.8170	0.8196	0.8214	0.8228	0.8239	0.8247	0.8253	0.8258	0.8262	0.8265	0.8279
12.0 X_0	0.3685	0.7014	0.7774	0.8064	0.8215	0.8304	0.8362	0.8401	0.8429	0.8449	0.8464	0.8476	0.8485	0.8492	0.8497	0.8501	0.8505	0.8520
12.5 X_0	0.3725	0.7135	0.7930	0.8237	0.8398	0.8494	0.8557	0.8600	0.8630	0.8651	0.8668	0.8681	0.8691	0.8698	0.8704	0.8708	0.8712	0.8729
13.0 X_0	0.3759	0.7237	0.8062	0.8385	0.8556	0.8659	0.8726	0.8772	0.8804	0.8828	0.8846	0.8860	0.8870	0.8878	0.8884	0.8889	0.8893	0.8912
13.5 X_0	0.3786	0.7321	0.8172	0.8509	0.8690	0.8798	0.8870	0.8919	0.8954	0.8979	0.8998	0.9013	0.9024	0.9033	0.9039	0.9044	0.9049	0.9068
14.0 X_0	0.3807	0.7392	0.8267	0.8617	0.8806	0.8920	0.8996	0.9049	0.9085	0.9112	0.9133	0.9148	0.9160	0.9169	0.9176	0.9182	0.9186	0.9207

14.5 X_0	0.3825	0.7451	0.8345	0.8707	0.8903	0.9023	0.9103	0.9158	0.9197	0.9225	0.9247	0.9263	0.9276	0.9285	0.9293	0.9299	0.9304	0.9326
15.0 X_0	0.3840	0.7499	0.8411	0.8782	0.8985	0.9109	0.9193	0.9250	0.9291	0.9321	0.9343	0.9361	0.9374	0.9384	0.9392	0.9398	0.9404	0.9427
15.5 X_0	0.3852	0.7538	0.8465	0.8845	0.9054	0.9183	0.9270	0.9330	0.9372	0.9403	0.9427	0.9445	0.9459	0.9470	0.9478	0.9485	0.9490	0.9515
16.0 X_0	0.3861	0.7570	0.8509	0.8898	0.9113	0.9245	0.9335	0.9397	0.9441	0.9474	0.9498	0.9517	0.9532	0.9543	0.9552	0.9559	0.9565	0.9590
16.5 X_0	0.3870	0.7597	0.8547	0.8943	0.9162	0.9298	0.9390	0.9455	0.9500	0.9534	0.9560	0.9579	0.9595	0.9606	0.9615	0.9622	0.9628	0.9655
17.0 X_0	0.3876	0.7620	0.8579	0.8981	0.9204	0.9343	0.9438	0.9504	0.9551	0.9586	0.9612	0.9633	0.9648	0.9660	0.9669	0.9677	0.9683	0.9711
17.5 X_0	0.3880	0.7637	0.8604	0.9011	0.9239	0.9380	0.9477	0.9544	0.9593	0.9629	0.9656	0.9677	0.9693	0.9705	0.9715	0.9723	0.9729	0.9758
18.0 X_0	0.3884	0.7650	0.8624	0.9036	0.9266	0.9410	0.9508	0.9577	0.9627	0.9664	0.9691	0.9713	0.9730	0.9742	0.9752	0.9760	0.9767	0.9797
18.5 X_0	0.3887	0.7662	0.8641	0.9056	0.9290	0.9435	0.9535	0.9606	0.9656	0.9694	0.9722	0.9744	0.9761	0.9774	0.9784	0.9792	0.9799	0.9830
19.0 X_0	0.3889	0.7671	0.8654	0.9073	0.9308	0.9456	0.9557	0.9629	0.9680	0.9718	0.9747	0.9769	0.9787	0.9800	0.9810	0.9819	0.9826	0.9858
19.5 X_0	0.3891	0.7678	0.8665	0.9086	0.9324	0.9473	0.9576	0.9648	0.9700	0.9739	0.9768	0.9791	0.9808	0.9822	0.9832	0.9841	0.9848	0.9881
20.0 X_0	0.3892	0.7684	0.8675	0.9098	0.9337	0.9487	0.9591	0.9664	0.9717	0.9756	0.9786	0.9809	0.9827	0.9841	0.9852	0.9861	0.9868	0.9901
20.5 X_0	0.3893	0.7688	0.8681	0.9106	0.9347	0.9499	0.9603	0.9677	0.9730	0.9770	0.9800	0.9824	0.9842	0.9856	0.9867	0.9876	0.9884	0.9918
21.0 X_0	0.3894	0.7692	0.8687	0.9113	0.9355	0.9508	0.9613	0.9688	0.9741	0.9782	0.9812	0.9836	0.9855	0.9869	0.9880	0.9889	0.9897	0.9931
21.5 X_0	0.3895	0.7694	0.8691	0.9119	0.9362	0.9515	0.9621	0.9696	0.9751	0.9791	0.9822	0.9846	0.9865	0.9879	0.9890	0.9900	0.9907	0.9943
22.0 X_0	0.3895	0.7696	0.8694	0.9123	0.9367	0.9521	0.9628	0.9703	0.9758	0.9799	0.9830	0.9854	0.9873	0.9888	0.9899	0.9909	0.9916	0.9952
22.5 X_0	0.3896	0.7698	0.8697	0.9127	0.9371	0.9526	0.9633	0.9709	0.9764	0.9805	0.9837	0.9861	0.9880	0.9895	0.9906	0.9916	0.9924	0.9960
23.0 X_0	0.3896	0.7699	0.8700	0.9130	0.9375	0.9530	0.9638	0.9714	0.9770	0.9811	0.9843	0.9867	0.9886	0.9901	0.9913	0.9922	0.9930	0.9967
23.5 X_0	0.3896	0.7700	0.8701	0.9132	0.9378	0.9534	0.9642	0.9718	0.9774	0.9815	0.9847	0.9872	0.9891	0.9906	0.9918	0.9927	0.9935	0.9972
24.0 X_0	0.3897	0.7701	0.8703	0.9134	0.9380	0.9536	0.9645	0.9722	0.9777	0.9819	0.9851	0.9876	0.9895	0.9910	0.9922	0.9932	0.9940	0.9977
24.5 X_0	0.3897	0.7702	0.8704	0.9136	0.9382	0.9538	0.9647	0.9724	0.9780	0.9822	0.9854	0.9879	0.9899	0.9913	0.9925	0.9935	0.9943	0.9981
25.0 X_0	0.3897	0.7703	0.8705	0.9137	0.9384	0.9540	0.9649	0.9727	0.9783	0.9825	0.9857	0.9882	0.9902	0.9917	0.9928	0.9938	0.9946	0.9984
25.5 X_0	0.3897	0.7703	0.8706	0.9138	0.9385	0.9542	0.9651	0.9728	0.9785	0.9827	0.9859	0.9884	0.9904	0.9919	0.9931	0.9941	0.9949	0.9987
26.0 X_0	0.3897	0.7703	0.8706	0.9139	0.9386	0.9543	0.9652	0.9730	0.9786	0.9828	0.9861	0.9886	0.9906	0.9921	0.9933	0.9943	0.9951	0.9989
26.5 X_0	0.3897	0.7704	0.8707	0.9140	0.9387	0.9544	0.9653	0.9731	0.9788	0.9830	0.9862	0.9888	0.9907	0.9923	0.9935	0.9945	0.9953	0.9991
27.0 X_0	0.3897	0.7704	0.8707	0.9140	0.9387	0.9545	0.9654	0.9732	0.9789	0.9831	0.9864	0.9889	0.9909	0.9924	0.9936	0.9946	0.9954	0.9993
27.5 X_0	0.3897	0.7704	0.8707	0.9141	0.9388	0.9545	0.9655	0.9733	0.9790	0.9832	0.9865	0.9890	0.9910	0.9925	0.9937	0.9947	0.9956	0.9994
28.0 X_0	0.3897	0.7704	0.8708	0.9141	0.9388	0.9546	0.9656	0.9734	0.9790	0.9833	0.9865	0.9891	0.9911	0.9926	0.9938	0.9948	0.9956	0.9995
28.5 X_0	0.3897	0.7704	0.8708	0.9141	0.9389	0.9546	0.9656	0.9734	0.9791	0.9833	0.9866	0.9891	0.9911	0.9926	0.9939	0.9949	0.9957	0.9996
29.0 X_0	0.3897	0.7704	0.8708	0.9141	0.9389	0.9547	0.9656	0.9734	0.9791	0.9834	0.9866	0.9892	0.9912	0.9927	0.9939	0.9949	0.9958	0.9997
29.5 X_0	0.3897	0.7704	0.8708	0.9141	0.9389	0.9547	0.9656	0.9735	0.9791	0.9834	0.9867	0.9892	0.9912	0.9927	0.9939	0.9950	0.9958	0.9997
30.0 X_0	0.3897	0.7705	0.8708	0.9142	0.9390	0.9548	0.9658	0.9736	0.9793	0.9836	0.9868	0.9894	0.9914	0.9930	0.9942	0.9952	0.9960	1.0000

TABLE 29. Integrated Cerenkov light production distribution of 64.000 GeV electrons based on 300 EGS generated showers.

Ring→ Depth↓	0	1	2	3	4	5	6	7	8	9	10	11	12	13	14	15	16	17
0.5 X0	0.0003	0.0003	0.0003	0.0003	0.0003	0.0003	0.0003	0.0003	0.0003	0.0004	0.0004	0.0004	0.0004	0.0004	0.0004	0.0004	0.0004	0.0004
1.0 X0	0.0013	0.0014	0.0014	0.0014	0.0014	0.0014	0.0014	0.0014	0.0014	0.0014	0.0014	0.0014	0.0014	0.0014	0.0014	0.0014	0.0014	0.0015
1.5 X0	0.0034	0.0039	0.0039	0.0039	0.0039	0.0039	0.0039	0.0040	0.0040	0.0040	0.0040	0.0040	0.0040	0.0040	0.0040	0.0040	0.0040	0.0041
2.0 X0	0.0075	0.0087	0.0088	0.0088	0.0089	0.0089	0.0089	0.0089	0.0089	0.0089	0.0089	0.0090	0.0090	0.0090	0.0090	0.0090	0.0090	0.0091
2.5 X0	0.0140	0.0170	0.0172	0.0173	0.0173	0.0173	0.0174	0.0174	0.0174	0.0174	0.0174	0.0175	0.0175	0.0175	0.0175	0.0175	0.0175	0.0176
3.0 X0	0.0233	0.0295	0.0299	0.0301	0.0301	0.0302	0.0302	0.0303	0.0303	0.0303	0.0303	0.0304	0.0304	0.0304	0.0304	0.0304	0.0304	0.0305
3.5 X0	0.0359	0.0472	0.0481	0.0484	0.0485	0.0486	0.0486	0.0487	0.0487	0.0488	0.0488	0.0488	0.0488	0.0489	0.0489	0.0489	0.0489	0.0490
4.0 X0	0.0517	0.0706	0.0722	0.0727	0.0729	0.0730	0.0731	0.0732	0.0732	0.0733	0.0733	0.0734	0.0734	0.0734	0.0735	0.0735	0.0735	0.0736
4.5 X0	0.0708	0.1000	0.1029	0.1036	0.1039	0.1041	0.1043	0.1044	0.1045	0.1046	0.1046	0.1047	0.1047	0.1047	0.1048	0.1048	0.1048	0.1050
5.0 X0	0.0923	0.1346	0.1390	0.1402	0.1407	0.1410	0.1412	0.1414	0.1415	0.1416	0.1417	0.1418	0.1418	0.1419	0.1419	0.1420	0.1420	0.1422
5.5 X0	0.1155	0.1738	0.1805	0.1822	0.1830	0.1835	0.1838	0.1840	0.1842	0.1843	0.1845	0.1845	0.1846	0.1847	0.1847	0.1848	0.1848	0.1850
6.0 X0	0.1398	0.2166	0.2261	0.2287	0.2298	0.2305	0.2309	0.2312	0.2315	0.2316	0.2318	0.2319	0.2320	0.2321	0.2321	0.2322	0.2322	0.2325
6.5 X0	0.1645	0.2617	0.2745	0.2781	0.2797	0.2806	0.2812	0.2817	0.2820	0.2822	0.2824	0.2826	0.2827	0.2828	0.2829	0.2829	0.2830	0.2833
7.0 X0	0.1887	0.3060	0.3248	0.3297	0.3318	0.3330	0.3339	0.3344	0.3349	0.3352	0.3354	0.3356	0.3357	0.3359	0.3360	0.3360	0.3361	0.3365
7.5 X0	0.2118	0.3541	0.3753	0.3817	0.3845	0.3861	0.3872	0.3879	0.3885	0.3889	0.3892	0.3894	0.3896	0.3897	0.3899	0.3900	0.3900	0.3905
8.0 X0	0.2336	0.3993	0.4253	0.4334	0.4369	0.4391	0.4404	0.4413	0.4420	0.4425	0.4429	0.4432	0.4434	0.4436	0.4437	0.4438	0.4439	0.4445
8.5 X0	0.2538	0.4424	0.4735	0.4835	0.4880	0.4906	0.4923	0.4935	0.4943	0.4949	0.4953	0.4957	0.4960	0.4962	0.4964	0.4965	0.4966	0.4972
9.0 X0	0.2721	0.4829	0.5193	0.5313	0.5368	0.5400	0.5421	0.5435	0.5445	0.5452	0.5457	0.5462	0.5465	0.5467	0.5470	0.5471	0.5473	0.5479
9.5 X0	0.2885	0.5206	0.5625	0.5765	0.5831	0.5869	0.5894	0.5911	0.5922	0.5931	0.5937	0.5942	0.5946	0.5949	0.5951	0.5953	0.5955	0.5963
10.0 X0	0.3031	0.5552	0.6026	0.6188	0.6265	0.6310	0.6339	0.6359	0.6372	0.6382	0.6390	0.6396	0.6400	0.6404	0.6407	0.6409	0.6411	0.6419
10.5 X0	0.3157	0.5862	0.6391	0.6576	0.6664	0.6716	0.6750	0.6773	0.6788	0.6800	0.6809	0.6815	0.6820	0.6824	0.6828	0.6830	0.6832	0.6842
11.0 X0	0.3265	0.6136	0.6718	0.6926	0.7025	0.7085	0.7124	0.7150	0.7167	0.7180	0.7191	0.7198	0.7204	0.7208	0.7212	0.7215	0.7217	0.7228
11.5 X0	0.3358	0.6375	0.7007	0.7238	0.7349	0.7417	0.7461	0.7490	0.7510	0.7525	0.7537	0.7545	0.7551	0.7557	0.7561	0.7564	0.7566	0.7579
12.0 X0	0.3435	0.6584	0.7262	0.7514	0.7637	0.7712	0.7761	0.7794	0.7817	0.7833	0.7846	0.7855	0.7863	0.7868	0.7873	0.7877	0.7879	0.7893
12.5 X0	0.3501	0.6765	0.7486	0.7757	0.7892	0.7974	0.8028	0.8064	0.8089	0.8108	0.8122	0.8133	0.8141	0.8147	0.8152	0.8156	0.8159	0.8173
13.0 X0	0.3556	0.6919	0.7678	0.7969	0.8116	0.8205	0.8264	0.8303	0.8331	0.8351	0.8366	0.8378	0.8387	0.8394	0.8399	0.8403	0.8407	0.8423
13.5 X0	0.3602	0.7050	0.7844	0.8153	0.8310	0.8406	0.8470	0.8513	0.8543	0.8564	0.8581	0.8594	0.8603	0.8611	0.8617	0.8621	0.8625	0.8642
14.0 X0	0.3638	0.7161	0.7987	0.8311	0.8478	0.8581	0.8649	0.8696	0.8728	0.8751	0.8770	0.8783	0.8794	0.8802	0.8808	0.8813	0.8817	0.8835

$14.5\,X_0$	0.3667	0.7252	0.8106	0.8445	0.8621	0.8730	0.8802	0.8852	0.8886	0.8911	0.8931	0.8945	0.8957	0.8965	0.8972	0.8977	0.8982	0.9001
$15.0\,X_0$	0.3692	0.7328	0.8207	0.8561	0.8744	0.8859	0.8935	0.8987	0.9024	0.9051	0.9072	0.9087	0.9099	0.9108	0.9116	0.9121	0.9126	0.9147
$15.5\,X_0$	0.3712	0.7393	0.8293	0.8658	0.8850	0.8969	0.9050	0.9105	0.9144	0.9172	0.9194	0.9210	0.9223	0.9233	0.9241	0.9247	0.9252	0.9274
$16.0\,X_0$	0.3728	0.7447	0.8365	0.8740	0.8938	0.9063	0.9147	0.9205	0.9246	0.9275	0.9298	0.9316	0.9329	0.9339	0.9348	0.9354	0.9359	0.9382
$16.5\,X_0$	0.3742	0.7492	0.8425	0.8810	0.9014	0.9143	0.9230	0.9291	0.9334	0.9364	0.9389	0.9407	0.9421	0.9431	0.9440	0.9447	0.9452	0.9477
$17.0\,X_0$	0.3753	0.7528	0.8476	0.8869	0.9079	0.9211	0.9301	0.9364	0.9408	0.9440	0.9465	0.9484	0.9499	0.9510	0.9519	0.9526	0.9532	0.9557
$17.5\,X_0$	0.3761	0.7558	0.8517	0.8917	0.9131	0.9268	0.9360	0.9425	0.9471	0.9504	0.9530	0.9550	0.9565	0.9577	0.9586	0.9593	0.9599	0.9626
$18.0\,X_0$	0.3768	0.7582	0.8551	0.8957	0.9176	0.9316	0.9410	0.9477	0.9525	0.9559	0.9586	0.9606	0.9622	0.9634	0.9644	0.9651	0.9657	0.9685
$18.5\,X_0$	0.3774	0.7602	0.8580	0.8991	0.9214	0.9356	0.9454	0.9522	0.9571	0.9606	0.9634	0.9655	0.9671	0.9683	0.9693	0.9701	0.9707	0.9736
$19.0\,X_0$	0.3778	0.7618	0.8603	0.9019	0.9246	0.9390	0.9489	0.9559	0.9609	0.9645	0.9674	0.9695	0.9712	0.9724	0.9735	0.9743	0.9749	0.9779
$19.5\,X_0$	0.3782	0.7631	0.8621	0.9041	0.9270	0.9417	0.9518	0.9589	0.9640	0.9677	0.9706	0.9728	0.9745	0.9758	0.9769	0.9777	0.9784	0.9814
$20.0\,X_0$	0.3784	0.7641	0.8636	0.9060	0.9291	0.9439	0.9542	0.9614	0.9666	0.9704	0.9733	0.9756	0.9773	0.9786	0.9797	0.9806	0.9813	0.9844
$20.5\,X_0$	0.3786	0.7649	0.8649	0.9074	0.9308	0.9458	0.9562	0.9635	0.9688	0.9726	0.9756	0.9779	0.9797	0.9811	0.9822	0.9830	0.9837	0.9869
$21.0\,X_0$	0.3788	0.7655	0.8658	0.9087	0.9322	0.9474	0.9578	0.9653	0.9706	0.9745	0.9776	0.9799	0.9817	0.9831	0.9842	0.9851	0.9858	0.9891
$21.5\,X_0$	0.3789	0.7660	0.8667	0.9097	0.9334	0.9487	0.9593	0.9668	0.9722	0.9761	0.9792	0.9816	0.9834	0.9848	0.9860	0.9869	0.9876	0.9909
$22.0\,X_0$	0.3790	0.7665	0.8673	0.9105	0.9343	0.9497	0.9604	0.9680	0.9734	0.9774	0.9806	0.9830	0.9848	0.9862	0.9874	0.9883	0.9890	0.9924
$22.5\,X_0$	0.3791	0.7668	0.8678	0.9112	0.9351	0.9506	0.9613	0.9690	0.9745	0.9785	0.9817	0.9841	0.9859	0.9874	0.9886	0.9895	0.9902	0.9937
$23.0\,X_0$	0.3791	0.7671	0.8682	0.9117	0.9357	0.9513	0.9621	0.9698	0.9753	0.9794	0.9826	0.9850	0.9869	0.9884	0.9896	0.9905	0.9913	0.9948
$23.5\,X_0$	0.3792	0.7673	0.8686	0.9121	0.9363	0.9519	0.9627	0.9705	0.9761	0.9802	0.9834	0.9858	0.9877	0.9892	0.9904	0.9914	0.9921	0.9957
$24.0\,X_0$	0.3792	0.7674	0.8688	0.9125	0.9366	0.9523	0.9632	0.9710	0.9766	0.9807	0.9840	0.9864	0.9884	0.9899	0.9911	0.9920	0.9928	0.9964
$24.5\,X_0$	0.3792	0.7675	0.8690	0.9127	0.9370	0.9527	0.9637	0.9715	0.9771	0.9812	0.9845	0.9870	0.9889	0.9904	0.9916	0.9926	0.9934	0.9970
$25.0\,X_0$	0.3792	0.7676	0.8692	0.9130	0.9373	0.9530	0.9640	0.9719	0.9775	0.9816	0.9849	0.9874	0.9894	0.9909	0.9921	0.9931	0.9938	0.9975
$25.5\,X_0$	0.3792	0.7677	0.8693	0.9131	0.9375	0.9533	0.9643	0.9722	0.9778	0.9820	0.9853	0.9877	0.9897	0.9912	0.9925	0.9935	0.9942	0.9979
$26.0\,X_0$	0.3793	0.7677	0.8694	0.9133	0.9376	0.9535	0.9645	0.9724	0.9781	0.9822	0.9855	0.9881	0.9900	0.9915	0.9928	0.9938	0.9946	0.9983
$26.5\,X_0$	0.3793	0.7678	0.8695	0.9134	0.9378	0.9536	0.9647	0.9726	0.9783	0.9824	0.9858	0.9883	0.9903	0.9918	0.9930	0.9940	0.9948	0.9986
$27.0\,X_0$	0.3793	0.7678	0.8695	0.9135	0.9379	0.9538	0.9648	0.9727	0.9784	0.9826	0.9859	0.9885	0.9905	0.9920	0.9932	0.9942	0.9950	0.9988
$27.5\,X_0$	0.3793	0.7679	0.8696	0.9135	0.9380	0.9539	0.9649	0.9729	0.9786	0.9828	0.9861	0.9886	0.9906	0.9922	0.9934	0.9944	0.9952	0.9990
$28.0\,X_0$	0.3793	0.7679	0.8696	0.9136	0.9380	0.9539	0.9650	0.9730	0.9787	0.9829	0.9862	0.9887	0.9907	0.9923	0.9936	0.9945	0.9953	0.9992
$28.5\,X_0$	0.3793	0.7679	0.8697	0.9136	0.9381	0.9540	0.9651	0.9731	0.9788	0.9830	0.9863	0.9889	0.9909	0.9924	0.9937	0.9947	0.9955	0.9993
$29.0\,X_0$	0.3793	0.7679	0.8697	0.9137	0.9381	0.9541	0.9652	0.9731	0.9788	0.9831	0.9864	0.9889	0.9909	0.9925	0.9938	0.9948	0.9956	0.9994
$29.5\,X_0$	0.3793	0.7679	0.8697	0.9137	0.9382	0.9541	0.9652	0.9732	0.9789	0.9831	0.9865	0.9890	0.9910	0.9926	0.9939	0.9949	0.9957	0.9995
$30.0\,X_0$	0.3793	0.7679	0.8698	0.9138	0.9383	0.9543	0.9654	0.9734	0.9792	0.9834	0.9868	0.9894	0.9914	0.9929	0.9942	0.9952	0.9961	1.0000

REFERENCES

[1] Schwinger, J. *Phys. Rev.* **82**, 914 (1951).

[2] Lüders, G. *Mat. Fys. Medd. Kongl. Dan. Vid. Selsk.* **28**, 1 (1954).

[3] Pauli, W. *Niehls Bohr and the Development of Physics* (Pergamon Press, Oxford, 1955).

[4] Lee, T.D. & Yang, C.N. *Phys. Rev.* **104**, 254 (1956).

[5] Wu, C.S. *Phys. Rev.* **105**, 1413 (1957).

[6] Landau, L. *JETP* **5**, 336 (1957).

[7] Christenson, J.H., Cronin, J.W., Fitch, V.L. & Turlay, R. *Phys. Rev. Lett.* **13**, 138 (1964).

[8] Commins, E.D. & Bucksbaum, P.H. *Weak Interactions of Leptons and Quarks* (Cambridge University Press, Cambridge, 1983).

[9] Jarlskog, C. in *CP Violation* (ed. Jarlskog, C.) (World Scientific Publishing, Singapore, 1989).

[10] Kleinknecht, K. in *CP Violation* (ed. Jarlskog, C.) (World Scientific Publishing, Singapore, 1989).

[11] Fitch, V.L., Roth, R.F., Russ, J.L. & Vernon, W. *Phys. Rev. Lett.* **15**, 73 (1965).

[12] Barmin, V.V., *et al. Nucl. Phys.* **B 247**, 293 (1984).

[13] Particle Data Group, Yost, G.P., *et al. Phys. Lett.* **B 204**, 1 (1988).

[14] Carosi, R., *et al. Phys. Lett.* **237 B**, 303 (1990).

[15] Karlsson, M., *et al. Phys. Rev. Lett.* **64**, 2976 (1990).

[16] Wolfenstein, L. *Phys. Rev. Lett.* **23**, 562 (1964).

[17] Wu, T.T. & Yang, C.N. *Phys. Rev. Lett.* **13**, 380 (1964).

[18] The CERN-Munich (MPI) Collaboration *presented at the* Fourth International Conference on Meson Spectroscopy (Boston, 1974).

[19] Losty, M.F., *et al. Nucl. Phys.* **B 69**, 185 (1974).

[20] Bernstein, R.H., *et al. Phys. Rev. Lett.* **54**, 1631 (1985).

[21] Black, J.K., *et al. Phys. Rev. Lett.* **54**, 1628 (1985).

[22] Woods, M., *et al. Phys. Rev. Lett.* **60**, 1695 (1988).

[23] Burkhardt, H., *et al. Phys. Lett.* **206 B**, 169 (1988).

[24] Gsponer, A., *et al. Phys. Rev. Lett.* **42**, 13 (1979).

[25] Roehrig, J., *et al. Phys. Rev. Lett.* **38**, 1116 (1977).

[26] Asner, M., *et al. NIM* **A291**, 577 (1990).

[27] Papadimitriou, V., Ph.D. Thesis (University of Chicago, December, 1990).

[28] Gibbons, L.K., Ph.D. Thesis (University of Chicago, to be written).

[29] Carroll, A.S., *et al. Phys. Rev. Lett.* **44**, 529 (1980).

[30] Case, K.M. *Phys. Rev.* **103**, 1449 (1956).

[31] Good, M.L. *Phys. Rev.* **106**, 591 (1957).

[32] Kleinknecht, K. *Ann. Rev. Nucl. Sci.* **26**, 1 (1976).

[33] Nelson, W.R., Hirayama, H. & Rogers, D.W.O. (SLAC-Report-265, Aug. 1985).

[34] Atwood, W.B., Ph.D. Thesis (Stanford University, June, 1975).

[35] Longo, E. & Sestili, I. *NIM* **128**, 283 (1975).

[36] Heitler, W. *The Quantum Theory of Radiation* (Clarendon Press, Oxford, Eng., 1954).

[37] Atherton, H.W., *et al.* (CERN report 80-07, 1980).

[38] Malensek, A.J. (FNAL report FN-341, Oct. 1981).

[39] Schiz, A., *et al. Phys. Rev. D* **21**, 3010 (1980).

[40] Weinberg, S. *Phys. Rev. Lett.* **37**, 657 (1976).

[41] Kobayashi, M. & Maskawa, T. *Prog. Theor. Phys.* **49**, 652 (1973).

[42] Wolfenstein, L. *Phys. Rev. Lett.* **51**, 1945 (1983).

[43] Dalitz, R.H. *Acta Physica Austriaca Suppl.* **XXIV**, 393 (1982).

[44] Shabalin, E.P. *Sov. J. Nucl. Phys.* **28**, 75 (1978).

[45] Buras, A.J. in *CP Violation* (ed. Jarlskog, C.) (World Scientific, Singapore, 1989).

[46] Chivukula, R.S., Flynn, J.M. & Georgi, H. *Phys. Lett.* **94 B**, 453 (1986).

[47] Sharpe, S.R. *presented at the* Annual Meeting of the Division of Particles and Fields of the APS (Storrs, Connnecticut, Aug. 15-18, 1988).

[48] Reinders, L.J. & Rubinstein, H.R. *Phys. Lett.* **145 B**, 108 (1984).

[49] Gasser, J. & Leutwyler, H. *Phys. Rep. C* **87**, 77 (1982).

[50] Dominguez, C.A. & Rafael, E.d. *Ann. of Phys.* **174**, 372 (1987).

[51] Buchalla, G., Buras, A.J. & Harlander, M.K. *Nucl. Phys.* **B 337**, 313 (1990).

[52] Donoghue, J.F., Golowich, E., Holstein, B.R. & Trampetic, J. *Phys. Lett.* **179 B**, 361 (1986).

[53] Flynn, J.M. & Randall, L. *Phys. Lett.* **224 B**, 221 (1989).

[54] Sharpe, S.R., Gupta, R., Guralnik, G. & Kilcup, G. *Phys. Lett.* **192 B**, 149 (1987).

[55] Kim, C.S., Rosner, J.L. & Yuan, C.-P. *Phys. Rev. D* **42**, 96 (1990).

[56] Schubert, K. *presented at the* Conference on Phenomenology in High Energy Physics (Trieste, Italy, July 25-29, 1988) (Karlsruhe Univ. report KA-IEKP 88-04, 1988).

[57] Fulton, R., *et al. Phys. Rev. Lett.* **64**, 16 (1990).

[58] Kreinick, D.L. *in Proceedings of the XIV International Symposium on Lepton and Photon Interactions* (Stanford, California, 1989) (ed. Riordan, M.) (World Scientific, Singapore, 1989).

[59] Inami, T. & Lim, C.S. *Prog. Theor. Phys.* **65**, 297 (1981).

[60] Pich, A. & de Rafael, E. *Phys. Lett.* **158 B**, 477 (1985).

[61] de Rafael, E. in *CP Violation* (ed. Jarlskog, C.) (World Scientific, Singapore, 1988).

[62] Decker, R. *Nucl. Phys.* **B 277**, 661 (1986).

[63] Kilcup, G.W., Sharpe, S.R., Gupta, R. & Patel, A. *Phys. Rev. Lett.* **64**, 25 (1990).

[64] Danilov, M.V. *in Proceedings of the XIV International Symposium on Lepton and Photon Interactions* (Stanford, California, 1989) (ed. Riordan, M.) (World Scientific, Singapore, 1989).

[65] Ong, R.A., *et al. Phys. Rev. Lett.* **62**, 1236 (1989).

[66] Wise, M.B. *in Proceedings of the Banff Summer Institute* (Banff, Alberta, Aug. 14-26, 1988) (eds. Kamal, A.N. & Khanna, F. C.) (World Scientific, Singapore, 1989).

[67] Adler, J., *et al. Phys. Rev. Lett.* **60**, 1375 (1988).

[68] Rosner, J.L. (Enrico Fermi Institute report EFI 90-52, 1990).

[69] Campagnari, C., *presented at the* Twenty-fifth International Conference on High Energy Physics (Singapore, Aug. 2-8, 1990) (to be published).

[70] Rosner, J.L. *in Proceedings of the Banff Summer Institute* (Banff, Alberta, Aug. 14-26, 1988) (eds. Kamal, A.N. & Khanna, F. C.) (World Scientific, Singapore, 1989).

[71] Barr, G.D., *et al.* (CERN report EP/90-69, 1990).

[72] Dib, C.O., Dunietz, I. & Gilman, F.J. *Phys. Rev. D* **39**, 2639 (1989).

[73] Ohl, K.E., *et al. Phys. Rev. Lett.* **64**, 2755 (1990).

[74] Barker, A., *et al. Phys. Rev. D* **41**, 3546 (1990).

[75] Dib, C.O., Dunietz, I. & Gilman, F.J. (SLAC report SLAC-PUB-4840, 1989).

[76] Littenberg, L.S. *Phys. Rev. D* **39**, 3322 (1989).

[77] *The Physics Program of a High Luminosity Asymmetric B factory at SLAC* (ed. Hitlin, D.) (SLAC report SLAC-353, 1989).